



Development of Brash Ice Growth Models and Estimation of the Energy Needs to Manage Ice in the Yamal LNG port in Sabetta

Kyriakos Chomatas



Master of Science Case Study

Development of Brash Ice Growth Models and Estimation of the Energy Needs to Manage Ice in the Yamal LNG port in Sabetta

Master of Science Case Study

In part fulfillment for the degree of Master of Science in Offshore and Dredging Engineering,
at Delft University of Technology.

Graduate Student : Kyriakos Chomatas
Graduation Date: September 24, 2015

Graduation Committee

Prof. Ir. Andrei Metrikine :
Ir. Jeroen Hoving:
Dr. Ir. K.N. (Karel) van Dalen:
Prof. Ir. Kaj Riska:

Delft University of Technology
Delft University of Technology
Delft University of Technology
TOTAL S.A

Abstract

Navigation in extreme cold conditions, means repeated ice breaking in navigation channels and harbour basins. The broken ice resulting from this repeating procedure, is called “Brash Ice”, in opposite to “sea ice” which is formed statically in calm water. Just after an ice breaking event, caused by a vessel transit, there is a lot of water near the surface, exposed to freezing without the insulation that the static ice has with either a snow or a thick ice cover on top. This means faster formation of ice, compared to the case of static or sea ice.

The main objective of this graduation study is the development of Brash Ice Growth Models (BIGMs), with the use of both analytical and numerical thermodynamic methods that would be able to predict the thickness of the total ice or brash ice layer developing immediately below a ship track transited by vessels, with the basic assumption being that all the ice grown remains within the ship track.

This study presents the formulation for two solutions of BIGMs, one completely analytical (BIGM 1) and one partly numerical (BIGM 2), that are able to describe the model of ice regrowth through an existing brash ice layer in a track, the model of ice breaking resulting from a vessel passage, and undertake simulations for different operational scenarios, in the context of the Yamal LNG port in Sabetta. Moreover the BIGMs developed, give the ability to the user to insert multiple sets of field data, if these are available, in order to make the simulation more pragmatic and realistic, and predict brash ice growth in different areas and hence for different projects.

BIGM 2, which uses numerical thermodynamic calculations, gives the ability to the user to include all the heat fluxes involved in the ice growth phenomenon, in addition to describing some physical processes that take place in ice while it is growing, such as the variation of thermal properties in different layers in the ice mass, and internal absorption of a proportion of solar radiation. Comparison of brash ice field measurements from the Lulea port, and ice thickness predictions from BIGM 2, when it takes as input field and metocean data from the Lulea port, show very good agreement.

Furthermore, the study presents parametric analyses for different simulation cases to test the sensitivity of the models’ results, and specifically of the total ice thickness prediction in the end of the cold season, to changes in different input parameters.

Finally, the study illustrates the introduction into the BIGMs of a Brash Ice Management system (BIMS) effect, from the basic principles of growth and melting of ice. The BIMS effect, is introduced as a continuous melting effect applied during the simulations, due to an external heat flux applied in the bottom of brash ice, causing a brash ice strip to melt in every simulation time step. Using the BIMS effect, estimates of power to manage ice in the Yamal LNG port are provided, with the assumption that this energy is solely used for melting of the ice, with 100% efficiency.

Contents

Abstract	iv
List of Figures.....	x
List of Tables	xvii
Preface and Acknowledgements	xix
1. Introduction.....	1
1.1 Context	1
1.2 Brash Ice Growth Modeling for YAMAL LNG port	1
1.3 Description of the content of this study.....	2
2. Description of Brash Ice and Channels.....	4
2.1 Transit of harbor and coastal channels and sideways movement	7
2.2 Sandkvist studies in Lulea, Sweden	8
2.3 Simplified description of brash ice formation in channels	11
2.4 Pictures of brash ice in the approach channel and port of Sabetta	13
3. Heat Conduction in Ice and the basic Sea-Ice Growth problem.....	16
3.1 Basic Equations of Heat conduction in Ice	16
3.2 Use of Analytic equations/models to predict sea-ice growth	17
4. Thermodynamic model of solid ice re-growth in BIGM 1: Modelling Brash Ice Growth using analytical equations for sea-ice growth	18
4.1 Thermodynamics of BIGM 1, use of the Stefan Law	18
4.1.1 Classical Stefan's Law for ice growth.....	18
4.1.2 Stefan's Law with the correction of ice-atmosphere coupling.....	19
4.1.3 Modified Stefan's Law extended to include the insulation effect due to a top layer ...	20
4.2 Introducing a brash ice melting effect into the model BIGM 1	22
4.3 Ice Growth Cycle in BIGM 1	23
4.3.1 No dry brash ice on top	23
4.3.2 BIGM 1 (with dry brash ice on top)	25
4.4 Advantages and Disadvantages of BIGM 1.....	27
4.4.1 Advantages	27
4.4.2 Disadvantages.....	27
5. Modeling of the growth of sea ice with numerical schemes	28

5.1	Choosing a numerical scheme for sea ice growth.....	29
5.2	The Upper Surface boundary condition	30
6.	Thermodynamic model of solid ice re-growth in BIGM 2: Modelling brash ice growth using numerical solutions for sea-ice growth	33
6.1	Thermodynamics of BIGM 2, use of the Ukita and Martinson numerical implicit scheme for solid ice growth	33
6.1.1	Structure of the model	34
6.1.2	Temperature Profile Calculation-Solution of the matrix system.....	34
6.1.3	Ice Growth Calculation	36
6.1.4	Grid System re-construction, in case of only solid ice growth system.....	37
6.1.5	Different Ice growth Implementation at initial time steps just after a breaking event	37
6.1.6	Extension of the matrix system to include dry brash ice or snow layers in the matrix formulation.....	38
6.1.7	Grid System re-construction in case of having a floating dry brash ice layer	40
6.1.8	Surface melting due to excessive radiation.....	41
6.1.9	Introducing the effect of solar radiation internal absorption in BIGM 2	42
6.1.10	Introducing the effect of varying conductivity and heat capacity.....	47
6.1.11	Inclusion of the latent heat flux equation to the top surface flux equilibrium equation	48
6.2	Introducing a brash ice melting effect into BIGM 2	49
6.3	Ice Growth Cycle in BIGM 2.....	49
6.3.1	No dry brash ice on top	49
6.3.2	With dry brash ice on top.....	49
6.4	Advantages and Disadvantages of BIGM 2.....	50
6.4.1	Advantages	50
6.4.2	Disadvantages.....	50
7.	Model for ice breaking (for both BIGM 1 and BIGM 2)	51
7.1	Description of the model.....	51
7.2	Main Assumptions of the ice breaking model.....	51
7.3	Calculation Procedure (no dry brash ice)	54
7.3.1	Description of the problem	54
7.3.2	Solution of the problem	54
7.4	Calculation procedure (with dry brash ice on top).....	56
7.4.1	Description of the problem	56
7.4.2	Solution of the problem	57

8.	Conditions of Brash Ice Growth in Sabetta	59
8.1	Air temperature	59
8.2	Wind Velocity	60
8.3	Radiation from the atmosphere, clouds and sun	61
8.4	Snow Precipitation	61
8.5	Sea Water Temperature	61
8.6	Seawater Salinity	62
9.	Description of the reference case for Sabetta	64
9.1	Scenario	64
9.2	Creating the reference case scenario in the matlab code.....	65
9.3	Reference case, chosen input data	67
9.4	Results with BIGM 1	70
9.5	Results with BIGM 2	74
9.6	Comparison between BIGM 1 and BIGM 2 for reference case of Sabetta.....	78
9.7	Parametric study for Sabetta reference case.....	80
9.7.1	Porosity.....	82
9.7.2	Thermal exchange coefficient	84
9.7.3	Temperature sets	85
9.7.4	Ship arrival time (time between ice breaking events in the same track).....	86
9.7.5	Conductivity of the dry brash ice layer (freeboard conductivity)	87
9.7.6	Long Wave Radiation Parametric study	88
9.7.7	Synthesis of the parametric study.....	90
9.8	Influence of a different channel navigation strategy, “successively navigated tracks”	91
10.	Lulea brash ice field measurements and their analysis.....	95
10.1	Measurement procedures and locations	95
10.1.1	Metocean data in Lulea	97
10.1.2	Brash Ice channel Measurements	100
10.2	Analysis of the measurements	102
10.2.1	Plotting brash ice cross section profiles of the channel.....	104
10.2.2	Average total ice, total wet ice and dry brash ice thickness calculation.....	106
10.2.3	Concept of horizontal motion	108
10.2.4	Estimation of the amount of ice that has moved outside the channel track.....	110
11.	Validation of the developed BIGM models, with Lulea Brash Ice field measurements.....	111
11.1	Comparison of the calculated and measured values	111

11.1.1	Results with BIGM 1 (Reference Case: Input temperature, wind, and porosity sets from Table 11-1).....	114
11.1.2	Results with BIGM 2: (Reference Case Input temperature, input wind, input porosity, input radiation sets from Table 11-1). Surface albedo used is 0.64.....	115
11.1.3	Comparison between the Results of BIGM 1 and BIGM 2 for Reference case	118
11.2	Investigation of how different properties/effects of BIGM 2 affect final total ice thickness results	120
11.2.1	BIGM 2 Reference Case Including variation of conductivity and specific heat capacity (depending on temperature and salinity)	120
11.2.2	BIGM 2 Reference case, including latent heat flux in the top surface flux balance equation	127
11.2.3	BIGM 2 reference case, including internal absorption.....	128
11.3	Parametric Study for Lulea reference case	133
11.3.1	Surface albedo	133
11.3.2	Proportion of solar radiation absorbed <i>io</i>	135
11.3.3	Conductivity of dry brash ice.....	138
11.3.4	Synthesis of the parametric study for Lulea Reference case	140
12.	Brash Ice Management System in Ports, and estimation of energy needs using BIGM 1 and BIGM 2	141
12.1	Ice control by melting.....	141
12.2	Energy estimates for brash ice melting in Sabetta.....	142
13.	Conclusions and Recommendations	144
Appendix.....		149
A.	Derivation of Porosity decrease (no dry brash ice, BIGM 1 and 2)	150
B.	Derivation of Eq. (4-15) Ice Growth Equation in the case of having dry brash ice (freeboard), Thermodynamics BIGM 1	152
C.	Relation between wet brash ice and dry brash ice just after breaking.....	153
D.	Inclusion of the latent heat flux equation to the top surface flux equilibrium equation	154
E.	Calculation sequence in ice growth cycle, BIGM 2 (no dbi)	157
F.	Viscaria tugboat specifications.....	158
G.	Metocean Data of Lulea Port Measurements	159
H.	Ice thickness plots from Lulea field Measurements.....	165
I.	Brash Ice Profiles along the tested channel in Lulea	169
J.	BIMS application in different situations	177
References.....		179

List of Figures

Figure 2-1 Accelerated formation of ice in ports due to ice breaking, and ice formation taking place without an insulating layer of snow or ice, (Saarinen, Suojanen, & Eranti, 2011).....	4
Figure 2-2 Helsinki port, Brash Ice conditions in Helsinki harbour in winter 2003 with 1000 FDD, (Saarinen, Suojanen, & Eranti, 2011)	5
Figure 2-3 Ice collar formation on a dock wall, (Saarinen, Suojanen, & Eranti, 2011).....	5
Figure 2-4 Brash ice blocks lifted with cranes from berth area to enable berthing. Ice blocks are glued together by slush in low temperatures forming larger blocks. Extracted from (Saarinen, Suojanen, & Eranti, 2011)	6
Figure 2-5 Typical cross section of a vessel track filled with brash ice. Extracted from (Ettema & Huang, 1990).	7
Figure 2-6 Cross section of a navigation channel covered with Brash ice when vessel beam was smaller than the channel track. Extracted from (Kannari, 1983).	7
Figure 2-7 Longitudinal profile of a navigation channel covered with brash ice. Extracted from (Kannari, 1983).	8
Figure 2-8 Field data on brash ice and ice cover thicknesses in ship tracks formed in Lulea Harbor, Sweden. Extracted from (Sandkvist, 1986).	9
Figure 2-9 Thickness distribution of brash ice fragments. Extracted from (Sandkvist, 1982).....	10
Figure 2-10 Sandkvist’s model of predicting brash ice accumulation. Extracted from (Sandkvist, 1986).	10
Figure 2-11 Brash Ice formation in a frequently transited navigation channel. Extracted from (Ettema & Huang, 1990).....	12
Figure 2-12 View astern of the vessel when inside the approach channel.....	13
Figure 2-13 Pictures of Ice floes in the approach channel	13
Figure 2-14 Occasionally large broken ice floes pulled from the channel edge into the centre, from the icebreaker and ship wake.....	14
Figure 2-15 Different sizes and shapes of brash ice fragments in the approach channel.	14
Figure 2-16 Brash Ice within the port of Sabetta	15
Figure 3-1 General schematic Illustration of the thermodynamic sea ice growth model.....	17
Figure 4-1. In this figure the processes that take place, and all the equations that are used, in the ice growth cycle, in case of no dry brash ice layer on top, are shown. Note that for convenience, the equations shown in this figure have different number from the one they have in the main text of this report.....	24
Figure 4-2 Temperature Profile. Situation shown, does not include a dry brash ice layer.	25
Figure 4-3 In this figure, the processes that take place and all the equations that are used in the ice growth cycle, in the situation of the existence of a dry brash ice layer on top, are shown. Note that for convenience, the equations shown in this figure have different numbers from the one they have in the main text of this report.	26
Figure 4-4 Temperature Profile. Situation shown, includes a dry brash ice layer.	26
Figure 5-1 Discretization of the solid ice layer.	29
Figure 5-2 All the fluxes involved in the sea ice growth problem	31
Figure 6-1 Illustration of the grid reconstruction procedure, in the case of not having a broken dry brash ice layer above the waterline	37

Figure 6-2 Illustration of the grid reconstruction procedure, in the case of having a broken dry brush ice layer above the waterline 40

Figure 6-3 Schematic showing distances of mid-layer temperatures from the top surface 43

Figure 6-4 Schematic showing distances of dry brush ice mid-layer temperatures from the top surface, and solid ice mid-layer temperatures from the top of the solid ice surface 46

Figure 7-1 Breaking model, no freeboard case 52

Figure 7-2 Breaking model, with dry brush ice (freeboard) case 53

Figure 8-1 The red spots in this figure correspond to the 3 locations where Metocean conditions and criteria were defined in the work of (Williams & Lattes, 2012), for the Ob bay. Extracted from (Williams & Lattes, 2012). 59

Figure 8-2 Ob bay, temperature data measurements at the locations with green pins. Left picture, shows Russian meteorological stations. Right picture, shows locations where CFSR took measurements. Pictures taken from (Williams & Lattes, 2012) 60

Figure 8-3 Ob' Bay sea temperatures. Top pair of pictures: Summer, Bottom pair of pictures Winter, A = near sea surface, B = near sea-bed. Extracted from (AARI, 2005). 62

Figure 9-1 BIGM 1. Total ice and Brash ice evolution thicknesses for freeboard (dry brush ice) VS no freeboard cases. Reference case inputs are used. No conservation of energy during breaking, hence no porosity decrease after return to thermal equilibrium..... 71

Figure 9-2 BIGM 1. Total ice and Brash ice evolution thicknesses for freeboard (dry brush ice) VS no freeboard cases. Reference case inputs are used. Conservation of energy during breaking is applied, hence there is some porosity decrease after return to thermal equilibrium of the cold blocks resulting from the breaking of solid ice and dry brush ice. 71

Figure 9-3 BIGM 1 with no dry brush ice using reference case and applying conservation of energy during breaking events. Evolution of brash ice porosity during the whole simulation period 72

Figure 9-4 BIGM 1 with dry brush ice using reference case and applying conservation of energy during breaking events. Evolution of brash ice porosity during the whole simulation period 72

Figure 9-5 BIGM 1 with reference case inputs. Evolution of the top surface temperature T_o , in the situation of bare ice growth (no dry brush ice). Conservation of energy during breaking is applied, hence there is some porosity decrease after return to thermal equilibrium of the cold blocks resulting from the breaking of the solid ice. 73

Figure 9-6 BIGM 1 with reference case inputs. Evolution of the top surface temperature T_o in the situation of solid ice growth with the insulation of dry brush ice. Conservation of energy during breaking is applied, hence there is some porosity decrease after return to thermal equilibrium of the cold blocks resulting from the breaking of the solid ice. 73

Figure 9-7 BIGM 2 with reference case input. Total ice and Brash ice evolution thicknesses for freeboard (dry brush ice) VS no freeboard cases. Reference case inputs are used. No conservation of energy during breaking, hence no porosity decrease after return to thermal equilibrium. Application of Long Wave Radiation effect. 74

Figure 9-8 BIGM 2 with reference case input. Total ice and Brash ice evolution thicknesses for freeboard (dry brush ice) VS no freeboard cases. Reference case inputs are used. Conservation of energy during breaking is applied, hence there is porosity decrease after return to thermal equilibrium of the cold ice blocks. Application of Long Wave Radiation effect..... 75

Figure 9-9 BIGM 2 with no dry brush ice using reference case and applying conservation of energy during breaking events. Evolution of brash ice porosity during the whole simulation period..... 75

Figure 9-10 BIGM 2 with dry brash ice using reference case and (long wave radiation values input) and applying conservation of energy during breaking events. Evolution of brash ice porosity during the whole simulation period 76

Figure 9-11 BIGM 2 with reference case input. Temperature profile evolution in the no dry brash ice situation (no freeboard). Conservation of energy during breaking is applied, hence there is porosity decrease after return to thermal equilibrium of the cold ice blocks. Application of Long Wave Radiation effect. 77

Figure 9-12 BIGM 2 with reference case input. Temperature profile evolution in the “with dry brash ice” situation (with freeboard). Reference case inputs are used. Conservation of energy during breaking is applied, hence there is porosity decrease after return to thermal equilibrium of the cold ice blocks. Application of Long Wave Radiation effect. 77

Figure 9-13 When LWR is not applied in BIGM 2, the results/graphs from BIGM 1 and BIGM 2, exactly coincide. This shows that under the same conditions the two models give exactly the same results. The plots above refer to the case of no freeboard (dry brash ice) layer. The black line represents the total ice prediction results obtained from the Aker Arctic model, see Aker Arctic (2011), which also assumes no dry brash ice (freeboard) layer. 78

Figure 9-14 When Long wave radiation (LWR) is applied in BIGM 2, the results/graphs of BIGM 2 are shifted upwards by about 0.5m. The plots above refer to the case of no freeboard (dry brash ice) layer. The black line represents the total ice prediction results obtained from the Aker Arctic model, see Aker Arctic (2011), which also assumes no freeboard layer in the form of dry brash ice. No application of conservation of energy..... 79

Figure 9-15 When LWR is applied in BIGM 2, the results/graphs of BIGM 2 are shifted upwards by about 0.2-0.3m, in the situation of having a freeboard (dry brash ice) layer above the solid ice. No application of conservation of energy..... 79

Figure 9-16 Evolution of the total ice thicknesses for the 3 possible values of porosity in the parametric study. All the other parameters are kept at their reference values..... 82

Figure 9-17 Evolution of the solid ice thicknesses for the 3 possible values of porosity in the parametric study. All the other parameters are kept at their reference values..... 83

Figure 9-18 Evolution of the total ice thicknesses for the 3 possible values of the thermal exchange coefficient, in the parametric study. All the other parameters are kept at their reference values. 84

Figure 9-19 Evolution of the total ice thicknesses for the 3 possible sets of temperatures used in this parametric study. All the other parameters are kept at their reference values..... 85

Figure 9-20 Evolution of the total ice thicknesses for the 3 possible track breaking frequency periods used in this parametric study. All the other parameters are kept at their reference values. 86

Figure 9-21 Evolution of the solid ice thicknesses for the 3 possible track breaking frequency periods used in this parametric study. All the other parameters are kept at their reference values. 87

Figure 9-22 Evolution of the total ice thicknesses for the 3 possible dry brash ice conductivity values used in this parametric study. All the other parameters are kept at their reference values. 87

Figure 9-23 Evolution of the total ice thicknesses for the 3 possible Long wave radiation sets of values used in this parametric study. All the other parameters are kept at their reference values. ... 88

Figure 9-24 Evolution of the solid ice thicknesses for the 3 possible LWR sets of values used in this parametric study. All the other parameters are kept at their reference values..... 89

Figure 9-25 Synthesis of the results of the parametric study. Sensitivity of the total ice thickness to the input parameters 90

Figure 9-26 Successively navigated track for BIGM 2 (with radiation) with no dry brash ice. Total ice equivalent thickness limit for navigation 6.25m. The figure shows that 4 tracks are going to be required during the whole cold season..... 93

Figure 9-27 Successively navigated tracks for BIGM 2 (with radiation) with dry brash ice. Total ice equivalent thickness limit for navigation 6.25m. The figure shows that 1 track is enough during the whole cold season, to accommodate traffic in the Sabetta port with the use of this navigation strategy..... 93

Figure 9-28 Successively navigated track for BIGM 2 (with radiation) with no dry brash ice. Total ice equivalent thickness limit for navigation 8m. 94

Figure 10-1 Location of measurements in Lulea. Image extracted from (Westerberg, 2013)..... 95

Figure 10-2 Time series plots of the air temperature, in the airport and harbour of Lulea 97

Figure 10-3 Time series plots of the wind speed, in the airport and harbour of Lulea..... 98

Figure 10-4 Time series plots of the short wave radiation, in the airport of Lulea..... 98

Figure 10-5 Time series plots of the relative humidity in the harbour and airport of Lulea..... 99

Figure 10-6 Drilling of holes to determine brash ice channel profiles. Extracted from (Westerberg, 2013)..... 100

Figure 10-7 Simple plan of the ship track and the arrangement of boreholes. Extracted from (Westerberg, 2013). The numbering here does not correspond to the codes of the boreholes. For the code names of boreholes see Figure 10-8..... 101

Figure 10-8 Example of protocol for documentation of the profile of brash ice in the channel expressed in numbers. Extracted from (Westerberg, 2013)..... 101

Figure 10-9 Brash Ice borehole-profile in the tested channel. Extracted from (Westerberg, 2013). . 102

Figure 10-10 Summary of ice thickness measurements. Boreholes 1-13=Channel Ice, Boreholes H1-H4 and L1-L4= Edge Ice, Boreholes H5-H6 and L5-L6= Level Ice. Data extracted from (Westerberg, 2013)..... 103

Figure 10-11 Summary of brash ice porosity measurements. Boreholes 1-13=Channel Ice, Boreholes H1-H4 and L1-L4= Edge Ice. The brash ice porosity measured from Level Ice=Boreholes H5-H6 and L5-L6, was zero in all the measurement and this is why no level ice plot is included in this graph. Data extracted from (Westerberg, 2013). 103

Figure 10-12 Cross sectional brash ice profile, plotted using field measurements from the 25/03/2013 104

Figure 10-13 Longitudinal brash ice profile, plotted using field measurements from the 25/03/2013 105

Figure 10-14 Method used for calculation of the average total ice thickness, average total wet ice thickness, and average dry brash ice thickness across different widths of the channel. 106

Figure 10-15 Average total Ice thickness for difference widths across the channel..... 107

Figure 10-16 Average total wet Ice thickness for different widths across the channel..... 107

Figure 10-17 Average dry brash Ice thickness for different widths across the channel 108

Figure 10-18 Creating equivalent ice thickness plots from the field data for comparison with the models' results 108

Figure 10-19 Equivalent total ice thickness plots for 12m channel width, for level ice distance from edge (dfe) of ship track, 0,1 and 2m..... 109

Figure 10-20 Equivalent dry brash ice thickness plot for 12m channel width. Dfe was taken as zero. 109

Figure 10-21. Plots of the proportion *apushed* , of ice that has moved outside of the shipping track (12m width), in each brash ice field measurement, for different distances of the level ice inner edge from the ship track edge. 110

Figure 11-1 Reference case BIGM 1. Cases with and without dry brash ice (dbi) are included. Field measurement plots of the average total ice across the channel and of the equivalent total ice average across the channel are also plotted. 114

Figure 11-2 Reference case BIGM 1, Plots of the top surface temperature for the cases with and without dry brash ice..... 115

Figure 11-3 Reference Case for BIGM 2 for with and without dry brash ice 116

Figure 11-4 Dry brash ice evolution for BIGM 2 (with dry brash ice in the formulation). Also the average dry brash ice plot in the 12m of the ship track from the field measurements, and the average equivalent dry brash ice plot in the 12m of the ship track. 116

Figure 11-5 Reference Case for BIGM 2. Temperature profile without having dry brash ice..... 117

Figure 11-6 Reference Case for BIGM 2. Temperature profile when there is a dry brash ice layer above the solid ice..... 117

Figure 11-7 Example of the agreement of the two models BIGM 1 and BIGM 2 when the simulations are based on input field data, for the reference case of Lulea port. No radiation input data is used in BIGM 2 in this case so that the two models take exactly the same input data. The plots correspond to the no dry brash ice situation..... 118

Figure 11-8 BIGM 1 reference case, BIGM 2 reference case with radiation input data also, no dry brash ice situation. 119

Figure 11-9 BIGM 1 reference case, BIGM 2 reference case with radiation input data also, with dry brash ice situation. 119

Figure 11-10 BIGM 2 reference case simulation with variation of heat conductivity and heat capacity, in each layer of the solid ice and dry brash ice (for the with dbi plot), depending on temperature and salinity..... 120

Figure 11-11 Effect on the total ice thickness in the end of the cold season, in the case of not having a dry brash ice layer, in BIGM 2 using the reference case, and having variation of the thermal properties in the ice layers. 121

Figure 11-12 Effect on the total ice thickness in the end of the cold season, in the case of having a dry brash ice layer, in BIGM 2 using the reference case. 122

Figure 11-13 Temperature profile in the case of no dry brash ice, and variation of the thermal properties in the solid ice layers. BIGM 2 reference case..... 123

Figure 11-14 Thermal conductivity of ice profile evolution with time, for BIGM 2 reference case, having no dry brash ice..... 123

Figure 11-15 Heat Capacity of ice profile evolution with time, for BIGM 2 reference case, having no dry brash ice. 124

Figure 11-16 Temperature profile in the case of having a dry brash ice on top of the solid ice, and variation of the thermal properties in the dry brash ice and solid ice layers. BIGM 2 reference case. 125

Figure 11-17 Thermal conductivity profile evolution with time for BIGM 2 reference case, having additionally a dry brash ice layer on top of the solid ice..... 125

Figure 11-18 Heat capacity profile evolution with time for BIGM 2 reference case, having additionally a dry brash ice layer on top of the solid ice. 126

Figure 11-19 Examining the effect of the latent heat flux on solid ice growth, using BIGM 2 reference case with no dry brash ice in the formulation..... 127

Figure 11-20 Examining the effect of the latent heat flux on solid ice growth, using BIGM 2 reference case with dry brash ice layer, on top of the solid ice, in the formulation..... 127

Figure 11-21 . Total Ice layer evolution for the reference case, including internal absorption of 31% of the net non-reflected solar radiation, for BIGM 2 for both the cases with and without dry brash ice. 128

Figure 11-22 Comparison between the reference case of BIGM 2, and the reference case of BIGM 2 with the inclusion of internal solar radiation absorption. No dry brash ice case. 129

Figure 11-23 Comparison between the reference case of BIGM 2, and the reference case of BIGM 2 with the inclusion of internal solar radiation absorption. Situation with inclusion of dry brash ice in the formulation. 129

Figure 11-24 Comparison between the reference case of BIGM 2 with the inclusion of internal solar radiation absorption, and the average dry brash ice across the ship track (12 m width)..... 130

Figure 11-25 Temperature profile in the case of no dry brash ice, for the reference case of BIGM 2 and having 31% internal solar absorption..... 130

Figure 11-26 Profile of the incremental temperatures in the case of no dry brash ice, for the reference case of BIGM 2 and having 31% internal solar absorption. 131

Figure 11-27 Temperature profile in the case of having a dry brash ice layer above the solid ice, for the reference case of BIGM 2 and having 31% internal solar absorption..... 131

Figure 11-28 Profile of the incremental temperatures in the case of having a dry brash ice layer above the solid ice, for the reference case of BIGM 2 and having 31% internal solar absorption..... 132

Figure 11-29 Parametric study for surface albedo using the Reference case of Lulea, see section 11.1.2. Total ice evolutions for different values of the surface albedo. 134

Figure 11-30 Parametric study for surface albedo using the reference case of Lulea. Solid ice evolutions for different values of the surface albedo..... 135

Figure 11-31 BIGM 2 with dry brash ice. Total ice evolutions for the 3 different possible values of solar radiation absorption proportion..... 136

Figure 11-32 Dry brash ice thickness evolutions for the 3 different possible values of solar radiation absorption proportion..... 136

Figure 11-33 Accumulated melting plots, in the 3 possible cases of solar radiation absorption proportion 137

Figure 11-34 Solid ice evolution for the 3 different possible cases of solar radiation absorption proportion. 137

Figure 11-35 Evolution of the total ice thickness, for the 3 possible cases for the thermal conductivity value of the top dry brash ice layer. Reference Lulea case using BIGM 2 with dry brash ice..... 138

Figure 11-36 Evolution of the solid ice thickness, for the 3 possible cases for the thermal conductivity value of the top dry brash ice layer. Reference Lulea case using BIGM 2 with dry brash ice..... 139

Figure 11-37 Synthesis of the results of the parametric study for Lulea reference case. Sensitivity of the total ice thickness to the three tested input parameters. 140

Figure 12-1 Bubbler system used for ice control in Oulu. About 100 MW of thermal effluents are released a few hundred meters upstream from the harbour basin. The bubbler system draws the warm water in and turns it into a surface current that melts brash ice. Extracted from (Saarinen, Suojanen, & Eranti, 2011). 141

Figure 12-2 BIMS application to decrease total ice thickness by 1m. BIGM 2 with freeboard and application of conservation of energy (porosity decrease after breakings), using Reference Sabetta case as input. A BIMS flux of $Q_w=20 \text{ W/m}^2$ was needed to achieve a 1m decrease in the total ice (1m was melted from the brash ice at the bottom)..... 142

List of Tables

Table 8-1 Sets of mean monthly air temperatures in Sabetta. Extracted from (Williams & Lattes, 2012).....	60
Table 8-2 Monthly values of Long Wave and Short Wave radiation in the Arctic. Extracted from (Fletcher, 1965).	61
Table 9-1 Schedule of all breaking events.....	66
Table 9-2 Basic reference set of temperatures: “Severe Winter” Case.....	67
Table 9-3 Summary of parameter inputs to be used for the Sabetta reference case.....	68
Table 9-4 List of physical parameters and constants used in the simulations throughout this study..	69
Table 9-5 Table with input parameters to be examined in a parametric study.....	80
Table 9-6 Set of temperatures to be used in the parametric analysis for air temperature sets	80
Table 9-7 Influence of porosity on total Ice thickness in the end of the cold season	82
Table 9-8 Influence of porosity value on maximum solid ice thickness before each vessel passage, during the cold season	83
Table 9-9 Influence of the thermal exchange coefficient on the total ice thickness in the end of the cold season	84
Table 9-10 Influence of the variation in the thermal exchange coefficient value on the maximum value of solid ice thickness before a breaking event, during the cold season	84
Table 9-11 Influence of the set of temperature on the total ice thickness in the end of the cold season	85
Table 9-12 Influence of the set of air temperatures used on the maximum value of solid ice thickness before a breaking event, during the cold season.....	86
Table 9-13 Influence of the track breaking frequency on the total ice thickness in the end of the cold season.....	86
Table 9-14 Influence of the track breaking frequency on the maximum value of solid ice thickness during the cold season	87
Table 9-15 Influence of the dry brash ice conductivity on the total ice thickness in the end of the cold season.....	88
Table 9-16 Influence of the dry brash ice conductivity on the value of the maximum solid ice thickness during the cold season	88
Table 9-17 Evaluation of the Influence of the variation in the long wave radiation set of values, on the total ice thickness in the end of the cold season.	89
Table 9-18 Evaluation of the Influence of the variation in the long wave radiation values, on the maximum solid ice thickness before a breaking event, during the cold season.....	89
Table 9-19 Example of list of time instants of vessel passages 9 (breaking events) for successively navigated tracks.	91
Table 9-20 List of breaking instants in the same track, with successive navigated tracks scenario, if only one track is used during the whole cold season.....	92
Table 10-1 Exact times of channel passages by Viscaria tugboat and exact times of brash ice channel measurements. Data collected from (Westerberg, 2013)	96
Table 10-2 Table showing the estimated level ice thickness at each of the measurements	110
Table 11-1 Data set used for validation.....	113
Table 11-2 Summary of the values that each tested parameter takes for this parametric study	133

Table 11-3 Variation of the surface albedo on the surface.....	134
Table 11-4 Quantitative analysis of the impact of solar radiation absorption on the total ice thickness in the end of the cold season,	138
Table 11-5 Quantitative analysis of the impact of solar radiation absorption on the maximum solid ice thickness during the cold season.	138
Table 11-6 Influence of the dry brash ice conductivity on the total ice thickness in the end of the cold season, BIGM 2 with dry brash ice, reference Lulea Case.....	139
Table 12-1 Heat flux and power needed to melt 1m of brash ice in the port of Sabetta. Estimates of flux and power were done with simulations using both BIGM 1 and BIGM 2(with long wave radiation), applying conservation of energy in all the simulations (porosity decrease after breaking event) and testing both the cases of having and not having a dry brash ice layer on the top of the solid ice.	143
Table 12-2 Heat flux and power needed to bring total ice thickness just below 4m, in the port of Sabetta. Estimates of flux and power were done with simulations using both BIGM 1 and BIGM 2(with long wave radiation), applying conservation of energy in all the simulations (porosity decrease after breaking event) and testing both the cases of having and not having a dry brash ice layer on the top of the solid ice.	143

Preface and Acknowledgements

The present report is an overview of the research project undertaken to obtain the degree of Master of Science at the Delft University of Technology. The subject of this Master Thesis is the development of Brash Ice Growth Models and the estimation of the energy needs to manage ice in the Yamal LNG port of Sabetta. The present study was supported and sponsored by TOTAL S.A. Completing a project of such an extent wouldn't be possible without the help of certain people that I would like to thank. Firstly, I would like to thank and express my gratitude to TOTAL S.A and especially to Prof. Kaj Riska, for offering me the opportunity to work on a real project in a challenging and authentic environment, within the Ice Engineering Team in La Defense, Paris. Working with him for 6 months, has helped me to develop and grow both professionally and personally, and significantly increase my knowledge on Arctic issues and Ice Engineering in general. His contribution to completing this work was very important. Additionally, I would like to thank Robert Bridges, another member of the Ice Engineering team, for providing with some nice pictures from the port of Sabetta that demonstrate the extent of the brash ice problem in the area, and thereby they have been included in this report.

Moreover, I would like to sincerely thank Jeroen Hoving and Prof. Andrei Metrikine, members of the graduation committee, for the important recommendations that they have given me for different parts of the project, and for the general supervision of the project from the TU Delft side.

Last but not least, I am very grateful to all of my friends and family for their mental support during this long journey.

Delft University of Technology,
September 24, 2015

Kyriakos Chomatas

1. Introduction

1.1 Context

YAMAL LNG is an integrated project encompassing natural gas production, liquefaction, and shipping. The company of the project, called OAO YAMAL LNG, is a joint venture company, owned by NOVATEK 60%, TOTAL 20% and CNPC 20%, and is responsible for the engineering and design work of the onshore LNG facility of the project. The YAMAL LNG project is based on the estuary of the Ob River, near Sabetta on the Yamal Peninsula, which is ice-covered at least 9 months of the year. The project is one of the largest industrial undertakings in the Arctic and is expected to ensure production and marketing of the Russian Arctic's vast natural gas reserves, and specifically of the nearby South Tambey field, which is a huge condensate gas field.

YAMAL LNG is a shallow water-onshore development, (15 m depth in the port and the approach channel) in extremely cold conditions and related ice formation. Due to these extreme climatic conditions in the region, the construction of the LNG plant and the LNG loading/unloading procedures of the commissioned icebreaker LNG tankers, would have to overcome significant challenges.

Navigation in extreme cold conditions, means repeated ice breaking in navigation channels and harbour basins. The broken ice resulting from this repeating procedure, is called "Brash Ice", in opposite to "sea ice" which is formed statically in calm water. Just after an ice breaking event, caused by a vessel transit, there is a lot of water near the surface, exposed to freezing without the insulation that the solid or static ice has with either a snow or a thick ice cover on top. This means faster formation of ice, compared to the case of static or sea ice.

In very low temperatures and with increased traffic, brash ice accumulates, especially on the sides of the ship tracks and near dock walls. The correct prediction of the amount of brash ice growth during the whole cold season, but most importantly between 1st of November-30th of April, is essential for YAMAL LNG to assess potential problems that could arise during operations in the port of Sabetta.

1.2 Brash Ice Growth Modeling for YAMAL LNG port

The YAMAL LNG port in Sabetta, which is currently under construction, is expected to be operational for LNG carriers by the end of 2016. In the first phase of the ports' operation, the traffic in the port is expected to be 85 tanker visits per year, but this would gradually increase to 232 tanker visits per year by the end of 2018. This corresponds to a carrier visit every 103 hours in 2016, and a carrier visit every 38 hours by the end of 2018. These dense traffic figures, are expected to induce the brash ice growth problem.

YAMAL LNG first appointed Aker Arctic in 2011, to pursue a study on brash ice thickness based on the weather conditions of Sabetta, see (Saarinen, Suojanen, & Eranti, 2011). The model by Aker Arctic, a combination of analytical and empirical methods, estimated a maximum of 8m of brash ice thickness, at the end of a severe winter in the Sabetta approach channel, if 3 vessel tracks are navigated successively. Assuming that half of the brash ice is pushed to the track side ridges, Aker Arctic claimed that each of the 3 successively navigated tracks would have less than 4 m brash ice thickness in the end of the navigation period. Here, it is noted that the brash ice thickness limit for operations in ports, is estimated to be around 4m, see (Bloquin [2], 2013).

In 2013, YAMAL LNG cooperated with Bertin Technologies for further investigation of the Brash Ice Growth phenomenon, expecting the development of a more sound, descriptive and applicable model in the context of the harsh weather conditions that prevail in the Tambey Bey and the dense traffic in the port of Sabetta. Bertin Technologies used both analytical and numerical methods and different strategies for the use of the approach channel, giving estimates of brash ice growth in the approach channel, in the range of 7-11m thickness. The two strategies for the use of the approach channel that were applied in their models, was:

1. The simultaneous use of alternating tracks across the whole width of the channel.
2. The use of a single track until it gets heavy, which would then lead to the opening of another track or tracks.

The fact that the methods used by the two companies have not been proved or validated with field measurements, in combination with their high predictions for brash ice growth in Sabetta, led the Arctic Engineering team of Total to proceed with its' own studies on Brash Ice Growth, in order to give its' predictions and suggestions to YAMAL LNG, independently.

1.3 Description of the content of this study

This study begins, see section 2, with the basics of the brash ice growth problem in navigation channels, using basic references such (Ettema & Huang, 1990), Sandkvist (1978-1986) and (Kannari, 1983), in combination with various pictures from ice-covered ports and channels to define and explain the problem and describe the work that has previously been done in predicting brash ice growth. Moreover, recent images from the port of Sabetta are provided in order to illustrate the extent of the brash ice growth problem in the area to which this study is dedicated.

In section 3 of this study, heat conduction in ice and the sea-ice growth problem are explained in order to give the reader a solid introduction into the thermodynamic processes that are involved in the growth of ice. These thermodynamics processes are present in the growth of brash ice as well, and they are essential for building brash ice growth models. This section explains to the reader that the thermal growth of sea ice is considered to be a one-dimensional and vertical problem, justified by the large vertical temperature gradients which correspond to significantly greater vertical than horizontal heat fluxes. The ice basically grows at the bottom by releasing latent heat due to ice freezing. This heat is conducted through ice and snow if it exists (or dry-brash ice layer in the context of a BIGM) and released to the atmosphere by radiation and turbulent heat fluxes. The study provides a series of references that describe these thermodynamic processes either analytically or numerically, sections 3 and 5, such as the Classical Stefan Law, (Stefan , 1891), analytic solution, the Maykut and Untersteiner (Maykut & Untersteiner, 1971) numerical explicit solution using multiple layers and the Ukita and Martinson (Ukita & Martinson, 2001), easily adjustable numerical implicit scheme.

In sections 4 and 6 of the study, the thermodynamic solutions, one analytical and one numerical, chosen to build brash ice growth models for this study are explained in detail. Using these two thermodynamic solutions, two Brash Ice Growth Models (BIGMs) were developed using efficient coding in Matlab. The first BIGM model, called BIGM 1 throughout this study, is based on an extension of the Classical Stefan Law for Ice Growth (1891) and the second BIGM model, called BIGM 2, is based on the multilayer numerical Ice Growth scheme of Ukita and Martinson (Ukita & Martinson, 2001). The reason for building one analytical and one numerical model is to illustrate the advantages that numerical models have over analytical, in describing the ice growth procedure. As it is explained in

(Leparanta , 1992), complete ice growth models that can describe most of the physical processes that take place into ice while it is growing, can only be solved numerically. Although there are multiple numerical Ice Growth models, the (Ukita & Martinson, 2001) was chosen to build BIGM 2, due to its implicit nature that gives no restrictions on the time step of the simulations and due to its' adjustability. Moreover Bertin Technology had used a similar ice growth model to build their own brash ice growth model, hence comparison between the results of this work and Bertin Technology results, if required, can be done easier.

In section 7 of this study, the model of the ice breaking calculations, which is applied in both BIGM 1 and BIGM 2, is thoroughly explained. The model is based on the conservation of mass and energy, and using certain assumptions is able calculate the evolution of brash ice thickness and total ice thickness after repeated ice breaking events.

In section 8, the environmental conditions in which brash ice is growing in Sabetta, are reviewed.

In section 9, the traffic scenarios defining the simulations run to predict brash ice growth in Sabetta, are explained. Moreover a reference case with certain input parameters is defined, and the results of the two BIGM models, for this case, are presented and discussed. Moreover, in order evaluate the impact of different parameters, on brash ice growth, a parametric study was performed.

In section 10, the brash ice field measurements in the port of Lulea, Sweden during the winter 2012/2013, under the coordination of SSPA AB are presented and analyzed. The conducted brash ice field measurements were aimed to support the investigation of the growth of brash ice in channels and to provide input data for brash ice growth models. These measurements, were carried out in cooperation between SSPA Sweden AB, Lulea University of Technology and Lulea Bogserbats AB, with SSPA Sweden AB being the project coordinator and responsible for reporting to Bertin Technologies, which was at the time contracted by Yamal LNG, to investigate the brash ice growth phenomenon.

In section 11, the two BIGM models developed in this study are validated. This is done by comparing the results of the models i.e. total and brash ice thickness in the end of the fast ice conditions period, when they take as input the environmental conditions at Lulea from the period of the field measurements, to the results (i.e. average brash ice thickness) of the field measurements. In order to perform this validation, the Matlab codes of the two BIGM models had to be modified, as they no longer use the scenarios explained in section 8. Instead, the two models take as input the breaking instants and the corresponding metocean data at those instants, such as temperatures, wind speeds, radiations etc., in order to predict the thickness of brash ice. Moreover, in this section the impact on brash ice growth, of various properties of BIGM 2, such as the application of internal absorption of solar radiation or the variation of thermal properties in different layers of the ice mass, are examined.

In section 12, the basic principles of the systems used to control ice by melting in ports are discussed. Moreover the way BIMS is introduced into the BIGM models is described, and estimates of power needs to manage ice in the Port of Sabetta are provided.

Section 13, summarizes the conclusions of this study.

2. Description of Brash Ice and Channels

The combination of extreme cold conditions and frequent traffic in ports and their entrance channels, may create significant navigation problems in the ports due to the growth of very thick layers of brash ice. Repeated ice breaking in harbour basins and ship tracks accelerates significantly the brash ice growth, verifying the saying among ice navigators that “ an ice breaker is an ice maker”. This is explained by the fact that after an ice breaking event, there is a lot of free water near the surface exposed to freezing, without the insulation of a snow or ice cover, see Figure 2-1.

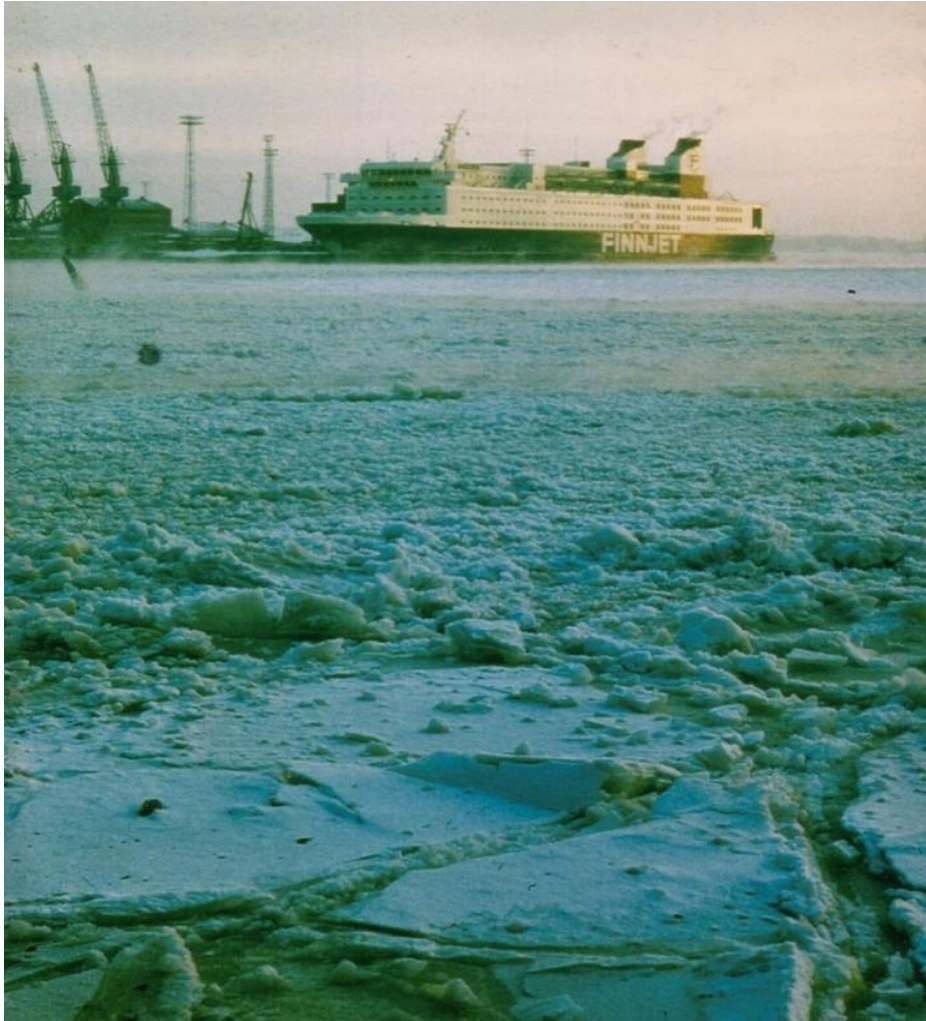


Figure 2-1 Accelerated formation of ice in ports due to ice breaking, and ice formation taking place without an insulating layer of snow or ice, (Saarinen, Suojanen, & Eranti, 2011).

Moreover, when the air temperature becomes very low, submerged brash ice blocks freeze together, increasing the brash ice cohesion and hence making the navigation increasingly heavy. In addition, ship tracks become tighter during and after snow storms, as snow slush acts like a glue between the ice blocks as it is explained in the report of (Saarinen, Suojanen, & Eranti, 2011).



Figure 2-2 Helsinki port, Brash Ice conditions in Helsinki harbour in winter 2003 with 1000 FDD, (Saarinen, Suojanen, & Eranti, 2011)

As the ice blocks significantly increase in size at low temperatures, compacted ice collars are commonly formed on dock walls making berthing very difficult, see Figure 2-2 and Figure 2-3. Harbour ice breakers are not always efficient in berthing assistance and breaking of this ice collar, hence other methods have been used, such as pneumatic tools for breaking the ice collar and harbor cranes to lift large ice blocks from the berth, see Figure 2-4.

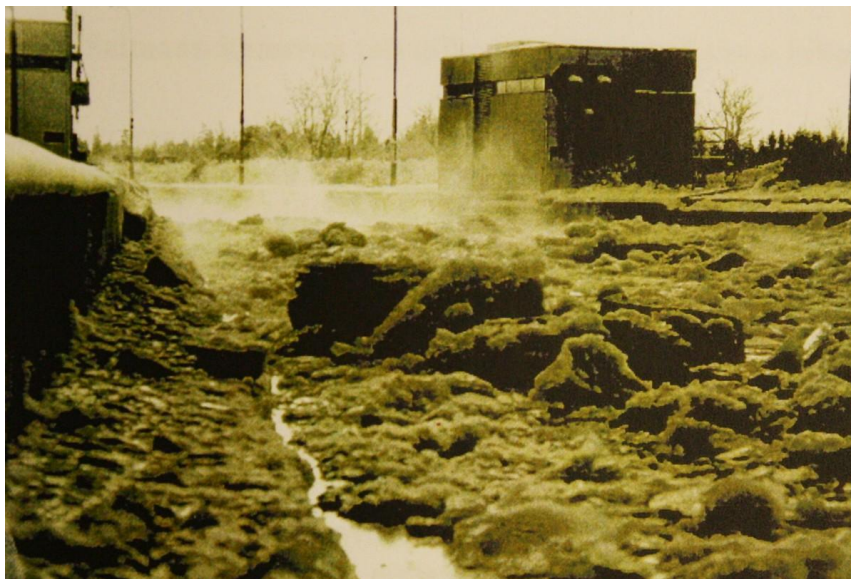


Figure 2-3 Ice collar formation on a dock wall, (Saarinen, Suojanen, & Eranti, 2011).



Figure 2-4 Brash ice blocks lifted with cranes from berth area to enable berthing. Ice blocks are glued together by slush in low temperatures forming larger blocks. Extracted from (Saarinen, Suojanen, & Eranti, 2011)

Increased activities in the arctic and projects like the Yamal LNG, have tremendously increased the interest for improving the use of navigation channels and ports during severe winter conditions, and managing ice within these areas. Not many brash-ice-filled navigation channel have been measured, and not a lot of measurements have been made of the size distribution and micro-morphology of brash ice in these channels. However it is clear that in addition to meteorological conditions, ice formation in navigation channels is influenced by the hull geometry and speed of transiting vessels, the frequency of transits, the channel geometry and water currents. None of these influences appears to have been examined extensively.

One of the most important studies in brash ice in ports, is (Ettema & Huang, 1990), which tried to address to some extent various potential concerns associated with vessel transits of ice-covered channels. These include predictions for brash ice growth in ports, and examination to some extent of the ways that frequency of transiting, hull forms of vessels, maneuvering activities, channel geometry and water-currents affect ice-cover formation.

Other informative studies, dealing with ice formation in frequently transited navigation channels or vessel tracks, are those by (Ashton, 1973), (Kannari, 1983) and (Sandkvist, 1986). However, these are limited to field investigations of particular channels traversed at irregular frequencies by vessels of quite different hull forms. The field study reported by Sandkvist constitutes perhaps the most detailed set of field observations on ice formation in a frequently transited navigation channel. His study was conducted with an icebreaker that, at irregular frequencies, plied two channels at Lulea Harbour in coastal northern Sweden. At a later section of this report, brash ice field measurements, from a similar channel close to the entrance of the port of Lulea, that was transited at an almost constant frequency in winter of 2013, would be analyzed and discussed.

2.1 Transit of harbor and coastal channels and sideways movement

Previous field studies about brash ice formation for specific harbor and coastal channels, such as (Sandkvist, 1978, 1980, 1981, 1982, 1986), (Tuovinen, 1978) and (Kannari, 1983), showed that frequent transits of harbor and coastal channels result in ship tracks that fill with more or less uniform layers of brash ice, flanked by ridges of brash ice accumulated beneath the ice cover (level ice) edges adjoining the tracks. Moreover their studies, showed that layers and ridges of brash ice resulted mainly from the repeated cycles of ice re-growth and ice-breaking, and not from brash ice being conveyed and collected by the water current or by vessel shoving. Figure 2-5, below indicates the typical cross section of a brash-ice filled track observed in these studies, as presented in (Ettema & Huang, 1990). However, the shape of this cross section may change and become more irregular as shown in Figure 2-6, depending on the relative magnitudes of navigation channel width and vessel beam. It was noticed that the closer the vessel beam dimension is to the channel width, the more the channel cross section will look like the section in Figure 2-5. The smaller the vessel beam becomes compared to the channel width, the more irregular the channel cross section would be, as it is shown in Figure 2-6.

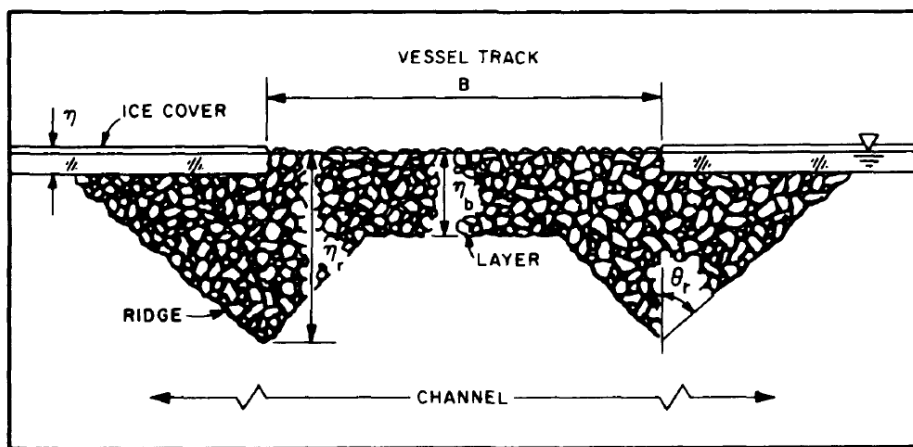


Figure 2-5 Typical cross section of a vessel track filled with brash ice. Extracted from (Ettema & Huang, 1990).

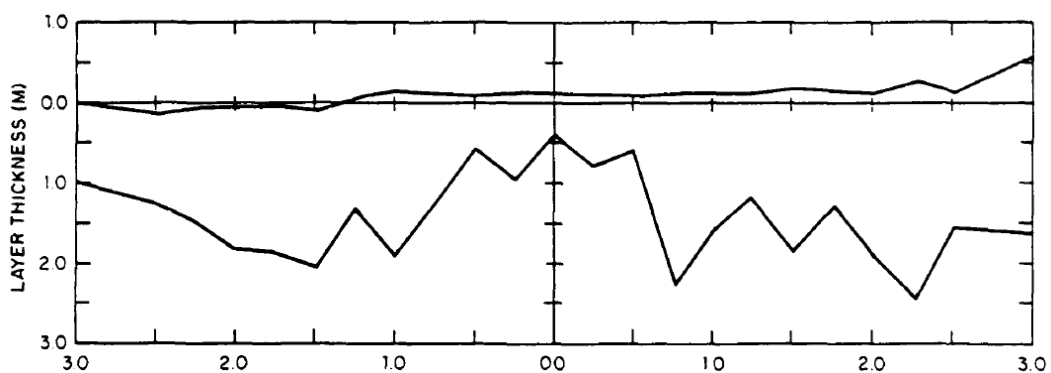


Figure 2-6 Cross section of a navigation channel covered with Brash ice when vessel beam was smaller than the channel track. Extracted from (Kannari, 1983).

Moreover, as (Kannari, 1983) explains, unsteady speeds or maneuvering may cause longitudinal profiles of brash ice accumulations to be somewhat irregular or undular, as indicated in Figure 2-7.

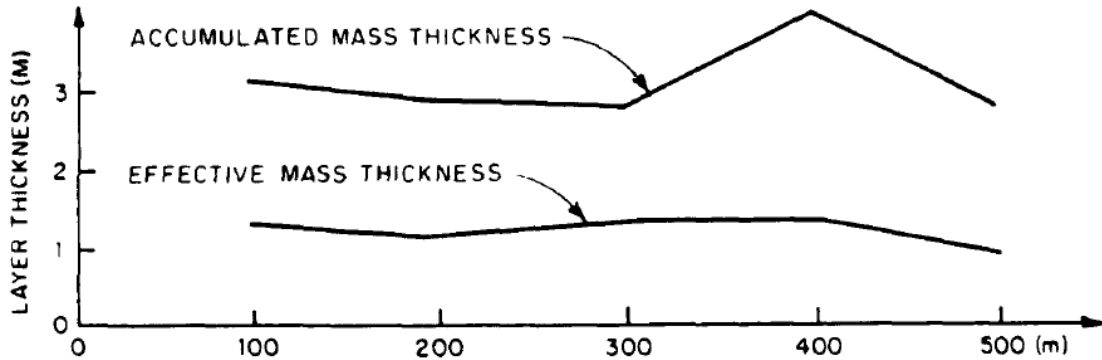


Figure 2-7 Longitudinal profile of a navigation channel covered with brash ice. Extracted from (Kannari, 1983).

In summary, with each transit of a vessel through a navigation channel, brash ice is displaced sideways beneath or above the bordering level ice (ice cover). Beneath the level ice border, brash ice accumulates to form the inverted, linear mounds or ridges, mentioned above, that run more or less parallel to the track so as to confine brash ice in the track. Freezing from above as well as local freezing at contact points between ice pieces, makes the ridges to solidify. If the channel is relatively wide compared to the vessel beam, an irregular series of furrows may form between the ridges as shown in Figure 2-6. In addition to that, brash ice accumulations (i.e. channel brash ice cross sections) may be particularly irregular for other reasons such as the vessels not following exactly the same track or vessels of different sizes transiting the channel.

2.2 Sandkvist studies in Lulea, Sweden

(Sandkvist, 1986) who studied ice formation in two 200m long channels at Lulea Harbour, Sweden, obtained information on the rates at which layers of brash ice formed and thickened in ship tracks, their cross sectional profiles, size distributions of their constituent brash ice, and layer porosities. The two channels were transited at different frequencies, however no major differences in ice formation, in the two channels were observed. Sandkvist's thickness plots for brash ice and solid ice layers from field data in the two tracks in Lulea, are shown in Figure 2-8. Detailed measurements of the sizes of individual brash-ice pieces led Sandkvist to conclude that the distribution of brash ice thickness was not log-normal, as had been found for the distribution of horizontal lengths of freshly broken ice pieces, see (Ettema & Huang, 1990). Moreover, he also observed that additional breaking caused the mean plan size of brash ice to decrease gradually with increasing number of transits, until it attained some constant minimum value. Finally, he reported that brash ice pieces become more spherical with increasing transits and that the vertical dimension of brash ice fragments increases to an asymptotic value, called the equilibrium vertical fragment thickness, see Figure 2-9, extracted from (Sandkvist, 1982).

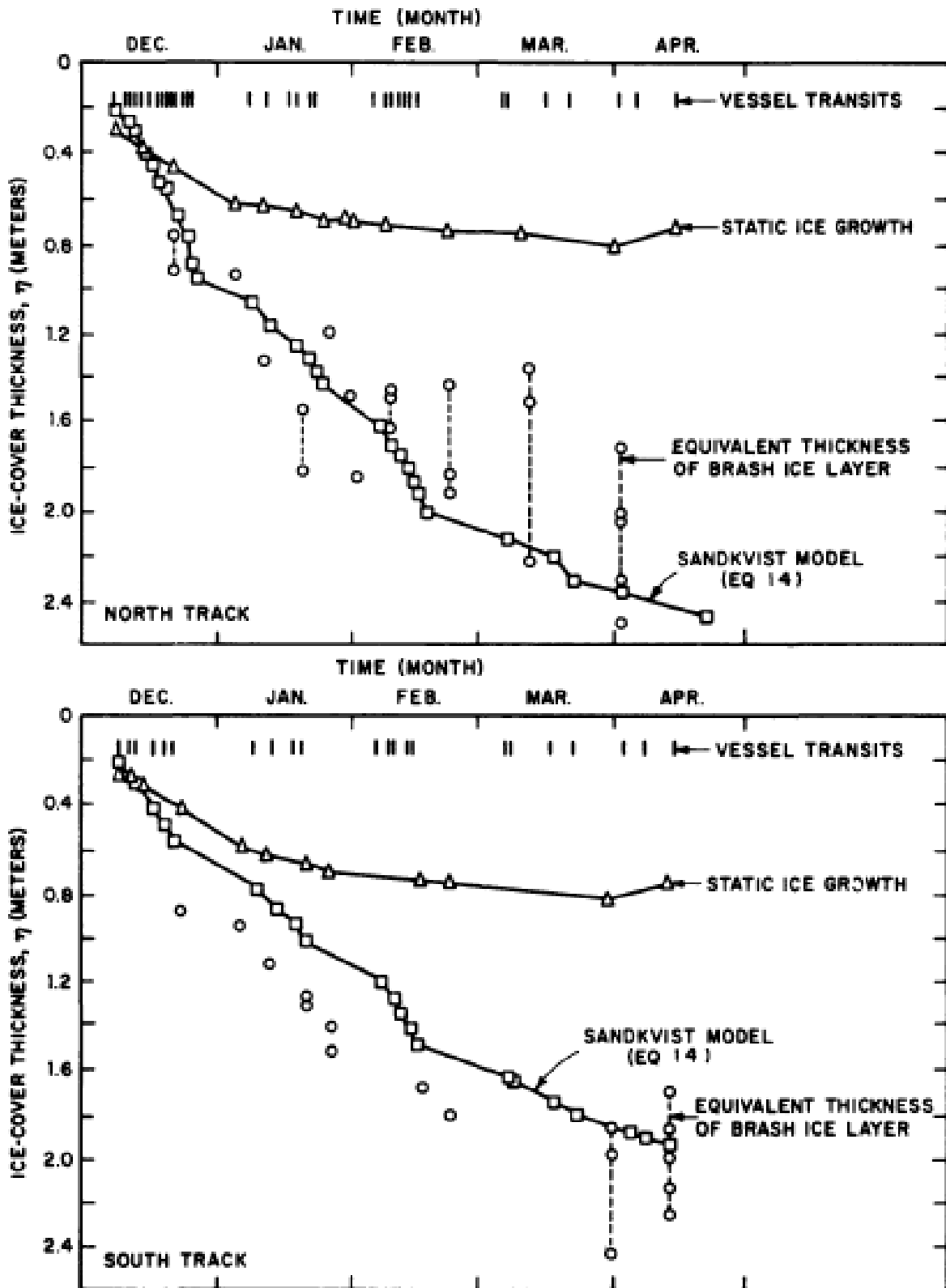


Figure 2-8 Field data on brash ice and ice cover thicknesses in ship tracks formed in Lulea Harbour, Sweden. Extracted from (Sandkvist, 1986).

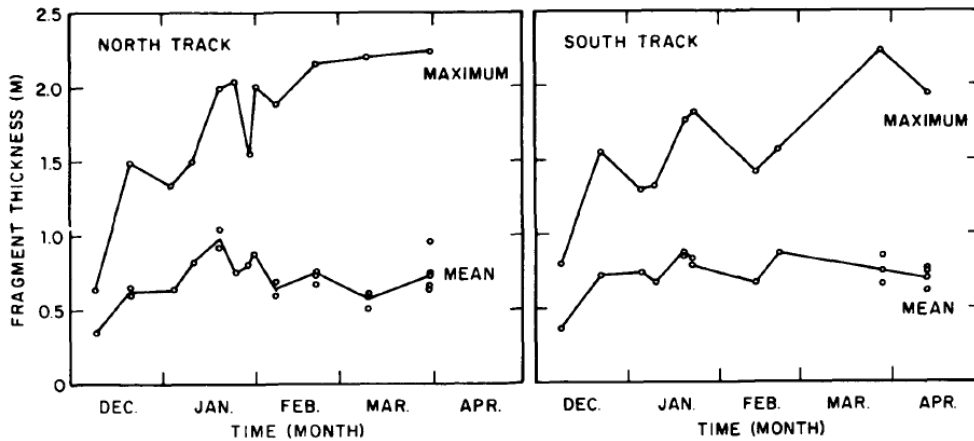


Figure 2-9 Thickness distribution of brash ice fragments. Extracted from (Sandkvist, 1982).

Sandkvist, as most of the previous researchers, proposed a simple formulation for the calculation of brash ice thickness, based on the basic and most simple version of the Stefan model. This formulation calculates the average or “equivalent” thickness of total brash ice formation, which he defined as the resulting thickness of brash ice accumulated in a vessel track, of width equal to the vessel beam, if all brash ice is contained in the track, as depicted in the Figure 2-10 below. The same definition and assumption holds for the brash ice growth models that would be presented in this study.

A disadvantage of these models, is that they do not take into account the influences on ice growth due to brash ice displacement during transiting. All models are based on the assumption that a full layer of brash ice develops immediately below a track transited by the vessels. Furthermore it is assumed for all models that all ice grown remains in the vessel tracks. This second assumption, prevents also the use of the models for the calculation of ridges thicknesses. (Ettema & Huang, 1990) presents some simple formulations, which under certain assumptions, can be used with the Sandkvist model for the calculation of the volume and thickness of ice in ridges aside of the tracks, however this is not one of the scopes of this study.

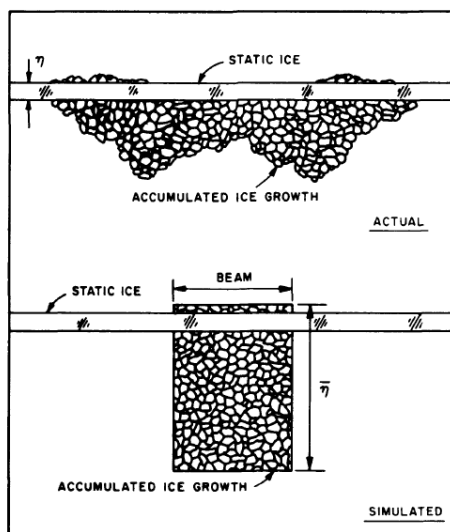


Figure 2-10 Sandkvist’s model of predicting brash ice accumulation. Extracted from (Sandkvist, 1986).

2.3 Simplified description of brash ice formation in channels

Having in mind three fundamental assumptions which are:

1. transiting vessels displace brash ice only sideways,
2. they do not shove significant amounts of it along their tracks,
3. and also that no fragments break from the level ice sheet bordering the track,

brash ice formation in frequently transited, ice-covered tracks can be described as follows:

The first few transits of an ice-covered navigation channel leave an open layer of broken ice or brash ice uniformly spread over a track opened through it, with some ice being forced beneath the adjoining level ice (ice cover) along each side of the track, see (2nd sketch from top) in Figure 2-11. With increasing number of transits and periods of ice regrowth, more ice is broken, causing the track to become increasingly covered by a thickening layer of brash ice. Brash ice forced laterally accumulates as inverted ridges on the edges of the channel, see (3rd sketch from top) Figure 2-11. Once the track is completely covered with a layer of brash ice, further transits cause the brash-ice layer to thicken uniformly in the center of the channel in addition to the extensive thickening of the ice ridges, because brash ice is always displaced sideways to ridges beneath the ice cover bordering the track, see (4th sketch from top) Figure 2-11. Also, each transit causes the entire brash-ice layer to be broken again such that refreezing and ice growth cycle commences again. It has to be noted though that in reality, some brief period of time is required for the water and ice in the track to calm sufficiently for ice to regrow. In the brash ice growth models of this study, this is assumed to be happening instantaneously after breaking. In relatively shallow channels the ridges may eventually extend down to the channel bed, see 5th sketch from top, Figure 2-11, confining brash ice within the track.

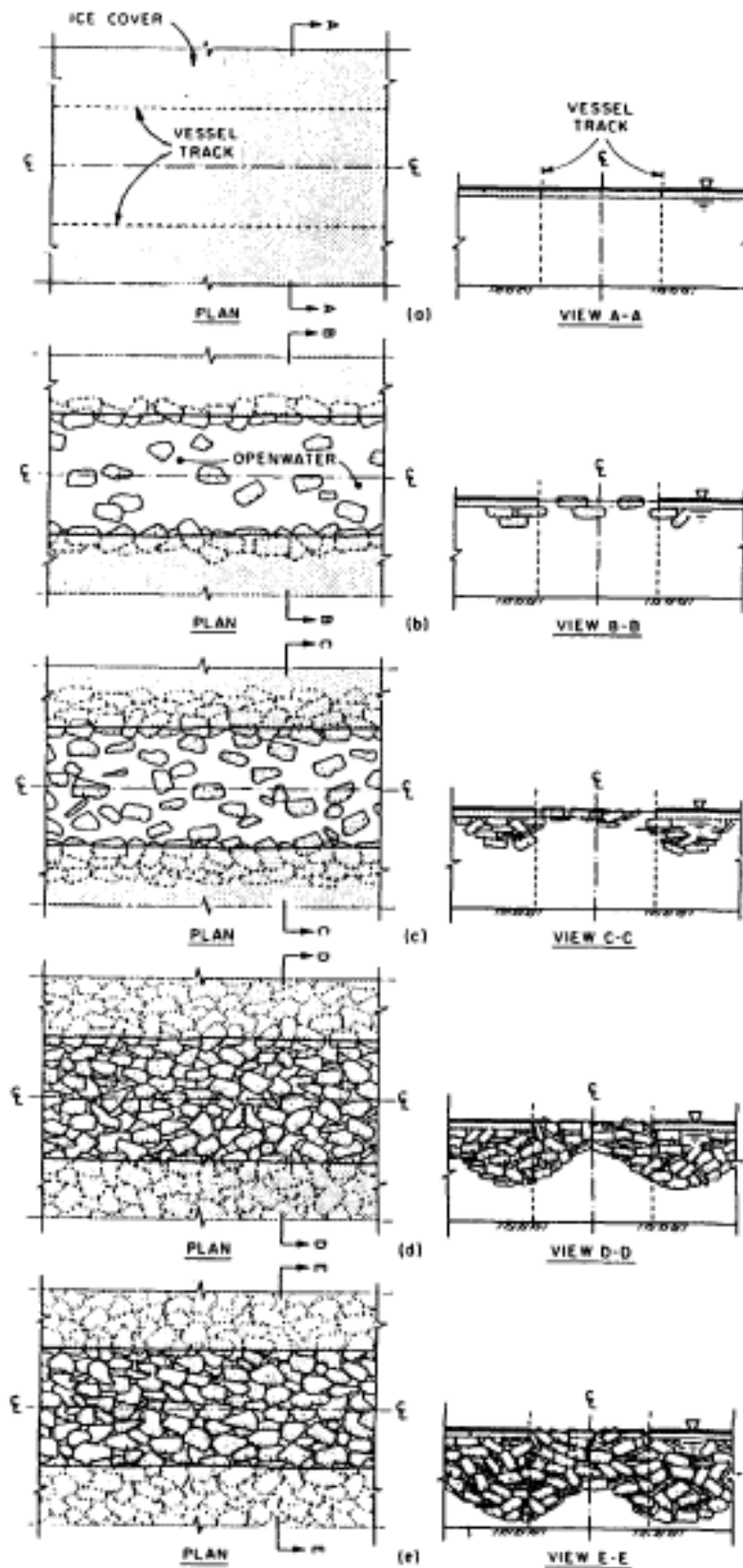


Figure 2-11 Brash Ice formation in a frequently transited navigation channel. Extracted from (Ettema & Huang, 1990).

2.4 Pictures of brash ice in the approach channel and port of Sabetta

In this section, recent brash ice pictures from the approach channel, just outside of the port of Sabetta, and from the inside of the port of Sabetta are presented, in order to illustrate the brash ice problem in the location to which this study is dedicated. The pictures have been provided by Robert Bridges, an Ice engineer and colleague during my internship with TOTAL, in the Ice Engineering Team of the Geotechnical Department. Robert has been on board a 180m bulk carrier in the area of Sabetta in May 2015, for a few weeks, and had the opportunity to take these brash ice pictures from the area.



©R.Bridges

Figure 2-12 View astern of the vessel when inside the approach channel



©R.Bridges

©R.Bridges

Figure 2-13 Pictures of Ice floes in the approach channel



Figure 2-14 Occasionally large broken ice floes pulled from the channel edge into the centre, from the icebreaker and ship wake



Figure 2-15 Different sizes and shapes of brash ice fragments in the approach channel.



Figure 2-16 Brash Ice within the port of Sabetta

3. Heat Conduction in Ice and the basic Sea-Ice Growth problem

3.1 Basic Equations of Heat conduction in Ice

Sea ice thermodynamics can be described with the classical heat conduction equation for ice, which is:

$$\frac{\partial}{\partial t}(\rho_i c_i T) = \nabla \cdot (\lambda_i \nabla T) + \nabla \cdot (q_{rad}) \quad (3-1)$$

where t is the time, ρ_i is the ice density, c_i is the specific heat capacity of ice, T is the ice temperature, λ_i is the heat conductivity of ice and q_{rad} is an internal source term, such as the solar radiation penetrating the ice from the top surface. Equation (3-1), expresses the phenomenon of heat transfer between the ice and the atmosphere and also between ice and the ocean, with solar wave radiation penetrating the upper surface of the ice and creating internal heat sources, at certain periods. For modeling ice growth, Eq. (3-1) can be simplified to:

$$\frac{\partial}{\partial t}(\rho_i c_i T) = \frac{\partial}{\partial z} \cdot (\lambda_i \frac{\partial T}{\partial z}) + (q_{rad}) \quad (3-2)$$

This results from assuming that the vertical temperature gradients are much larger than the horizontal ones, which allows us to neglect the horizontal derivatives. In order to solve the above equation, the boundary conditions need to be specified at both the ice-atmosphere boundary (upper surface) and ice-ocean boundary (lower surface). These two boundary conditions are as follows:

$$\text{Top B.C:} \quad Q_T + \lambda_i \frac{\partial T}{\partial z} = 0 \quad \text{if} \quad T_0 < T_f \quad (3-3a)$$

$$Q_T + \lambda_i \frac{\partial T}{\partial z} = -\rho_i L_i (dh_i / dt)_0 \quad \text{if} \quad T_0 = T_f \quad (3-3b)$$

$$\text{Bottom B.C:} \quad Q_w - \lambda_i \frac{\partial T}{\partial z} = -\rho_i L_i (dh_i / dt)_{hi} \quad \text{as} \quad T_{bot} = T_f \quad (3-4)$$

where Q_T is the heat flux at the top surface, $\lambda_i \frac{\partial T}{\partial z}$, is the conductive flux that comes from the ice, L_i the latent heat of fusion of ice, h_i , the solid ice thickness and Q_w is the heat flux from the ocean.

Figure 3-1, shows a simplified schematic illustration of the basic sea-ice growth problem. Ice basically grows at the bottom while latent heat is taken from the ocean water. However ice thickness can also change at the top, by melting during the summer due to excessive solar radiation at the top surface.

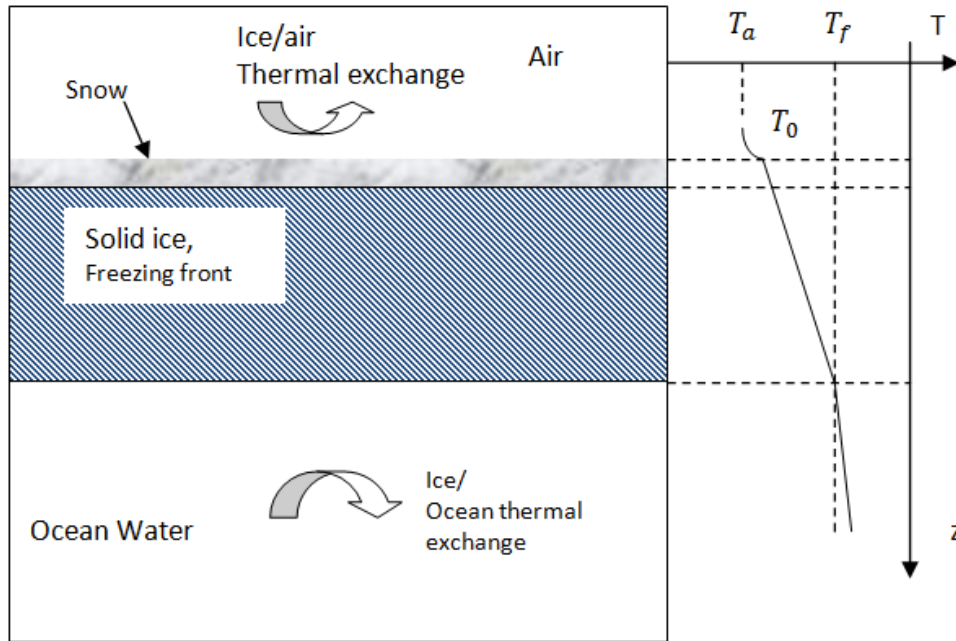


Figure 3-1 General schematic illustration of the thermodynamic sea ice growth model

3.2 Use of Analytic equations/models to predict sea-ice growth

Despite of the existence of great uncertainty and high sensitivity regarding various factors in the sea ice growth problem, it has been observed that simple analytic models can provide rather sufficiently accurate results, see (Leparanta , 1992), on predicting ice growth in various locations. The thermal properties of ice used in analytic models are generally taken as constants, and this can be justified by saying that ice remains cold during the growth season i.e. the winter months, and hence the thermal properties do not vary much. In addition, during the ice growth season, the solar radiation is considered insignificant and the diurnal temperature variations have been observed to be small.

The ability of analytic models to give good predictions of ice growth, was the reason that it was decided to build first a Brash Ice Growth Model, BIGM 1, based on analytic equations. The basic analytic model is the Classical Stefan's Law, (Stefan , 1891). The basic Stefan model, was the basis for all predictive studies and models of ice formation in frequently transited channels, such as (Sandkvist, 1986), (Kannari, 1983) and (Ettema & Huang, 1990). The explanation of the theory of the Stefan model and its' extensions as well as all the relevant equations would be explained in section 4, where BIGM 1 is thoroughly presented and explained.

4. Thermodynamic model of solid ice re-growth in BIGM 1: Modelling Brash Ice Growth using analytical equations for sea-ice growth

4.1 Thermodynamics of BIGM 1, use of the Stefan Law

4.1.1 Classical Stefan's Law for ice growth

As it was mentioned in the previous section, the basic analytic model for ice growth is the classical Stefan's law, (Stefan , 1891). This model is based simply on the idea that the heat released by freezing at the ice bottom is conducted away through the ice with a constant temperature gradient. The classical Stefan's Law is based on the following assumptions:

1. *No thermal inertia.*
2. *No internal heat sources.*
3. *The temperature at the top surface, T_0 , is supposed to follow the air temperature, T_a , and hence it is a function of time as well since $T_a(t)$.*
4. *The input heat flux from the ocean water at the bottom surface is neglected.*

From the assumptions above, the system of equations to be solved is:

$$\text{Simplified heat conduction equation: } \frac{\partial}{\partial z} (\lambda_i \frac{\partial T}{\partial z}) = 0 \quad (4-1)$$

$$\text{Top Surface: } T_0 = T_a(t) \quad (4-2)$$

$$\text{Bottom Surface: } \rho_i L_i (dh_i / dt)_{hi} = \lambda_i (T_f - T_a) / h_i \quad (4-3)$$

where $\frac{\partial T}{\partial z}$ is constant, hence giving a linear temperature profile within the ice. Assuming the initial condition as, $h_i(t=0) = h_0$, the analytical solution of the moving boundary condition at the bottom, Eq.(4-3), gives the following expression for solid ice thickness $h_i(t)$:

$$h_i(t) = \sqrt{h_0^2 + \alpha^2 \theta(t)} \quad (4-4)$$

where

$$a = \sqrt{\frac{2\lambda_i}{\rho_i L_i}} \quad (4-5)$$

$$\theta(t) = \int_0^t (T_f - T_a(\tau)) d\tau \quad (4-6)$$

The Equations (4-4 to 4-6) are the Classical Stefan's Law equations where $\theta(t)$ is the cumulative freezing degree days and a typical value of a is $3.3 \text{ cm } (^\circ\text{C} \cdot \text{day})^{-1/2}$. The simplifications made to derive Stefan's Law, all tend to bias the ice thickness of the model upward, see (Leparanta , 1992).

The greatest disadvantage of Stefan's Law, is the poor estimation of the top boundary condition. The surface temperature T_o , has to be estimated from the air temperature, something that is not easy to do, especially when the ice is thin or when there is a dry-brash-ice cover or snow cover on the ice. Also, neglecting the heat flux from the ocean water at the bottom of the ice, Q_w , can lead to incorrect results.

Summarizing, classical Stefan's Law assumes that the thermodynamic properties of sea ice are constants. The specific heat capacity is not taken into account as the thermal inertia is neglected, and the heat conductivity, λ_i , is assumed constant, although in reality it depends on temperature and salinity, hence it would generally be slightly lower in the lower layers of solid ice. However, this usually does not usually have a significant effect on the final ice thickness results.

The analytic model of the classical Stefan's Law can be improved and extended to include more features, by making some more simplifying assumptions, and hence be used as a tool for qualitative understanding of the ice growth problem and ice thickness predictions. However, complete models can only be solved numerically, such as in (Maykut & Untersteiner, 1971), (Semtner, 1976) and (Ukita & Martinson, 2001).

4.1.2 Stefan's Law with the correction of ice-atmosphere coupling

The atmospheric temperature T_a , at some height above the ice surface is usually known, however the actual ice top surface temperature T_o , is not. The total heat flux at the top surface of the ice Q_T , can be expressed by an ice/air heat exchange relation, which can also be used to estimate T_o . This relation is:

$$Q_T = h_c(T_o - T_a) \quad (4-7)$$

where h_c is a convective heat exchange coefficient at the ice/air interface. The use of flux continuity at the solid ice/air interface gives:

$$h_c(T_o - T_a) = \lambda_i \frac{(T_f - T_o)}{h_i} = q_i \quad (4-8)$$

Equations (4-7) and (4-8), can be used to express the heat flux, q_i , through the solid ice as a function of T_a , T_f , and h_i . This makes it possible to re-arrange the ice growth equation, Eq. (4-3) as:

$$\rho_i L_i (dh_i / dt)_{hi} = \frac{h_c(T_f - T_a)}{1 + h_c h_i / \lambda_i} \quad (4-9)$$

Using the assumption that the initial condition is $h_i(t=0) = h_0$, and that h_c is constant, the analytical solution of the moving boundary condition at the bottom, Eq.(4-9), can be analytically integrated to give the following modified expression for ice thickness $h_i(t)$:

$$h_i(t) = \sqrt{\left(h_0 + \frac{\lambda_i}{h_c}\right)^2 + \alpha^2 \theta} - \frac{\lambda_i}{h_c} \quad (4-10)$$

A typical mean value of h_c is $20 \text{ W} / \text{m}^2 \text{ K}$, giving a ratio of $\frac{\lambda_i}{h_c}$ of about 0.1 m, see (Lepparanta , 1992).

The modified Stefan's Law described in this section, was first presented in (Anderson, 1961). (Anderson, 1961), proved that the ice-atmosphere coupling has a major effect on ice growth in its early stage due to the finite value of the thermal exchange coefficient h_c that limits the heat flux extracted from the ice, in comparison with the Classical Stefan's Law. Therefore it was concluded that the Classical Stefan's Law derivation largely overestimates the speed of ice growth when the ice is still thin.

In the context of a brash ice growth model, where a solid ice freezing front is growing through a brash ice layer, Equations (4-9) and (4-10) that are related to the solid ice growth, are transformed into Equations (4-11) and (4-12):

$$\rho_i p L_i (dh_i / dt)_{hi} = \frac{h_c (T_f - T_a)}{1 + h_c h_i / \lambda_i} \quad (4-11)$$

$$h_i(t) = \sqrt{\left(h_0 + \frac{\lambda_i}{h_c}\right)^2 + \frac{\alpha^2}{p} \theta} - \frac{\lambda_i}{h_c} \quad (4-12)$$

where P is the porosity of the brash ice. Note that porosity of the brash ice, P , is defined as the volume of voids (water), V_{void} , over the total volume of the brash ice ($V_{void} + V_{ice}$), hence:

$$p = V_{void} / (V_{void} + V_{ice}) \quad (4-13)$$

4.1.3 Modified Stefan's Law extended to include the insulation effect due to a top layer

This extension assumes the existence of a dry brash ice layer or snow over the growing solid ice layer. The assumptions stated previously (1-3) for ice, in the Classical Stefan's Law section are applicable to the dry brash ice layer as well. T_0 is now the temperature at the top of the dry brash ice layer, a layer which is also assumed having a linear temperature profile. An assumption for this extension is that the dry brash ice layer forms, simply from ice floating fragments produced from previous ice breaking due to a ship visit, just after a thin brash ice layer has converted to solid ice so that the dry brash ice layer acts as an insulating cover, of thickness h_{dbi} and thermal conductivity λ_{dbi} . This insulating cover would have a constant thickness h_{dbi} , between two consecutive ice breaking occurrences (ship vessel passages), and would be broken and re-calculated at every new vessel passage, using the Archimedes buoyancy principle. Defining a temperature T_{si} , at the dry brash ice-solid ice interface, and applying heat flux continuity between the solid ice layer, the dry brash ice layer and the atmosphere, gives:

$$h_c (T_0 - T_a) = \lambda_i \frac{(T_f - T_{si})}{h_i} = \lambda_{dbi} \frac{(T_{si} - T_0)}{h_{dbi}} = q_{tot} \quad (4-14)$$

where q_{tot} is the heat flux through the bulk layer of solid and dry brash ice. Using the quasi steady heat equation in the bulk solid ice and dry brash ice layers, together with the condition of continuity, as presented in Eq. (4-14), the total heat flux q_{tot} , can be expressed as a function of T_a, T_f, h_i and h_{dbi} , as follows:

$$\rho_i p L_i (dh_i / dt)_{hi} = \frac{h_c (T_f - T_a)}{1 + h_c h_i / \lambda_i + h_c h_{dbi} / \lambda_{dbi}} \quad (4-15)$$

The detailed derivation of Eq. (4-15) can be found in appendix B. Assuming as before the initial condition as $h_i(t=0) = h_0$, and that h_c is constant, the analytical solution of the moving boundary condition at the bottom, Eq. (4-15), can be analytically integrated to give the following modified expression for ice thickness $h_i(t)$, in case of the existence of a dry brash ice (or snow) layer on top:

$$h_i(t) = \sqrt{(h_0 + \frac{\lambda_i}{h_c} + \frac{\lambda_i h_{dbi}}{\lambda_{dbi}})^2 + \frac{\alpha^2}{p} \theta} - (\frac{\lambda_i}{h_c} + \frac{\lambda_i h_{dbi}}{\lambda_{dbi}}) \quad (4-16)$$

Equation (4-16), can be expressed in the same form as, Eq. (4-12), as follows:

$$h_i(t) = \sqrt{(h_0 + \frac{\lambda_i}{h_{c,eq}})^2 + \frac{\alpha^2}{p} \theta} - \frac{\lambda_i}{h_{c,eq}} \quad (4-17)$$

where,

$$h_{c,eq} = (\frac{1}{h_c} + \frac{h_{dbi}}{\lambda_{dbi}})^{-1} = \frac{h_c}{1 + \frac{h_{dbi} h_c}{\lambda_{dbi}}} < h_c \quad (4-18)$$

The term $h_{c,eq}$ is the equivalent convective coefficient of thermal heat exchange due to the existence of the dry brash ice layer. As it is shown in Eq. (4-18), its' value is lower than h_c demonstrating the insulating effect of the dry brash ice cover.

The intermediate temperature T_{si} , at the solid ice-dry brash ice interface can be calculated by applying conductive flux interface continuity as follows:

$$\lambda_i \frac{(T_f - T_{si})}{h_i} = \lambda_{dbi} \frac{(T_{si} - T_0)}{h_{dbi}} \quad (4-19)$$

and solving towards T_{si} , to get:

$$T_{si} = \frac{T_0 + \frac{h_{dbi} \lambda_i}{\lambda_{dbi} h_i} T_f}{1 + \frac{h_{dbi} \lambda_i}{\lambda_{dbi} h_i}} \quad (4-20)$$

Using the result from Eq. (4-11), and still applying flux continuity an expression for, T_0 , can be obtained as follows:

$$\lambda_{dbi} \frac{(T_{si} - T_0)}{h_{dbi}} = \frac{h_{c,eq} (T_{si} - T_a)}{1 + \frac{h_{c,eq} h_{dbi}}{\lambda_{dbi}}} \quad (4-21)$$

and re-arranging to get:

$$T_0 = \frac{h_{dbi} h_{c,eq} T_a + T_{si} \lambda_{dbi}}{\lambda_{dbi} + h_{c,eq} h_{dbi}} \quad (4-22)$$

By inserting Eq. (4-22), into Eq. (4-20), and re-arranging towards T_{si} , T_{si} can be calculated directly without needing to use the value of T_0 :

$$T_{si} = \frac{h_{c,eq} T_a h_i + \lambda_i T_f \left(1 + \frac{h_{c,eq} h_{dbi}}{\lambda_{dbi}}\right)}{\lambda_i + h_{c,eq} h_i + \frac{h_{c,eq} h_{dbi} \lambda_i}{\lambda_{dbi}}} \quad (4-23)$$

However, note that T_0 , if required, can be easily calculated from Eq. (4-22), in the case of the existence of a dry brash ice layer, and from re-arranging Eq. (4-8) in the case of bare ice.

4.2 Introducing a brash ice melting effect into BIGM 1

One of the main goals of this study is the calculation of the energy required to decrease the thickness of brash ice in ports, specifically the Yamal LNG port in this case, to a desired acceptable level. Melting of ice in these cases is typically done with the use of thermal effluents from the bottom of the port. The bottom layer of the total ice column is the brash ice layer, which was created from the last ice breaking event, and all the thermal energy supplied from the thermal effluents is assumed to be used solely for melting this layer. The warm water energy can be expressed in the form of a heat flux Q_w , which can be provided either by the ocean or by a brash ice management system (BIMS) such as an air bubble system. The use of this warm water system (BIMS) is assumed to be continuous during the winter months therefore causing a continuous melting of brash ice during these months. Hence this effect has to be included in the ice growth cycle of a brash ice model simulation, which is defined as the time between two ice breaking events i.e. two vessel passages. The amount of brash ice melted by the BIMS in terms of brash ice thickness, per time step of the simulation can be found from:

$$\Delta h_{bi_{melted}} = \frac{dh_{bi_{melted}}}{dt} \Delta t \quad (4-24)$$

where the rate of brash ice melting can be expressed as:

$$\frac{dh_{bi_{melted}}}{dt} (t)^{m+1} = \frac{Q_w}{\rho_i (1-p) L_i} \quad (4-25)$$

where Q_w is the heat flux provided by the BIMS, and $(1-p)$ represents the amount of ice pieces within the brash ice layer. Then this amount of brash ice melted Δh_{bi} , is subtracted by the previously calculated wet brash ice thickness h_{bi} , at the end of every time step within an ice growth cycle. Hence at the end of time step $m+1$:

$$h_{bi_{final}} (t)^{m+1} = h_{bi} (t)^m - \frac{dh_{bi_{melted}}}{dt} (t)^{m+1} \times \Delta t \quad (4-26)$$

Remember here that BIMS is assumed not to cause any effect on the growth and thickness of the solid ice layer h_i .

4.3 Ice Growth Cycle in BIGM 1

The brash ice growth models developed in this study consist of two main parts. The solid ice growth cycle, which is solved partly differently in BIGM 1 and BIGM 2, and the model of ice breaking which is exactly the same in BIGM 1 and BIGM 2. The solid ice growth cycle part, as it was explained above, is the period between two consecutive vessel transits or breaking events, and describes the growth of the solid ice through the bulk brash ice layer. The model of ice breaking describes how the different layers of ice, namely the solid ice, wet brash ice, and dry brash ice if it exists, change at the instant of breaking. In this section the ice growth cycle part of BIGM 1 would be described for the cases of the existence and non-existence of a dry brash ice layer above the solid ice. The model of ice breaking which is identical for both BIGM 1 and BIGM 2 would be explained at section 7 of this study.

4.3.1 No dry brash ice on top

While a time step m of the simulation, is within a solid ice growth cycle (a period between 2 vessel passages) the calculation procedure in the growth cycle is as follows:

1. Given as input the air temperature, T_a , and knowing the initial solid ice thickness condition after a breaking event, $h_i(t=m) = h_0 \approx 0$, Eq. (4-12) is used to calculate the amount of total solid ice thickness h_i at this time step.
2. In order to calculate the amount by which solid ice thickness has grown during time step m , the derivative of Eq. (4-12) is used and multiplied by the time step duration, Δt . Hence,
$$\Delta h_i = \frac{dh_i(t)}{dt} \times \Delta t.$$
3. The amount by which brash ice layer has decreased during this time step is equal to the amount by which solid ice has increased during this time step, as solid ice grows through the the brash

ice layer. Hence the brush ice layer, at the end of this time step is calculated from:

$$h_{bi}(t)^m = h_{bi}(t)^{m-1} - \frac{dh_i}{dt}(t)^m \Delta t .$$

- If the effect of a brush ice management system is included, then the amount by which the brush ice has melted, $\Delta h_{bi, melted}$, during this time step has to be calculated and subtracted from the remaining brush ice that was calculated in step 3. This is done using Equations (4-24), (4-25) and (4-26).

The processes that take place in the ice growth cycle, when there is no dry brush ice, along with the relevant equations are all shown in Figure 4-1 below.

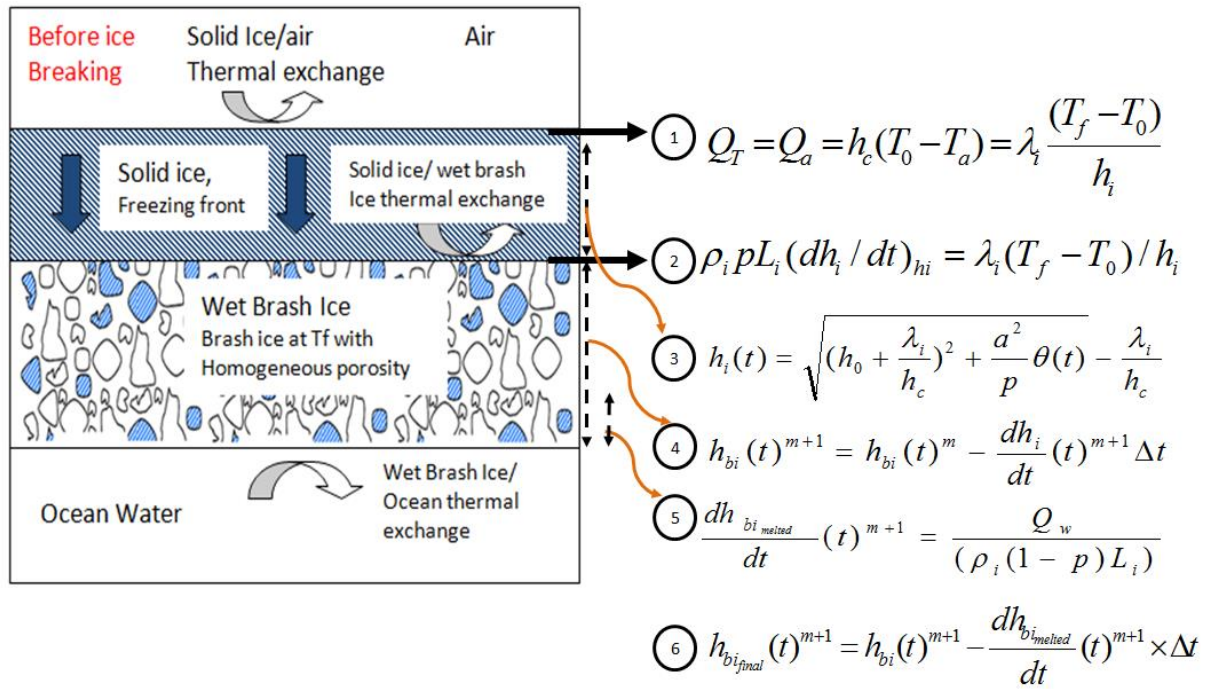


Figure 4-1. In this figure the processes that take place, and all the equations that are used, in the ice growth cycle, in case of no dry brush ice layer on top, are shown. Note that for convenience, the equations shown in this figure have different number from the one they have in the main text of this report.

As you can see in Figure 4-1 there are two main layers of ice, the solid ice layer and the wet brush ice layer. The solid ice layer is seen to be growing through the brush ice layer. Equation 1 (using figure equation numbering), describes the upper surface boundary condition. All the fluxes going towards the top surface of the solid ice, except from the conductive flux, are approximated by a flux Q_T , calculated by the product of the thermal exchange coefficient h_c , and the difference in temperature between the top surface of the ice T_o and the air temperature T_a . The conductive flux coming through the solid ice layer balances this Q_T flux. Equation 2, shows the bottom moving boundary condition, which when integrated gives the ice growth equation of solid ice, Equation 3. Equation 4, shows the formula for the calculation of the brush ice layer at the end of each time step, after subtracting the amount by which solid ice has grown in that time step. Equations 5 and 6, as it was also mentioned previously, are only used when the effect of a Brush Ice Management System (BIMS)

is taken into account, and they are used for the re-calculation of the wet brush ice when the melting effect is included.

Figure 4-2, demonstrates the temperature profile in the total ice column during the ice-growth cycle. Note the linear temperature profile within the solid ice layer, the straight vertical line within the brush ice layer which means that there is no heat flux conduction, and the linear input heat flux from the ocean water or BIMS into the brush ice layer.

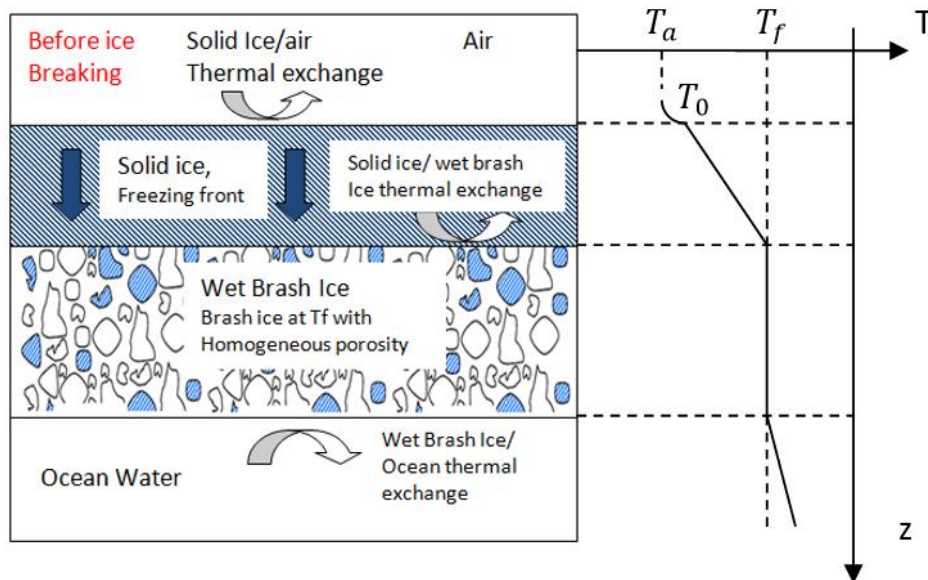


Figure 4-2 Temperature Profile. Situation shown, does not include a dry brush ice layer.

4.3.2 With dry brush ice on top

The calculation procedure with the existence of a dry brush ice layer on the top of the solid ice layer, is almost identical. The processes that take place in the ice growth cycle, in this case, along with the relevant equations are all shown in Figure 4-3 below. A dry brush ice layer thickness is calculated using Archimedes principle just after a breaking event and remains constant until the next breaking event i.e. during the whole ice growth cycle, and a solid ice layer is growing through the wet brush ice layer.

Equation 1 (using figure equation numbering) shows the balance of fluxes at the upper boundary condition of the dry brush ice layer, similarly as before in the case of bare ice, and Equation 2 shows the balance of conductive fluxes at the dry brush ice-solid ice interface. Using Equation 2 to re-arrange Equation 3 and integrating Equation 3, results in Equation 4, which is the equation for the calculation of the thickness of solid ice h_i , in the case of the existence of a dry brush ice layer on top. The rest of the steps are exactly identical.

Figure 4-4, demonstrates the temperature profile in the total ice column during the ice-growth cycle. Note again, the linear temperature profile within the solid ice layer, as well as within the dry brush ice layer. Also note, the straight vertical line within the wet brush ice layer, which means that there is no heat flux conduction within that layer. Finally, note the linear input heat flux from the ocean water or BIMS into the brush ice layer.

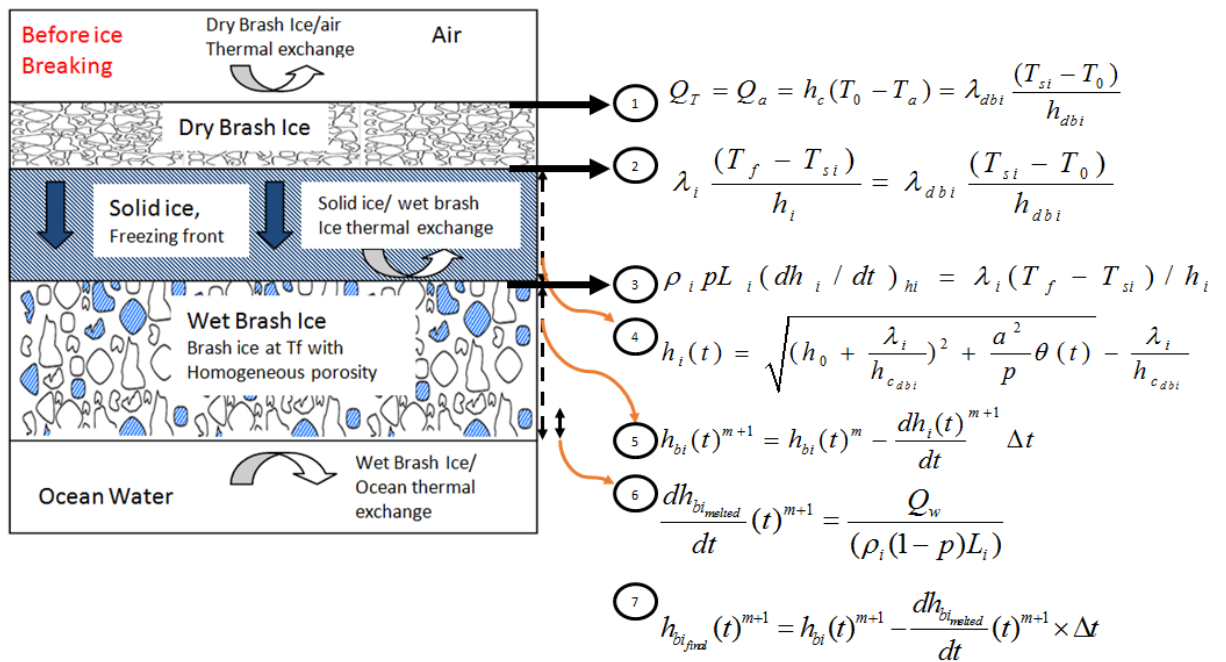


Figure 4-3 In this figure, the processes that take place and all the equations that are used in the ice growth cycle, in the situation of the existence of a dry brush ice layer on top, are shown. Note that for convenience, the equations shown in this figure have different numbers from the one they have in the main text of this report.

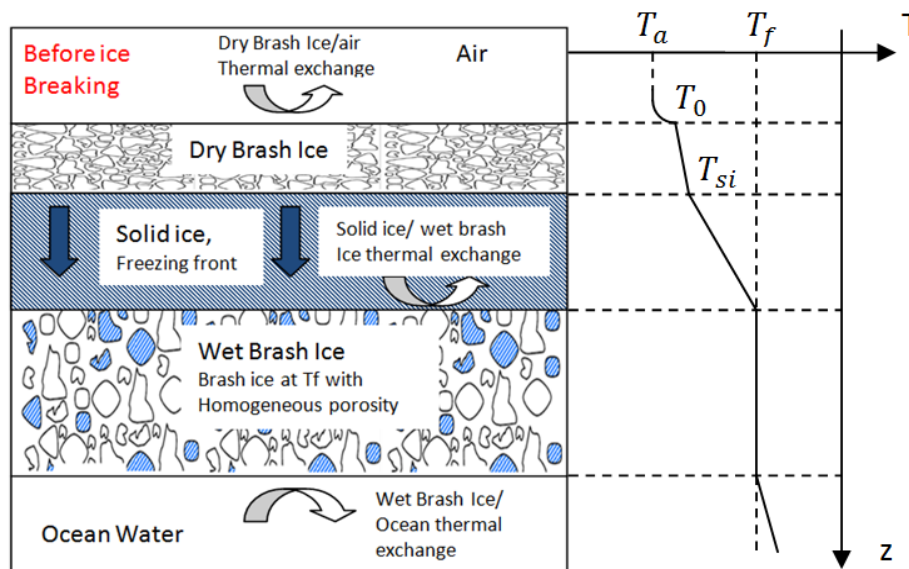


Figure 4-4 Temperature Profile. Situation shown, includes a dry brush ice layer.

4.4 Advantages and Disadvantages of BIGM 1

4.4.1 Advantages

1. Model based on analytic methods, so no need to question the validity of the method under certain assumptions.
2. Very simple to model and simulate. It consumes less computing time compared to any numerical model.

4.4.2 Disadvantages

1. It does not take into account the real boundary conditions. More specifically at the top surface, it uses a very rough approximation of the upper surface boundary condition, by approximating all the heat fluxes, except from the conductive flux, through the solid ice, with a flux Q_T .
2. As the analytical model for ice growth is based on several simplistic assumptions, it cannot model various physical changes that take place in the total ice column, such as the absorption of solar radiation from lower layers of the solid ice, variations in the thermal properties of solid ice such as the ice thermal conductivity and specific heat capacity, changes in salinity etc.

5. Modeling of the growth of sea ice with numerical schemes

Using analytic models for the thermal growth of sea ice, such as above, is an efficient way of examining the physics of the problem, and an easy tool to obtain first-order approximations for the ice thickness under various environmental conditions, see (Leparanta , 1992). However, in order to achieve a quantitative analysis of sea ice growth, the use of a numerical model is essential, in order to manage the complications introduced by varying ice thermal properties, snow or freeboard cover, and of course the boundary conditions. The first ever numerical model with the solution of the full vertical sea ice heat conduction equation was done by (Maykut & Untersteiner, 1971), and had been a basic reference model for most of the numerical models that followed.

Treating of the heat flow within the ice and snow sub-layers in numerical models is relatively easy, however treating of the boundary conditions is more complicated. Because of the heat flux dependency between the underlying ice and snow layers and the heat flux balance on the upper surface of the snow or the ice (depending on whether there is snow on top of the solid ice), this boundary condition needs to be solved simultaneously with the heat conduction equations, see (Leparanta , 1992).

The classical 1-D thermodynamic model in the solid ice layer, can be solved with various numerical methods, by solving numerically the 1-D heat equation, see Eq. (3-2), in order to determine the temperature profile through the solid ice layer, whose thickness varies with time. Thermal properties such as the heat capacity (density times the specific heat capacity) or the conductivity, can either be assumed constant or being varied via empirical equations that are functions of the ice temperature and salinity, such as in (Maykut & Untersteiner, 1971). All the numerical methods, are based on a vertical discretization of the solid ice layer of thickness, h_i , with N_i ice layers of thickness:

$$\Delta h_i = \frac{h_i}{N_i} \quad (5-1)$$

The temperature of the top surface T_o , whether this is solid ice, dry brash ice or snow, should not be greater than the freezing temperature $T_f = -0.2^\circ C$, and the temperature at the mid-point of each ice layer is $T_{i,k}$, where $k_i = 1, \dots, N_i$. The vertical discretization of the solid ice layer is as in Figure 5-1 below.

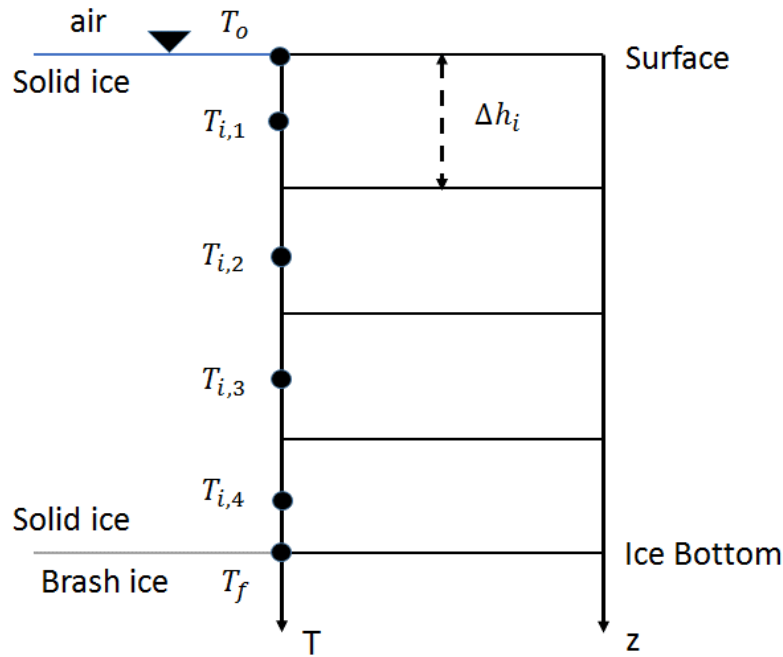


Figure 5-1 Discretization of the solid ice layer.

There are two ways to divide the solid ice layer into multiple layers. The first way is to set a maximum value of an individual solid ice layer thickness Δh_i , and the number of layers changes according to the thickening of solid ice so as to avoid the burden of more layers than required in order to satisfy the thermal equilibrium condition, see (Ukita & Martinson, 2001). The second way is to fix the number of ice layers N_i , such as in the numerical models of (Maykut & Untersteiner, 1971) and (Ebert & Curry, 1993), making an individual ice layer thickness Δh_i , depending on the total ice thickness. In order for these models to properly simulate thermal inertia in the ice and obey thermal relaxation, relatively thin layers have to be used.

5.1 Choosing a numerical scheme for sea ice growth

The chronological order of the most notable ice growth models is as follows:

1. Stefan's Model (1891). Simple Analytic model with various assumptions
2. Maykut and Untersteiner (1971). Detailed Numerical Scheme, using a stable alternating direction explicit method with a fixed grid-point separation of 10 cm.
3. Stemner (1976). Simplified the Maykut and Untersteiner model to obtain a 0- or 3- layer numerical model that is less computing time consuming, used often in climatological studies.
4. Ebert and Curry (1993). An explicit absolutely stable Dufort- Frankel algorithm
5. Flato and Brown (1996). An implicit absolutely stable Crank-Nicholson scheme
6. Ukita and Martinson model (2001), Full Detailed Implicit Numerical Scheme, absolutely stable, very easily adjustable, solved using tri-diagonal matrices. Also used by Bertin technologies for the Yamal LNG project.
7. Huwald (2005), A multilayer sigma coordinate sea ice model. The heat conduction equation is integrated using a forward in time finite difference numerical scheme of Lagrangian nature.

In this study the (Ukita & Martinson, 2001) numerical scheme, was chosen as the basis for the thermodynamics of the second Brash Ice Growth model, BIGM 2. The choice was based firstly on the fact that this is an implicit scheme, which means there are no restrictions on the ratio of the discretization space over time step, and that the scheme remains absolutely stable, see (Bloquin [2], 2013). An explicit scheme would have required the satisfaction of the Courant–Friedrichs–Lewy (CFL) condition which in this case would have been:

$$\Delta t \leq \frac{(\Delta h_i)^2}{\lambda_i / (\rho c_i)} \quad (5-2)$$

The use of an implicit scheme enables to avoid having any constraint on the time step of the simulations, hence avoiding using really small time steps that can drop to an order of a few seconds.

5.2 The Upper Surface boundary condition

In this section, the upper surface boundary condition and each flux that is directed towards it, would be examined. The major energy fluxes on the top surface of an ice column, whether bare ice, dry brash ice or snow are:

1. Incoming long wave radiation from the atmosphere and clouds, Q_{LWR}
2. Incoming short wave radiation, Q_{SWR} , i.e. solar radiation
3. Reflected short wave radiation, aQ_{SWR}
4. Outgoing long wave radiation, $\varepsilon_{RAD}\sigma T_0^4$

where a is a surface albedo, ε_{RAD} is the long wave radiation emissivity and σ is the Stefan-Boltzmann constant. In addition there are some other minor, however important, fluxes such as:

1. The fluxes of sensible heat Q_S ,
2. Fluxes of latent heat in the adjacent air Q_L ,
3. Heat conduction flux towards the top surface whether it is bare ice, snow or dry brash ice Q_o
4. And a flux of solar radiation that penetrates the top surface and creates internal heat sources into the lower solid ice layers and dry brash ice layers (or snow layers) if these are assumed to exist, I_o .

All the fluxes are schematically illustrated in Figure 5-2. The convention adopted for energy flux description is that a flux towards the surface is positive and one away from the surface is negative. In determining the balance equation for the upper surface, two possible cases have to be considered. If the top surface temperature T_0 , is lower than the freezing temperature T_f , T_0 would have to be adjusted to balance all the fluxes.

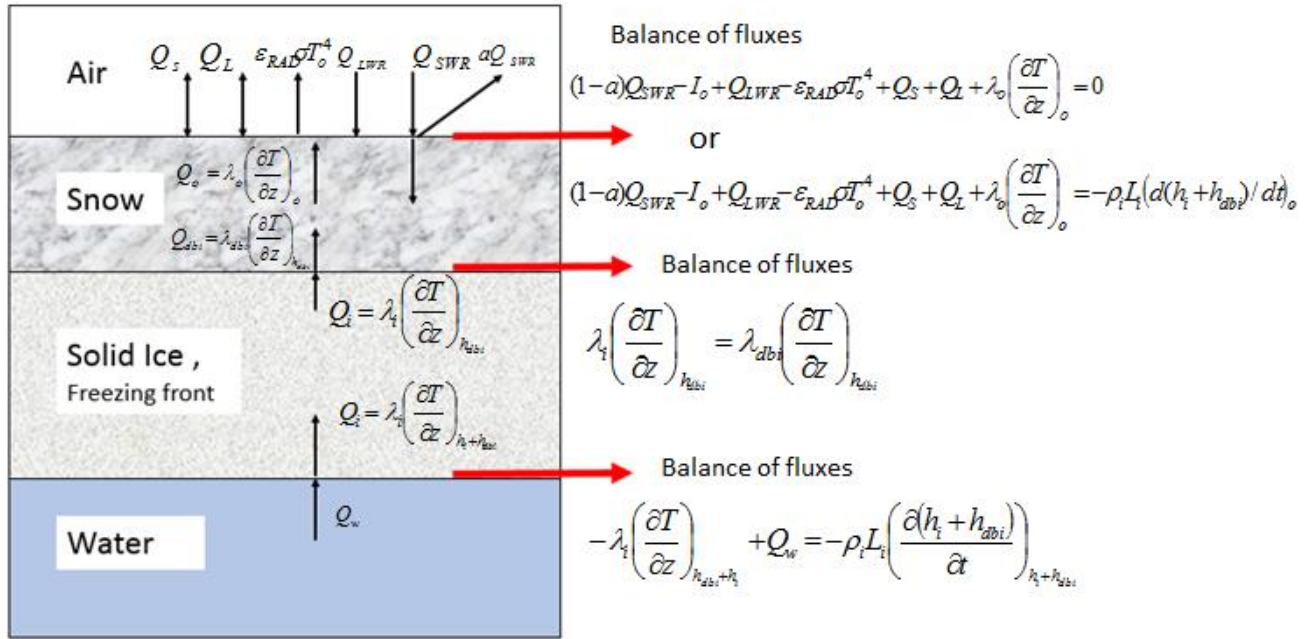


Figure 5-2 All the fluxes involved in the sea ice growth problem

However, in case T_o is equal or higher than the freezing temperature, a certain amount of ice must be melted to take into account of any surplus of energy flux towards the surface. Therefore:

$$(1-a)Q_{SWR} - I_o + Q_{LWR} - \epsilon_{RAD}\sigma T_o^4 + Q_S + Q_L + \lambda_o \left(\frac{\partial T}{\partial z}\right)_o = 0 \quad \text{If } T_o < T_f \quad (5-3a)$$

$$(1-a)Q_{SWR} - I_o + Q_{LWR} - \epsilon_{RAD}\sigma T_o^4 + Q_S + Q_L + \lambda_o \left(\frac{\partial T}{\partial z}\right)_o = -\rho_i L_i \left(\frac{d(h_i + h_{dbi})}{dt}\right)_o \quad \text{If } T_o = T_f \quad (5-3b)$$

where h_{dbi} is the thickness of the dry brash ice layer(or snow), h_i is the thickness of the solid ice layer, L_i is the latent heat of fusion of ice and λ_i is the conductivity of ice . Note that the subscript o refers to the upper surface. Note also that the turbulent fluxes, which are the sensible heat flux Q_S , and the latent heat flux Q_L , although given positive, can in fact have either direction. The parameters of Eq. (5-3) that can be described as time dependent external parameters are a , Q_{SWR} , Q_{LWR} , I_o , Q_S and Q_L . This basically means that in any numerical model used, these parameters would be inserted as input data in the model, for a certain simulation. On the other hand, any changes in temperatures and ice thicknesses would be determined by the numerical scheme.

According to a study made by Bertin Technologies for the Yamal LNG (Bloquin [1], 2013) in relation to the weather conditions in Sabetta, the turbulent latent heat flux Q_L , can be completely neglected, as its' magnitude is negligible compared to the other fluxes. Moreover the solar short wave radiation incoming and reflected Q_{SWR} and aQ_{SWR} , and also the radiative energy through the upper

surface T_o , can be neglected as well, as the purpose of the model is to examine ice growth during the cold season, when these fluxes have relatively low values. Therefore, for the Sabetta reference case simulations that are going to be presented in section 9, Eq. (5-3) was simplified to:

$$Q_{LWR} - \varepsilon_{RAD} \sigma T_o^4 + Q_S + \lambda_o \left(\frac{\partial T}{\partial z} \right)_o = 0 \quad (5-4)$$

The sensible heat flux Q_S , was expressed as the product of the temperature difference between the potential air temperature T_a , and the surface temperature of ice, T_o and the turbulent convective coefficient, h_c . Hence:

$$Q_S = h_c (T_a - T_o) \quad (5-5)$$

where the thermal exchange coefficient, h_c , can be expressed as:

$$h_c = \rho_a c_a C_s u_a \quad (5-6)$$

where ρ_a is the air density, c_a is the specific heat capacity of air, C_s is the sensible heat transfer coefficient and u_a is the wind speed.

Note that the simplified Eq. (5-4), was only used for the Sabetta reference case simulations. The brash ice growth model developed, BIGM 2, has the option to include all the fluxes of Eq. (5-3) if there is available metocean data. This is shown in section 11, where field metocean data from the Lulea area, were used as input in the model, in order to aid comparison between the models' predictions and brash ice field measurements from a channel just outside the port of Lulea. The solution and properties of BIGM 2 are presented in section 6.

6. Thermodynamic model of solid ice re-growth in BIGM 2: Modelling brash ice growth using numerical solutions for sea-ice growth

6.1 Thermodynamics of BIGM 2, use of the Ukita and Martinson numerical implicit scheme for solid ice growth

As it was stated in the previous section of the report, the chosen numerical scheme to solve the thermodynamic part of BIGM 2 related to solid ice growth, is the scheme proposed by (Ukita & Martinson, 2001). The model is based in solving the 1-D fully non-linear heat conduction equation with a moving boundary associated with freezing and melting, shown in Eq.(3-2), in order to describe with time, the evolution of the temperature profile through the vertical column of the solid ice layer. If the solar radiation penetrating the surface layer, q_{rad} , is ignored, Eq.(3-2), can be re-written as:

$$\rho_i c_i \frac{\partial}{\partial t} (T_i) = \lambda_i \left(\frac{\partial^2 T_i}{\partial z^2} \right) \quad (6-1)$$

which is the form of the heat conduction equation that the model uses.

The upper surface boundary condition shown in Eq. (5-3), can be re-written using a standard bulk parameterization of the sensible heat flux given from Eq. (5-5) as:

$$Q_{RAD} - \varepsilon_{RAD} \sigma T_o^4 + h_c (T_a - T_o) + \lambda_i \left(\frac{\partial T_i}{\partial z} \right)_{z=0} = 0 \quad (6-2)$$

where T_o is the surface temperature, T_a is the air temperature, and Q_{RAD} is the sum of the net shortwave radiation, the incoming longwave radiation, and the latent heat flux which are all kept constant to facilitate illustration.

The basal boundary condition, at the ice-brash ice interface is:

$$T_b = T_f \quad (6-3a)$$

$$\lambda_i (T_i - T_z) / h_i = \rho_i p L_i (dh_i / dt)_{hi} \quad (6-3b)$$

where T_b is the temperature at the bottom of the solid ice, which is fixed to the freezing temperature of water, see Eq. (6-3a). Equation (6-3b) is a moving boundary condition that expresses the fact that solid ice grows through an existing layer of brash ice of porosity p , which is defined as the fraction of volume occupied by sea water between ice blocks, see Eq. (4-13). In case the solid ice layer reaches the bottom of the brash ice layer, the porosity should be set to 1, and this goes back to the classical condition of the Stefan problem. The oceanic heat flux Q_w , exchanged at the bottom surface of the brash ice layer, has not been taken into account for now.

Note, that some processes that take place in ice growth are omitted in this first explanation, however these will be added step by step in the following sub-sections of section 6. These include the penetration of solar radiation into the solid ice layers, and dry brash ice layers if they exist, variation of

the conductivity and heat capacity between layers, depending on ice temperature of the layer and salinity of the layer, the formulation of the top surface equation with the latent heat flux as an independent component and not as a bulk formulation of Q_{RAD} , and the inclusion of the effect of a freeboard in the form of dry brush ice.

6.1.1 Structure of the model

The solid ice layer would be discretized in multiple layers as it shown in Figure 5-1, and temperature points are set at the middle of each of these layers. As it was explained in the previous section of the report, the number of layers in the solid ice would be fixed, and the thickness of each layer Δh_i would be re-calculated at every time step, using Eq. (5-1). As it was mentioned before, in order to allow the model to obey thermal relaxation and to properly simulate the thermal inertia of ice, it must has relatively thin layers, see (Ukita & Martinson, 2001). However, unnecessary many layers would create a high computational burden. The choice for setting a fixed number of layers instead of a fixed layer thickness, for constructing the grid, was based on the fact that the total solid ice layer thickness range that is expected to re-grow over brush ice in Sabetta is in the range of 0-1m. This range was derived based on the operating conditions at the port of Sabetta. Therefore the number of layers required to simulate thermal inertia properly can be accurately determined and an unnecessary great number of layers can be avoided. It was noticed that 5 layers is the best compromise between computation speed and precision of the results.

6.1.2 Temperature Profile Calculation-Solution of the matrix system

Once the number of layers N_i and the time step Δt are defined, the heat conduction equation, Eq. (6-1) can be converted to its finite difference form as follows:

$$(\rho c)_i \frac{T_i^{m+1} - T_i^m}{\Delta t} = \frac{1}{\Delta h_i} \left(\tilde{\lambda}_{i,k+1} \frac{T_{i,k+1}^{m+1} - T_{i,k}^{m+1}}{\Delta h_i} - \tilde{\lambda}_{i,k} \frac{T_{i,k}^{m+1} - T_{i,k-1}^{m+1}}{\Delta h_i} \right) \quad (6-4)$$

Using the temperatures T_0^m , T_f and $T_{i,k}^m$, where k is the number of the layer, at time step m , this finite difference formulation is solved to give the new temperature $T_{i,k}^{m+1}$ at each layer. The fact that the discretization is centered assures a second order accuracy in space except at the boundaries. By treating the heat conduction equation implicitly, the temperature of each layer is coupled to the temperatures of layers immediately above and immediately below that layer.

A system of equations can now be built for the new temperatures of each ice layer. Hence, N_i equations are needed for the N_i mid-layer temperatures, where N_i is the number of solid ice layers, in addition to an extra equation for the upper surface of the solid ice, for the calculation of the top surface temperature T_0 . All the temperatures are evaluated at time step $m + 1$.

(Ukita & Martinson, 2001), explains the necessity of calculating the surface temperature T_0 , to a high degree of accuracy especially when high-frequency forcing is present. High frequency forcing takes place when the externally applied heat fluxes, have values that vary quickly and rapidly. When the fluxes do not vary quickly, the surface flux boundary condition can be decoupled from the rest of

must be calculated after each iteration as it depends on the surface temperature T_0^* and

$$a = \frac{\Delta t(\lambda_i)}{(\rho c)_i (\Delta h_i)^2} \quad (6-10)$$

is a dimensionless parameter, a , that is calculated at the beginning of each time step m .

In Eq. (6-8), the R.H.S of the matrix system contains the temperatures of each layer at the beginning of time step m in addition to the R.H.S of the flux balance equation, Eq. (6-7), on the top of the column vector. The new temperatures, at time step $m + 1$, of each layer including the temperature on the top surface T_o , are in the column vector in the L.H.S of the matrix system, that is labeled with the subscript $m + 1$. This new set of temperatures is obtained after heat diffusion, by solving the matrix system of Eq. (6-8) iteratively. Before the calculation of the new temperature profile at each time step is completed, two conditions must be satisfied:

1. The surface temperature T_0^* , must be equal or lower than the freezing temperature T_f .
2. The change in T_0^* compared to the last iteration must be less than a pre-determined value (i.e. $\Delta T_{\max} \leq 0.01K$) as suggested by (Bloquin [2], 2013).

6.1.3 Ice Growth Calculation

The change in ice thickness at every time step m is governed by the boundary equation, Eq. (6-3b), at the ice-brash ice interface. Discretizing this boundary equation, the solid ice increment δh , at the current time step m , can be determined as follows:

$$\delta h = \frac{2\lambda_i \Delta t}{\rho_i p L_i} \frac{T_f - T_{Ni}^{m+1}}{\Delta h_i} \geq 0 \quad (6-11)$$

The factor of 2, at the front of Eq. (6-11), origins from the fact that the distance in the grid between the mid temperature at the bottom ice layer T_{Ni}^{m+1} , and the temperature at the bottom solid ice layer-brash ice layer interface T_f , is $\frac{\Delta h_i}{2}$.

The new total solid ice layer thickness at the end of time step $m + 1$ is given by:

$$h_i^{m+1} = h_i^m + \delta h \quad (6-12)$$

In case the solid ice layer grows through the whole brash ice layer, it then progresses through sea water, and not brash ice of porosity p . Hence in Eq. (6-11), p would be set to 1.

6.1.4 Grid System re-construction, in case of only solid ice growth system

After the bottom layer has increased its thickness by δh , the layer interfaces have to be adjusted in order to obtain layers of equal thickness $\Delta h_i^m = h_i^m / N_i$, at the end of the current time step m . This procedure is demonstrated in Figure 6-1.

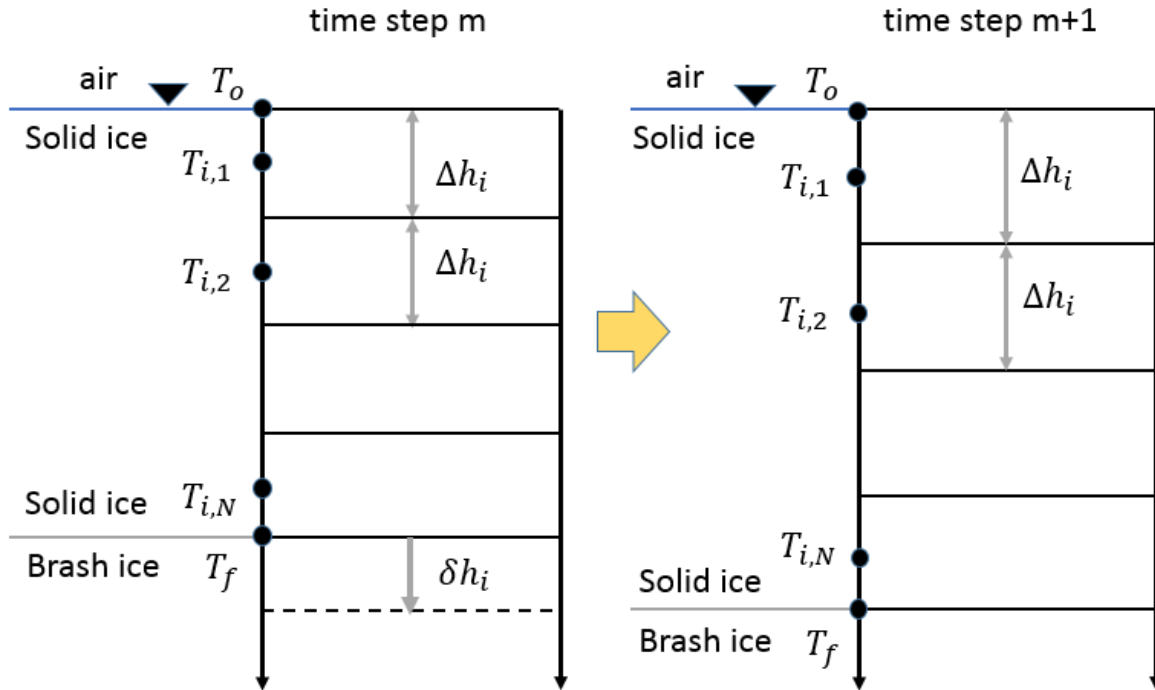


Figure 6-1 Illustration of the grid reconstruction procedure, in the case of not having a dry brash ice layer above the waterline

6.1.5 Different Ice growth Implementation at initial time steps just after a breaking event

A vessel passage converts the solid ice layer completely into brash ice of porosity P . Hence the solid ice thickness h_i is set to 0 as well as the thickness of each ice layer Δh_i . Therefore the dimensionless parameter a , see Eq. (6-10), can no longer be calculated and the numerical procedure with the tri-diagonal matrix system cannot be applied.

At this stage of the simulation, the thermal inertia of the solid ice can be neglected as the solid ice thickness is zero. Therefore Eq. (6-1) is simplified to Eq. (3-3a). This basically means that the conductive flux q_i , is homogeneous inside the tiny solid ice layer that would start growing again over the brash ice. The value of this conductive flux can be obtained by setting T_0 equal to T_f in Eq. (6-2) and solving towards the conductive flux. Then by equating the R.H.S part of Eq. (6-3b) to this q_i , the rate of change of ice growth, $(dh_i / dt)_{hi}$, can be obtained as follows:

$$q_i = \lambda_i(T_f - T_0) / h_i = \rho_i p L_i (dh_i / dt)_{hi} \quad (6-13)$$

$$B_{12} = \begin{bmatrix} 0 & \cdot & \cdot & \cdot & \cdot \\ \cdot & \cdot & \cdot & \cdot & \cdot \\ \cdot & \cdot & \cdot & \cdot & \cdot \\ \cdot & \cdot & \cdot & \cdot & \cdot \\ \cdot & \cdot & \cdot & \cdot & \cdot \\ -2(1-s)a_{dbi} & \cdot & \cdot & \cdot & 0 \end{bmatrix} \quad (6-19)$$

$$B_{21} = \begin{bmatrix} 0 & \cdot & \cdot & \cdot & \cdot & -2sa_i \\ \cdot & \cdot & \cdot & \cdot & \cdot & \cdot \\ \cdot & \cdot & \cdot & \cdot & \cdot & \cdot \\ \cdot & \cdot & \cdot & \cdot & \cdot & \cdot \\ \cdot & \cdot & \cdot & \cdot & \cdot & \cdot \\ \cdot & \cdot & \cdot & \cdot & \cdot & 0 \end{bmatrix} \quad (6-20)$$

$$T_{dbi} = [T_o, T_{dbi}(1), T_{dbi}(2), \dots, T_{dbi}(N_{dbi})]_{m+1}^T \quad (6-21)$$

$$T_i = [T_i(1), T_i(2), T_i(3), \dots, T_i(N_i)]_{m+1}^T \quad (6-22)$$

$$Q_{db} = \begin{bmatrix} Q_{RAD} + 3\varepsilon_{RAD}\sigma(T_0^*)^4 + h_c T_a \\ T_{dbi,1} \\ T_{dbi,2} \\ \cdot \\ T_{dbi,N_{dbi}} \end{bmatrix}_m \quad (6-23)$$

$$Q_i = \begin{bmatrix} T_{i,1} \\ T_{i,2} \\ \cdot \\ 2a_i T_f + T_{i,NI} \end{bmatrix}_m \quad (6-24)$$

In the system of equations above, $T_{dbi}(j)$ is the temperature in the middle of the j^{th} dry brush ice layer for the current time step for ($j=1\dots N_{dbi}$) and $T_i(j)$ is the temperature in the middle of the k^{th} solid ice layer for the current time step for ($k=1\dots N_i$), where N_{dbi} and N_i are the numbers of dry brush ice and solid ice layers respectively. Δh_{dbi} and Δh_i , are their individual layer thicknesses, and a_{dbi} and a_i , are the dimensionless parameters of the matrix system for dry brush ice and solid ice respectively. Moreover, s , is another dimensionless parameter given by:

$$s = (\lambda_{dbi} / Dh_{dbi}) / ((\lambda_{dbi} / Dh_{dbi}) + (\lambda_i / Dh_i)) \quad (6-25)$$

where λ_{dbi} is the conductivity of the dry brush ice layer (or snow).

6.1.7 **Grid System re-construction in case of having a floating dry brush ice layer**

Similarly as before, after the bottom sub-layer has increased its thickness by δh , the solid ice layer structure have to be adjusted in order to obtain sub-layers of equal thickness, $\Delta h_i^m = h_i^m / N_i$, at the end of the current time step m . If time step m represents the last time step or moment before a breaking event, and time step $m + 1$ represents the first time step or moment after a breaking event, the structure of the dry brush ice has to be adjusted as well, in order to obtain dry brush ice sub-layers of equal thickness:

$$\Delta h_{dbi} = \frac{h_{dbi}}{N_{dbi}} \tag{6-26}$$

see Figure 6-2. Here it has to be reminded that dry brush ice is assumed to grow only after a breaking event, and the amount by which it grows is determined by the ice breaking model that is used in this work. The ice breaking model that is explained in section 7, is based on the conservation of mass and energy. If time steps m and $m + 1$ were instants of the same ice growth cycle, the dry brush ice structure would have been identical.

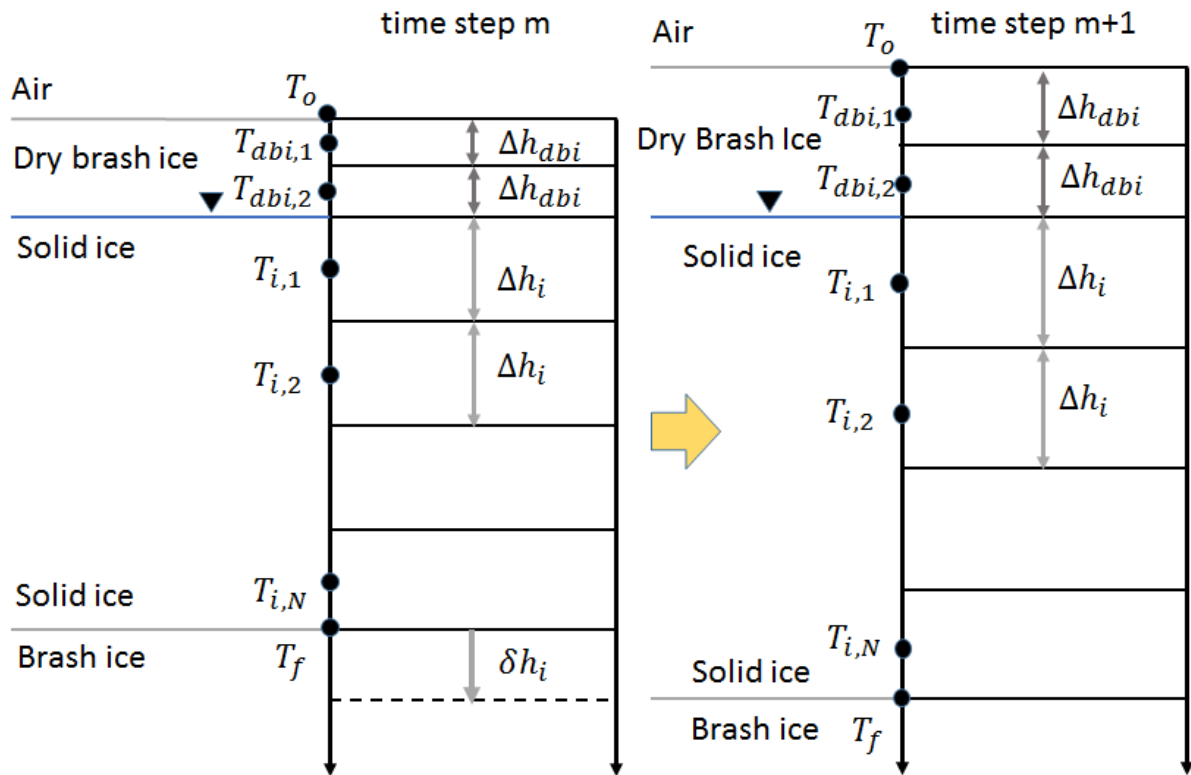


Figure 6-2 Illustration of the grid reconstruction procedure, in the case of having a broken dry brush ice layer above the waterline

6.1.8 Surface melting due to excessive radiation

In the summer months when solar radiation becomes significantly higher than the cold months, surface ablation can take place. As the situation with bare ice solid growth, as defined in this study, assumes that solid ice mass is completely below the waterline, surface ablation is assumed that it can only take place when a dry brush ice layer is included above the solid ice, i.e. only in the extended situation described in section 6.1.6. Surface ablation takes place, because there is an energy surplus on the top surface which is used to melt ice, and in this case, dry brush ice. This energy surplus in the form of a heat flux, if it exists, is calculated at every time step, as well as the amount of surface melting that would take place. If the top surface temperature, T_o , at any time step of the simulation, exceeds the freezing temperature T_f , the temperature profile is recalculated, with T_o , fixed at T_f .

The amount of surface melting is computed from the resulting imbalance of the net atmospheric heat flux and the conductive heat flux on the surface, see (Huwald, 2005). This is done by solving again the top surface equation, but using Eq. (5-3b) this time instead of Eq. (5-3a), as $T_o \geq T_f$. Hence,

$$\left(\frac{d(h_i)}{dt}\right)_{\text{melted}} = \frac{(1-a)Q_{SWR} - I_o + Q_{LWR} - \varepsilon_{RAD}\sigma T_f^4 + h_c(T_a - T_f) + Q_L + \lambda_i \left(\frac{T_i - T_f}{h_i}\right)_o}{-\rho_i L_i} \quad (6-27)$$

Note that Eq. (6-27), which is a re-arrangement of Eq. (5-3b), assumes the existence of a solid ice mass only and hence the properties in the equation refer to solid ice (subscript i). Using the appropriate discretized form of BIGM 2 and all the simplifications mentioned previously in section 6, in addition to the fact that the top surface is dry brush ice, when this effect is taking place according to the definitions of this study, Eq. (6-27) is transformed to:

$$\left(\frac{d(h_{dbi})}{dt}\right)_{\text{melted}} = \frac{Q_{RAD} + 3\varepsilon_{RAD}\sigma(T_0^*)^4 - 4\varepsilon_{RAD}\sigma(T_0^*)^3 T_f + h_c(T_a - T_f) + 2\lambda_{dbi} \left(\frac{T_{dbi}^{m+1} - T_f}{\Delta h_i}\right)}{-\rho_{dbi} L_{dbi}} \quad (6-28)$$

where T_{dbi}^{m+1} is the mid-layer temperature of the top dry brush ice layer. In order to include Eq. (6-28) into the matrix system (the matrix system described in section 6.1.6 in this case), Eq. (6-28) has to be re-arranged into:

$$\left(4\varepsilon_{RAD}\sigma(T_0^*)^3 + h_c + \frac{2\lambda_{dbi}}{\Delta h_{dbi}}\right)T_0^{m+1} - \frac{2\lambda_{dbi}}{\Delta h_{dbi}}T_{dbi}^{m+1} = Q_{RAD} + 3\varepsilon_{RAD}\sigma(T_0^*)^4 + h_c T_a + \rho_i L_i \left(\frac{d(h_{dbi})}{dt}\right)_{\text{melted}}$$

Note that this re-arranged form of Eq. (6-28) substitutes the top surface equation in the matrix system described in section 6.1.6. Every time in a temperature profile calculation, the top surface temperature is found to be $T_o \geq T_f$, the temperature profile is re-calculated giving a pre-determined increment to the value of $\left(\frac{d(h_{dbi})}{dt}\right)_{\text{melted}}$. The temperature profile is re-calculated and $\left(\frac{d(h_{dbi})}{dt}\right)_{\text{melted}}$ is increased by the pre-determined increment as many times as necessary, until the necessary condition of $T_o < T_f$, is satisfied. The melting effect can be included in exactly the same way, in the situation of bare solid ice

growth, and the corresponding matrix system described in section 6.1.2. Although the melting effect, has been included in the Matlab code developed, during this study, for both the situations of “having” and “not having a dry brush ice layer” above the solid ice, melting results were only shown in the case of “having a dry brush ice layer”, something that was expected.

6.1.9 Introducing the effect of solar radiation internal absorption in BIGM 2

No freeboard Case (no dry brush ice above solid ice)

In reality, an amount of the solar radiation, passes through the top surface of the solid ice, into the lower layers of solid ice. This creates internal heat sources which raise the average temperatures inside these layers. In order to introduce this effect into the numerical thermodynamic model, the total increase in temperature that would be caused inside the solid ice, due to a solar heat flux I_o , penetrating the top surface of the ice and going into the lower ice sub-layers, was first calculated. This was done using Eq. (6-29) shown below:

$$\Delta T_{I_o} = \frac{I_o h_i}{\lambda_i} \quad (6-29)$$

Then this temperature change has to be distributed accordingly into each of the solid ice layers. This was done by calculating the ratio $\frac{\lambda_i}{h_{d_i}}$ for every solid ice layer, where h_{d_i} is the distance from the top surface, to the middle of each solid ice layer, see Figure 6-3. Then the sum of all these ratios was found, and the proportion of the ratio corresponding to each layer over the sum of the ratios was calculated. By multiplying this proportion, for one layer, with the total increase in temperature ΔT_{I_o} , in the solid ice, the incremental temperature corresponding to that layer T_{inc_i} is calculated.

In summary:

1. First $\frac{\lambda_{i_1}}{h_{d_1}}, \frac{\lambda_{i_2}}{h_{d_2}}, \frac{\lambda_{i_3}}{h_{d_3}}, \frac{\lambda_{i_4}}{h_{d_4}}$ is calculated.
2. Then the sum of these ratios is found, $\sum \frac{\lambda_{i_1}}{h_{d_1}}, \frac{\lambda_{i_2}}{h_{d_2}}, \frac{\lambda_{i_3}}{h_{d_3}}, \frac{\lambda_{i_4}}{h_{d_4}}$
3. Then the proportion of each ratio in the total sum of the ratios is calculated. For example, for solid ice layer 1:

$$\frac{\frac{\lambda_{i_1}}{h_{d_1}}}{\sum \frac{\lambda_{i_1}}{h_{d_1}}, \frac{\lambda_{i_2}}{h_{d_2}}, \frac{\lambda_{i_3}}{h_{d_3}}, \frac{\lambda_{i_4}}{h_{d_4}}}$$

Note that Q_{RAD} has been replaced by Q_{RAD}^* , which is a reduced bulk radiation term, since a proportion of the solar radiation, for example 31%, is penetrating the ice surface instead of being balanced at the surface. If we call this proportion i_o , then the solar heat flux penetrating the surface can be expressed as :

$$I_o = i_o Q_{SWR} (1 - a) \quad (6-31)$$

This proportion i_o is a function of sky conditions and optical properties of ice or dry brash ice or snow thickness. It usually ranges between 0.17 and 0.50 according to (Cheng, 2002).

With freeboard Case (dry brash ice above solid ice)

For the case of solar radiation absorption, with a floating layer of dry brash ice above the solid ice, the same procedure is followed. The total increase in temperature in the total ice column, due to a flux I_o , penetrating the top surface of the dry brash ice and going into the lower layers of dry brash ice and solid ice, is first calculated. This is done using Eq. (6-32) shown below, see (Semtner, 1976):

$$\Delta T_{I_o} = \frac{I_o \left(h_{dbi} + \frac{h_i \lambda_{dbi}}{\lambda_i} \right)}{\lambda_{dbi}} \quad (6-32)$$

Then in order to distribute this increase in temperature into the lower layers of dry brash ice and solid ice, the ratio of the conductivity of every layer to the distance of its mid-point from the top surface was found. The ratio for the solid ice layers is calculated a bit differently in this case as:

$$\frac{\lambda_{dbi_{av}}}{\left(h_{dbi} + \frac{h_{di} \lambda_{dbi_{av}}}{\lambda_i} \right)}$$

where $\lambda_{dbi_{av}}$ is the average conductivity of the whole dry brash ice (freeboard) layer, and h_{di} is the distance from the solid ice sub-layer to the top of the solid ice layer, see Figure 6-4. Therefore, in the case of 2 freeboard layers and 4 solid ice layers:

$$1. \text{ First, } \frac{\lambda_{dbi_1}}{h_{d_1}}, \frac{\lambda_{dbi_2}}{h_{d_2}}, \frac{\lambda_{dbi_{av}}}{\left(h_{dbi} + \frac{h_{di_1} \lambda_{dbi_{av}}}{\lambda_{i_1}} \right)}, \frac{\lambda_{dbi_{av}}}{\left(h_{dbi} + \frac{h_{di_2} \lambda_{dbi_{av}}}{\lambda_{i_2}} \right)}, \frac{\lambda_{dbi_{av}}}{\left(h_{dbi} + \frac{h_{di_3} \lambda_{dbi_{av}}}{\lambda_{i_3}} \right)}, \frac{\lambda_{dbi_{av}}}{\left(h_{dbi} + \frac{h_{di_4} \lambda_{dbi_{av}}}{\lambda_{i_4}} \right)}$$

is calculated.

2. Then the sum of these ratios is found:

$$\sum \frac{\lambda_{dbi_1}}{h_{d_1}} + \frac{\lambda_{dbi_2}}{h_{d_2}} + \frac{\lambda_{dbi_{av}}}{\left(h_{dbi} + \frac{h_{di_1} \lambda_{dbi_{av}}}{\lambda_{i_1}}\right)} + \dots + \frac{\lambda_{dbi_{av}}}{\left(h_{dbi} + \frac{h_{di_4} \lambda_{dbi_{av}}}{\lambda_{i_4}}\right)}$$

3. Then the proportion of each ratio to the total sum of the ratios is calculated. For example for the 1st freeboard layer:

$$\frac{\frac{\lambda_{dbi_1}}{h_{d_1}}}{\sum \frac{\lambda_{dbi_1}}{h_{d_1}} + \frac{\lambda_{dbi_2}}{h_{d_2}} + \frac{\lambda_{dbi_{av}}}{\left(h_{dbi} + \frac{h_{di_1} \lambda_{dbi_{av}}}{\lambda_{i_1}}\right)} + \dots + \frac{\lambda_{dbi_{av}}}{\left(h_{dbi} + \frac{h_{di_4} \lambda_{dbi_{av}}}{\lambda_{i_4}}\right)}}$$

4. Then this proportion, for each layer, is multiplied by the total increase in temperature caused by the ΔT_{I_o} , to find the incremental temperature corresponding to that layer. For example, for dry brash ice layer 1, the incremental temperature is found from:

$$T_{inc_1} = \left(\frac{\frac{\lambda_{dbi_1}}{h_{d_1}}}{\sum \frac{\lambda_{dbi_1}}{h_{d_1}} + \frac{\lambda_{dbi_2}}{h_{d_2}} + \frac{\lambda_{dbi_{av}}}{\left(h_{dbi} + \frac{h_{di_1} \lambda_{dbi_{av}}}{\lambda_{i_1}}\right)} + \dots + \frac{\lambda_{dbi_{av}}}{\left(h_{dbi} + \frac{h_{di_4} \lambda_{dbi_{av}}}{\lambda_{i_4}}\right)}} \right) \times \Delta T_{I_o}$$

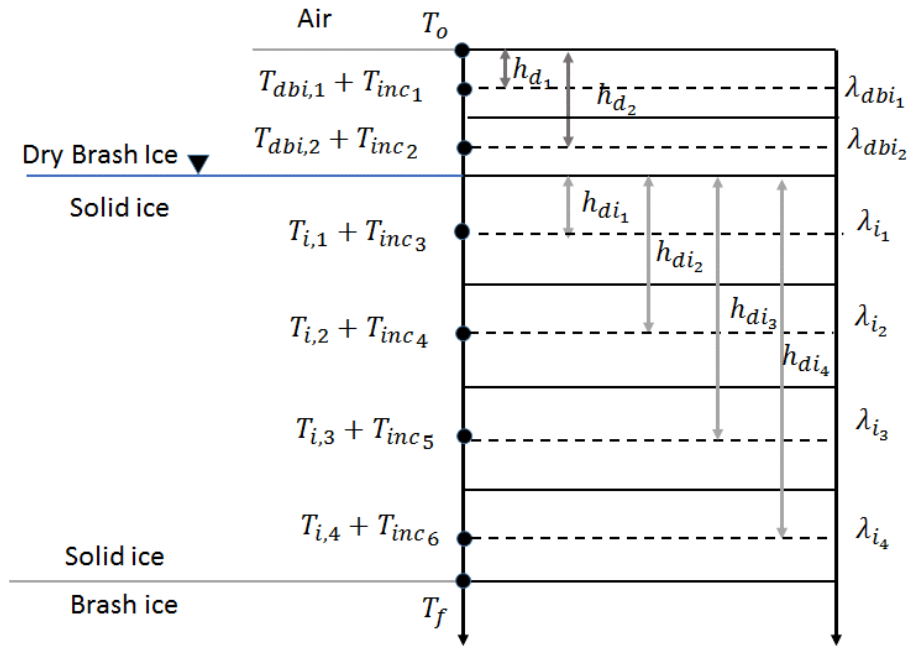


Figure 6-4 Schematic showing distances of dry brush ice mid-layer temperatures from the top surface, and solid ice mid-layer temperatures from the top of the solid ice surface

Finally, Equations (6-23) and (6-24), are transformed into Equations (6-33) and (6-34) respectively, see below:

$$Q_{db} = \begin{bmatrix} Q_{RAD} + 3\varepsilon_{RAD}\sigma(T_0^*)^4 + h_c T_a \\ T_{dbi,1} + T_{inc1} \\ T_{dbi,2} + T_{inc2} \\ \vdots \\ T_{dbi,N_{dbi}} + T_{inc_{N_{dbi}}} \end{bmatrix}_m \quad (6-33)$$

$$Q_i = \begin{bmatrix} T_{i,1} + T_{inc3} \\ T_{i,2} + T_{inc4} \\ \vdots \\ 2a_i T_f + T_{i,N_i} + T_{inc_{N_i}} \end{bmatrix}_m \quad (6-34)$$

6.1.10 Introducing the effect of varying conductivity and heat capacity

The presence of brine pockets that are trapped inside the sea ice, makes bulk thermal constants such as thermal conductivity and heat capacity to be depended on temperature and salinity of the ice. Temperature and salinity change with depth within the ice, and therefore the bulk thermal constants also change. The variation of thermal constants, through solid ice and dry brash ice layers, as a function of temperature and salinity was another effect that was added into this numerical implementation. The variations of these constants was applied using the following equations, developed by (Untersteiner, 1961):

$$\lambda_{i,dbi}(T, S) = \lambda_{i,dbi,k} + \frac{\beta S(z)}{T - 273.15} \quad (6-35)$$

$$(\rho c)_{i,dbi}(T, S) = (\rho c)_{i,dbi,k} + \frac{\gamma S(z)}{(T - 273.15)^2} \quad (6-36)$$

where $\lambda_{i,k} = 2 \text{ Wm}^{-1}\text{K}^{-1}$, $\beta = 0.1172 \text{ Wm}^{-1}\text{ppt}^{-1}$, $\gamma = 1.715 \times 10^7 \text{ JKm}^{-3}\text{ppt}^{-1}$ and

$(\rho c)_{i,k} = 1.911 \times 10^6 \text{ Jm}^{-3}\text{K}^{-1}$. T is the mid-layer temperature of every sub-layer of either the solid ice or the dry brash ice. $S(z)$ in the equations above represents the salinity of the solid ice or dry brash ice layers as a function of depth z within the ice (or dry brash ice), measured from the top surface of the ice. Although there are various proposed salinity equation profiles, such as the equilibrium profile suggested by (Schwarzacher, 1959), it is very difficult to guess how the profile would change under varying conditions of temperature and speed of growth. A closer examination of Equations (6-35) and (6-36), reveals that salinity has a considerable effect on the calculation of the thermal properties, $\lambda_{i,dbi}$ and $(\rho c)_{i,dbi}$, only at temperatures close to the freezing point. Hence, it is only important to know the salinity profiles accurately in the summer months and closer to the ice/waterline interface. Salinity of sea ice at greater depths within the ice mass is relatively constant and equal to $S = 3.2 \text{ ppt}$, see (Maykut & Untersteiner, 1971). Since the seawater salinity in Sabetta shows relatively small values, see (Bloquin [1], 2013), around $S = 3.1 \text{ ppt}$ and the brash ice layer is constantly filled with this water, it is reasonable to assume a constant ice salinity in the range of $S = 3.1 - 3.2 \text{ ppt}$ for this project.

In the present formulation, the sets of these variables are re-calculated with the above functions, at the temperature from the previous time step, and substituted into the matrix system explained before. This basically means that the thermal properties are assumed to be constant within each layer, and that a temperature profile does not change significantly in a single time step, an approach also used by (Ebert & Curry, 1993) and (Bitz & Lipscomb, 1999). Two sources of error are introduced into the model in this case. The first one is due to assuming constant coefficient values for each layer and the other one from using old (from the previous time step) temperatures to evaluate them, see (Ukita & Martinson, 2001). The first one is related to the layer thickness and can be controlled by choosing a bigger number of layers and hence thinner layers. The latter is a function of the time-step (the shorter the time-step the smaller the change in temperature), and so can be controlled by choosing a shorter time step.

6.1.11 Inclusion of the latent heat flux equation to the top surface flux equilibrium equation

From (Maykut, 1978), the latent heat flux is expressed as:

$$Q_L = 0.622\rho_a L_v C_e u_a \frac{(fe_{sa} - e_{so})}{p_o} \quad (6-37)$$

where ,

C_e is the evaporation coefficient, e_{so} saturation vapour pressure at the ice surface, e_{sa} saturation vapour pressure in the air (at a reference height), f is the relative humidity (%), p_o is the surface pressure, L_v is the latent heat of vapourization, ρ_a is the density of the air, and u_a is the wind speed.

The saturation vapour pressure for either ice or air, can be expressed as:

$$e_s = aT^4 + bT^3 + cT^2 + dT + e' \quad (6-38)$$

where a, b, c, d and e' are constants and T is the temperature of the surface of the ice or air respectively, depending on which saturation vapour pressure is calculated.

The constants shown in Eq. (6-38) have the following values:

$$a = 2.7798202 \times 10^{-6}$$

$$b = -2.6913393 \times 10^{-3}$$

$$c = 0.97920849$$

$$e' = 9653.1925$$

Moreover $C_e = 1.75 \times 10^{-3}$ and $L_v = 2.49 \times 10^6 J / kg^{-1}$, see (Deardorff, 1968). The top surface flux equilibrium equation, Eq. (6-2), when latent heat flux is included in the formulation, is modified as follows:

$$Q_{RAD} - \varepsilon_{RAD} \sigma T_o^4 + h_c(T_a - T_o) + 0.622\rho_a L_v C_e u_a \frac{(fe_{sa} - e_{so})}{p_o} + \lambda_i \left(\frac{\partial T_i}{\partial z} \right)_{z=0} = 0 \quad (6-39)$$

and in more detail:

$$Q_{RAD} - \varepsilon_{RAD} \sigma T_o^4 + h_c(T_a - T_o) + 0.622\rho_a L_v C_e u_a \frac{(f[aT_{air}^4 + bT_{air}^3 + cT_{air}^2 + dT_{air} + e'] - [aT_o^4 + bT_o^3 + cT_o^2 + dT_o + e'])}{p_o} + \lambda_i \left(\frac{\partial T_i}{\partial z} \right)_{z=0} = 0 \quad (6-40)$$

In order for the modified surface equation to be included into the matrix system a re-arrangement of the equation is necessary. Firstly, the terms containing the top surface temperature T_o , where T_o is equal or higher than the second order, need to be linearized.

Hence from the linearization of $T_{o_{m+1}}^4$, $T_{o_{m+1}}^3$, $T_{o_{m+1}}^2$:

$$T_{o_{m+1}}^4 = T_o^4 + 4T_o^3(T_{o_{m+1}} - T_o) = T_o^4 + 4T_o^3T_{o_{m+1}} - 4T_o^4 = -3T_o^4 + 4T_o^3T_{o_{m+1}} \quad (6-41)$$

$$T_{o_{m+1}}^3 = T_o^3 + 3T_o^2(T_{o_{m+1}} - T_o) = T_o^3 + 3T_o^2T_{o_{m+1}} - 3T_o^3 = -2T_o^3 + 3T_o^2T_{o_{m+1}} \quad (6-42)$$

$$T_{o_{m+1}}^2 = T_o^2 + 2T_o(T_{o_{m+1}} - T_o) = T_o^2 + 2T_oT_{o_{m+1}} - 2T_o^2 = -T_o^2 + 2T_oT_{o_{m+1}} \quad (6-43)$$

Substituting back the linearized terms into the top surface equation, Eq. (6-40), and re-arranging we have the appropriate form for inclusion into the matrix system:

$$\begin{aligned} & Q_{RAD} + 3\varepsilon_{RAD}\sigma T_o^4 + h_c T_a + h_L f \left[aT_{air}^4 + bT_{air}^3 + cT_{air}^2 + dT_{air} + e' \right] \\ & + 3h_L aT_o^4 + 2h_L bT_o^3 + h_L cT_o^2 - h_L e' = \\ & T_{o_{m+1}} \left[4\varepsilon_{RAD}\sigma T_o^3 + h_c + 4h_L aT_o^3 + 3h_L bT_o^2 + 2h_L cT_o + h_L d + \frac{2\lambda_i}{\Delta h_i} \right] - \frac{2\lambda_i}{\Delta h_i} (T_1) \end{aligned} \quad (6-44)$$

where
$$h_L = 0.622\rho_a L_v C_e u_a \quad (6-45)$$

6.2 Introducing a brash ice melting effect into BIGM 2

The melting of brash ice in BIGM 2 due to a Brash Ice Management System, is introduced in exactly the same way as in BIGM 1, using Equations (4-24), (4-25) and (4-26). The amount of brash ice melted $\Delta h_{bi,melted}$ at every time step of the simulation is calculated and subtracted from the remaining brash ice layer, see section 4.2.

6.3 Ice Growth Cycle in BIGM 2

6.3.1 No dry brash ice on top

Similar to BIGM 1. The only basic difference being the calculation of the temperature profile described in section 6.1.2, for BIGM 2 and the ice growth formula. Appendix E shows a diagram with the sequence with which the calculations are made in an ice growth cycle of BIGM 2. In this situation the matrix system mentioned in the sequence is the one described in section 6.1.2.

6.3.2 With dry brash ice on top

Similar to BIGM 1. The only basic difference being the calculation of the temperature profile described in section 6.1.6, for BIGM 2 and the ice growth formula. Appendix E shows a diagram with the sequence with which the calculations are made in an ice growth cycle of BIGM 2. In this situation the matrix system mentioned in the sequence is the one described in section 6.1.6.

6.4 Advantages and Disadvantages of BIGM 2

6.4.1 Advantages

1. A full detailed numerical scheme that has the potential to include all aspects and physical changes that take place in solid ice growth, and the ice breaking procedure such as: the changes in heat conductivity and specific heat capacity within the total solid ice and dry brash ice layer, which depend on both temperature and salinity, the internal absorption of solar radiation and surface melting due to excessive radiation.
2. It takes into account the real boundary conditions(i.e. all the relevant fluxes)
3. It is easily adjustable.
4. It has the ability to model thermal inertia appropriately even in the case of high frequency forcing (rapidly varying fluxes with time).

6.4.2 Disadvantages

1. A highly computational time consuming model.
2. More complicated model to build.

7. Model for ice breaking (for both BIGM 1 and BIGM 2)

7.1 Description of the model

The breaking model used in this study, consists of a series of instantaneous events. The passing of a vessel causes breaking of a solid ice layer, and a dry brash ice layer if it exists, whose thicknesses and temperature profiles are determined from the thermodynamic models used in BIGM 1 and BIGM 2. The breaking event causes a homogeneous mixing of the cold ice blocks resulting from the broken solid ice, with the ice blocks that are already present in the wet brash ice layer. Then, the homogeneous bulk ice mixture of an assumed breaking porosity, p , must return to thermal equilibrium, and according to the conservation of energy, this happens when the temperature of the uniform medium returns back to the freezing temperature T_f . The description of the above procedure in the case of having and not having a dry brash ice layer is illustrated in Figure 7-1 and Figure 7-2 respectively. Note that in the case which includes a dry brash ice layer, when a vessel passes, it breaks the dry brash ice layer as well. However the thickness of the dry brash ice layer is assumed to remain unchanged until the cold blocks from the solid ice return to thermal equilibrium causing a decrease in porosity in the wet brash ice layer, and a re-adjustment in the total ice column, which brings the waterline lower and increases the freeboard (dry brash ice thickness), see Figure 7-2. Also note, that at breaking, some fraction of the brash ice volume is pushed outside of the track. However, this is not taken into account by the model. If someone wants to include this effect, he can simply multiply the thicknesses results with $(1 - a_{pushed})$, where a_{pushed} is a coefficient between 0 and 1, which can be taken empirically.

7.2 Main Assumptions of the ice breaking model

The main assumptions of the model are:

1. It does not take into account the presence of open water in the ship track and considers that the fraction area of open water β , is 0. The typical ship track for which the model is applicable is shown in Figure 2-11e (last diagram).
2. The model does not take into account that a fraction of the brash ice is pushed out of the ship track at each vessel passage. It considers that all the brash ice stays in the track, using the "equivalent thickness" calculation, first introduced by Sandkvist.
3. There is no expansion of solid ice when solid ice grows because water is assumed to be pushed out of the pores (expulsion of water during freezing).
4. After breaking, freezing is assumed to start again instantaneously.
5. After breaking and before return to thermal equilibrium, the brash ice mixture is assumed to be at a Temperature $T_{av} \leq T_f$.
6. In the case of the inclusion of a dry brash ice layer, for simplicity, it is assumed that at all times the porosity of the dry brash ice part is equal to the changing porosity of the wet brash ice part. In reality after a breaking event, the wet brash ice part acquires a smaller porosity value, than the dry brash ice part, after the return to thermal equilibrium of its' cold blocks, resulting from the breaking of the solid ice, see Figure 7-2.

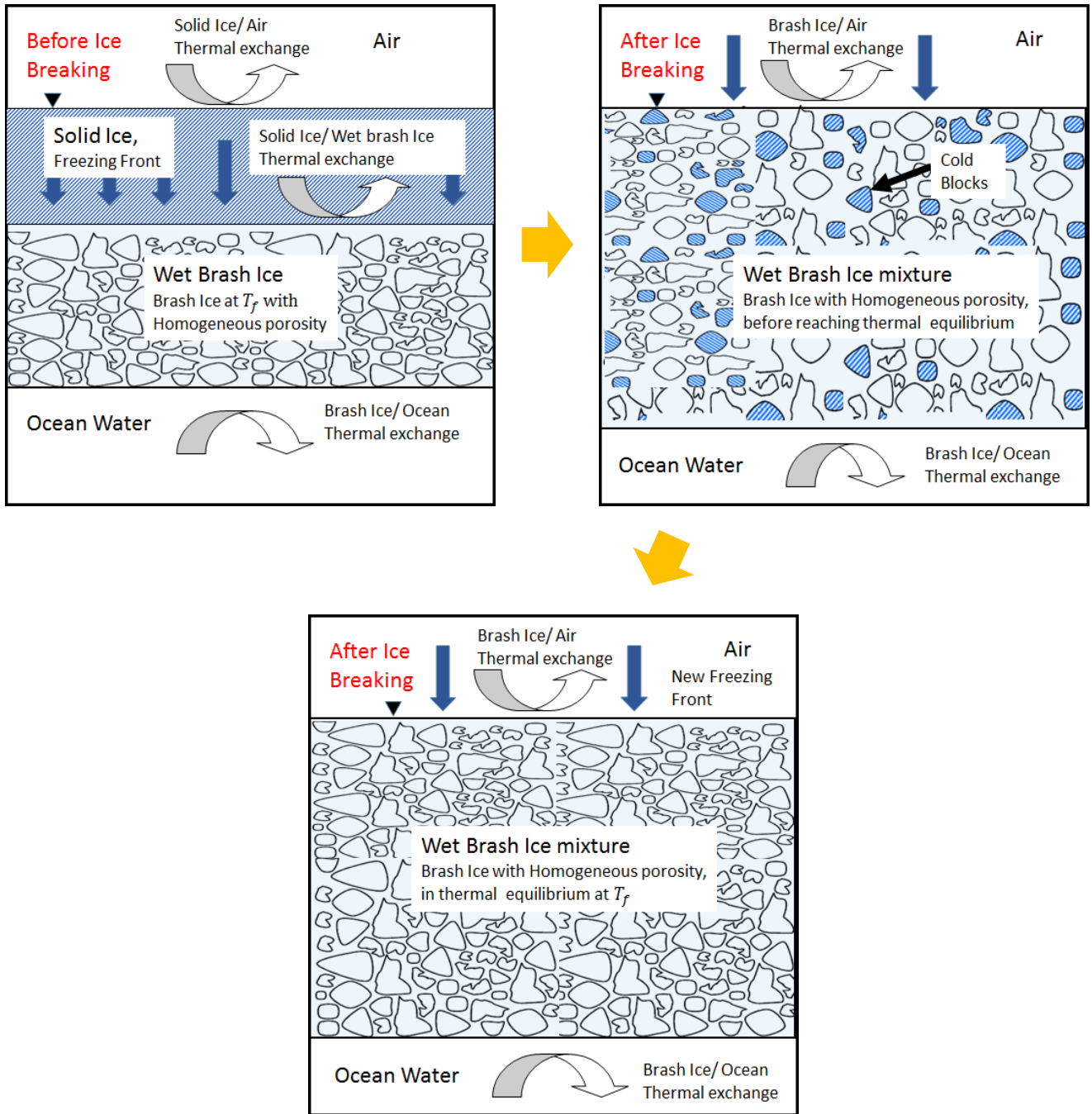


Figure 7-1 Breaking model, no dry brash ice (freeboard) case

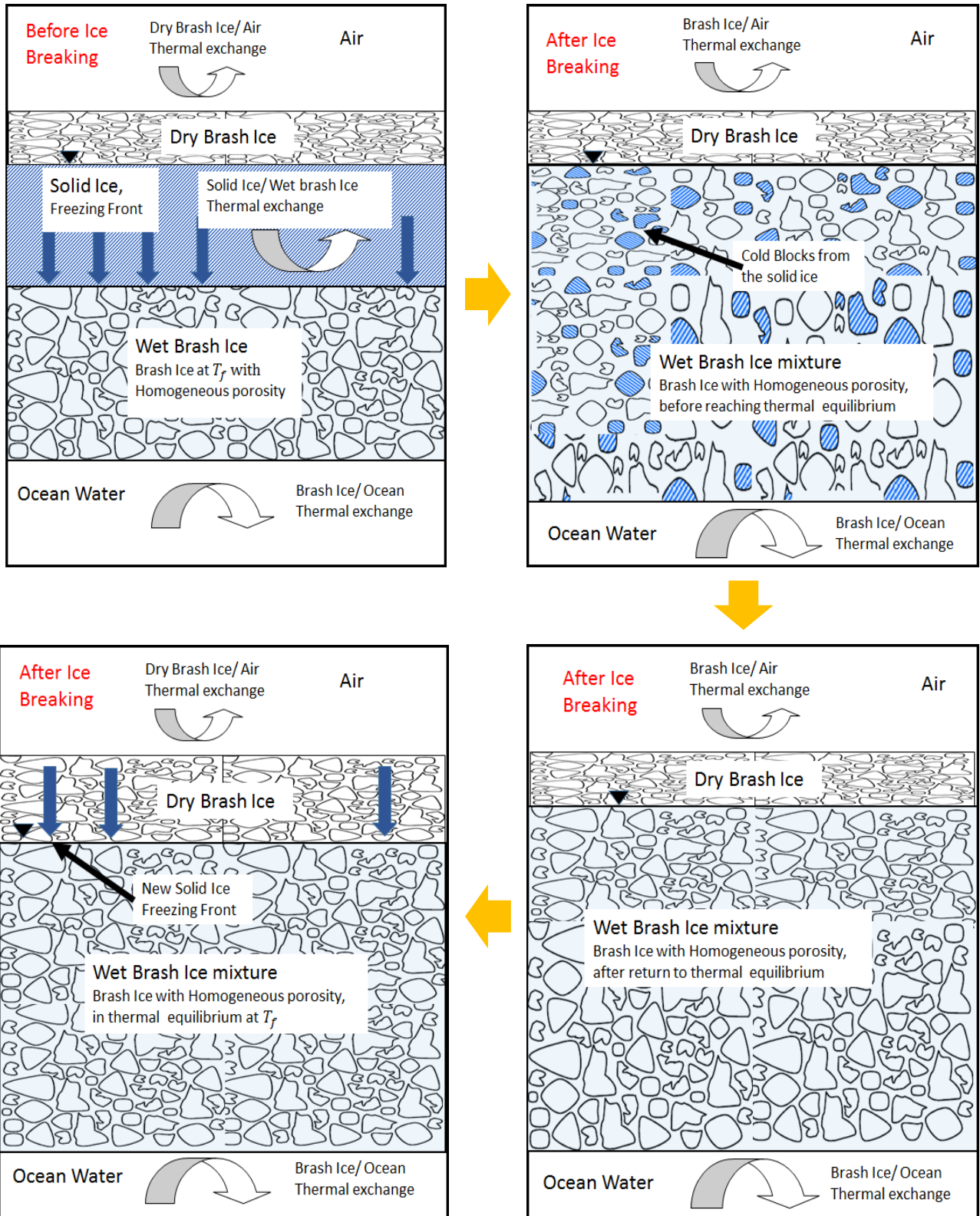


Figure 7-2 Breaking model, with dry brush ice (freeboard) case

7.3 Calculation Procedure (no dry brash ice)

7.3.1 Description of the problem

The situation just before ice breaking can be described by the 1st diagram of Figure 7-1. From upper surface to bottom there is:

1. A solid ice layer of thickness h_i
2. A wet brash ice layer of thickness h_{bi} and porosity p_{bi} (resulting from return to thermal equilibrium after last breaking event).

The situation just after ice breaking can be described by the 2nd diagram of Figure 7-1. From upper surface to bottom there is a brash ice layer of thickness $h_{bi_{new}}$ and porosity p , where p is an assumed breaking event porosity given by the user.

Finally the situation just after return to thermal equilibrium can be described by the 3rd diagram of Figure 7-1. After return to thermal equilibrium there is a brash ice layer of the same thickness $h_{bi_{new}}$ but with a decreased porosity $p_{bi_{new}}$, resulting from the return to thermal equilibrium at temperature T_f . During this phase, cold blocks resulting from the breaking of the solid ice return at freezing temperature T_f by taking energy from the surrounding water and causing it to freeze. As a result, the final porosity $p_{bi_{new}}$ is lower than p .

7.3.2 Solution of the problem

The thickness of the new brash ice layer after breaking as well as the new porosity value, $p_{bi_{new}}$, that results from thermal equilibrium, can be obtained from conservation of mass and energy respectively.

Conservation of mass

The model considers that the volume of ice is conserved during the ice breaking process. The total amount of ice before an ice breaking event can be expressed as follows:

$$h_{solid_total} = h_i + h_{bi}(1 - p_{bi}) \quad (7-1)$$

where h_i is the thickness of the solid ice layer and $h_{bi}(1 - p)$ is the thickness corresponding to the ice parts of the pre-existing brash ice layer. This would result in a new brash ice layer thickness, $h_{bi_{new}}$, with porosity p after ice breaking:

$$h_{bi_{new}} = \frac{h_i + h_{bi}(1 - p)}{1 - p} = h_{bi} + \frac{h_i}{1 - p_{bi}} \quad (7-2)$$

The amount of water contained in this brash ice layer, just after ice breaking is:

$$h_w = p h_{bi_{new}} \quad (7-3)$$

and the amount of water in the brash ice after return to thermal equilibrium is:

$$h_w = p_{bi_{new}} h_{bi_{new}} \quad (7-4)$$

Conservation of Energy

BIGM 1

The model considers that the energy, in terms of enthalpy, contained in the brash ice layer after ice breaking is conserved during the whole ice breaking process. The enthalpy of the brash ice layer just after ice breaking can be expressed as:

$$H_{tot} = h_i (H_i(T_f) + Cp_i(T_{av} - T_f)) + H_i(T_f) h_{bi} (1 - p_{bi}) + H_w(T_f) \cdot p \cdot h_{bi_{new}} \quad (7-5)$$

where $H_i(T_f)$ and $H_w(T_f)$ are the enthalpies of ice and water respectively at the freezing temperature T_f , h_i is the thickness of the solid ice and T_{av} is the average temperature of the brash ice mixture just after breaking. Also here it is reminded that the enthalpy of fusion at T_f , L_i , is equal to $H_w(T_f) - H_i(T_f)$.

The enthalpy of brash ice layer after return to thermal equilibrium is given by:

$$H_{tot} = H_i(T_f) \cdot (1 - p_{bi_{new}}) \cdot h_{bi_{new}} + H_w(T_f) \cdot p_{bi_{new}} \cdot h_{bi_{new}} \quad (7-6)$$

Equating the R.H.S of Equations (7-5) and (7-6), and solving towards $p_{bi_{new}}$ it gives:

$$p_{bi_{new}} = p + \frac{h_i Cp_i (T_{av} - T_f)}{L_i h_{bi_{new}}} \leq p \quad (7-7)$$

which is calculated after each return to thermal equilibrium, after a breaking event.

After breaking, the brash ice mixture takes instantaneously an average temperature, $T_{av} \leq T_f$, as a result of the mixing of the cold ice clocks resulting from the breaking of the solid ice, with the pre-existing brash ice layer which was at the freezing temperature T_f . When the brash ice mixture returns to thermal equilibrium its average temperature increases to T_f . The calculation of this average temperature, before the mixture reaches thermal equilibrium, can be done using the "mean area method" and the known temperatures from the temperature profile produced with the thermodynamic model of BIGM 1. In the case of "no dry brash ice layer" above the solid ice, see Figure 4-2, only the top temperature T_o is needed and the average temperature of the mixture is calculated as follows:

$$T_{av} = \frac{\left((h_{bi} \times T_f) + (h_i \times T_f) + (T_o - T_f) \times \frac{h_i}{2} \right)}{(h_i + h_{bi})} \quad (7-8)$$

where h_i and h_{bi} are the thicknesses of the solid ice and wet brash ice respectively before the breaking event.

BIGM 2

The conservation of energy part of the solution for BIGM 2, uses exactly the same idea but has slightly different equations due to the different thermodynamic model that it uses. Therefore Eq. (7-5) is changed to:

$$H_{tot} = \sum_{k=1}^{Ni} h_{i,k} (H_i(T_f) + Cp_i(T_{i,k} - T_f)) + H_i(T_f) \cdot h_{bi} (1 - p_{bi}) + H_w(T_f) \cdot p \cdot h_{bi_{new}} \quad (7-9)$$

where $h_{i,k}$ and $T_{i,k}$ are the thickness and temperature of the kth sub-layer of solid ice layer $k = 1, \dots, Ni$. The rest of the terms are exactly the same. Note, that in this case in order to apply the idea of the return back to thermal equilibrium, the individual ice sub-layer temperatures are being used which are known from the solution of the numerical thermodynamic model that is used in BIGM 2. Hence there is no need to calculate an average brash ice mixture temperature here.

Equation (7-6) remains exactly the same for BIGM 2. Similarly to Eq. (7-5), Eq. (7-7) is changed to:

$$p_{bi_{new}} = p + \frac{\sum_{k=1}^{Ni} h_{i,k} Cp_i (T_{i,k} - T_f)}{L_i h_{bi_{new}}} \leq p \quad (7-10)$$

7.4 Calculation procedure (with dry brash ice on top)

7.4.1 Description of the problem

The situation just before ice breaking can be described by the 1st diagram of Figure 7-2. From upper surface to bottom there is:

1. A dry brash ice layer of thickness h_{dbi}
2. A solid ice layer of thickness h_i
3. A wet brash ice layer of thickness h_{bi} and porosity p_{bi} (resulting from return to thermal equilibrium after the last breaking event).

The situation just after ice breaking can be described by the 2nd diagram of Figure 7-2. From upper surface to bottom there is a dry brash ice layer h_{dbi} , which has exactly the same thickness as the dry brash ice layer before breaking, and a new wet brash ice layer of greater thickness $h_{bi_{new}}$. Both of these layers have a porosity p , where p is an assumed breaking event porosity given by the user, as explained before. Together the two layers they form the new total ice thickness layer $h_{tot_{new}}$.

The situation just after return to thermal equilibrium can be described by the 3rd and 4th diagrams of Figure 7-2. After return to thermal equilibrium, the wet brash ice layer of thickness h_{bi_new} , would have a decreased porosity p_{bi_new} and this is assumed to be the porosity in the dry brash ice layer as well (although in reality the porosity is still p in the dry brash ice layer). The decreased porosity p_{bi_new} , results from the return of the wet brash ice mixture in thermal equilibrium at temperature T_f . During this phase, the cold blocks resulting from the breaking of the solid ice layer, return to thermal equilibrium at the freezing temperature T_f , by taking energy from the surrounding water and causing it to freeze, just as in the case without dry brash ice. As the amount of solid ice in the wet brash ice layer increases due to freezing, a re-adjustment in the total ice column takes place, which brings the waterline lower and increases the thickness of the freeboard part (dry brash ice thickness) which has now a thickness of h_{dbi_new} , see 4th diagram in Figure 7-2.

7.4.2 Solution of the problem

The thickness of the new wet brash ice layer after breaking, the new dry brash ice layer after breaking, as well as the new porosity value, p_{bi_new} , that results from thermal equilibrium, can be obtained from conservation of mass and energy respectively.

Conservation of mass

Again the model considers that the volume of ice is conserved during the ice breaking process. The total amount of ice before an ice breaking event can be expressed as follows:

$$h_{solid_total} = h_i + h_{bi}(1 - p_{bi}) + h_{dbi}(1 - p_{bi}) \quad (7-11)$$

where h_i is the thickness of the solid ice layer, $h_{bi}(1 - p)$ is the thickness corresponding to the ice parts of the pre-breaking wet brash ice layer and $h_{dbi}(1 - p_{bi})$ is the thickness corresponding to ice parts of the pre-breaking dry brash ice layer. After breaking, the result would be a total brash ice thickness layer h_{tot_new} , with porosity p :

$$h_{tot_new} = \frac{h_i + h_{bi}(1 - p_{bi}) + h_{dbi}(1 - p_{bi})}{1 - p} \quad (7-12)$$

However, instantaneously, this new total brash ice layer would be split into a new dry brash ice part and a new wet brash ice part:

$$h_{tot_new} = h_{bi_new} + h_{dbi_new} \quad (7-13)$$

The relation between the dry brash ice part and the wet brash ice part, just after breaking, is determined, by applying the Archimedes' principle, which gives:

$$h_{dbi_new} = h_{bi_new} \left(\frac{\rho_w - \rho_i}{\rho_i} \right) \quad (7-14)$$

see appendix C for the derivation. Therefore using Eq. (7-14), Eq. (7-13) can be re-written as:

$$h_{tot_{new}} = h_{bi_{new}} \left(\frac{\rho_w - \rho_i}{\rho_i} + 1 \right) \quad (7-15)$$

Then from Eq. (7-15) the new wet brash ice layer can be calculated as follows:

$$h_{bi_{new}} = \frac{h_{tot_{new}}}{\left(\frac{\rho_w - \rho_i}{\rho_i} + 1 \right)}$$

which is basically re-arranging the same equation.

Hence the new dry brash ice layer can be calculated from:

$$h_{dbi_{new}} = h_{tot_{new}} - h_{bi_{new}} \quad (7-16)$$

The amount of water contained in the brash ice, just after ice breaking is:

$$h_w = p h_{bi_{new}} \quad (7-17)$$

and the amount of water in the brash ice, after return to thermal equilibrium is:

$$h_w = p_{bi_{new}} h_{bi_{new}} \quad (7-18)$$

Conservation of Energy

Conservation of energy in the wet brash ice part does not change because of the inclusion of a dry brash ice layer. This is because, at a breaking event, although the dry brash ice layer is broken as well, together with the solid ice layer, the pieces from the dry brash ice layer remain dry and are not mixed with the solid ice cold blocks and the pre-existing wet brash ice layer. Therefore conservation of energy equations which result in a decreased porosity $p_{bi_{new}}$ in the wet brash ice part, remain exactly the same as in the case of not having a dry brash ice layer, see section 7.3.2 and Equations (7-5) to (7-10). For simplicity, the porosity in the dry brash ice part is assumed, at all times, to be equal to the porosity of the wet brash ice part. In reality though, the dry brash ice part is expected to have a bigger porosity than the wet brash ice part as there is no water to freeze in the dry brash ice part. The exact porosity of the dry brash ice part, after return to thermal equilibrium of the cold blocks from the solid ice in the wet brash ice part, would result from a calculation of the conservation of energy between the initial dry brash ice layer (just before and just after breaking, see first two diagrams in Figure 7-2) and the incremental freeboard layer, after a breaking event, which results after the return to thermal equilibrium of the wet brash ice layer(the cold blocks inside the wet brash ice layer).

8. Conditions of Brash Ice Growth in Sabetta

In this section the environmental conditions in Sabetta, based on the work of (Williams & Lattes, 2012), a cooperation between BMT ARGOSS and TOTAL, would be discussed. The work provided metocean criteria at three locations between the northern entrance to Ob' Bay in Northern Russia and proposed LNG export facilities at Sabetta, see Figure 8-1.

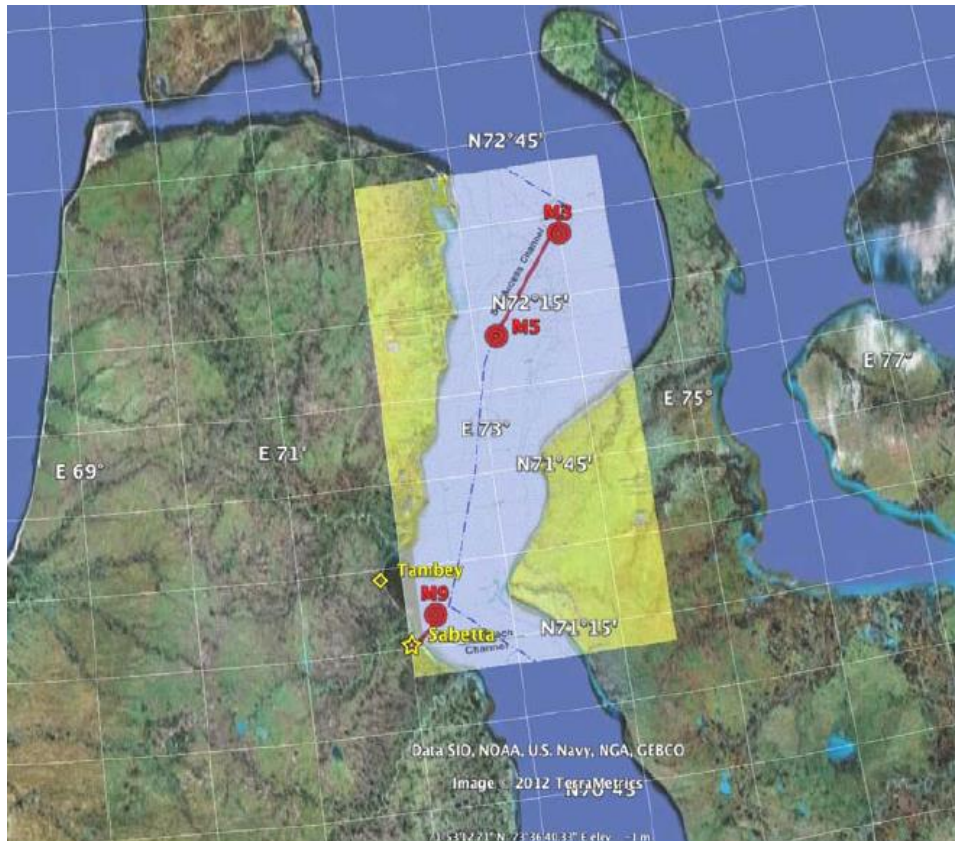


Figure 8-1 The red spots in this figure correspond to the 3 locations where Metocean conditions and criteria were defined in the work of (Williams & Lattes, 2012), for the Ob bay. Extracted from (Williams & Lattes, 2012).

The metocean aspects involved in the ice growth procedure that are going to be examined include, the air temperature, the wind velocity, radiation from the atmosphere, clouds and sun, precipitation in the form of snow, sea temperature and seawater salinity.

8.1 Air temperature

In (Williams & Lattes, 2012) report, various samples of temperature data at different dates, were collected from sources, such as the NOAA Earth System Research Laboratory, the Climate Forecast System Reanalysis (CFSR) and the Russian meteorological stations, and these were analyzed appropriately and fitted in probability density functions such as the Weibull distribution and the Gumbel distribution. Using these functions, sets of monthly temperatures corresponding to different probabilities of exceedance were created. The exact locations where temperature data was collected is shown with green pins, in Figure 8-2. In Table 8-1, the set of temperatures corresponding to probabilities of exceedance 10%, 50% and 90% are presented together with sets of temperatures corresponding to maximum and minimum temperature envelopes and a monthly mean set of temperatures, as determined in (Williams & Lattes, 2012). Some of the sets of temperatures presented in Table 8-1 would be chosen to run simulations to determine brash ice growth in Sabetta.

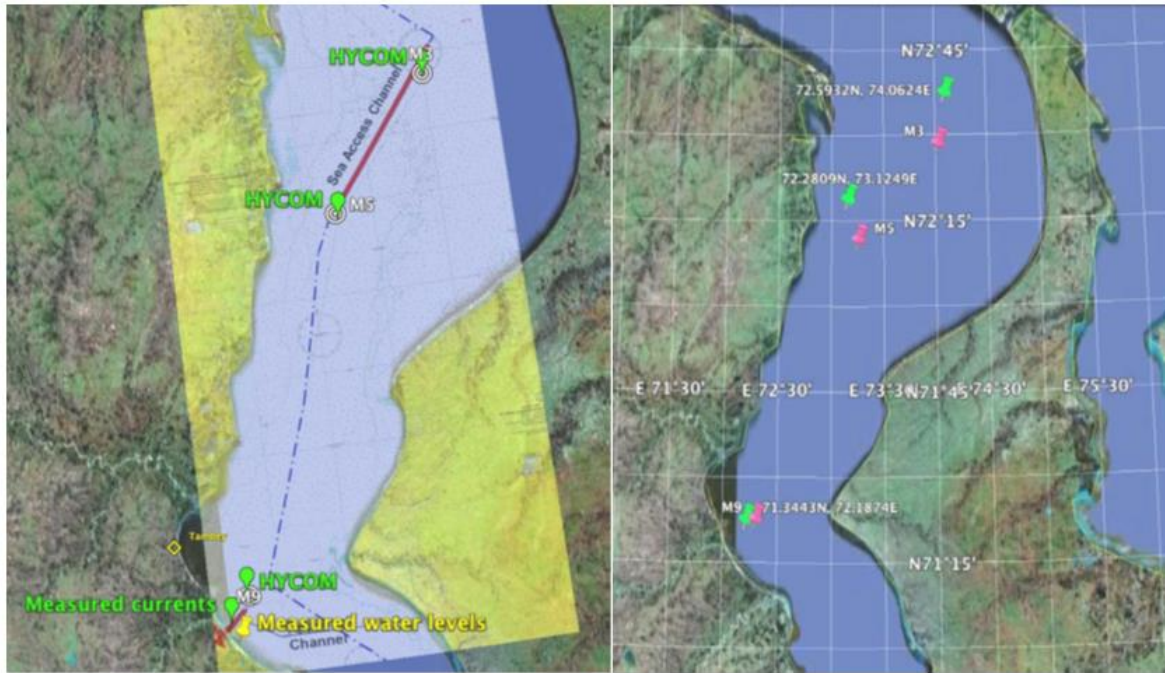


Figure 8-2 Ob bay, temperature data measurements at the locations with green pins. Left picture, shows Russian meteorological stations. Right picture, shows locations where CFSR took measurements. Pictures taken from (Williams & Lattes, 2012)

Table 8-1 Sets of mean monthly air temperatures in Sabetta. Extracted from (Williams & Lattes, 2012).

Mean Monthly air temperature in Celsius						
Month	% exceedence			Max	Min	Mean
	10%	50%	90%			
Oct.	0.8	-2.8	-5.3	1	-49.2	-5.6
Nov.	-4.7	-13.2	-19.1	1.3	-50.2	-16.3
Dec.	-8.7	-19.1	-24.4	2.0	-48.9	-21.5
Jan.	-10.8	-20.9	-25.8	3.8	-36.5	-23.1
Feb.	-9.8	-20.5	-26.1	7.9	-25.9	-22.7
Mar.	-6.9	-15.7	-20.7	7.9	-33.2	-18.0
Apr.	-2.6	-11.8	-16.2	1.5	-39.8	-13.6
May.	0.3	-3.4	-5.8	1.0	-48.9	-5.1

8.2 Wind Velocity

Hourly data for wind speed, at 10 m above sea level, was available from all the 3 sites shown in Figure 8-1, and for every month. The analysis by (Williams & Lattes, 2012) showed that the mean wind speeds over Ob' Bay are about (8 m/s) and vary little from season to season, with the strongest winds occurring in the autumn and winter months as a result of enhanced cyclonic activity, particularly from the north and west. It was also noted that hourly mean wind speeds as high as 25 m/s can occur under storm conditions. The mean wind speed mentioned above can be used as a reference wind speed for the evaluation of the thermal exchange coefficient on the ice-air interface. Therefore using:

$$h_c = \rho_a c_a C_s u_a$$

$$h_c = (1.3)(1.0044 \times 10^{-3}) \times 10^6 (1.75 \times 10^{-3}) 8 = 18.28 \text{ W} / \text{m}^2 / \text{K}$$

8.3 Radiation from the atmosphere, clouds and sun

As it was explained in section 5.2, radiation fluxes and especially long wave and short wave radiation fluxes, are important factors in the growth of sea ice. Unfortunately there are no available measurements of these fluxes in the area of Sabetta. In order to include these fluxes into the simulations with the models developed in this study, it was decided to use the average monthly values, for central Arctic basin, compiled by (Fletcher, 1965), and also presented in (Maykut & Untersteiner, 1971). The sets of these values are presented in Table 8-2.

Table 8-2 Monthly values of Long Wave and Short Wave radiation in the Arctic. Extracted from (Fletcher, 1965).

Surface flux (W/m ²)	Jan.	Feb.	March	April	May	June	July
Incoming short-wave radiation Q_{SW}	0	0	30,67	159,81	285,71	309,93	219,53
Incoming long-wave radiation Q_{LW}	167,88	166,26	166,26	187,25	243,74	290,56	308,31
Surface flux (W/m ²)	Aug.	Sept.	Oct.	Nov.	Dec.	Year (mean)	Winter (winter mean)
Incoming short-wave radiation Q_{SW}	145,28	59,73	6,46	0	0	101,43	31,75
Incoming long-wave radiation Q_{LW}	301,85	266,34	224,37	180,79	175,95	223,30	174,06

8.4 Snow Precipitation

In the general climate description of (Williams & Lattes, 2012), it is stated that the average precipitation in Sabetta is about 320 mm/year, which is a relatively low value. However it is stated that snow cover thickness can sometimes reach 40cm. In busy periods though at the port of Sabetta and in the approach channel, when ship tracks are going to be repetitively broken in short time periods, it is considered unrealistic for the snow to obtain such a high thickness. Therefore snow is not going to be included as a part or a property of the brash ice growth models developed in this study. Snow's role as an insulating material in static ice growth, cannot be applied in the context of brash ice growth. Instead, the role of the insulator in brash ice growth models is taken over by the dry brash ice pieces, resulting from the breaking events, and which float above the wet brash ice (separated by the waterline) on the basis of Archimedes principle.

8.5 Sea Water Temperature

Around 50 years of observations from over 1,000 stations throughout Ob' Bay, were analyzed in the work of (AARI, 2005) and produced the sea water temperature contour plots in Figure 8-3. As it is shown in Figure 8-3, in winter the sea water temperature is almost uniform over the Ob Bay with the value near Sabetta being -0.4 Celsius. It is also shown that in winter the temperature difference in the water between surface and seabed is negligible (no significant gradient as -0.4 C at the top and -0.5 C at the bottom). During the period (March- May) 2011, AARI gives a mean sea water temperature, near Sabetta, of -0.16 Celsius near the water surface, and a mean sea temperature of -0.8 near sea-bed. In the context of a brash ice growth model, sea water temperature is involved in the heat flux balance at

the ice-sea water interface. As brash ice thickness is not expected to exceed 10 m thickness below the waterline, the sea water temperature of -0.16 Celsius can be assumed to be the water temperature in the ice-seawater interface.

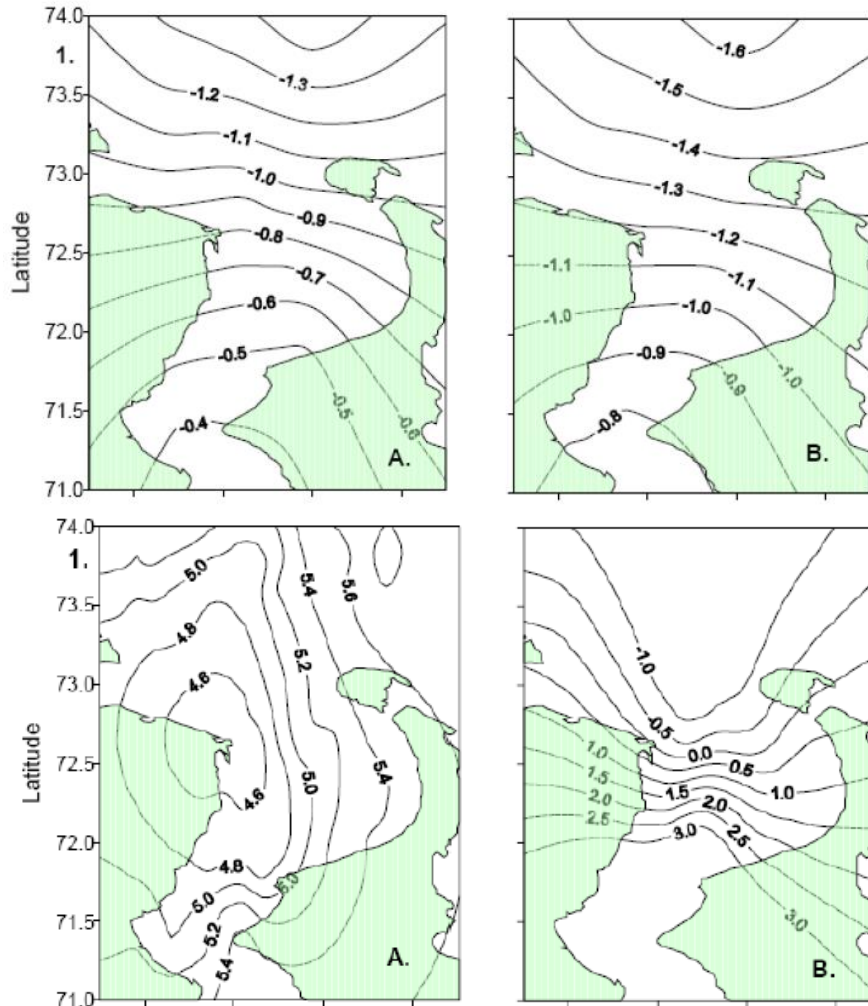


Figure 8-3 Ob' Bay sea temperatures. Top pair of pictures: Summer, Bottom pair of pictures Winter, A = near sea surface, B = near sea-bed. Extracted from (AARI, 2005).

8.6 Seawater Salinity

In the case of sea water salinity, again (AARI, 2005), gives a mean sea water salinity, near Sabetta, of 3.1 ppt near the water surface, and a mean sea water salinity of 20.2 ppt near sea-bed if water depth is greater than 10m, during the period (March- May) 2011. In the context of a brash ice growth model, salinity is involved firstly in determining the freezing temperature of the sea water and secondly in determining thermal properties of solid ice such as the specific heat capacity and the thermal conductivity. Again, as the brash ice total thickness is expected to be less than 10m, close-to surface salinity values can be applied in the BIGM models.

Finally, regarding the freezing temperature of sea water T_f , (Assur, 1958) states that the freezing temperature of a saline solution is a linear function of its salinity, and it is obtained by the relation:

$$T_f = -\mu S \quad (8-1)$$

where $\mu = 0.054 \text{ Celsius/pppt}^{-1}$. Hence using Eq. (8-1), an approximation of T_f , in Sabetta is obtained as:

$$T_f = -0.054 \times 3.1 = -0.1674^\circ C$$

which is very close to the sea water temperature chosen from the contour plots of Figure 8-3.

9. Description of the reference case for Sabetta

9.1 Scenario

The Yamal LNG port of Sabetta is expected to be operational for the first train of LNG carriers for delivery to the market by the end of 2016. The number of ships visiting the port is expected to gradually increase from 85 ships visits per year in Phase 1 of the project to 233 ship visits in Phase 3 of the project, in the end of 2018, see (Bloquin [2], 2013). The ship visits figures correspond to a combination of LNG carriers and condensate tankers. This corresponds to a frequency of LNG-carrier visits that ranges from one every 103 hours in 2016 to one every 38 hours in the end of 2018.

The harsh weather conditions in Sabetta, require the use of multiple tracks in the vicinity of the port of Sabetta, in order to accommodate the above numbers of ship visits. For the reference case of this study it is assumed that the 300m wide approach channel is divided into 5 tracks. Moreover it is assumed that an icebreaker is opening the track for an arriving LNG carrier into the harbour basin and then returns using the same track, to open it for a departing LNG carrier. Hence each ship causes two ice breaking events i.e. 1 at its arrival and 1 at its departure. Assuming that the amount of time that ships remain in the port is about half of the frequency/period with which ships arrive at the port, then the frequency with which an ice breaking event is taking place is 51.5 hours for Phase 1 and 19 hours for phase 3.

As the ship tracks are open and navigated simultaneously at the above frequencies, one can use these frequencies to obtain the frequency of ship visits and hence breaking events at each phase of the project, for an individual track. For example 19 hours breaking event frequency for 5 tracks, would be a breaking event frequency of 95 hours for an individual track.

The dimensions of the ships that are expected to be used in the port are listed below as a reference, (Saarinen, Suojanen, & Eranti, 2011), however note here that no ship dimensions are used as part of the simulations:

1. LNG carrier, L=300m , B=50 m
2. Ice breaker, L=100m, B=26m
3. Terminal Ice breaker, L=68m, B=18m
4. Ice breaking tugs, L=38m, B=13m

Ship dimensions could be used to interpret and re-arrange field measurements from transits of the above ships, if these were available, and make comparisons of the field data with the model results.

The period to which the simulations correspond, is the fast ice conditions period, which is considered to start from the beginning of November (with initial value of solid ice thickness of 0.2m) and last until the end of April. In May, it is supposed that the solar radiation is sufficient to stop the brash ice growth, see (Bloquin [1], 2013).

9.2 Creating the reference case scenario in the matlab code

The user of the code is asked to:

1. Define the instants of the beginning and the end of the simulation. If a simulation corresponds to the whole fast ice conditions period, then the beginning of the simulation should be set to the 1st of November. The user is asked to define the initial month of the simulation with the variable `t_init_month` (0= November, 1= December, 2=January ...etc.) and the simulation is assumed to start at `time=0s` of that month. Moreover the user is asked to define the duration of the simulation using `scenar_length_month` which gives two choices 1) number 6 which runs a simulation for 6 months assuming the cold season lasts until the end of April and 2) number 7 which runs a simulation for 7 months assuming the cold season lasts until the end of May.
2. Define the initial values of the solid ice thickness, the wet brash ice thicknesses, and the dry brash ice thickness, if it exists, denoted by `h_i_init`, `h_bi_init` and `h_fb_init` respectively, to be used at the beginning of the computation.
3. Define the time between two consecutive ship arrivals `scenar_dship_h`. The choices here are: 103 hours for phase 1 of the project, 54 hours for phase 2 of the project and 38 hours for phase 3 of the project.
4. Define the time, in hours, between in and out passage of the same vessel, `scenar_dtloading_h`, which in the approach channel to the harbour corresponds to the loading time.
5. Define the number of alternative navigated tracks in the channel, `nb_open_tracks`.

Before starting the computations of temperature profiles and ice thicknesses, with either BIGM 1 or BIGM 2, the code determines the list of all the instants of ice breaking events corresponding to the vessel passages. This is done as follows:

1. First, calculating the time between breaking events inside a single track, `scenar_devent_h`. This is determined from:
`scenar_devent_h= scenar_dship_h/2 * nb_open_tracks,`
 because a vessel causes a breaking event on arrival and a breaking event on departure in the same track.
2. Then the number of breaking events during the whole simulation period is calculated. This is done by first transforming the whole period of the simulation in seconds as follows:

```
scenar_length = scenar_length_month*seconds_in_month;
where          seconds_in_month= 30.5*24*3600;
```

and also doing the same with the time between breaking events in a single track:

```
scenar_devent = scenar_devent_h*3600; % [hours] --> [s]
```

The number of breaking events, `n_crush`, in a single track is determined from:

```
n_crush = ceil (scenar_length-t_init)/scenar_devent);
% [#] of breaking events
where t_init = t_init_month.*seconds_in_month;
```

3. Then the breaking time instants vector, t_{crush} , is built as follows:

```
dt_crush = scenar_devent;
t_crush = zeros(sum(n_crush),1) ;

j = 0;

while (j <= int64(n_crush(i))) %
    t_crush(index) = j*dt_crush(i);
    index = index + 1;
    j = j + 1;
end
```

An assumption made here regarding the loading time of a ship i.e. the time between in and out passage of the same vessel, denoted by $scenar_dtloading_h$, is that it is always equal to half of the time between ship arrivals in any phase of the project (Phase 1, 2 or 3).

For the reference case scenario, which assumes the use of five alternative tracks navigated simultaneously, the list of the time instants corresponding to all the breaking instants, in all of the five tracks is shown in the second column of Table 9-1. The list of the time instants corresponding to the breaking instants taking place in a single track, the computed track by the code, are shown in the fourth column of Table 9-1. Note the factor of 5, between the time instants in the two columns, corresponding to the number of tracks navigated simultaneously and alternatively.

Table 9-1 Schedule of all breaking events

Summary of breaking events in all the tracks		Summary of breaking events in the computed track	
Nr. Breaking event	Time of breaking instants[h]	Nr. Breaking event	Time of breaking instants[h]
1	t_{init}	1	t_{init}
2	$t_{init} + 19h$	2	$t_{init} + 95h$
3	$t_{init} + 2*19h$	3	$t_{init} + 2*95h$
.	.	.	.
.	.	.	.
.	.	.	.
233	$t_{init} + 232*19h$	45	$t_{init} + 44*95h$
234	$t_{init} + 233*19h$	46	$t_{init} + 45*95h$
235	$t_{init} + 234*19h$	47	$t_{init} + 46*95h$
236	$t_{init} + 235*19h$	48	$t_{init} + 47*95h$

The code provides calculation results for the total ice thickness, the wet brash ice thickness and the dry brash ice thickness during the cold season as well as calculations of the temperature profile within the solid ice mass and dry brash ice mass, if it exists, brash ice porosity variation and the thickness of solid ice within the computed track.

9.3 Reference case, chosen input data

The basic input data for the reference case is a set of monthly temperatures, T_a , a value for the assumed brash ice porosity just after a breaking event, a value for the thermal convective coefficient h_c , and an assumed ice breaking frequency. The set of monthly temperatures that would be used in this project as a basic case, was chosen from Table 8-1, and it is the set of temperatures that corresponds to a 90% probability of exceedance. This set was classified as a “Sever Winter” case. At section 9.7.3 of this study, a parametric analysis with different sets of temperatures is performed.

The porosity of the brash ice in the reference case would have a value of 0.2. This is an average brash ice porosity value that was used by previous studies for Sabetta and the Yamal LNG project such as, the studies of Bertin Technologies (Bloquin [3], 2013) and (Saarinen, Suojanen, & Eranti, 2011). This is an ambiguous value, therefore a parametric study for brash ice porosity would take place at section 9.7.1 of this report.

Table 9-2 Basic reference set of temperatures: “Severe Winter” Case

Month	Severe winter (°C) (90% exceed.)
Oct.	-5.3
Nov.	-19.1
Dec.	-24.4
Jan.	-25.8
Feb.	-26.1
Mar.	-20.7
Apr	-16.2
May	-5.8
Cumulative freezing air temperature with $T_f = -0.2$ °C	4283.2

The convective thermal exchange coefficient h_c was chosen to be $20 W/m^2/K$, for the reference case, based on the mean wind speed value and the calculation mentioned in section 8.2. However, there is also an ambiguity in this value, as previous studies showed that the wind speeds in Sabetta can vary significantly and that the thermal coefficient can be in the range of $10 - 33 W/m^2/K$. Aker Arctic, in their own studies for Yamal LNG, used a different formula for the estimation of h_c , instead of Eq. (5-6), extracted from (Jobson, 1973):

$$h_c = 3.4 + 4.4v_a \tag{9-1}$$

and assuming a mean wind velocity, v_a , of 6.6 m/s. This gave them a value of $h_c = 32.4 W/m^2/K$. In order to investigate the sensitivity of the ice thickness results, in comparison to the reference case, to great changes in the value of h_c , parametric analysis for this parameter is also performed, in section 9.7.2.

The time between ship arrivals for the reference case was chosen to be the one of the 3rd and final operational phase of the Yamal LNG project. In this phase, it is expected that 1 ship would be

arriving at the port every 38 hours. Therefore a breaking event would take place in the port every 19 hours (ships cause breakings on both arrival and departure), and a breaking event would take place in the same track every 95 hours assuming the existence of 5 tracks as explained previously. Parametric study for the time between ship arrivals is applied as well, see section 9.7.4.

For the conductivity of the freeboard, λ_{dbi} , a reference value of 1.31 W/m/K was estimated using assumptions from (Hoobs, 1974). A parametric study for this value is going to be performed in section 9.7.5.

As it was explained in sections 5.2 and 8.3, from various literature and specifically from (Maykut, 1977) and (Maykut, 1982), it is stated that the impact on ice growth due to radiation fluxes, such as the long wave radiation from space and the atmosphere and the solar radiation, is significant. As it was mentioned in section 8.3, for Sabetta there are no available measurements of these fluxes. However due to their importance, specifically of the long wave radiation on the final ice growth results, the reference case for Sabetta will include the impact of long wave radiation by using the set of monthly average values in the Arctic, shown in Table 8-2. The monthly set of solar (short-wave) radiation values of Table 8-2, is not going to be included in the reference case, as its' overall impact is expected to be non-significant. The simulations refer to the fast ice conditions period, 1st of November -30th of April, and the only month during this period that the solar radiation has a significant value is April, see Table 8-2. Parametric for long wave radiation values ($\pm 30\%$) is going to be applied as well, see section 9.7.6.

Concluding, the set of parameter values used for the reference case of Sabetta, is summarized in Table 9-3. It is reminded here that only simulations with BIGM 2, which uses a numerical thermodynamic scheme, can include sets of values for the long wave radiation.

Table 9-3 Summary of parameter inputs to be used for the Sabetta reference case

Month	"Severe winter" (°C)	QLW (W/m ²)	Porosity	h_c W/(m ² K)	Breaking event in same track (hours)	λ_{dbi} W/m/K
Oct.	-5.3	224.37	0.2	20	95	1.31
Nov.	-19.1	180.79				
Dec.	-24.4	175.95				
Jan.	-25.8	167.88				
Feb.	-26.1	166.26				
Mar.	-20.7	166.26				
Apr.	-16.2	187.25				
May.	-5.8	243.74				

A list of all the physical parameters and constants used in the simulations, not just for the Sabetta reference case, but throughout this study, is provided in the table below.

Table 9-4 List of physical parameters and constants used in the simulations throughout this study.

Description of parameter/constant	Symbol	Values	Units
Thermal conductivity of ice	λ_i	2.0	$W/m/K$
Thermal conductivity of dry brash ice	λ_{dbi}	1.31 (varying)	$W/m/K$
Thermal convective coefficient	h_c	20 (varying)	$W/m^2/K$
Brash ice porosity	p	0.2 (varying)	-
Latent heat of fusion of solid ice	L_i	335×10^3	J/kg
Latent heat of fusion of dry brash ice	L_{dbi}	268×10^3	J/kg
Density of ice	ρ_i	910	kg/m^3
Density of dry brash ice	ρ_{dbi}	728	kg/m^3
Density of Water	ρ_w	997	kg/m^3
Density of air	ρ_a	1.3	kg/m^3
Freezing temperature of seawater	T_f	-0.2	Celsius
Specific heat capacity of air	c_a	1.01×10^3	$J/kg/K$
Specific heat capacity of Ice	c_i	2100	$J/kg/K$
Specific heat capacity of dry brash ice	c_{dbi}	1680	$J/kg/K$
Heat Capacity of ice	$\rho_i c_i$	1.911×10^6	$Jm^{-3}K^{-1}$
Surface albedo of the top surface	a	0.64 (varying)	-
Emissivity of solid ice or dry brash ice	ϵ_{RAD}	1	-
Stefan-Boltzmann constant	σ	5.67×10^{-8}	$Wm^{-2}K^{-4}$
Salinity of surface ocean water	S	3.1	ppt
Fraction of net shortwave radiation penetrating the dry brash ice or solid ice surface	i_o	0.31 (varying)	-
Empirical constant, Eq.(6-35)	β	0.1172	$Wm^{-1}K^{-1}$
Empirical constant, Eq. (6-36)	γ	1.715×10^7	$JKm^{-3}ppt^{-1}$
Sensible heat transfer coefficient	C_s	1.75×10^{-3}	-
Evaporation coefficient	C_e	1.75×10^{-3}	-
Latent heat of vaporization	L_v	2.49×10^6	J/kg
Pressure on ice surface	P_o	101.3	kPa
Empirical constant, Eq. (6-38)	a	2.779×10^{-6}	-
Empirical constant, Eq. (6-38)	b	-2.691×10^{-3}	-
Empirical constant, Eq. (6-38)	c	0.979208	-
Empirical constant, Eq. (6-38)	d	-158.63779	-
Empirical constant, Eq. (6-38)	$'e$	9653.1925	-

It is noted here that values of the properties of dry brash ice, were estimated using values of corresponding properties of solid ice and the brash ice porosity.

9.4 Results with BIGM 1

In this section the simulation results, obtained with the brash ice growth model, BIGM 1, using the input for the reference case as explained above, are going to be presented. It is again reminded here that BIGM 1 does not take as input radiation values, hence the impact of radiations, either long wave or short wave, is not included in this model.

Figure 9-1, shows plots from the simulations with BIGM 1 for two situations, which are the inclusion or not of a dry brash ice layer above the growing solid ice.

For the situation that bare solid ice is growing above the brash ice without any insulating layer above it, the evolutions of brash ice and total ice have been plotted. Before going further to discuss any results, the shape of these two plots is going to be explained. Firstly, it has to be reminded here that total ice in this case is just (brash ice (wet) + solid ice). This is the reason why the total ice plot is always above the brash ice plot. At a breaking event, the thickness of solid ice drops to zero, and the brash ice thickness becomes equal to the total ice thickness. The almost diagonal drops of the brash ice plot, represent solid ice growth cycles where the solid ice is growing through brash ice, causing the brash ice thickness to decrease. As it is shown, both plots at the end of the fast ice conditions period (beginning of November-end of April), have a thickness of 7.1m.

For the situation that solid ice is growing above the brash ice, with an insulating layer of dry brash above it, the evolutions of wet brash ice, dry brash ice, total brash ice (wet brash ice +dry brash ice) and total ice have been plotted. The total ice plot in this case consists of the (wet brash ice + solid ice+ dry brash ice). Similarly as before at a breaking event, the thickness of solid ice drops to zero, and the total brash ice thickness becomes equal to the total ice thickness. The almost diagonal drops of the total brash ice plot and the wet brash ice plot, represent solid ice growth cycles where the solid ice is growing through the wet brash ice, causing the wet brash ice thickness to decrease. The dry brash ice thickness is increased step-wisely like the total ice plot, at every breaking event and remains constant until the next breaking event. As it is shown in Figure 9-1, the total brash ice and total ice plots, at the end of the fast ice conditions period have a thickness of 4.7m.

The decreased ice thicknesses in the results of BIGM 1, when the existence of a dry brash ice layer is included in the simulations, illustrates clearly the insulating effect that a dry brash ice layer has in the growth of solid ice and eventually in the evolution of brash ice, as this was explained in section 4.1.3.

In the simulation with which the results of Figure 9-1 were obtained, conservation of energy during a breaking event as this was presented in Section 7.3.2 was not applied. Conservation of energy requires that after breaking event and return to thermal equilibrium of the ice cold blocks, see Figure 7-1 and Figure 7-2, the breaking event porosity p decreases by a certain amount, see Equations (7-7) and (7-10). Running exactly the same simulation, and applying conservation of energy, results in increased brash ice and total ice thicknesses, and these are shown in Figure 9-2. Note that in the "no dry brash ice" situation, the total ice thickness has increased from 7.1m to 7.6m, and in the situation "with dry brash ice", the total ice thickness has increased from 4.7m to 5m. The variation of the brash ice porosity for the two situations during the whole period of the simulation, is shown in Figure 9-3 and Figure 9-4 respectively. As it is expected, the variation of porosity during breaking is almost identical in the two situations. As it was explained in section 7.4.2, the addition of a dry brash ice layer would not change the conservation of energy procedure in the wet brash ice layer. The slight

differences in the two graphs are explained by the different wet brush ice thickness, h_{bi_new} , in the two situations just after a breaking event, see Eq. (7-10).

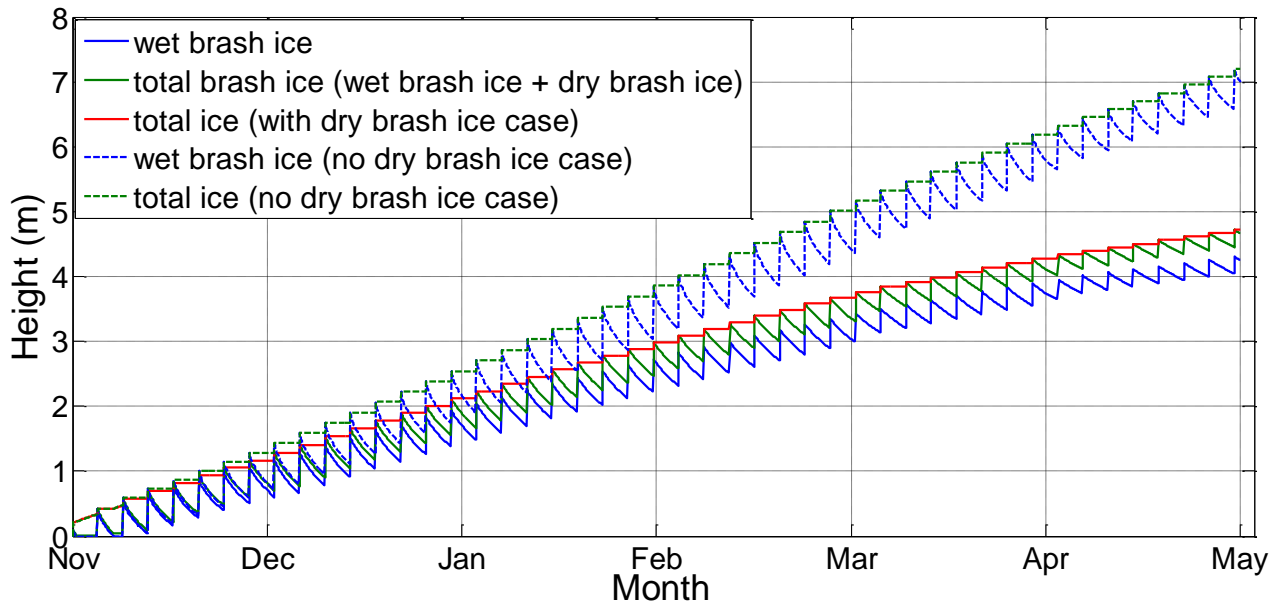


Figure 9-1 BIGM 1. Total ice and Brush ice evolution thicknesses for freeboard (dry brush ice) VS no freeboard cases. Reference case inputs are used. No conservation of energy during breaking, hence no porosity decrease after return to thermal equilibrium.

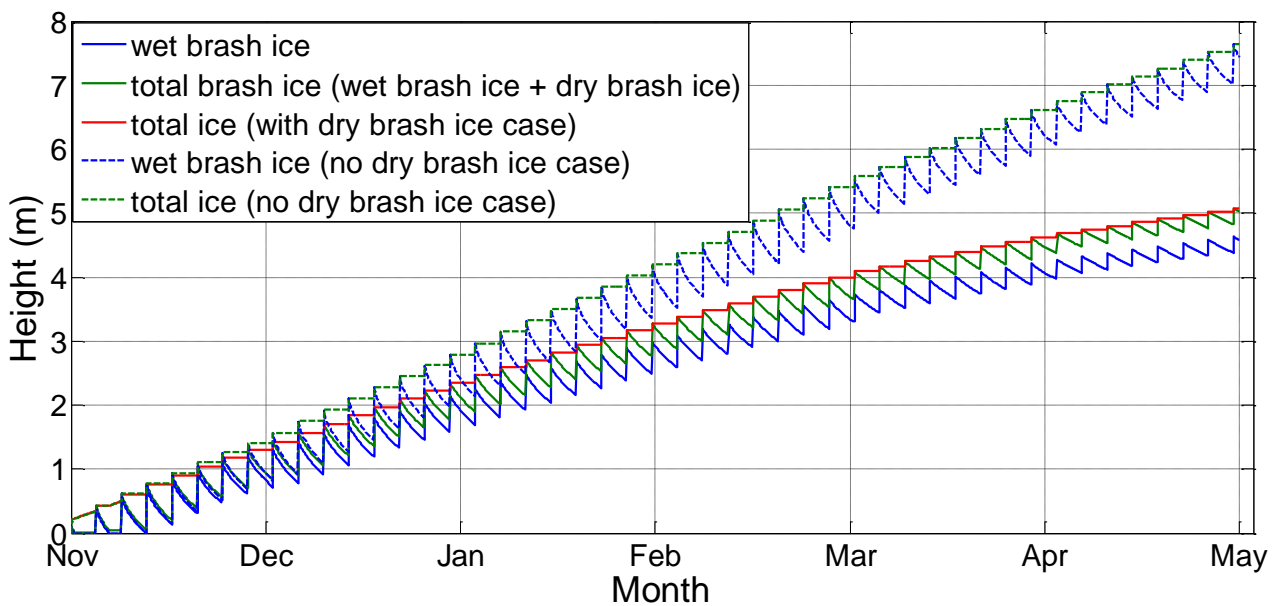


Figure 9-2 BIGM 1. Total ice and Brush ice evolution thicknesses for freeboard (dry brush ice) VS no freeboard cases. Reference case inputs are used. Conservation of energy during breaking is applied, hence there is some porosity decrease after return to thermal equilibrium of the cold blocks resulting from the breaking of solid ice.

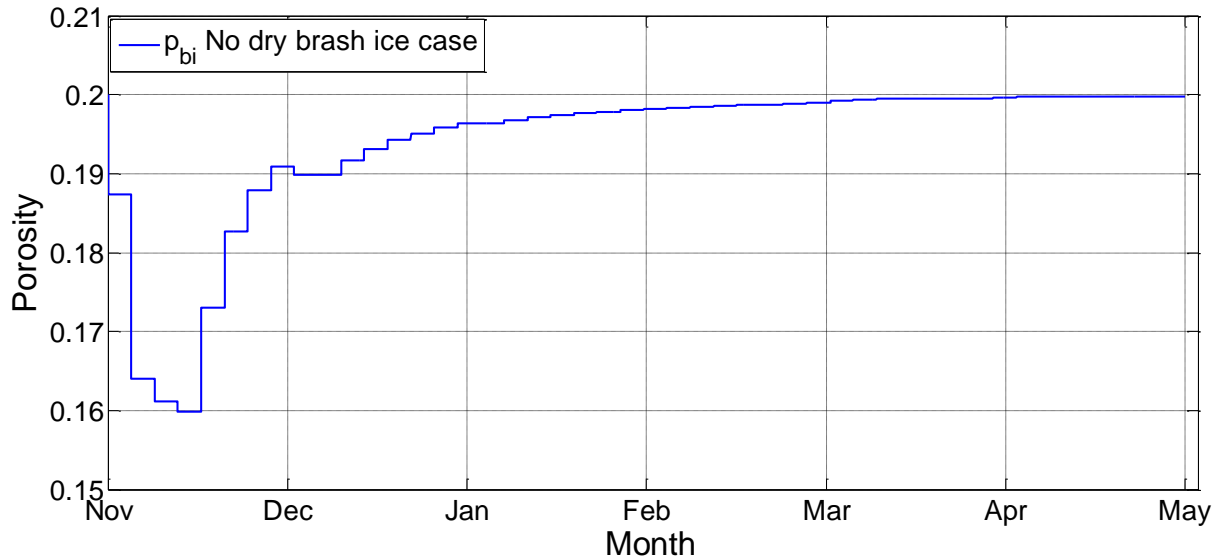


Figure 9-3 BIGM 1 with no dry brush ice using reference case and applying conservation of energy during breaking events. Evolution of brush ice porosity during the whole simulation period

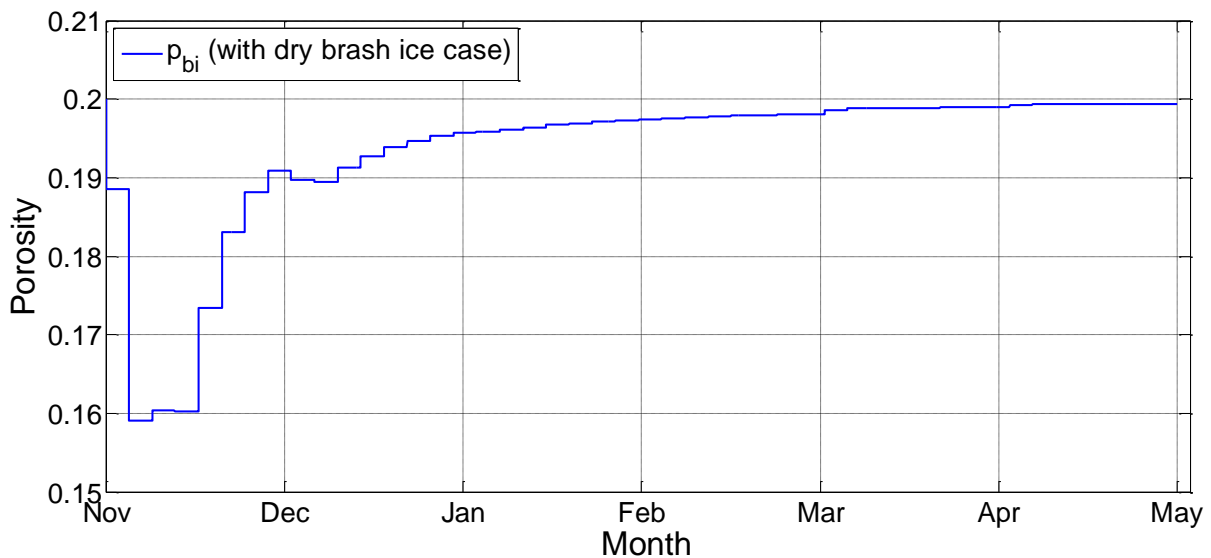


Figure 9-4 BIGM 1 with dry brush ice using reference case and applying conservation of energy during breaking events. Evolution of brush ice porosity during the whole simulation period

In Figure 9-5 and Figure 9-6 the top surface temperature evolutions, for the above simulation, for the cases of not having and having a dry brush ice layer are plotted respectively. Note, that the top surface temperature in the case of no dry brush ice, is the top temperature of solid ice, and the top surface temperature in the case of the inclusion of dry brush ice, is the top temperature of dry brush ice. At the end of the ice growth cycles in the two graphs, see bottom peaks, the top surface temperature in the two graphs is very similar. The case with dry brush ice layer, Figure 9-6, has slightly lower temperatures, in the order of 1°C lower. The obvious difference though, between the 2 graphs, is the rise of the top surface temperature at the instants of breaking events. In Figure 9-5 which is the case with no dry brush ice, at the breaking instants, the top surface temperature rises to the freezing

temperature, then it starts getting lower again within the solid ice growth cycles, until the next breaking instant. This is explained by the fact that at a breaking event solid ice is completely converted into wet brash ice, which is at freezing temperature. On the other hand, in Figure 9-6, at the breaking instants, the top surface temperature does not rise to freezing temperature. Instead, it rises only about a few degrees of °C. This is physically correct, as in the case of the existence of a dry brash ice layer, even at the instants of breaking events, the dry brash ice would still be there, it does not disappear and of course it has temperatures way lower than the freezing temperature.

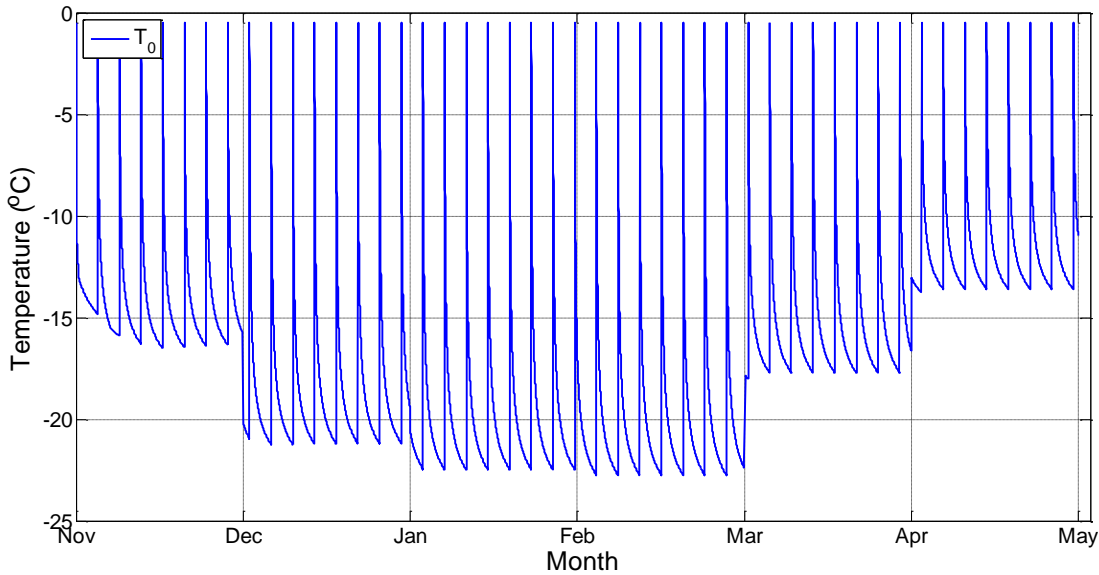


Figure 9-5 BIGM 1 with reference case inputs. Evolution of the top surface temperature T_0 , in the situation of bare ice growth (no dry brash ice). Conservation of energy during breaking is applied, hence there is some porosity decrease after return to thermal equilibrium of the cold blocks resulting from the breaking of the solid ice.

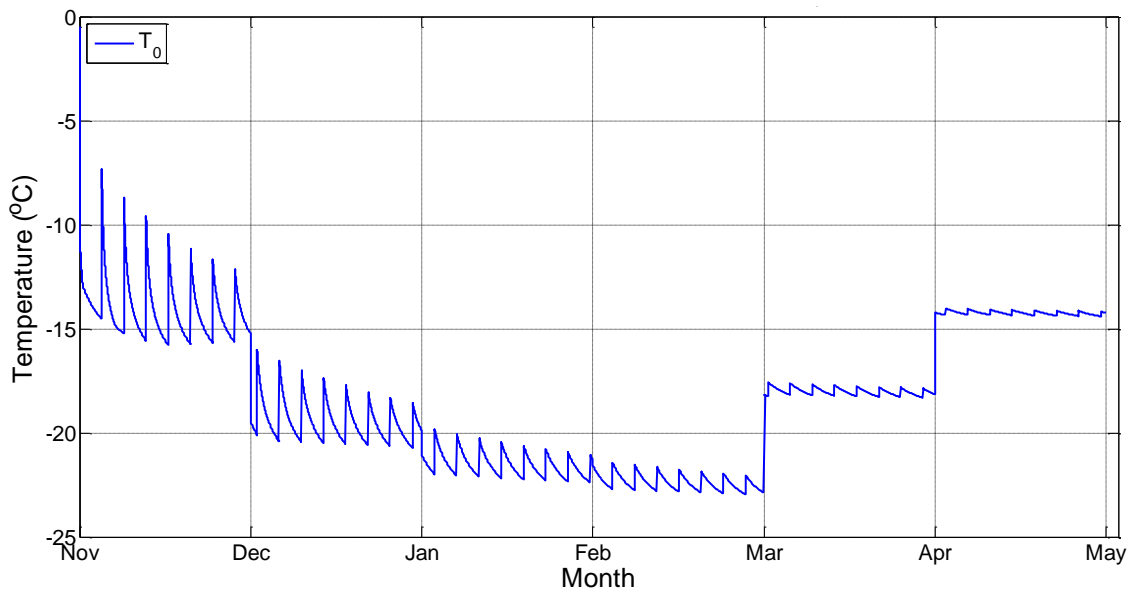


Figure 9-6 BIGM 1 with reference case inputs. Evolution of the top surface temperature T_0 in the situation of solid ice growth with the insulation of dry brash ice. Conservation of energy during breaking is applied, hence there is some porosity decrease after return to thermal equilibrium of the cold blocks resulting from the breaking of the solid ice.

9.5 Results with BIGM 2

In this section the simulation results, obtained with brash ice growth model, BIGM 2, using the input for the reference case explained in section 9.3 are going to be presented. With BIGM 2, the user has the possibility to include input for radiation values, hence in this section the long wave radiation effect is going to be examined, using as input the values listed in the reference case, Table 9-3.

Figure 9-7, shows exactly the same plots as the ones presented in Figure 9-1 and Figure 9-2, in section 9.4. It is the corresponding case to Figure 9-1 where conservation of energy during breaking is not applied, with the addition of the long wave radiation effect. Comparing the two Figures, it is observed that the long wave radiation effect has caused an increase in the total ice plots in both the cases of having and not having a dry brash ice layer. In the case of non-existent dry brash ice layer on top, the increase was about 0.5m, and in the case of having a dry brash ice layer on top the increase was about 0.15m. The increase in ice thicknesses due to the inclusion of the long wave radiation effect, into the formulation of the problem, is explained by the fact that the outgoing long wave radiation is greater than the incoming long wave radiation. This is justified by the fact that in Eq. (5-3) the top surface temperature T_o , in the outgoing long wave radiation term, is in the 4th power, and therefore the input monthly long wave radiation value has to be significantly high to overcome it.

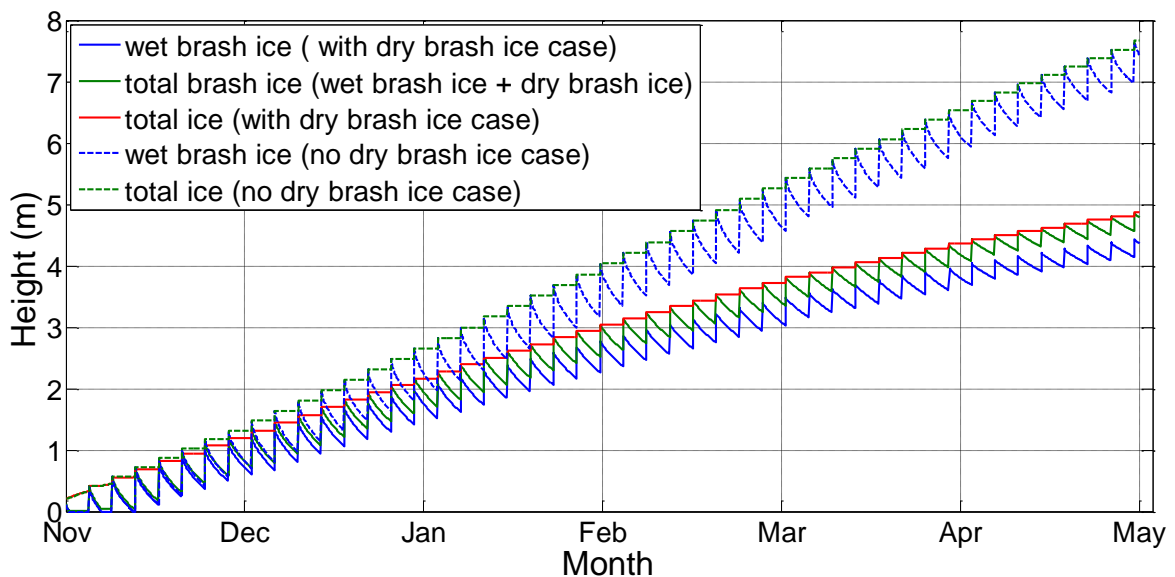


Figure 9-7 BIGM 2 with reference case input. Total ice and Brash ice evolution thicknesses for freeboard (dry brash ice) VS no freeboard cases. Reference case inputs are used. No conservation of energy during breaking, hence no porosity decrease after return to thermal equilibrium. Application of Long Wave Radiation effect.

Running again the same simulation, with the application of the conservation of energy as this is explained in section 7.3.2, which results in a decreased porosity value p_{bi} after every breaking event, gives the results shown in Figure 9-8. Again, as it is expected, conservation of energy gives increased brash ice and total ice thicknesses results. In the no dry brash ice situation, the total ice thickness has increased from 7.5m to 9.7m, and in the situation with dry brash ice, the total ice thickness has increased from 4.7m to 5.3m. Note, that the increase in the ice thicknesses with the application of the conservation of energy, when there is also a radiation effect, is greater. The variation of the brash ice porosity for the two situations, with and without dry brash ice, during the whole period of the simulation, is shown in Figure 9-9 and Figure 9-10 respectively. As in the results for BIGM 1, the variation of porosity during breaking is almost identical in the two situations. The slight differences in

the two graphs are explained by the different wet brash ice thickness, $h_{bi_{new}}$, in the two situations just after a breaking event, see Eq. (7-10).

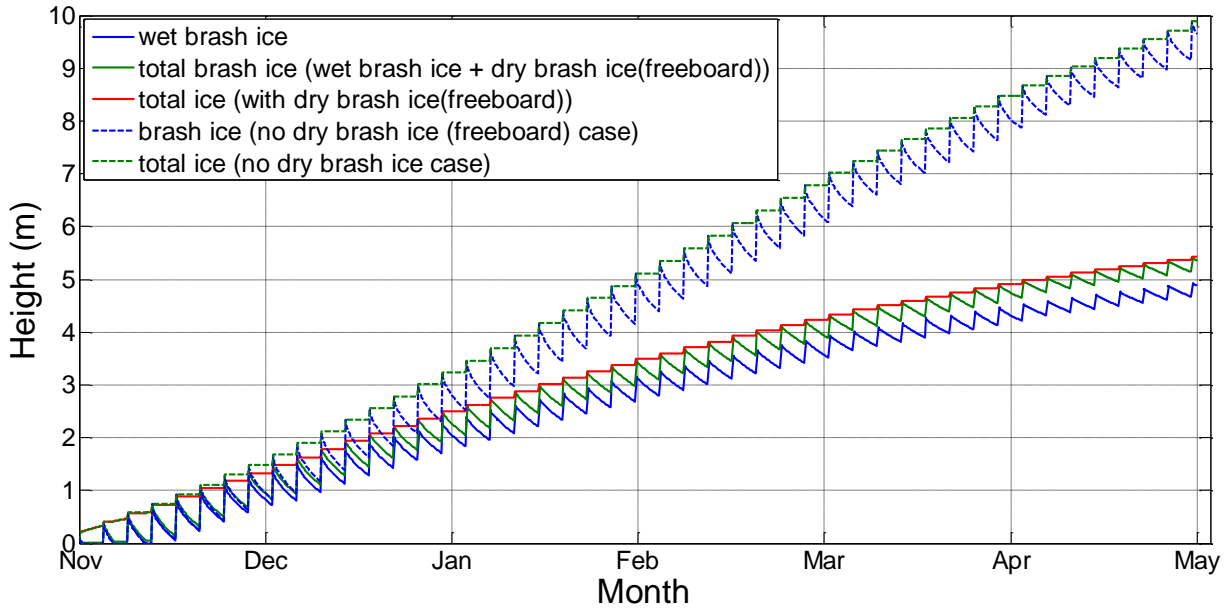


Figure 9-8 BIGM 2 with reference case input. Total ice and Brash ice evolution thicknesses for freeboard (dry brash ice) VS no freeboard cases. Reference case inputs are used. Conservation of energy during breaking is applied, hence there is porosity decrease after return to thermal equilibrium of the cold ice blocks. Application of Long Wave Radiation effect.

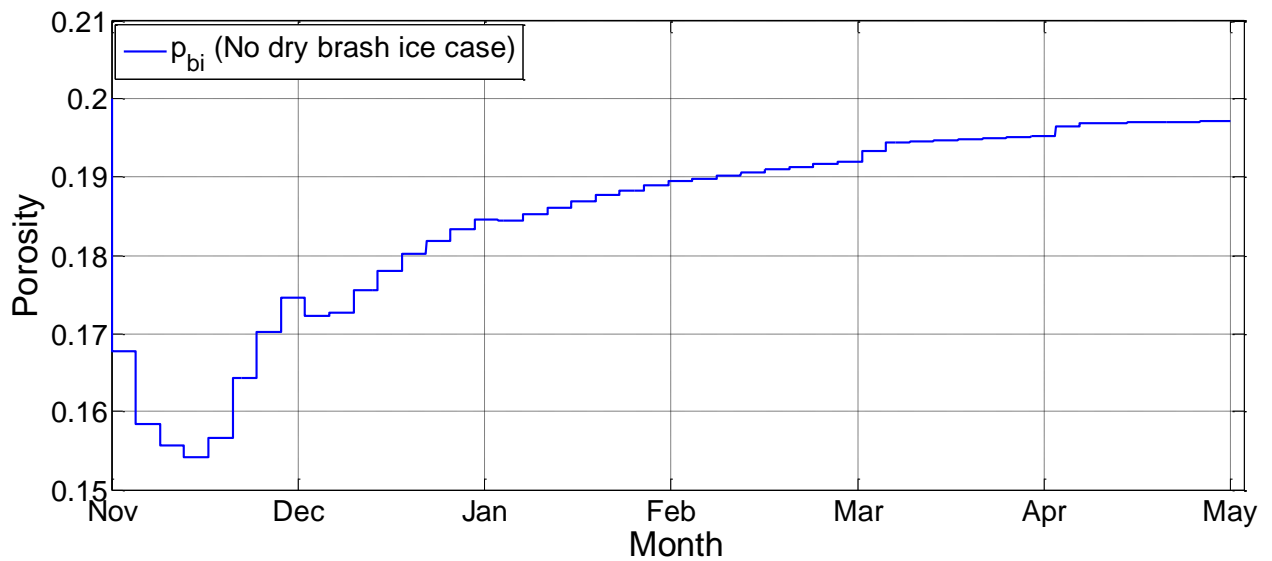


Figure 9-9 BIGM 2 with no dry brash ice using reference case and applying conservation of energy during breaking events. Evolution of brash ice porosity during the whole simulation period.

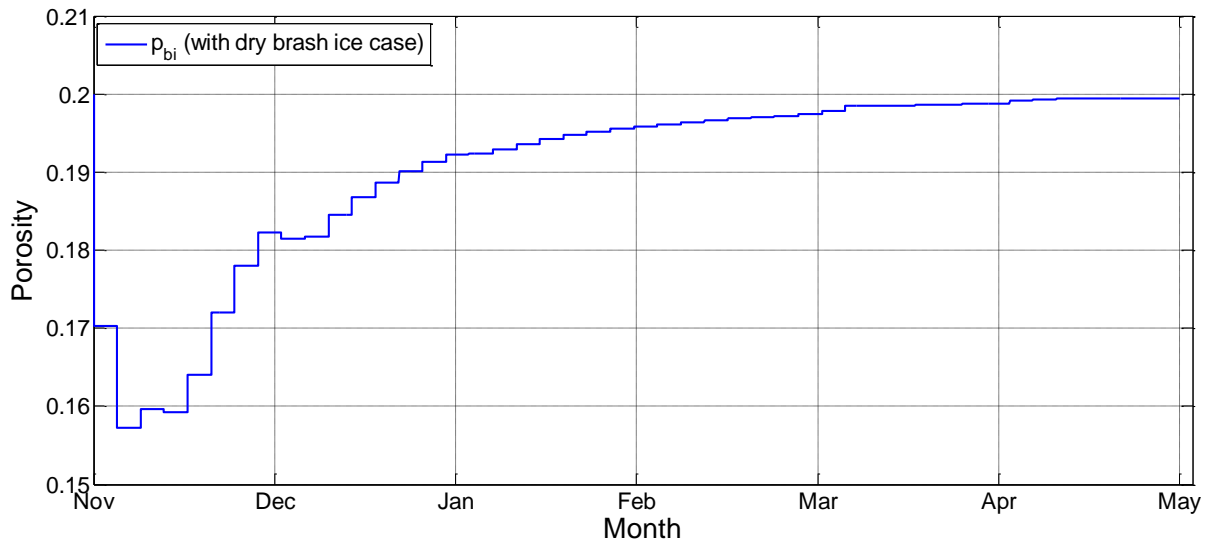


Figure 9-10 BIGM 2 with dry brash ice using reference case and (long wave radiation values input) and applying conservation of energy during breaking events. Evolution of brash ice porosity during the whole simulation period

For the simulation corresponding to Figure 9-8, the temperatures inside the solid ice and dry brash ice multiple layers, for the cases of not having and having a dry brash ice layer, are plotted in Figure 9-11 and Figure 9-12 respectively. Similar observations as with the top surface temperature in BIGM 1 are done here as well. At the end of the ice growth cycles in the two temperature profiles, Figure 9-11 and Figure 9-12, see bottom peaks, the top surface temperatures has very similar values, with the one in the temperature profile that includes the dry brash ice layer, Figure 9-12, having slightly lower values.

The additional observation here is that the temperatures in the solid ice multiple layers, are increasing almost linearly, as the dry brash ice thickness (freeboard) increases, see Figure 9-12. Hence solid ice layers in, Figure 9-12 have higher temperatures than corresponding solid ice layers in Figure 9-11. This can be explained mathematically from the balance of fluxes in the top surface and in the interface between solid ice and dry brash ice, see Eq. (4-14) for BIGM 1, and Eq. (6-16)-Eq. (6-25) for BIGM 2. This is also a proof of the insulating role that the dry brash ice has in relation to the growth of solid ice. The dry brash ice, which has a lower conductivity than the solid ice, acts as an insulating layer which decreases the rate with which the solid ice grows and hence it decreases the thickness/volume of brash ice in the end of the cold season. This is achieved by keeping the solid ice mass at higher temperatures, compared to the case of bare solid ice growth, which results in lower temperature difference between the bottom of the solid ice and the brash ice mass, which is at freezing temperature, and this causes a smaller amount of solid ice growth in each simulation step.

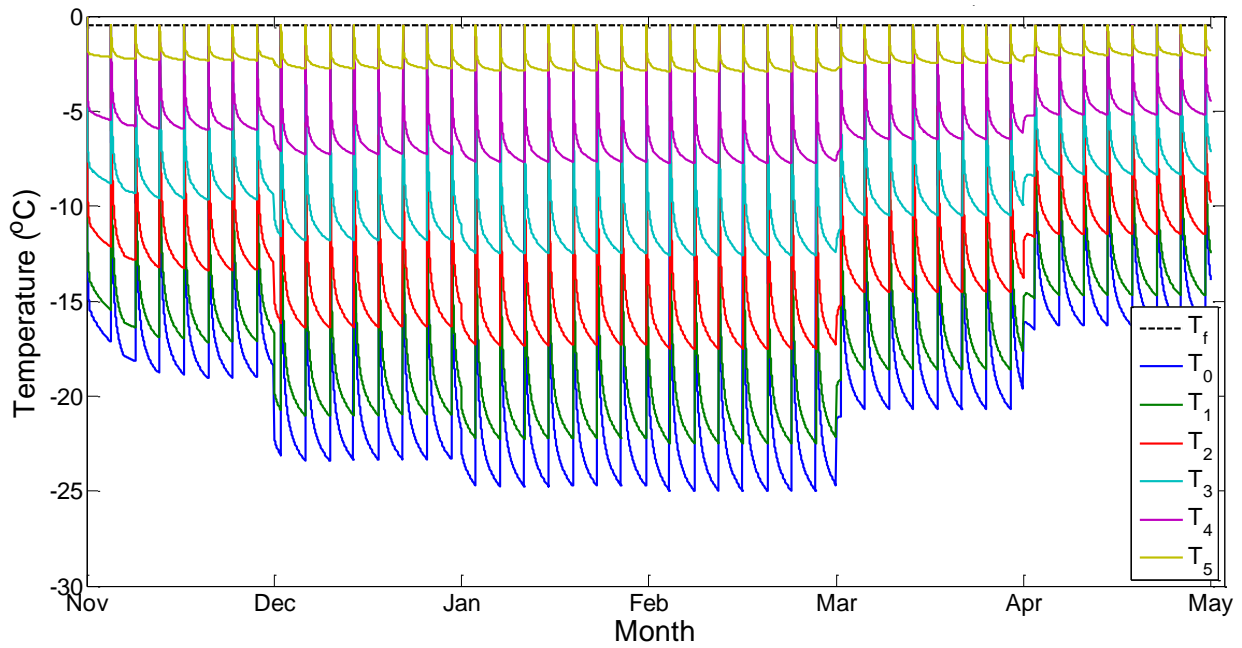


Figure 9-11 BIGM 2 with reference case input. Temperature profile evolution in the no dry brash ice situation (no freeboard). Conservation of energy during breaking is applied, hence there is porosity decrease after return to thermal equilibrium of the cold ice blocks. Application of Long Wave Radiation effect.

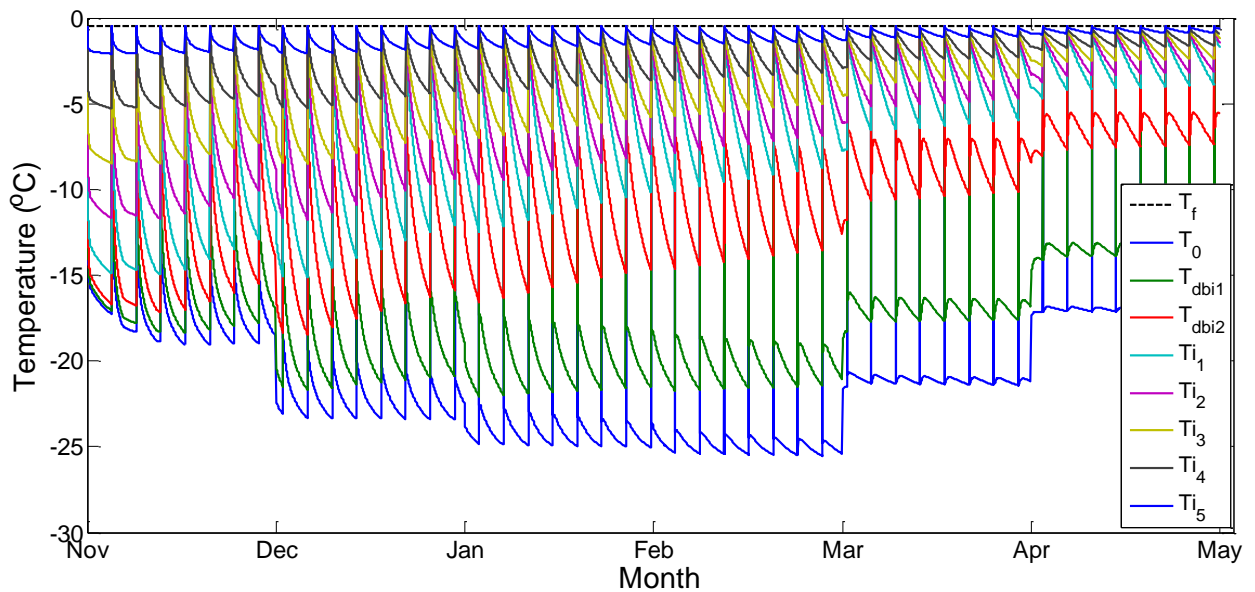


Figure 9-12 BIGM 2 with reference case input. Temperature profile evolution in the "with dry brash ice" situation (with freeboard). Reference case inputs are used. Conservation of energy during breaking is applied, hence there is porosity decrease after return to thermal equilibrium of the cold ice blocks. Application of Long Wave Radiation effect.

9.6 Comparison between BIGM 1 and BIGM 2 for reference case of Sabetta

In this section, the results of BIGM 1 and BIGM 2, with input data the reference case for Sabetta, are going to be briefly compared. Figure 9-13, shows the results of the two models for the no dry brash ice situation, without applying the long wave radiation effect in BIGM 2. In addition, Figure 9-13 includes a plot of the total ice evolution as this was predicted from Aker Arctic’s work for Yamal LNG, see (Saarinen, Suojanen, & Eranti, 2011). Aker Arctic’s model did not assume a freeboard (in the form of dry brash ice) as well, and this is the reason why the results of this model are included in this figure. The fact that corresponding plots, from BIGM 1 and BIGM 2, coincide with each other, is a proof for the correct implementation of the numerical model, as the two models, analytical and numerical, under the same conditions give exactly the same results. Aker Arctic’s prediction for the total ice thickness is about 1.3m higher than this study’s prediction, when long wave radiation is not taken into account.

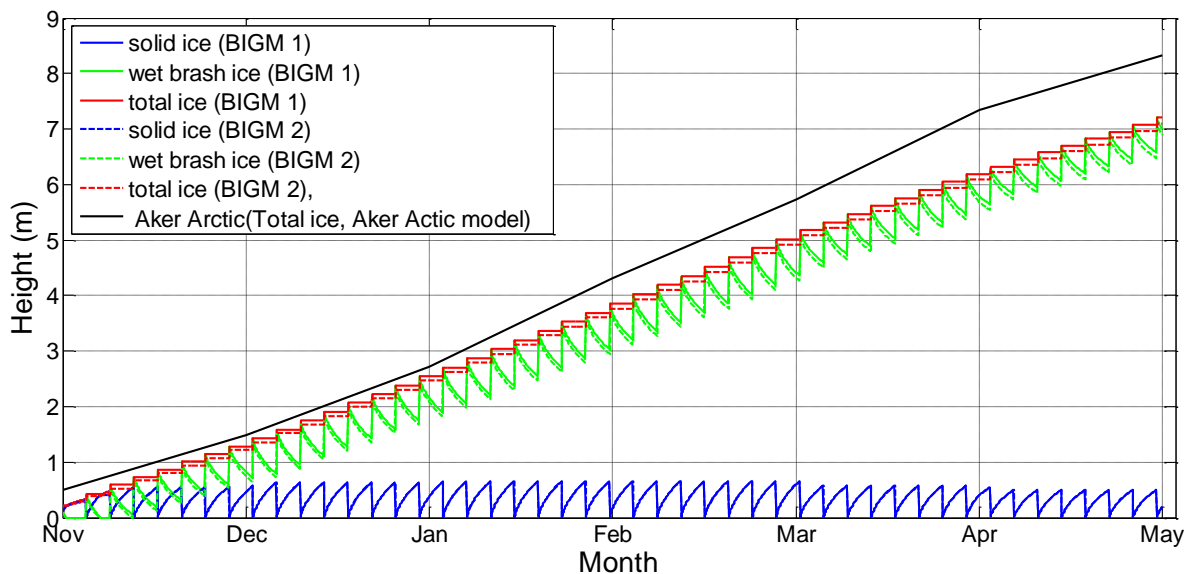


Figure 9-13 When LWR is not applied in BIGM 2, the results/graphs from BIGM 1 and BIGM 2, exactly coincide. This shows that under the same conditions the two models give exactly the same results. The plots above refer to the case of no freeboard (dry brash ice) layer. The black line represents the total ice prediction results obtained from the Aker Arctic model, see Aker Arctic (2011), which also assumes no dry brash ice (freeboard) layer.

In Figure 9-14, the same ice layers thicknesses are plotted, with the inclusion of the long wave radiation inside the formulation of BIGM 2. As it was also observed in section 9.5, the thickness of the total ice for BIGM 2 is increased about 0.5m, and the difference with the Aker Arctic’s result, becomes 0.8m.

In Figure 9-15, the results of the two models, BIGM 1 and BIGM 2, for the case that a dry brash ice layer is considered on top of the growing solid ice, and long wave radiation is included in the formulation of BIGM 2, are presented. Again, as it was also observed in section 9.5, the thickness of the total ice for BIGM 2 is increased by about 0.15m due to the inclusion of the long wave radiation. BIGM 1 and BIGM 2, in the case of the inclusion of a dry brash ice layer, show exactly the same results if the long wave radiation is not considered in the formulation of BIGM 2, as it was the case for the no dry brash ice situation (freeboard), see Figure 9-13.

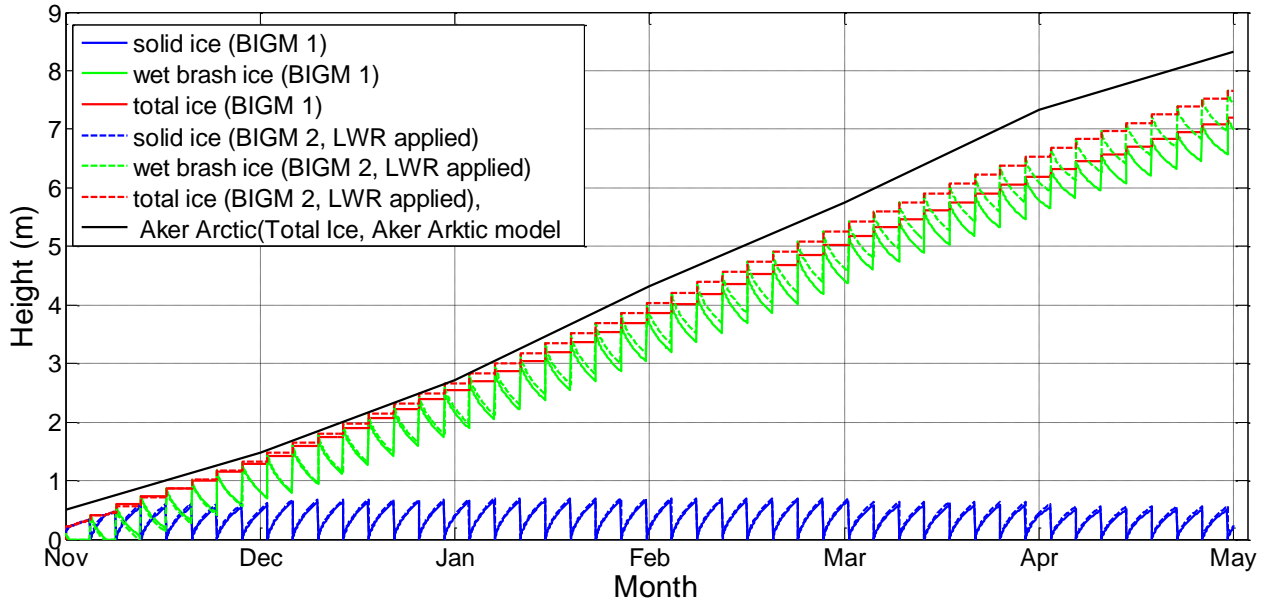


Figure 9-14 When Long wave radiation (LWR) is applied in BIGM 2, the results/graphs of BIGM 2 are shifted upwards by about 0.5m. The plots above refer to the case of no freeboard (dry brash ice) layer. The black line represents the total ice prediction results obtained from the Aker Arctic model, see Aker Arctic (2011), which also assumes no freeboard layer in the form of dry brash ice. No application of conservation of energy.

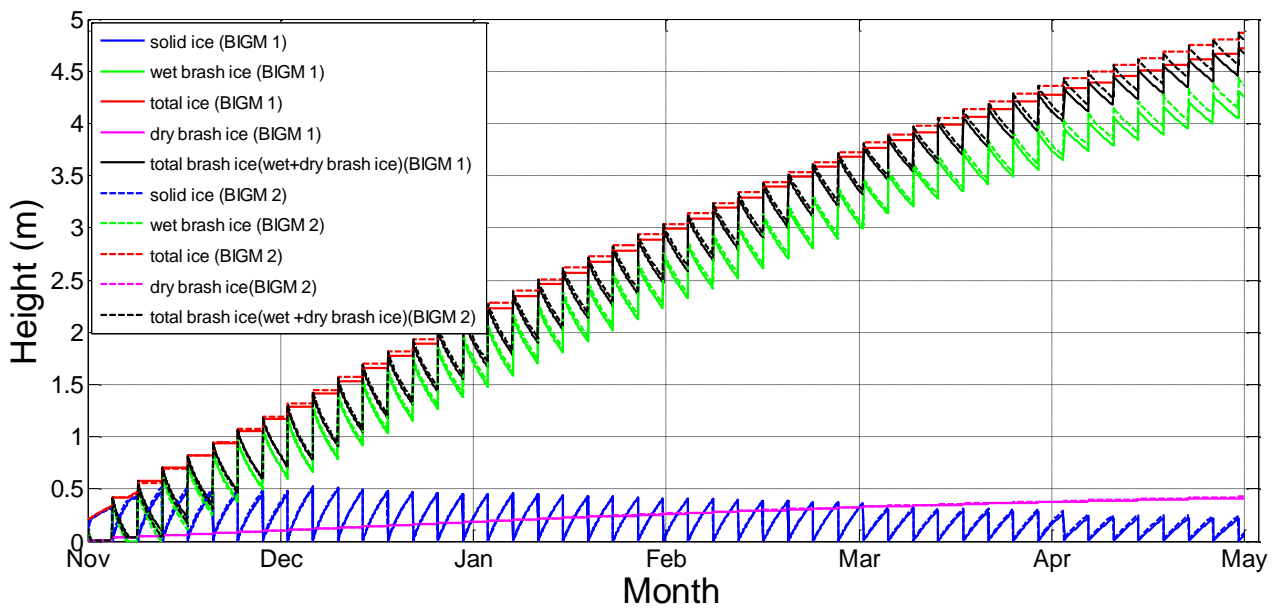


Figure 9-15 When LWR is applied in BIGM 2, the results/graphs of BIGM 2 are shifted upwards by about 0.2-0.3m, in the situation of having a freeboard (dry brash ice) layer above the solid ice. No application of conservation of energy.

9.7 Parametric study for Sabetta reference case

In this section, a parametric study is performed in order to evaluate the impact of input parameter variation on the total ice thickness, in the approach channel of Sabetta. The parameters chosen to be varied for this parametric study are listed in Table 9-5. Each of these parameters has its reference value which is the value used in the reference case, and also a minimum and a maximum value, with some of these values being obtained from previous relevant studies such as (Bloquin [3], 2013) and (Saarinen, Suojanen, & Eranti, 2011).

Table 9-5 Table with input parameters to be examined in a parametric study

Parameter Name	Maximum value	Reference value	Minimum Value
Brash Ice Porosity	0.3	0.2	0.1
Convective Coefficient ($W/m^2/K$)	33	20	10
Sets of monthly air temperatures (Celsius)	"Aker Arctic's Severe Winter"	"Severe Winter"	"Mean Winter"
Breaking event frequency in the same track in hours	1 in 50 hours	1 in 95 hours	1 in 135 hours
Freeboard Conductivity ($W/m/K$)	1.706(+30%)	1.312	0.919(-30%)
Sets of monthly long wave radiation values (W/m^2)	QLW Reference (+30%)	QLW Reference	QLW Reference (-30%)

The reference value for the brash ice porosity is 0.2, which is the value used in the Sabetta reference case. As it was mentioned previously, this is an average brash ice porosity value that was used by previous studies for Sabetta and the Yamal LNG project such as, the studies of Bertin Technologies (Bloquin [3], 2013) and (Saarinen, Suojanen, & Eranti, 2011). The maximum and minimum values that are used in this parametric study for the brash ice porosity would be 0.3 and 0.1 respectively.

The sets of temperatures to be used in this parametric study are taken from Table 8-1("Severe Winter" and "Mean Winter") and (Saarinen, Suojanen, & Eranti, 2011) ("Aker Arctic's Severe Winter"), and are presented below in Table 9-6.

Table 9-6 Set of temperatures to be used in the parametric analysis for air temperature sets

Sets of mean Monthly air temperatures, in Celsius, for parametric study			
	Max. set	Reference set	Min. set
Month	"Aker Arctic's Severe Winter"	"Severe Winter", From Table 8-1	"Mean Winter", From Table 8-1
Oct.	-6.0	-5.3	-5.6
Nov.	-16.0	-19.1	-16.3
Dec.	-21.0	-24.4	-21.5
Jan.	-30.0	-25.8	-23.1
Feb.	-30.0	-26.1	-22.7
Mar.	-30.0	-20.7	-18.0
Apr.	-16.0	-16.2	-13.6
May.	-7.0	-5.8	-5.1

For the convective coefficient, h_c , the reference value of $20 \text{ W/m}^2/\text{K}$ was estimated from the metocean investigation for wind velocity in Sabetta, in section 8.2. Moreover, the maximum value of $33 \text{ W/m}^2/\text{K}$, was obtained from the studies of Aker Arctic, see (Saarinen, Suojanen, & Eranti, 2011) and the minimum value chosen, of $10 \text{ W/m}^2/\text{K}$, was used in the parametric study for the convective coefficient in (Bloquin [3], 2013). The minimum value of $h_c = 10 \text{ W/m}^2/\text{K}$, is considered a conservative value for ice, however in the presence of snow accumulation on the dry brash ice surface this can be significantly reduced to $3 \text{ W/m}^2/\text{K}$.

For the breaking frequency in the same track, the reference value chosen is "1 in 95 hours". This is the breaking frequency corresponding to the last and final operational phase of the Yamal LNG port, which assumes a ship arrival in the port at every 38 hours, and the use of 5 alternative ship tracks in the approach channel. The minimum value of "1 in 135 hours", corresponds to the second operational phase of the Yamal LNG port, which assumes a ship visiting the port every 54 hours. The maximum value of "1 in 50 hours", is an extreme scenario used in this study, which assumes a ship arriving in the port every 20 hours, and the use again of 5 alternative ship tracks in the approach channel.

For the conductivity of the freeboard λ_{dbi} , as it was mentioned before, a reference value was obtained using some assumptions from (Hoobs, 1974). The maximum and minimum values of the parametric study were based on $\pm 30\%$ of this reference value.

Similarly, for the long wave radiation, Q_{LWR} , the reference set of values for the parametric study is the one used in the reference case, see Table 9-3, extracted from (Maykut & Untersteiner, 1971). Parametric study for long wave radiation is going to be performed using monthly maximum and minimum long wave radiation sets of values, corresponding to ($\pm 30\%$) of the reference set of values.

For this parametric study, simulations with BIGM 2 including the dry brash ice layer and the long wave radiation effects in the formulation of the problem, are going to be used. This is considered the most physically correct case. As one of the parameters examined in the parametric study is the brash ice porosity p , it was decided not to vary the porosity value during the simulations for the parametric study analysis i.e. not applying conservation of energy during breaking as this explained in section 7.

9.7.1 Porosity

In this section the evolution of the total ice thickness (wet brash ice +solid ice +dry brash ice) for $p=0.1, 0.2$ and 0.3 is plotted, see Figure 9-16.

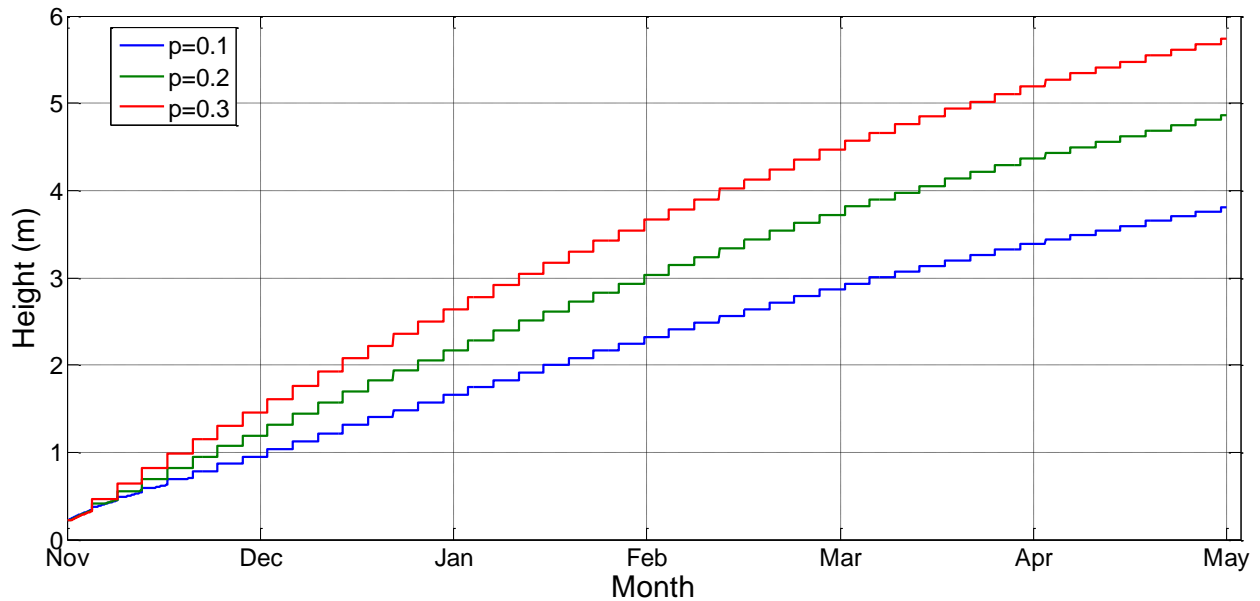


Figure 9-16 Evolution of the total ice thicknesses for the 3 possible values of porosity in the parametric study. All the other parameters are kept at their reference values.

Figure 9-16, confirms that the lower the porosity of brash ice after breaking, the lower the brash ice thickness and hence the total ice thickness at the end of the cold season.

The impact of brash ice porosity in the thickness of total ice at the end of the cold season is evaluated in Table 9-7.

Table 9-7 Influence of porosity on total Ice thickness in the end of the cold season

Brash Ice Porosity p	Total Ice thickness at the end of the cold season	
	$h_{tot}(m)$	Impact of porosity (%)
p=0.10	3.81	-1.06/-22%
P=0.20	4.87	-
P=0.30	5.79	+0.92/+19%

Table 9-7, shows that modifying the value of porosity by ± 0.1 , modifies the total ice thickness roughly by $\pm 20\%$.

Moreover, it is interesting to see the influence of the brash ice porosity on the evolution of the solid ice thickness, which develops within the wet brash ice layer, see Figure 9-17.

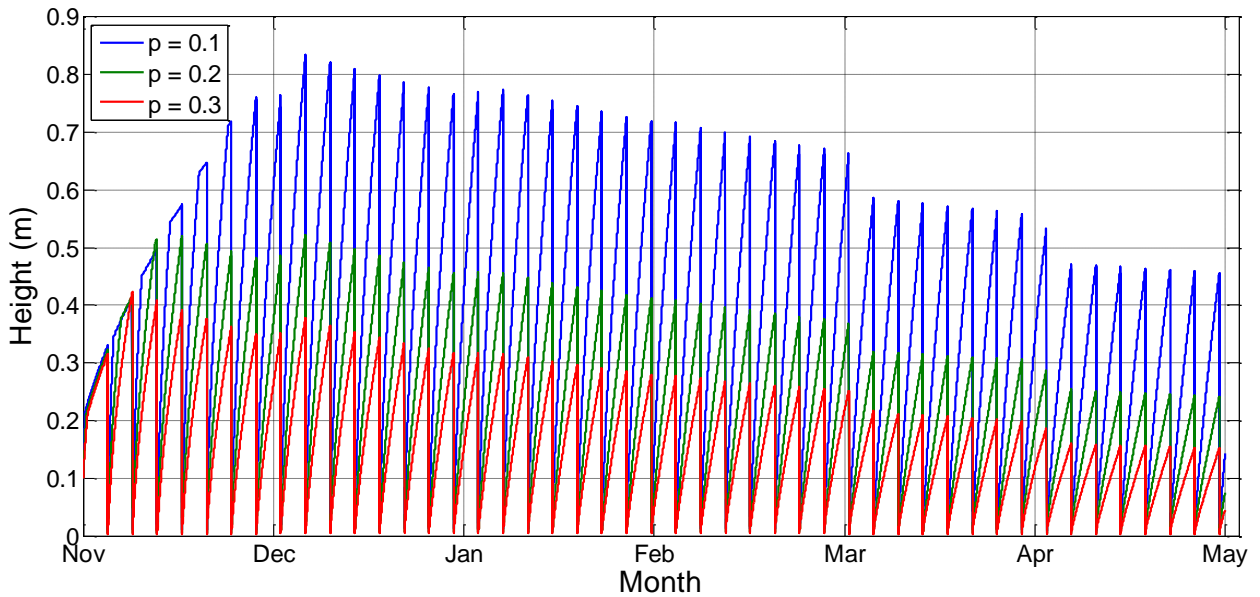


Figure 9-17 Evolution of the solid ice thicknesses for the 3 possible values of porosity in the parametric study. All the other parameters are kept at their reference values.

In order to evaluate the impact of brash ice porosity on solid ice growth, it is chosen to examine the maximum value of solid ice through the cold season, for the 3 cases. As it is shown from the analysis in Table 9-8, contrary to what happens in the total ice thickness, lowering the porosity increases the thickness of solid ice growth within the wet brash ice. This is physically expected and is explained from Eq. (6-11).

Table 9-8 Influence of porosity value on maximum solid ice thickness before each vessel passage, during the cold season

Brash Ice Porosity p	Maximum solid ice thickness during the cold season	
	$h_{i_max}(m)$	Impact of porosity (%)
p=0.10	0.83	+0.31/+60%
P=0.20	0.52	-
P=0.30	0.38	-0.14/-0.27%

These findings, from the parametric study for brash ice porosity, are important when it comes to discussing and determining the resistance from ice to navigation in brash ice covered ship tracks. It might be preferable navigating through a brash ice covered channel of higher total ice thickness but lower solid thickness, than through a brash ice covered channel of lower total ice thickness but higher solid ice thickness. However, this issue is not going to be examined further in this study, as it is related on the strength of different types of ice, which is not part of the scope here.

9.7.2 Thermal exchange coefficient

In Figure 9-18, the evolution of the total ice thickness, has been drawn for the 3 values of the parametric study.

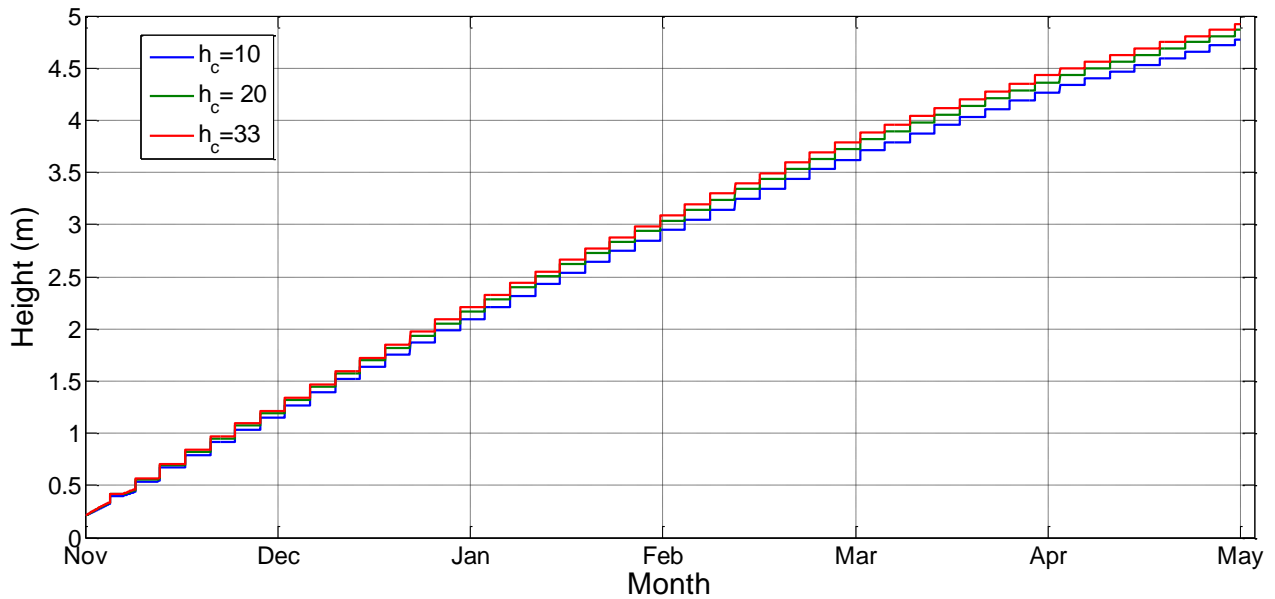


Figure 9-18 Evolution of the total ice thicknesses for the 3 possible values of the thermal exchange coefficient, in the parametric study. All the other parameters are kept at their reference values.

Figure 9-18, confirms that the higher the value of the thermal convective coefficient, the higher the total ice thickness at the end of the cold season. However, the impact of thermal exchange coefficient on the final total ice thickness value is not considered significant. This is proved in Table 9-9.

Table 9-9 Influence of the thermal exchange coefficient on the total ice thickness in the end of the cold season

Thermal exchange coefficient	Total Ice thickness at the end of the cold season	
	$h_{tot}(m)$	Impact of h_c (%)
$h_c=10$	4.78	-0.09/-1.84%
$h_c=20$	4.87	-
$h_c=33$	4.92	+0.05/+1.03%

Moreover the impact of the thermal exchange coefficient on the solid ice thickness is negligible, see Table 9-10, and the plots of the evolution of the solid ice thickness for these 3 different values of thermal exchange coefficient, coincide with each other. That is why the solid ice thickness plots are not shown here.

Table 9-10 Influence of the variation in the thermal exchange coefficient value on the maximum value of solid ice thickness before a breaking event, during the cold season

Thermal exchange coefficient	Maximum solid ice thickness during the cold season	
	$h_{i_max}(m)$	Impact of h_c (%)
$h_c=10$	0.50	-0.02/-3.85%
$h_c=20$	0.52	-
$h_c=33$	0.53	+0.01/+1.92%

9.7.3 Temperature sets

In Figure 9-19, the evolution of the total ice thickness, has been drawn for the sets of monthly temperatures used in this parametric study. These sets of temperatures are summarized in Table 9-6.

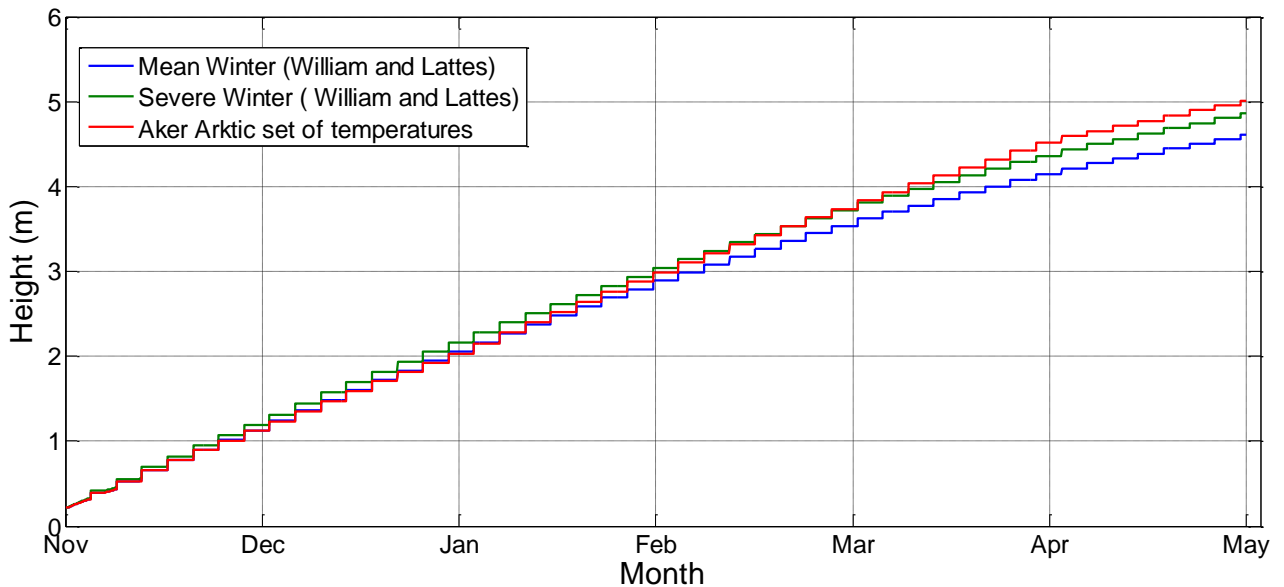


Figure 9-19 Evolution of the total ice thicknesses for the 3 possible sets of temperatures used in this parametric study. All the other parameters are kept at their reference values.

Figure 9-19 confirms the physically expected fact that the lower the temperatures are, the higher the total ice thickness is at the end of the cold season. In the first part of the simulation, November and December, the green line that represents the “Severe Winter” case, extracted from (Williams & Lattes, 2012), is higher than the red line which represents the “Aker Arctic’s severe winter”, as it has lower temperatures for these months. However in January, February and March, the Aker Arctic’s set of temperatures has colder temperatures, and this has as a result the red line growth curve exceeding the green line growth curve at the beginning of March and ending the cold season period with a higher thickness of total ice. The exact total ice thickness in the end of the cold season and the maximum solid ice thickness value during the cold season, corresponding to the three sets of temperatures used in the parametric study are shown, in Table 9-11 and Table 9-12 respectively. In these tables there is also an evaluation of the impact of the change of the temperature set, on the ice thicknesses results.

Table 9-11 Influence of the set of temperature on the total ice thickness in the end of the cold season

Temperature Set	Total Ice thickness at the end of the cold season	
	Temperature Set	Impact of temp. Set (%)
Mean Winter	4.62	-0.25/-5.1%
“Severe Winter”	4.87	-
“Aker Arctic’s Severe Winter”	5.01	0.14/+2.87%

Table 9-12 Influence of the set of air temperatures used on the maximum value of solid ice thickness before a breaking event, during the cold season.

Temperature Set	Maximum Solid Ice thickness during the cold season	
	Temperature Set	Impact of temp. Set (%)
Mean Winter	0.5	-0.02/-3.8%
“Severe Winter”	0.52	-
“Aker Arctic’s Severe Winter”	0.51	-0.01/-1.92%

9.7.4 Ship arrival time (time between ice breaking events in the same track)

Figure 9-20, shows the evolution of the total ice thickness for three different track breaking frequencies/periods.

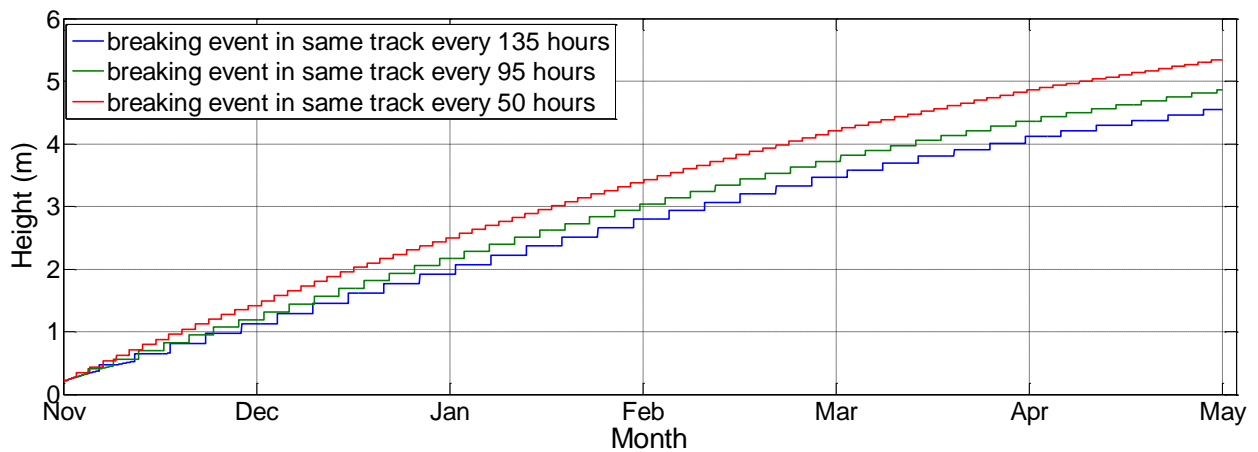


Figure 9-20 Evolution of the total ice thicknesses for the 3 possible track breaking frequency periods used in this parametric study. All the other parameters are kept at their reference values.

Figure 9-20 confirms the expected fact that the shorter the period between ice breaking events in a track during the cold season, the higher the amount of brash ice and hence total ice in the track. Moreover, Figure 9-21 confirms the expected fact that the more frequent the track breakings are, the less the thickness of solid ice, since there is less amount of time for the solid ice freezing front to proceed and grow. The exact total ice thickness value in the end of the cold season and the maximum solid ice thickness value during the cold season, for the three possible values of track breaking frequency, are listed in Table 9-13 and Table 9-14 respectively. Again, an evaluation of the impact of this parameter, on the ice thicknesses results is included.

Table 9-13 Influence of the track breaking frequency on the total ice thickness in the end of the cold season

Frequency of breaking event in the same track in hours	Total Ice thickness at the end of the cold season	
	$h_{tot}(m)$	Impact of brk frq.(%)
135	4.54	-0.33/-6.78%
95	4.87	-
50	5.33	+0.46/+9.45%

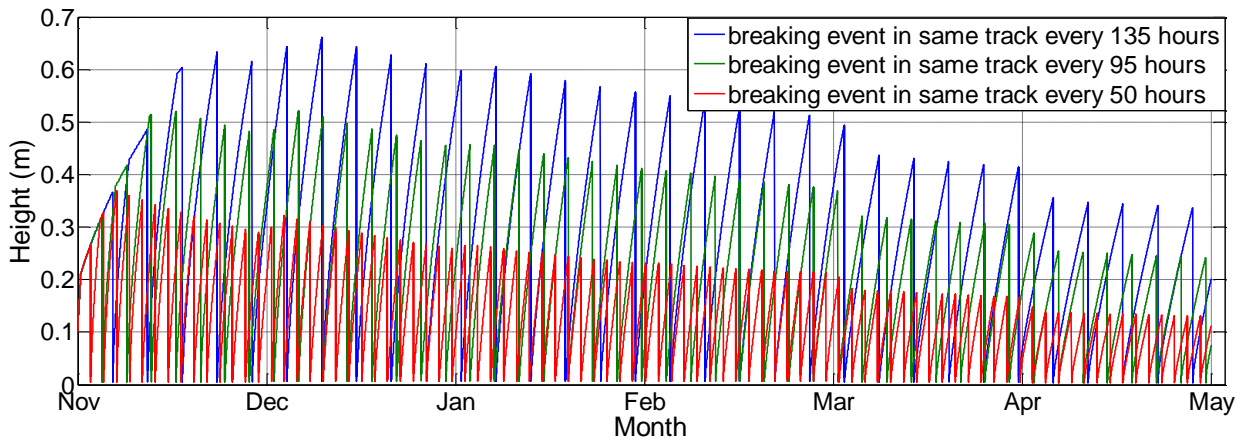


Figure 9-21 Evolution of the solid ice thicknesses for the 3 possible track breaking frequency periods used in this parametric study. All the other parameters are kept at their reference values.

Table 9-14 Influence of the track breaking frequency on the maximum value of solid ice thickness during the cold season

Frequency of breaking event in the same track in hours	Max Solid Ice thickness during the cold season	
	$h_i(m)$	Impact of brk freq. (%)
135	0.66	+0.14/+26.9%
95	0.52	-
50	0.37	-0.15/-28.8%

9.7.5 Conductivity of the dry brash ice layer (freeboard conductivity)

Figure 9-22, shows the evolution of the total ice thickness for the three possible dry brash ice conductivity values used in this study. As it is expected the greater the top surface conductivity, the greater the amount of total ice thickness produced in the end of the cold season. The impact of the change in conductivity on the maximum solid ice thickness value during the cold season, seems to be negligible, see Table 9-15. For exact values of the total ice thickness in the end of the cold season and the maximum solid ice thickness during the cold season, for the three possible dry brash ice conductivity values, see Table 9-15 and Table 9-16, respectively.

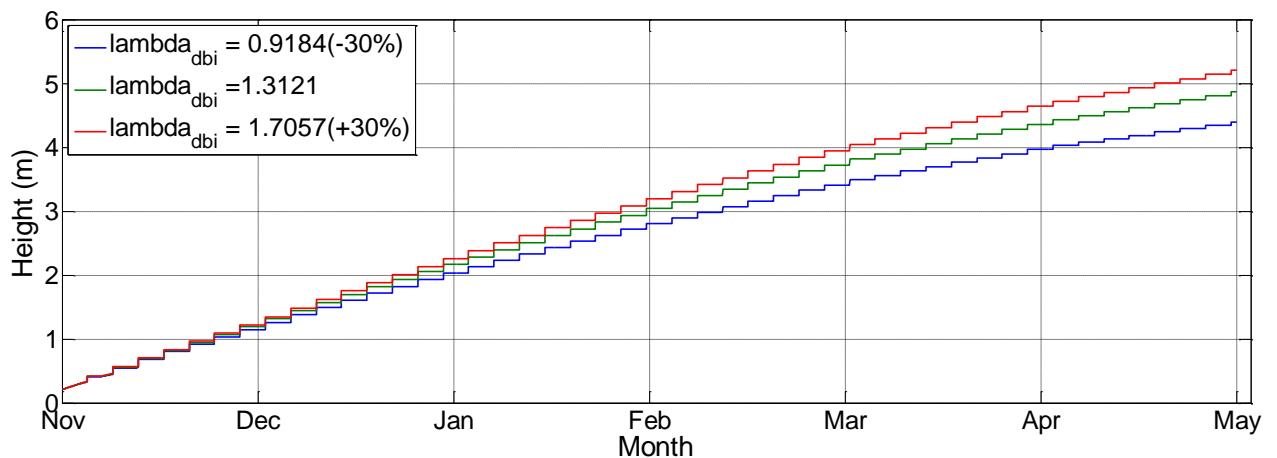


Figure 9-22 Evolution of the total ice thicknesses for the 3 possible dry brash ice conductivity values used in this parametric study. All the other parameters are kept at their reference values.

Table 9-15 Influence of the dry brash ice conductivity on the total ice thickness in the end of the cold season

Dry brash Ice conductivity	Total Ice thickness at the end of the cold season	
	$h_{tot}(m)$	Impact of λ_{dbi} (%)
$\lambda_{dbi} (-30\%)$	4.39	-0.48/-9.86%
λ_{dbi}	4.87	-
$\lambda_{dbi} (+30\%)$	5.21	+0.34/+6.98%

Table 9-16 Influence of the dry brash ice conductivity on the value of the maximum solid ice thickness during the cold season

Dry brash Ice conductivity	Maximum Solid Ice thickness during the cold season	
	$h_i(m)$	Impact of λ_{dbi} (%)
$\lambda_{dbi}(-30\%)$	0.50	-0.02/-3.85%
λ_{dbi}	0.52	-
$\lambda_{dbi}(+30\%)$	0.55	+0.03/+5.77%

9.7.6 Long Wave Radiation Parametric study

Figure 9-23, shows the evolution of the total ice thickness for the three sets of monthly average long wave radiation values, used in this parametric study. As it is expected the lower the values of the input longwave radiation, the greater the thickness of total ice in the end of the cold season. This applies to solid ice thickness as well during the cold season. The lower the values of the input longwave radiation, the greater the thickness of solid ice during the cold season, see Figure 9-24. An evaluation of the exact impact on total ice and solid thicknesses, due to a change in the set of long wave radiation values used, is presented in Table 9-17 and Table 9-18 respectively.

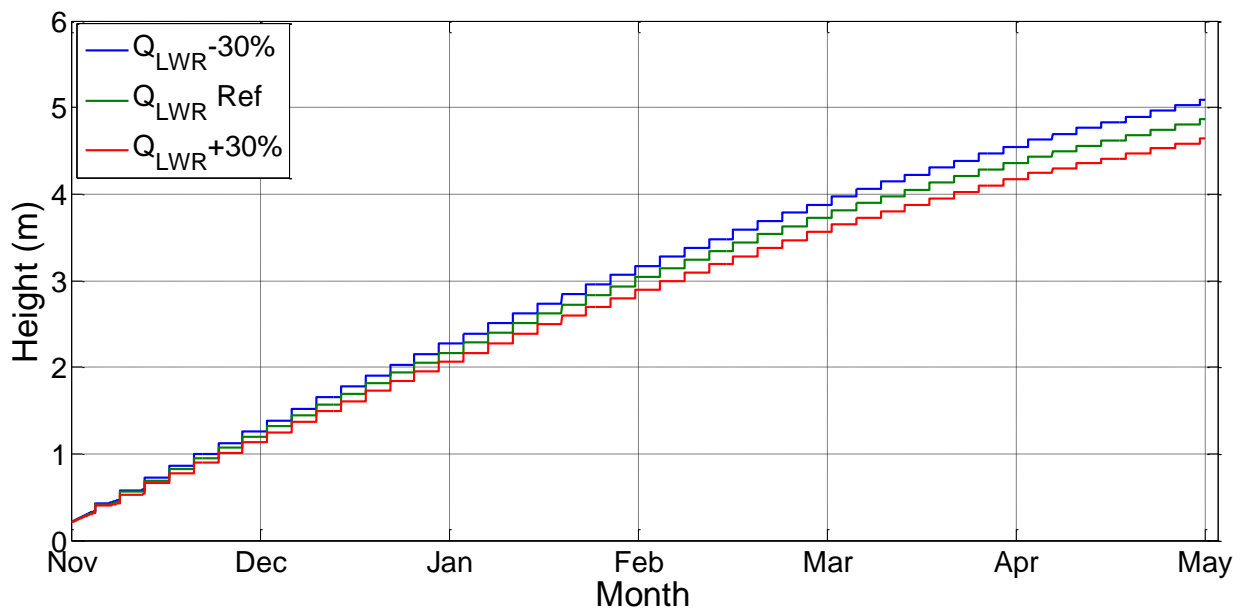


Figure 9-23 Evolution of the total ice thicknesses for the 3 possible Long wave radiation sets of values used in this parametric study. All the other parameters are kept at their reference values.

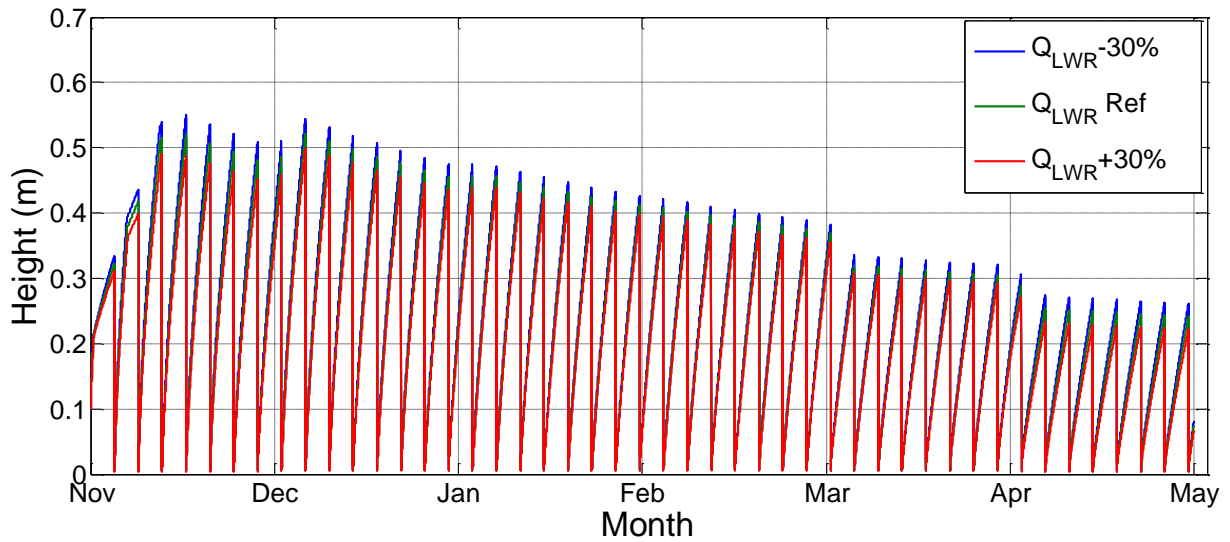


Figure 9-24 Evolution of the solid ice thicknesses for the 3 possible LWR sets of values used in this parametric study. All the other parameters are kept at their reference values.

Table 9-17 Evaluation of the Influence of the variation in the long wave radiation set of values, on the total ice thickness in the end of the cold season.

Set of monthly Long Wave Radiation	Total Ice thickness at the end of the cold season	
	$h_{tot}(m)$	Impact of LWR (%)
+30%	4.64	-0.23/-4.7%
Reference	4.87	-
-30%	5.09	+0.22/4.6%

Table 9-18 Evaluation of the Influence of the variation in the long wave radiation values, on the maximum solid ice thickness before a breaking event, during the cold season.

Set of monthly Long Wave Radiation	Maximum Solid Ice thickness during the cold season	
	$h_i(m)$	Impact of LWR (%)
+30%	0.50	-0.02/-4.47%
Reference	0.52	-
-30%	0.55	+0.03/+5.46%

9.7.7 Synthesis of the parametric study

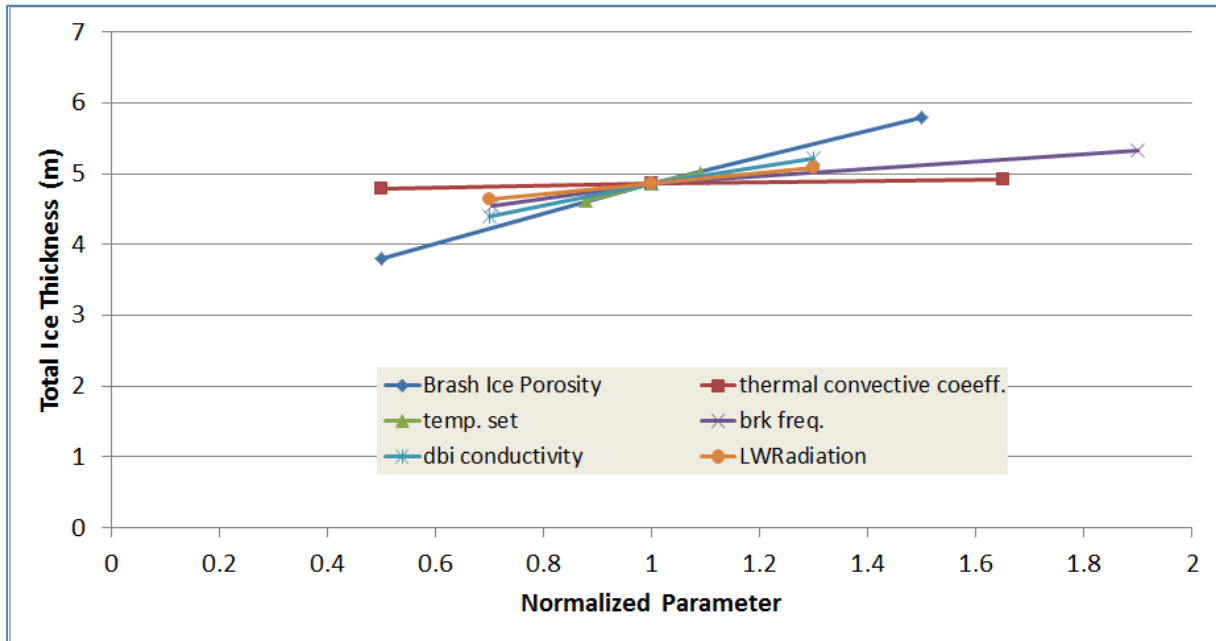


Figure 9-25 Synthesis of the results of the parametric study. Sensitivity of the total ice thickness in the end of the cold season to the input parameters

In this section, the impact of the variation of each examined parameter on the value of the total ice thickness in the end of the cold season, is going to be compared against the impact of the other examined parameters.

In order to be able to include all the examined parameters on the abscissa axis, the parameter input values were transformed into a dimensionless form with respect to their reference value. For example the dimensionless value of $p=0.1$, is 0.5, because its reference value is 0.2, see Table 9-5. For the sets of temperatures, the normalized input was the cumulating freezing degree days based on the duration of the simulation(beginning of November – end of April), and for the long wave radiation sets the normalized input was the mean long wave radiation value for each set.

From the plots in Figure 9-25, it is confirmed that for the cases examined, the input parameters that have the greatest impact on the total ice thickness in the end of the cold season are:

1. Brash ice porosity, p
2. The conductivity of the top dry brash ice layer, λ_{dbi}
3. The breaking event frequency in the same track

sorted in ascending order from maximum to minimum impact.

9.8 Influence of a different channel navigation strategy, “successively navigated tracks”

In this section a different channel navigation strategy, which was also examined by (Saarinen, Suojanen, & Eranti, 2011) and (Bloquin [3], 2013), is going to be tested. This strategy has been named “successively navigated channels” in the previously mentioned studies and though this name is kept the same in this study as well, for consistency. This strategy assumes that a first ship track is open and navigated until the total ice thickness has reached a maximum navigable value $h_{tot_nav_max}$. Then this first track can no longer be used for navigation and a second track is opened, with this being continued until the end of the cold season is reached. The total loading time (time inside the port) for this calculation has been assumed to be 19h, from (Meurant, 2012), which means that the same vessel breaks the navigated track in the approach channel 19 hours after its arrival. Note that this time period (19h), is half of the time period with which ships are arriving in the Sabetta port, in the 3rd phase of the Yamal LNG project (every 38h), which is also the period used for the reference case of this study see 9.3. But since now there is a single track navigated at any instant and not five tracks simultaneously, the track transiting frequency (ice breaking event frequency in the track) is every 19 hours, and not every 95 hours (reference case).

In order to create this scenario on the matlab code, the user has to define all the variables mentioned in the first 4 points of section 9.2 and additionally define the maximum navigable total ice thickness, $h_{tot_nav_max}$, denoted by `hbi_nav_max`, in the code. Note that the variable `nb_open_tracks` is no longer used in this case as only one track is navigated at a given time instant.

As in the reference case scenario, before starting the temperature computation, the code determines the list of all the instants of ice breaking associated with the vessel passages. Using the time between two consecutive ship arrivals of the reference case, 38h, and taking the time between forward and return passages of the same vessel (loading time) to be 19h, the time instants of forward and return passages of the vessels can be computed. These times instants are listed in Table 9-19.

Table 9-19 Example of list of time instants of vessel passages 9 (breaking events) for successively navigated tracks.

Vessel number	Time of forward passage[h]	Time of return passage[h]
1	t_init	t_init+ 19 h
2	t_init+38 h	t_init+ 38+19 h
3	t_init+38*2 h	t_init+ 38*2+19 h
.	.	.
.	.	.
.	.	.
117	t_init+38*116 h	t_init+38*116+19 h
118	t_init+38*117 h	t_init+38*117+19 h

If the same track is used during the whole cold season, i.e. if this track does not exceed the $h_{tot_nav_max}$, making it necessary to change track, the breaking events in this track and the corresponding time instants are listed in Table 9-20.

Table 9-20 List of breaking instants in the same track, with successive navigated tracks scenario, if only one track is used during the whole cold season.

Summary of breaking events in the computed track (if only one track is required to be used during the whole cold season)	
Nr. Breaking event	Time of breaking instants[h]
1	t_init
2	t_init +19h
3	t_init +2*19h
.	.
.	.
.	.
233	t_init +232*19h
234	t_init +233*19h
235	t_init +234*19h
236	t_init +235*19h

The maximum navigable value in the Sabetta area, has been assumed by the Yamal LNG, to be around 4m. However, a proportion of brash ice as this was explained in section 2.1, is always pushed outside of the ship track. Using this proportion a_{pushed} , the 4m maximum total ice thickness has to be transformed into an equivalent maximum navigable total ice thickness as follows:

$$h_{tot_nav_max_equiv} = \frac{h_{(tot_nav_max)}}{1 - a_{pushed}} \quad (9-1)$$

in order to be able to be used with the models developed in this study. This study has estimated a_{pushed} to be 0.36, see section 10.2.4, in contrast with previous studies that have estimated and used a_{pushed} values of 0.5 in their studies. Therefore using Eq. (9-1), the maximum navigable total ice thickness value is 6.25m. This means that the Brash Ice Growth models (BIGMs) of this study will open a new ship track, when the total ice thickness in the transiting ship track has reached a value that is equal or greater than 6.25m. Hence, BIGMs can provide the total number of ship tracks required to be used during the cold season if this channel navigation strategy is used.

To test this channel navigation approach, simulations of BIGM 2, with and without the dry brash ice layer, with the inclusion of the long wave radiation effect were used.

Figure 9-26, shows the evolution of the total ice thickness as well as the solid ice thickness in the navigated ship tracks and the level ice (solid ice as well) evolution outside the navigated ship tracks, for the case of not having a dry brash ice layer. The model predicts that the use of a total of 4 tracks, during the whole cold season is going to be needed, if this channel navigation approach is used. The figure shows clearly that every time the total ice thickness reaches the limit of 6.25m, the track is abandoned (vertical drops of the total ice thickness plot), and the navigation of ships continues in a new track. Also note that the brash ice created in the new track, after the first passage of a ship, forms from the breaking of a solid ice layer of thickness equal to the thickness of level ice at the moment of the passage of the ship. Level ice (solid ice), denoted h_{level_i} in the code, in the new track had been growing undisturbed (see black line in Figure 9-26) until the opening of the track for navigation and the first passage of a ship through it.

Figure 9-27, shows the same plots as Figure 9-26, in the case that there is an insulating dry brush ice layer in the formulation of the model (BIGM 2 with dry brush ice). The models' prediction is that a single track, even with the "successively navigated channels" strategy is enough to accommodate the traffic in the Sabetta port during the cold season, as the limit of 6.25m total ice thickness is not exceeded.

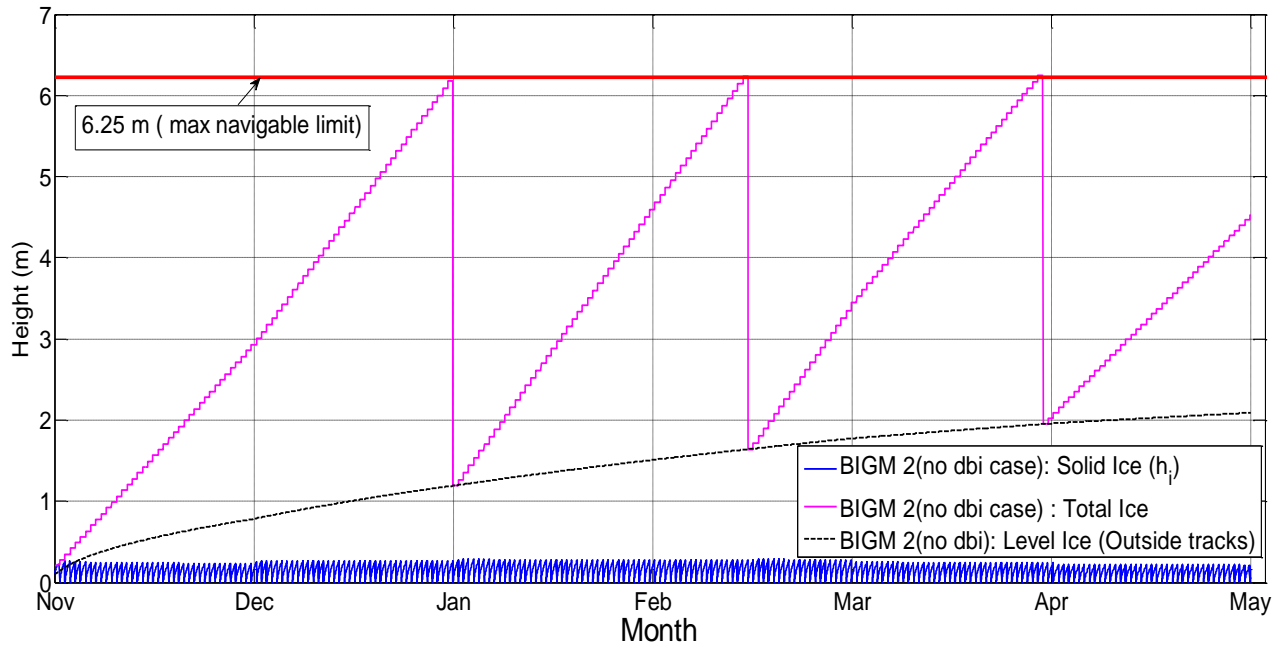


Figure 9-26 Successively navigated track for BIGM 2 (with radiation) with no dry brush ice. Total ice equivalent thickness limit for navigation 6.25m. The figure shows that 4 tracks are going to be required during the whole cold season.

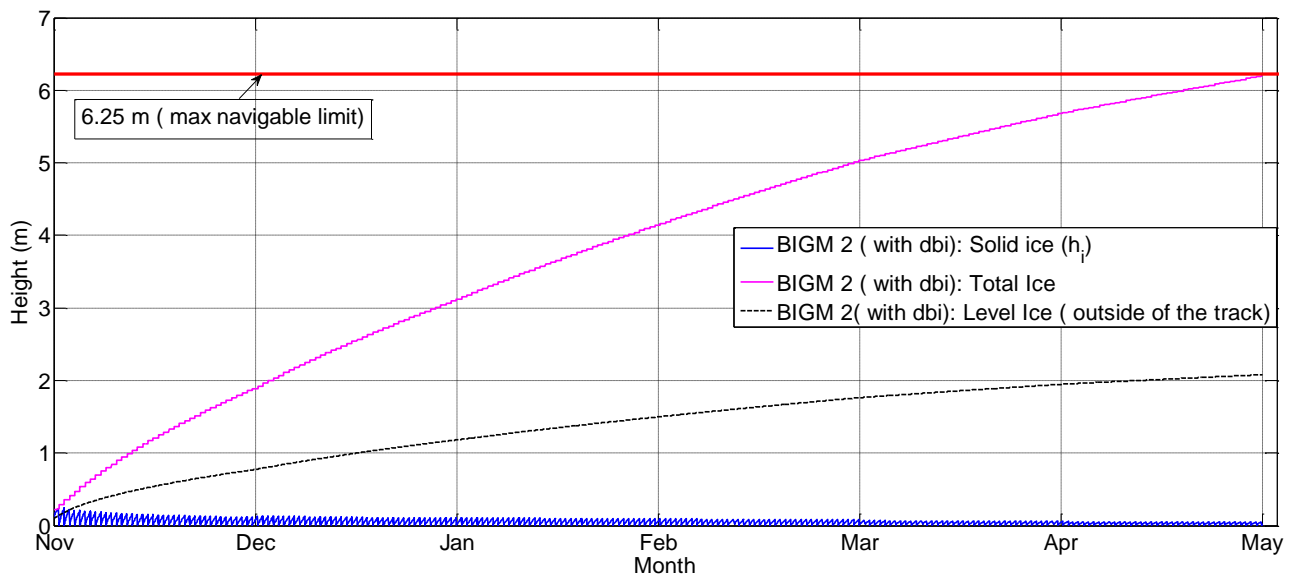


Figure 9-27 Successively navigated tracks for BIGM 2 (with radiation) with dry brush ice. Total ice equivalent thickness limit for navigation 6.25m. The figure shows that 1 track is enough during the whole cold season, to accommodate traffic in the Sabetta port with the use of this navigation strategy.

Using an a_{pushed} coefficient of 0.5 as it was done in (Saarinen, Suojanen, & Eranti, 2011) and (Bloquin [3], 2013), which gives an equivalent total ice thickness limit of 8m, BIGM 2 with radiation and

no dry brash ice, predicts that 3 tracks are needed to be used during the whole cold season using the “successively navigated tracks” navigation strategy, see Figure 9-28 . This result agrees with what (Saarinen, Suojanen, & Eranti, 2011) and (Bloquin [3], 2013), predicted under same conditions.

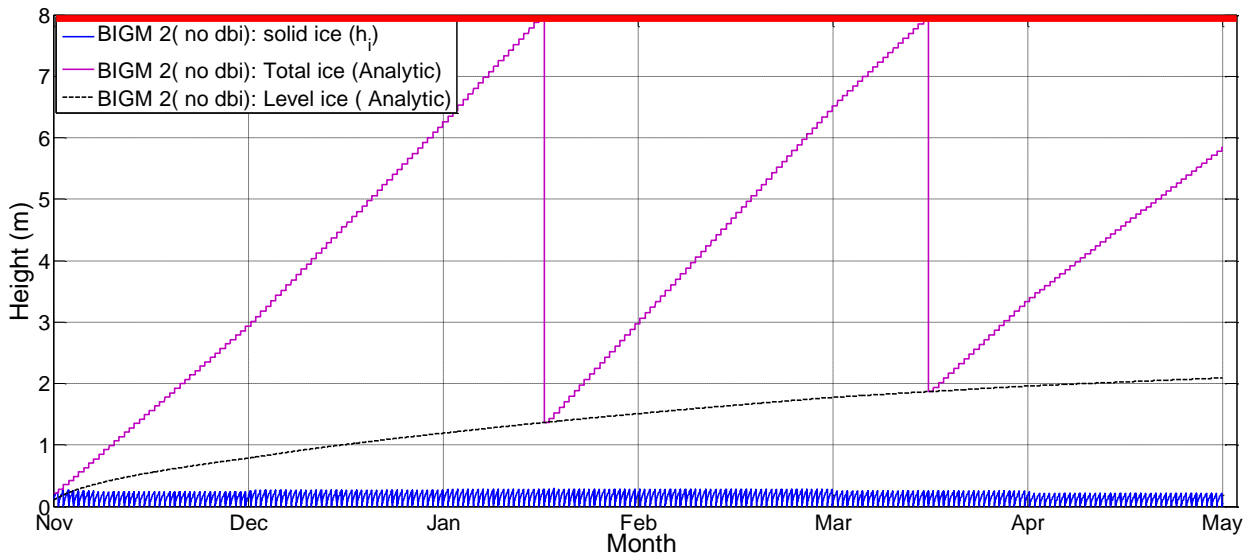


Figure 9-28 Successively navigated track for BIGM 2 (with radiation) with no dry brash ice. Total ice equivalent thickness limit for navigation 8m.

10. Lulea brash ice field measurements and their analysis

In order to reduce the uncertainties around the critical issue of the growth of brash ice, Yamal LNG in cooperation with Bertin technologies and SSPA AB Sweden, decided to proceed with brash ice field measurements in channels in the port of Lulea, Sweden, in the winter of 2012-2013. The aim of the conducted ice measurements was to support the investigation of the growth of brash ice in channels and to provide important input data for mathematical models predicting the brash ice thickness, see (Westerberg, 2013). More specifically, the goal was to compare the ice field measurements, i.e. brash ice thickness/volume, to the results given by the theoretical models used by Bertin Technologies, when the theoretical models take as input data the environmental conditions in Lulea at the time the brash ice field measurements were undertaken.

The measurements in Lulea were carried out in cooperation between SSPA Sweden AB, Lulea University of Technology and Lulea Bogserbats AB, with SSPA Sweden AB being the project coordinator and responsible for reporting to Bertin Technologies and Yamal LNG.

The measurements were aided by the ice breaking tug Viscaria which performed passages of the channel under examination, at regular time intervals. The measured data is divided into the subcategories: metocean data, brash ice channel measurements and vessel measurements.

10.1 Measurement procedures and locations

As it was mentioned above, the measurements were conducted in the port of Lulea, located in the northern part of the Bay of Bothnia. Brash ice channel measurements and vessel measurements started in early January 2013 and proceeded until mid of April 2013. Metocean data have been collected in the harbour of Luleå and from the nearby airport of Luleå, Kallax, see Figure 10-1. Daily observations were also made and noted down by the crew on board the icebreaking tug Viscaria.

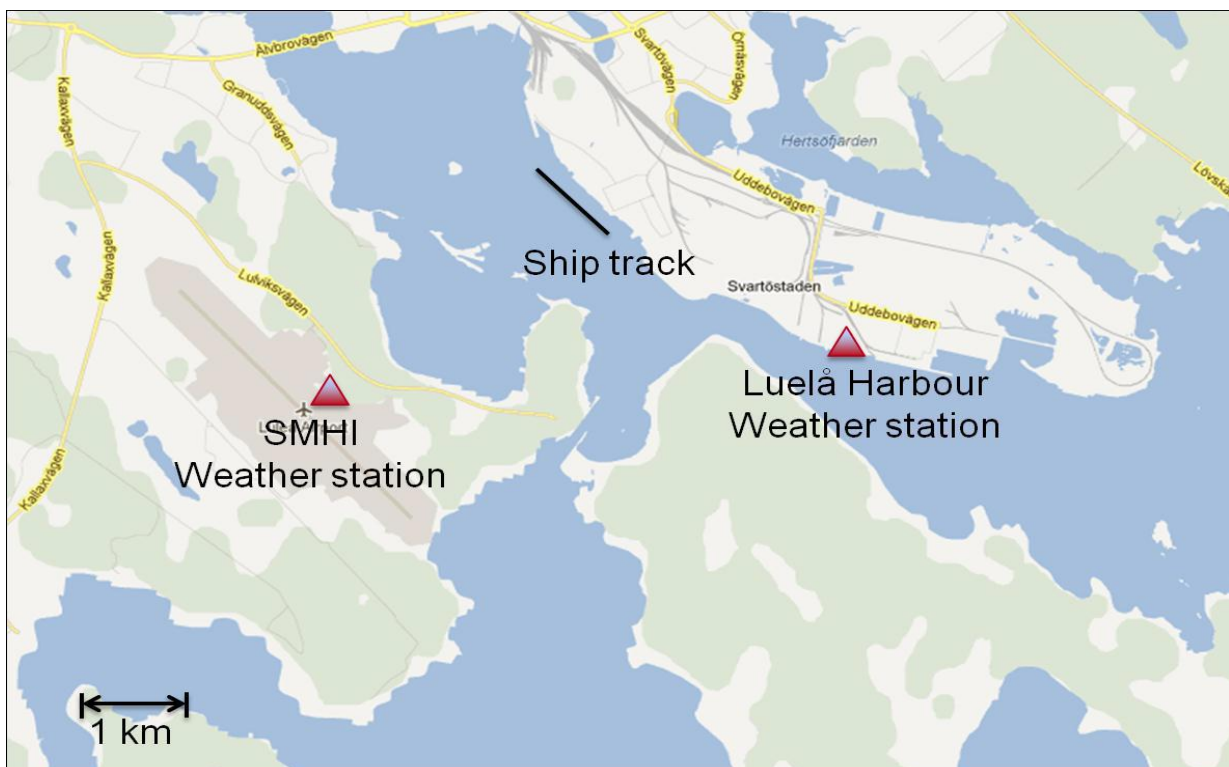


Figure 10-1 Location of measurements in Lulea. Image extracted from (Westerberg, 2013)

The exact times of the channel passages by Viscaria and the exact times of the brash ice channel measurements, are summarized in Table 10-1.

Table 10-1 Exact times of channel passages by Viscaria tugboat and exact times of brash ice channel measurements. Data collected from (Westerberg, 2013)

Channel Passage	Date and Time of Passage/ Time of Breaking Event	Brash Ice measurements in the channel	Date and Time of brash ice measurements
1	1/4/2013 13:00	1	07/01/2013 14:00
2	1/8/2013 11:00	2	14/01/2013 10:00
3	1/12/2013 23:00	3	21/01/2013 14:30
4	1/15/2013 23:00	4	28/01/2013 09:00
5	1/18/2013 18:45	5	04/02/2013 10:00
6	1/22/2013 20:20	6	11/02/2013 10:00
7	1/25/2013 12:00	7	18/02/2013 10:00
8	1/29/2013 9:00	8	25/02/2013 10:00
9	2/1/2013 21:45	9	04/03/2013 13:00
10	2/5/2013 11:37	10	11/03/2013 11:00
11	2/8/2013 14:30	11	18/03/2013 09:00
12	2/12/2013 22:30	12	25/03/2013 10:00
13	2/15/2013 19:40	13	01/04/2013 10:30
14	2/19/2013 19:20	14	08/04/2013 11:00
15	2/22/2013 10:00		
16	2/27/2013 0:00		
17	3/1/2013 17:45		
18	3/5/2013 11:50		
19	3/9/2013 14:00		
20	3/12/2013 13:30		
21	3/15/2013 16:00		
22	3/19/2013 13:30		
23	3/22/2013 13:15		
24	3/26/2013 11:00		
25	3/29/2013 16:15		
26	4/2/2013 16:40		
27	4/6/2013 22:40		
28	4/9/2013 11:40		
29	4/12/2013 9:00		
30	4/16/2013 11:00		

10.1.1 **Metocean data in Lulea**

Metocean data was collected from two weather stations, one in the harbour of Lulea and one in the airport (SMHI), see Figure 10-1. From the weather station of the Lulea harbour, in the period 03/01/2013-15/04/2013, variables measured include, the air temperature, the wind speed, the wind direction, the barometric pressure, and the relative humidity. The measurements were recorded at intervals of 10 minutes for all the variables. From the weather station of the airport, in the period 01/10/2012-15/04/2013 variables measured include, all the variables that were also measured by the harbour weather station mentioned above, and additionally measurements for short wave radiation, cloudiness and precipitation. The measurements from the airport weather station were recorded at intervals of the order of a few hours.

The most important Metocean data for the analysis presented in this study, are the data for the air temperature, wind speed, relative humidity, and short wave radiation. Time series plots for these metocean variables are presented below.

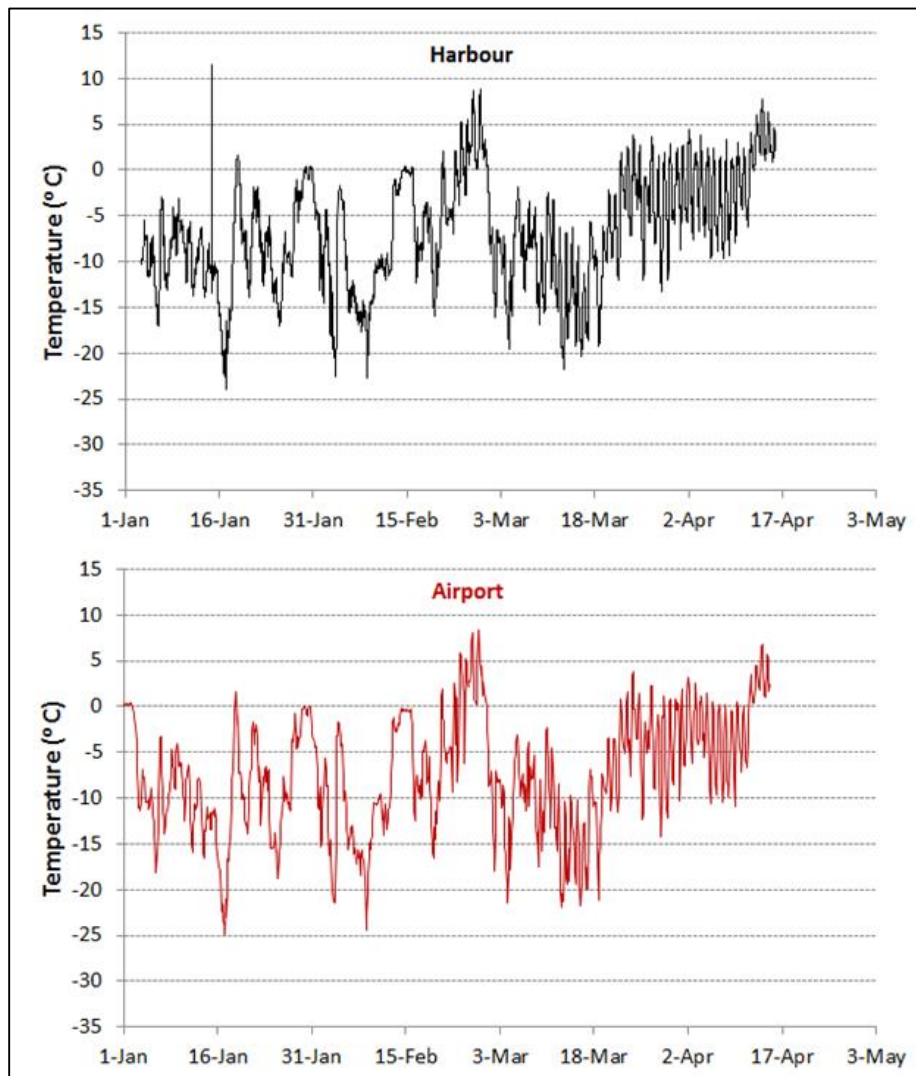


Figure 10-2 Time series plots of the air temperature, in the airport and harbour of Lulea

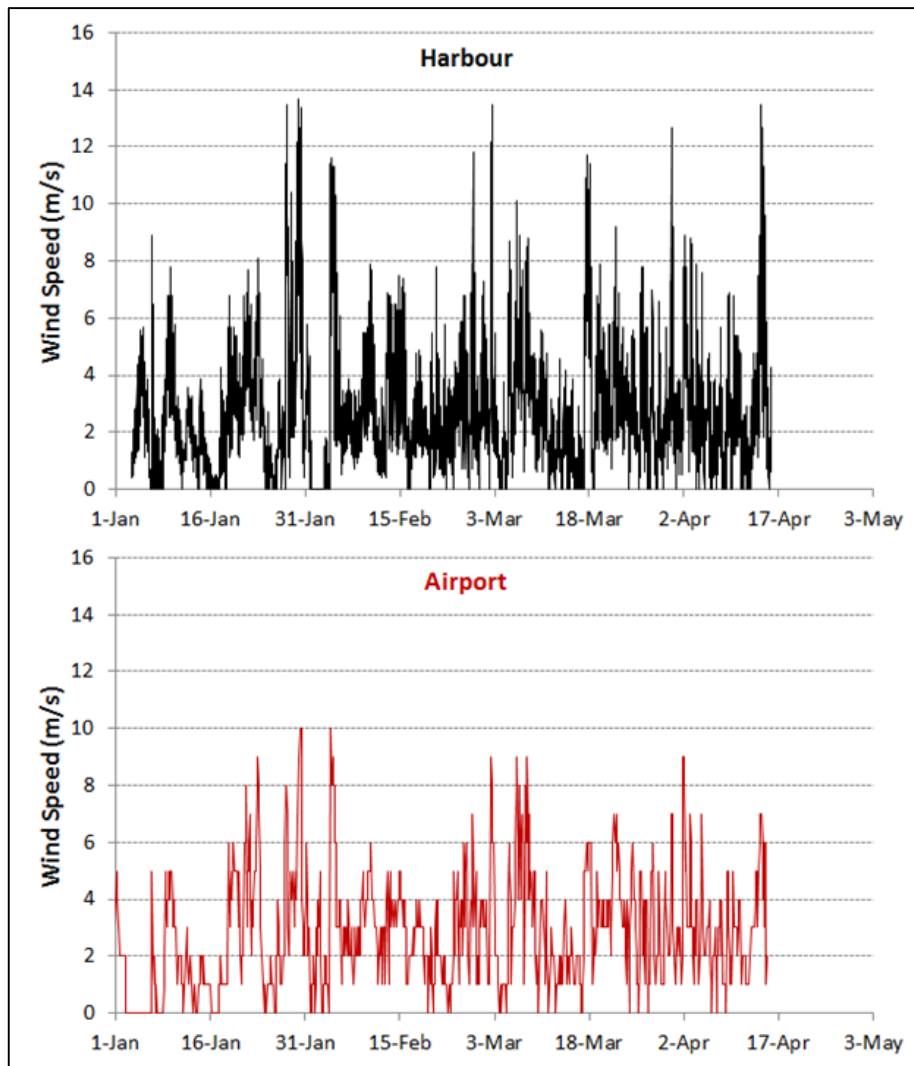


Figure 10-3 Time series plots of the wind speed, in the airport and harbour of Lulea

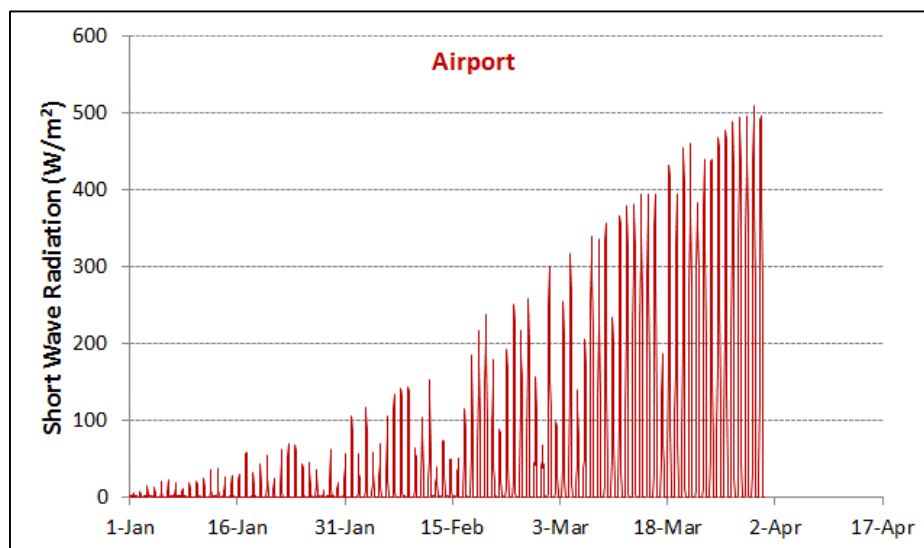


Figure 10-4 Time series plots of the short wave radiation, in the airport of Lulea

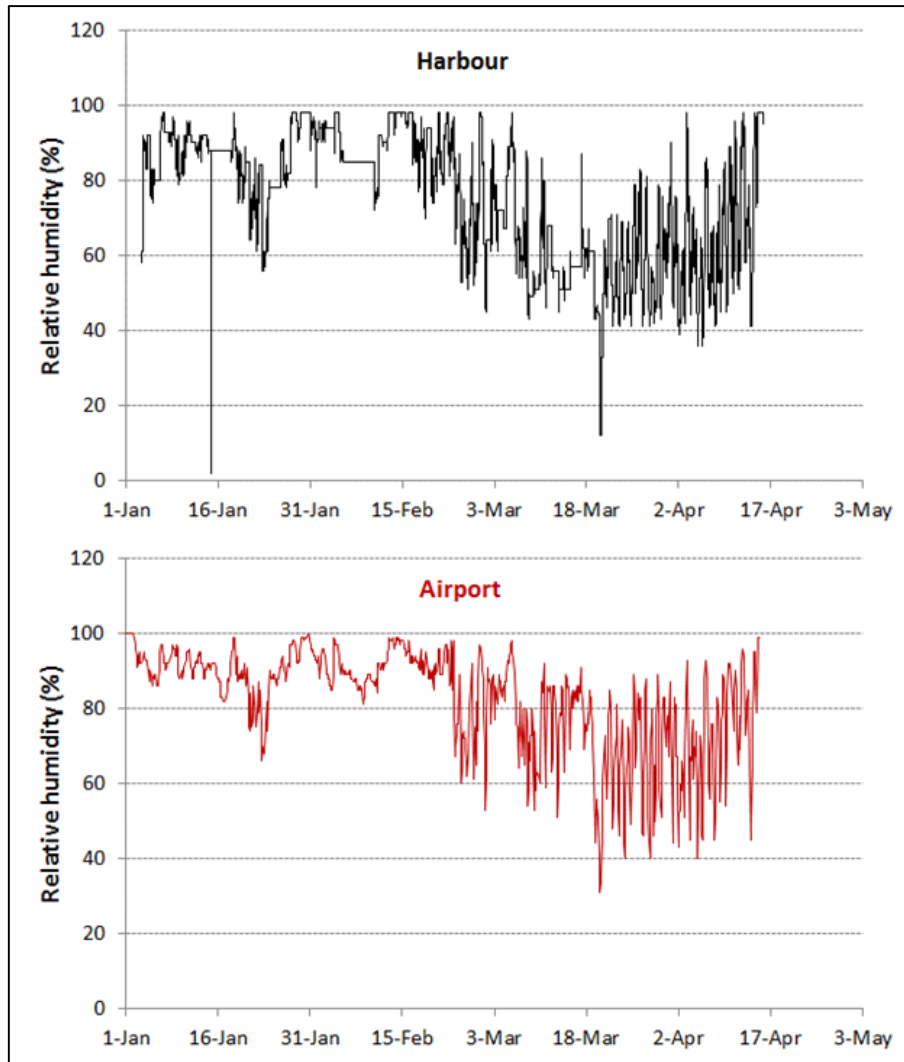


Figure 10-5 Time series plots of the relative humidity in the harbour and airport of Lulea

10.1.2 Brash Ice channel Measurements

In total 14 brash ice channel measurements have been performed, between 2013-01-07 and 2013-04-15, with one measurement being performed every week.

In order to determine the profile of the brash ice in the channel, during every measurement, an approximate number of 25 boreholes, was drilled perpendicularly to the heading to the channel, with a distance of 1m between each borehole, see Figure 10-6 and Figure 10-7. Figure 10-7 shows a simple plan of the ship track and the arrangement of the boreholes. The black crosses in Figure 10-7 correspond to the 25 boreholes drilled to determine the brash ice cross sectional profile, in 14 measurements. The red crosses correspond to the 18 (9+9) boreholes drilled, to produce 2 longitudinal brash ice profiles along the channel. All depths were recorded in cm and in relation to the waterline. Snow thickness and ice thickness above the waterline were reported as positive values, and the ones below the waterline were recorded as negative values.

Drilling regime through solid ice and slush ice or water (i.e. voids) was separated by the change of resistance while drilling. The depth of each drilling regime, and hence the depth/thickness of each ice regime, was measured and documented in a protocol, see Figure 10-8. Moreover, loose rubbles underneath the brash ice channel profile were also identified and documented in the borehole-profile of the tested channel, see Figure 10-9.

Finally, by the separation of different drilling regimes the proportion of slush ice or water in relation to solid ice could be determined which enabled the calculation of porosity at each borehole i.e. each drilling location, using Eq. (4-13). Note that these porosity measurements were one-dimensional, i.e. calculation of the proportion of the thickness of slush ice or water, in the total thickness which was composed from slush ice, water and solid ice.



Figure 10-6 Drilling of holes to determine brash ice channel profiles. Extracted from (Westerberg, 2013).

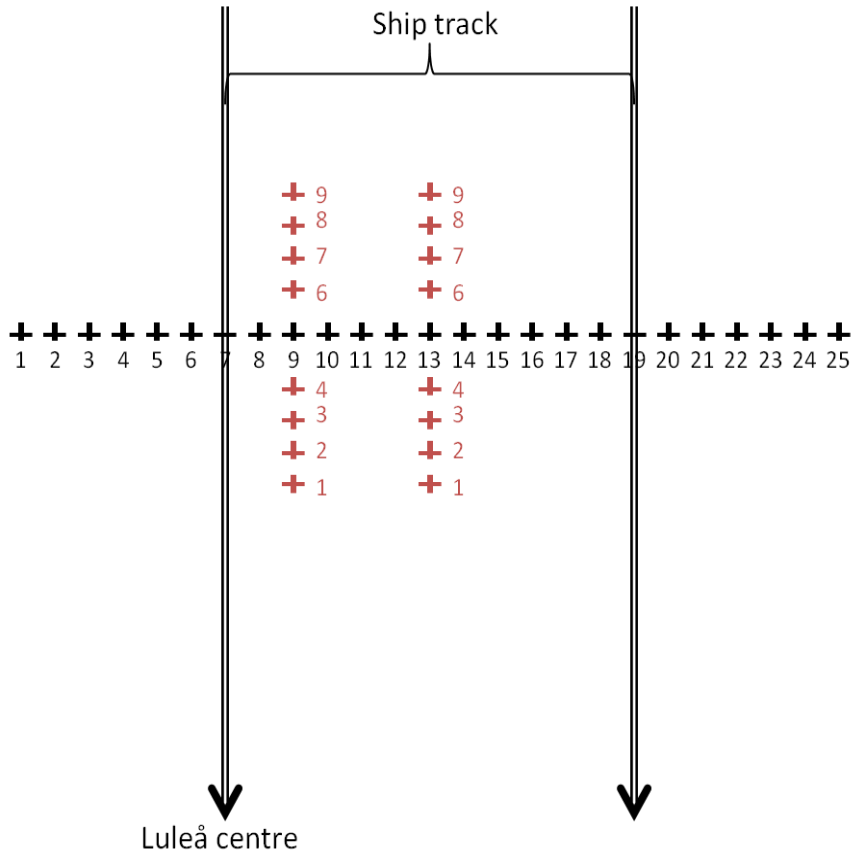


Figure 10-7 Simple plan of the ship track and the arrangement of boreholes. Extracted from (Westerberg, 2013). The numbering here does not correspond to the codes of the boreholes. For the code names of boreholes see Figure 10-8.

Mätningar: 04/02/2013													Land													Hav					
Mätpunkt	L6	L5	L4	L3	L2	L1	1	2	3	4	5	6	7	8	9	10	11	12	13	H1	H2	H3	H4	H5	H6						
Snö		25	20	26	25	25	35	12	7	18	5	2	3	4	4	14	6	5	6	50	29	29	28	28	23						
is		3	3	7	8	18	16	4	4	16	3	0	1	2	2	12	4	3	4	8	7	7	6	6	7						
is		0	0	0	0	0	0	0	0	0	0	0	0	0	0	0	0	0	0	0	0	0	0	0	0						
WL		1	2	3	4	5	6	7	8	9	10	11	12	13	14	15	16	17	18	19	20	21	22	23	24	25					
is		0	0	0	0	0	0	0	0	0	0	0	0	0	0	0	0	0	0	0	0	0	0	0	0						
Vatten		-51	-52	-55	-55	-54	-45	-10	-15	-35	-35	-42	-40	-10	-10	-21	-9	-8	-10	-43	-55	-58	-59	-55	-55						
is																															
Vatten																															
is																															
Vatten																															
is																															
Vatten																															
is																															
Vatten																															
is																															
Vatten																															
is																															
Vatten																															
is																															
Vatten																															
is																															
Vatten																															
is																															
Vatten																															
is																															
Vatten																															
is																															
Vatten																															
is																															
Vatten																															
is																															
Vatten																															
is																															
Vatten																															
is																															
Vatten																															
is																															
Vatten																															
is																															
Vatten																															
is																															
Vatten																															
is																															
Vatten																															
is																															
Vatten																															
is																															
Vatten																															
is																															
Vatten																															
is																															
Vatten																															
is																															
Vatten																															
is																															
Vatten																															
is																															
Vatten																															
is																															
Vatten																															
is																															
Vatten																															
is																															
Vatten																															
is																															
Vatten																															
is																															
Vatten																															
is																															
Vatten																															
is																															
Vatten																															
is																															
Vatten																															
is																															
Vatten																															
is																															
Vatten																															
is																															
Vatten																															
is																															
Vatten																															
is																															

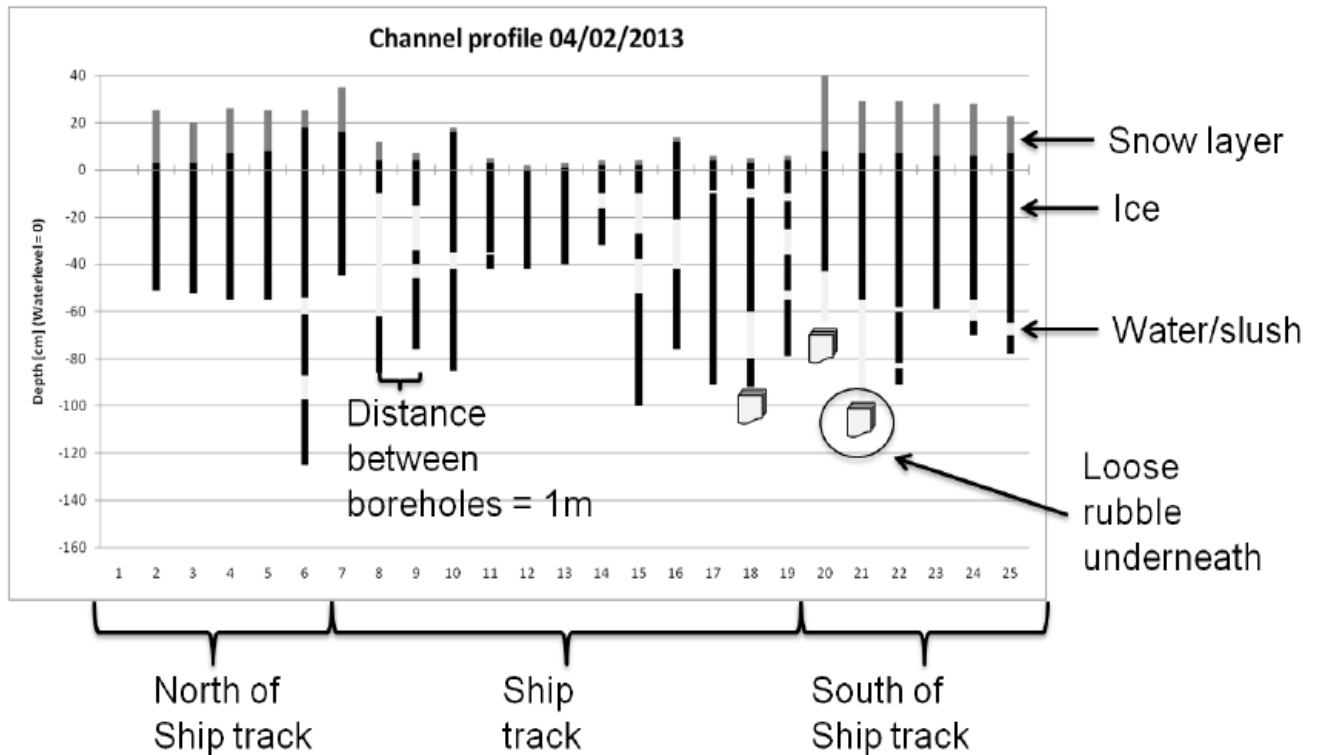


Figure 10-9 Brash Ice borehole-profile in the tested channel. Extracted from (Westerberg, 2013).

10.2 Analysis of the measurements

In (Westerberg, 2013), the boreholes and the data in each borehole were separated in 3 groups, see Figure 10-8. The groups and the boreholes within each group were as follows:

1. Channel/ship track boreholes: boreholes names 1-13
2. North of ship track boreholes: boreholes names L1-L6
3. South of ship track boreholes: boreholes names H1-H6

Moreover the ice/snow from the borehole-profiles, see Figure 10-9, documented in the protocols shown above, see Figure 10-8, was also separated in 3 groups, with each group having certain boreholes that defined the type of ice/snow within that group. The different groups of ice/snow were as follows:

1. Channel/ship track Ice: data from boreholes 1-13
2. Edge Ice: data from boreholes H1-H4 and L1-L4
3. Level Ice: data from boreholes H5-H6 and L5-L6

For each of the 3 groups of ice data above, in each of the 14 brash ice channel measurements, the average snow thickness, average ice thickness and average brash ice porosity were calculated. The quantities of interest here, regarding the scope of this study are the average ice thickness and the average brash ice porosity for the 3 groups of ice mentioned above. Collecting data from (Westerberg, 2013), it was possible to reproduce time evolution plots for these quantities, see Figure 10-10 and Figure 10-11.

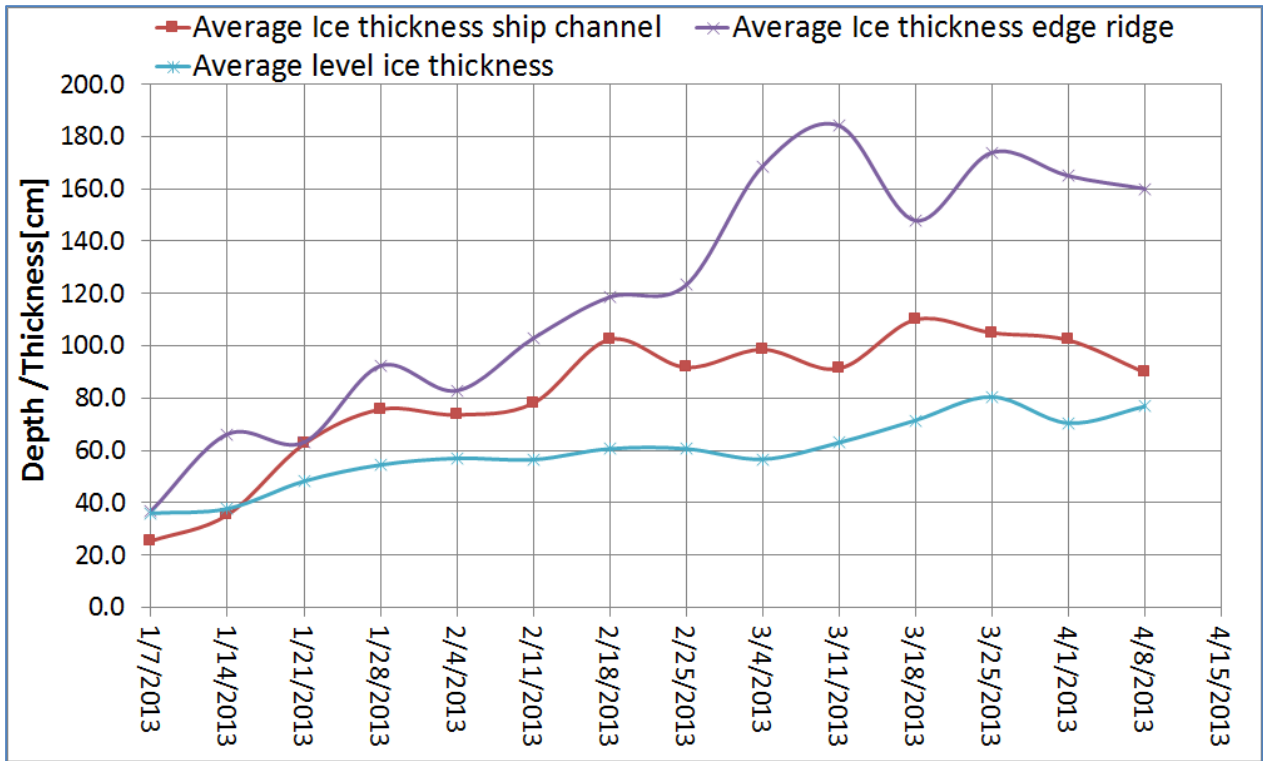


Figure 10-10 Summary of ice thickness measurements. Boreholes 1-13=Channel Ice, Boreholes H1-H4 and L1-L4= Edge Ice, Boreholes H5-H6 and L5-L6= Level Ice. Data extracted from (Westerberg, 2013).

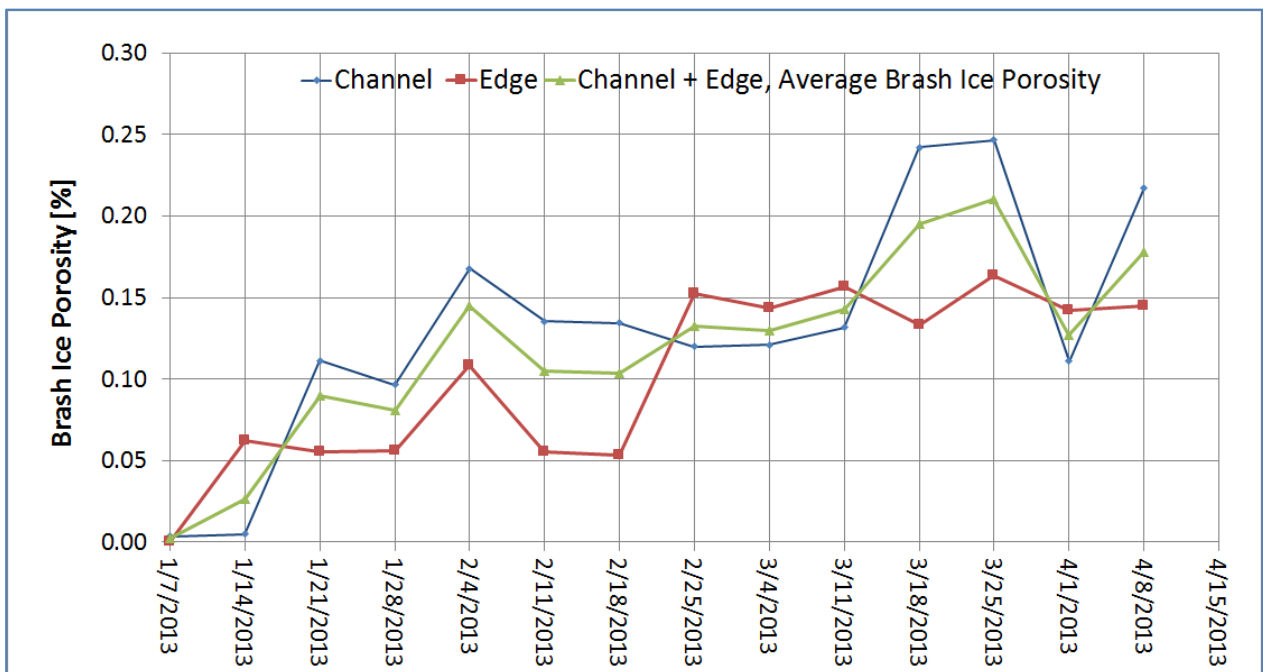


Figure 10-11 Summary of brush ice porosity measurements. Boreholes 1-13=Channel Ice, Boreholes H1-H4 and L1-L4= Edge Ice. The brush ice porosity measured from Level Ice=Boreholes H5-H6 and L5-L6, was zero in all the measurement and this is why no level ice plot is included in this graph. Data extracted from (Westerberg, 2013).

10.2.1 Plotting brash ice cross section profiles of the channel

Using the data from each of the 14 borehole-profiles of (Westerberg, 2013), as it is shown in Figure 10-8 and Figure 10-9, it was possible to produce 14 cross sections profiles of brash ice in the channel, in order to aid the purpose of this study which is the analysis of the brash ice field measurements and their comparison with the models' results. Additionally using data from the two series of boreholes along the channel, see Figure 10-7, it was possible to produce two longitudinal profiles for the specific sections of the channel. Before plotting these profiles it was decided to exclude the thickness of snow, which corresponds to the first line of numbers in the documented protocol, see Figure 10-8, and in the top gray parts of the lines in the borehole-profiles, see Figure 10-9. The reason for deciding this, is that although snow might act as a glue helping pieces of ice to stick together, is not part of the brash ice thickness. Therefore as the average thickness of brash ice, from the field measurements in Lulea, is going to be compared with the thickness of brash ice predicted from BIGM 1 and BIGM 2, developed in this study, snow thickness has to be excluded from the field measurements. As snow comes from the atmosphere, it is an external parameter in the ice growth process, and it is irrelevant with the ice breaking procedure in vessel transits. The dry brash ice calculated from BIGM 1 and BIGM 2, which consists of solid ice pieces floating, is produced from the ice breaking procedure, and its' thickness is determined from Archimedes' principle.

The cross sectional and longitudinal (along borehole 9) profiles of the channel, from the field data collected on the 25/03/2013, are shown below, in Figure 10-12 and Figure 10-13 respectively.

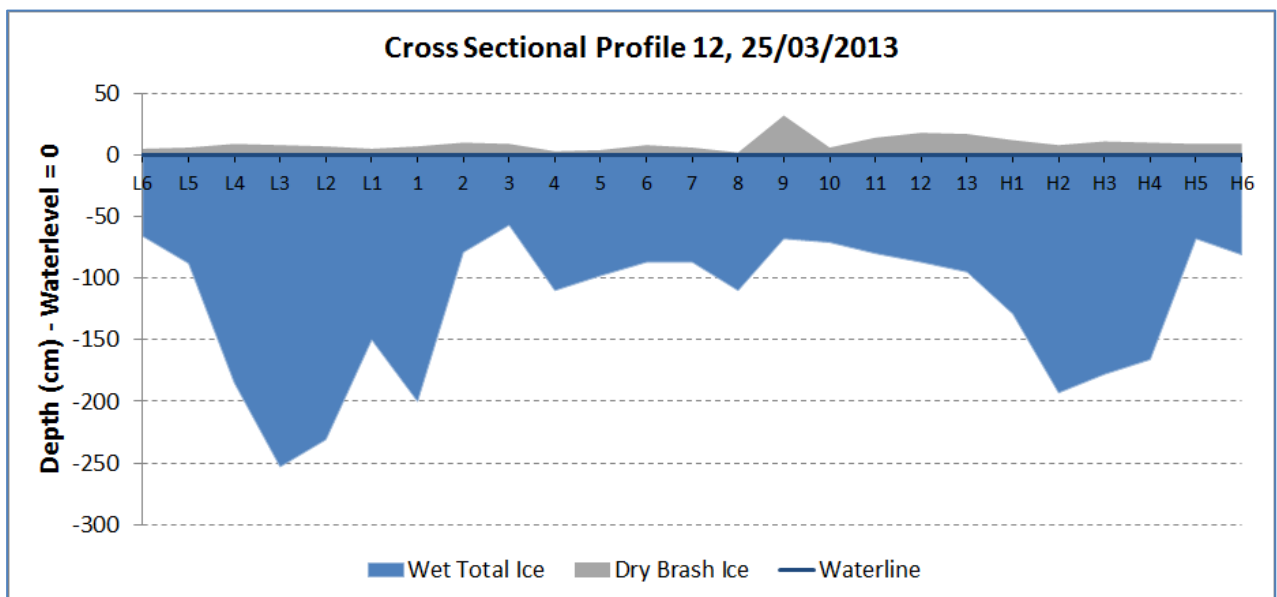


Figure 10-12 Cross sectional brash ice profile, plotted using field measurements from the 25/03/2013

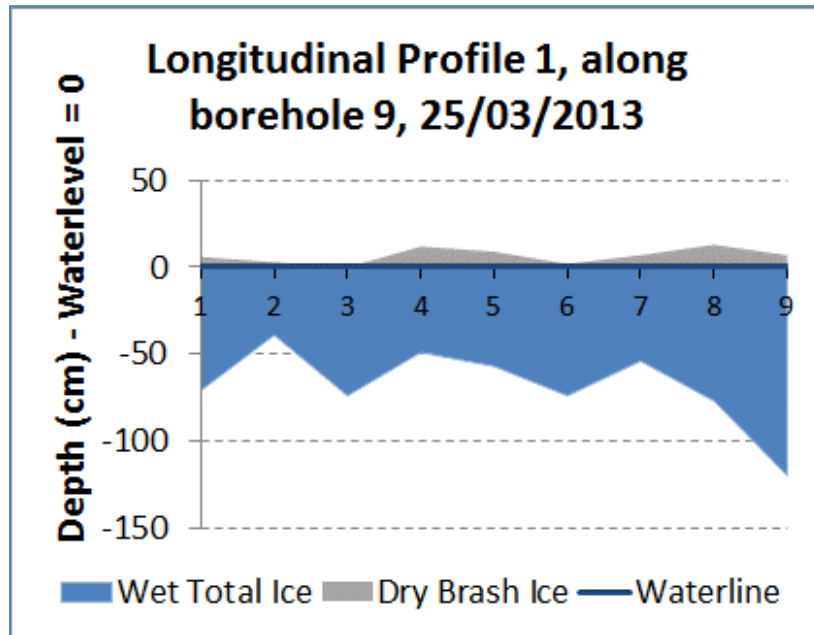


Figure 10-13 Longitudinal brash ice profile, plotted using field measurements from the 25/03/2013

All the cross sectional and longitudinal brash ice profiles can be found in appendix I.

10.2.2 Average total ice, total wet ice and dry brash ice thickness calculation

In order to allow comparison between the results of the developed models, BIGM 1 and BIGM 2, and the field measurements, characteristic average ice thickness values of the channels should be calculated. As the ship track is 12m, since the Viscaria ice breaker tug had a beam of 12m, the average thickness that should be compared with the theoretical models results, is the average thickness calculated between boreholes 1 and 13, see Figure 10-12, as these are the boreholes at the edges of the ship track. However, in order to illustrate how average ice thicknesses across the channel change, as the width from the center of the channel increases or decreases, average thicknesses for different channel widths were calculated and plotted, see Figure 10-14 and Figure 10-15. Figure 10-14 shows examples of different channel widths across which average total ice thickness values were calculated i.e. $CW_1 = 2m$, $CW_2 = 4m$, $CW_3 = 6m$, $CW_4 = 8m$, $CW_5 = 10m$, $CW_6 = 12m$. The area of the ice channel profile included within each of these widths was calculated using the trapezium rule, and the corresponding average ice thickness to that area was calculated by simply dividing it with the corresponding channel width to which the area is included. Average thicknesses of the total ice (Wet total ice + dry brash ice), wet total ice, and dry brash ice were calculated for the widths mentioned above and also for some other additional widths. The plots of these average thicknesses are shown in Figure 10-15, Figure 10-16 and Figure 10-17 respectively.

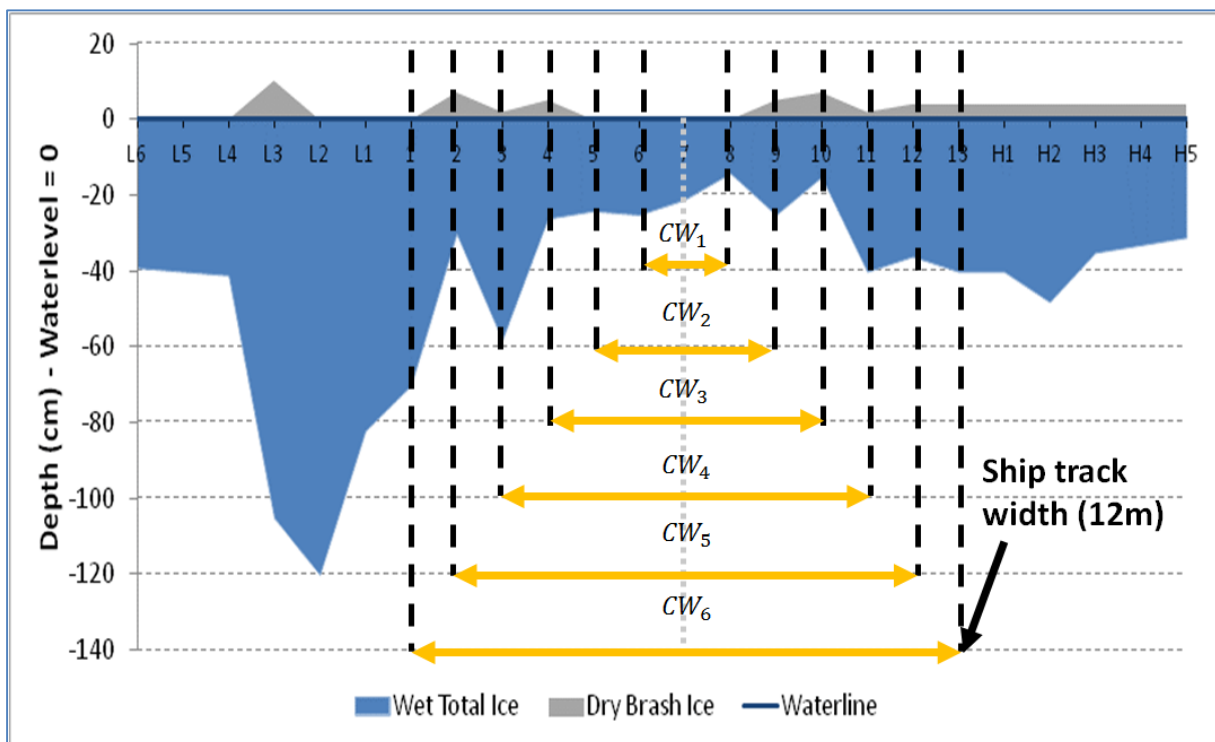


Figure 10-14 Method used for calculation of the average total ice thickness, average total wet ice thickness, and average dry brash ice thickness across different widths of the channel.

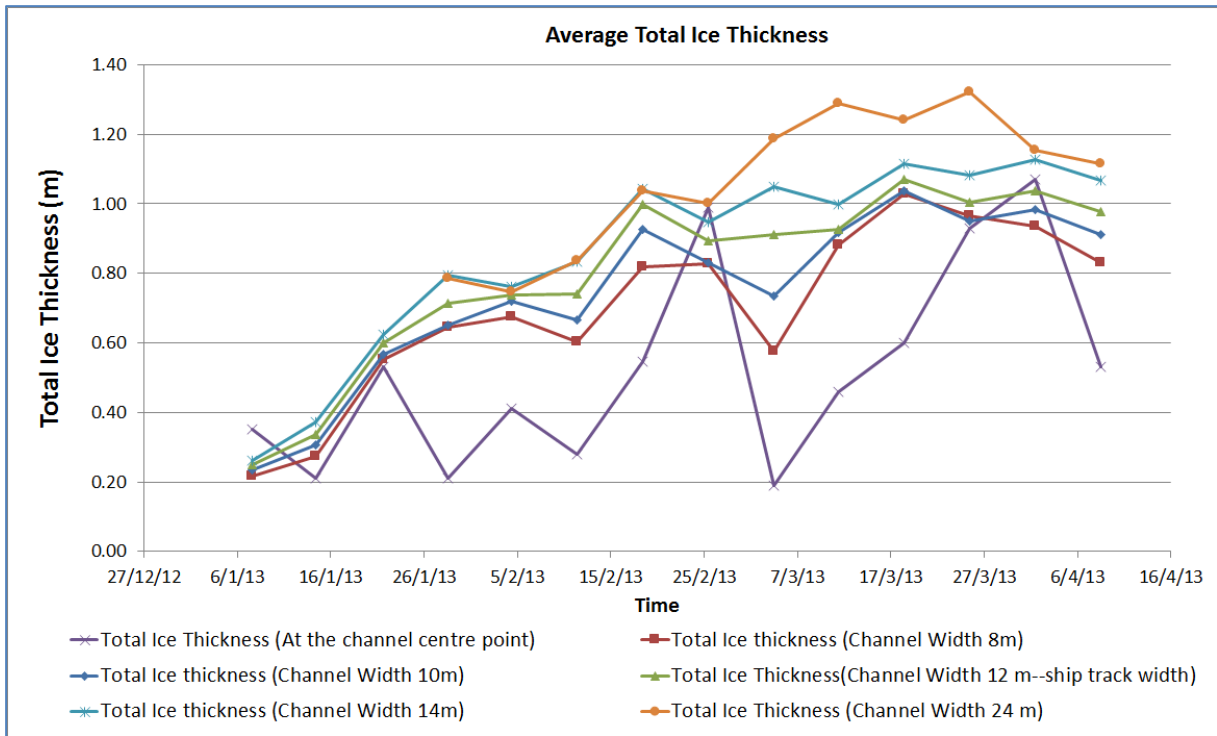


Figure 10-15 Average total Ice thickness for difference widths across the channel.

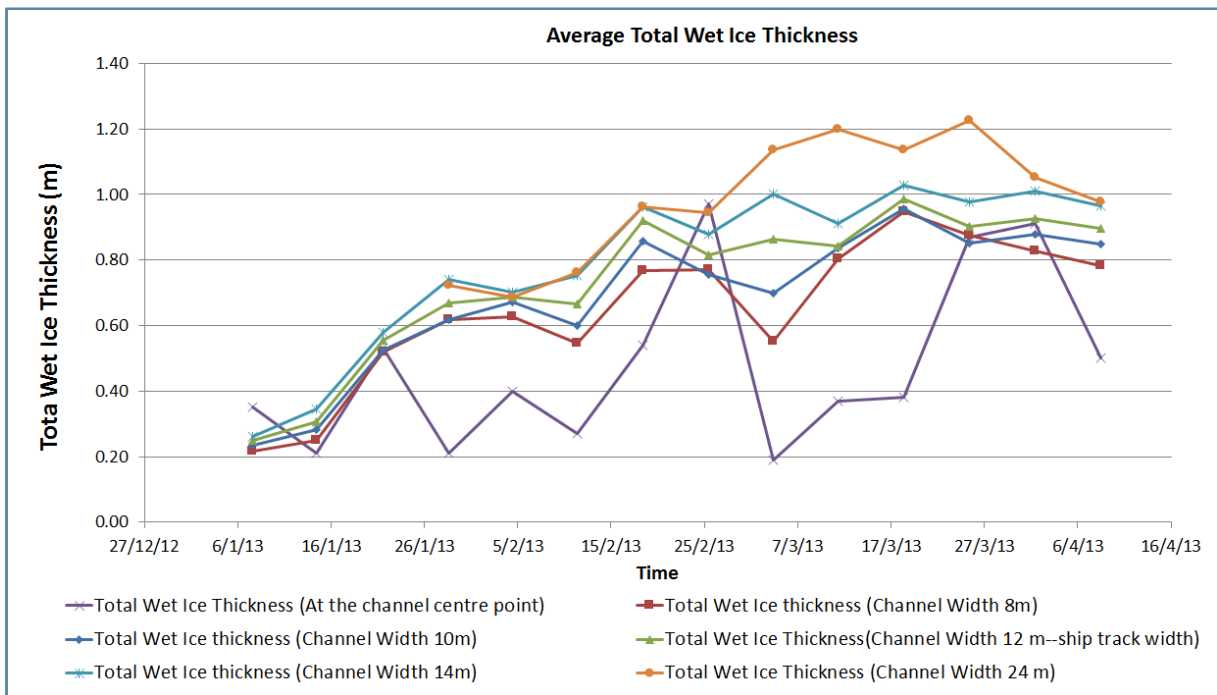


Figure 10-16 Average total wet Ice thickness for different widths across the channel.

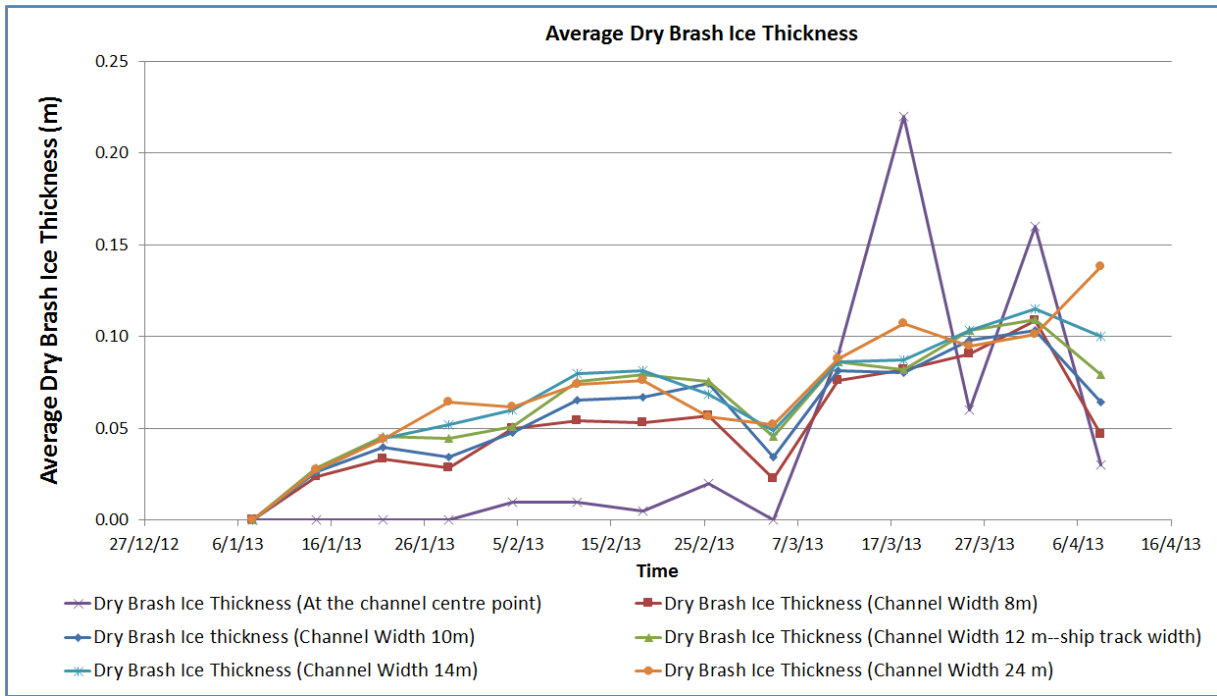


Figure 10-17 Average dry brush ice thickness for different widths across the channel

10.2.3 Concept of horizontal motion

Since the theoretical models developed in this study calculate the so called “equivalent brush ice” thickness defined by Sandkvist, see Figure 2-10, which assumes that all the brush ice is included within the ship track transited by the vessel, the average ice thickness plots shown in the previous section need to be adjusted so that all the ice is included within the track. Hence, in order to transform the average ice thickness plots into “equivalent ice thickness plots”, all the amount of ice that is outside of the ship track, has to be included within the ship track width, see Figure 10-18, except from the amount of ice that is assumed to be level ice or ice cover, see Figure 2-5 and Figure 10-18.

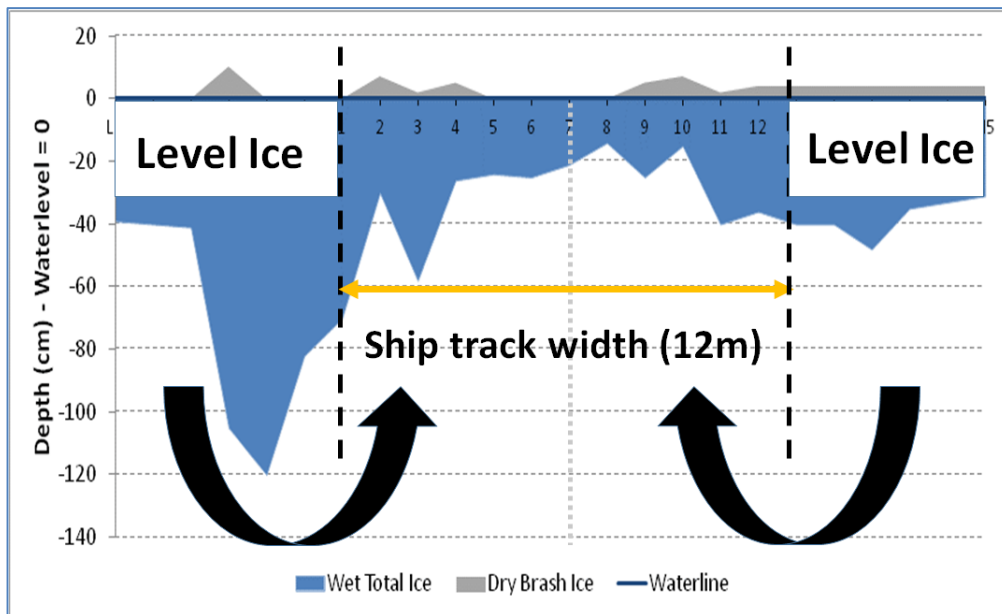


Figure 10-18 Creating equivalent ice thickness plots from the field data for comparison with the models’ results

The average level ice thickness at each brush ice channel measurement can be seen in Table 10-2 at the end of this section, and its evolution is plotted in Figure 10-10. However the distance from the level ice inner edge to the edge of the track cannot be determined with certainty. In Figure 10-18, the level ice is shown to be extended from the far edges of the channel to the edges of the ship track, following the typical cross section of a channel filled with brush ice as this was presented by (Ettema & Huang, 1990), see Figure 2-5. However the distance of the level ice inner edge from the edge of the ship track can be 1 m, 2m or even greater sometimes. Therefore in creating “equivalent ice thickness” plots, the distance of the level ice inner edge from the edge of the ship track was varied between 0-2m., see Figure 10-18. Equivalent ice thickness plots were calculated for the total ice thickness and for the dry brush ice thickness, and are shown in Figure 10-19 and Figure 10-20, respectively.

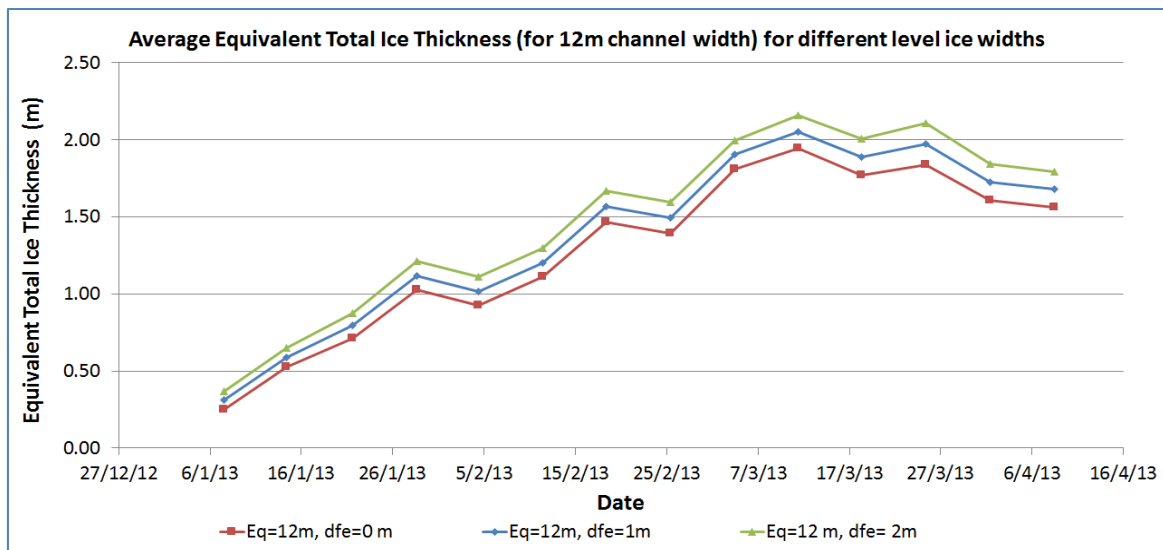


Figure 10-19 Equivalent total ice thickness plots for 12m channel width, for level ice distance from edge (DFE) of ship track, 0,1 and 2m.

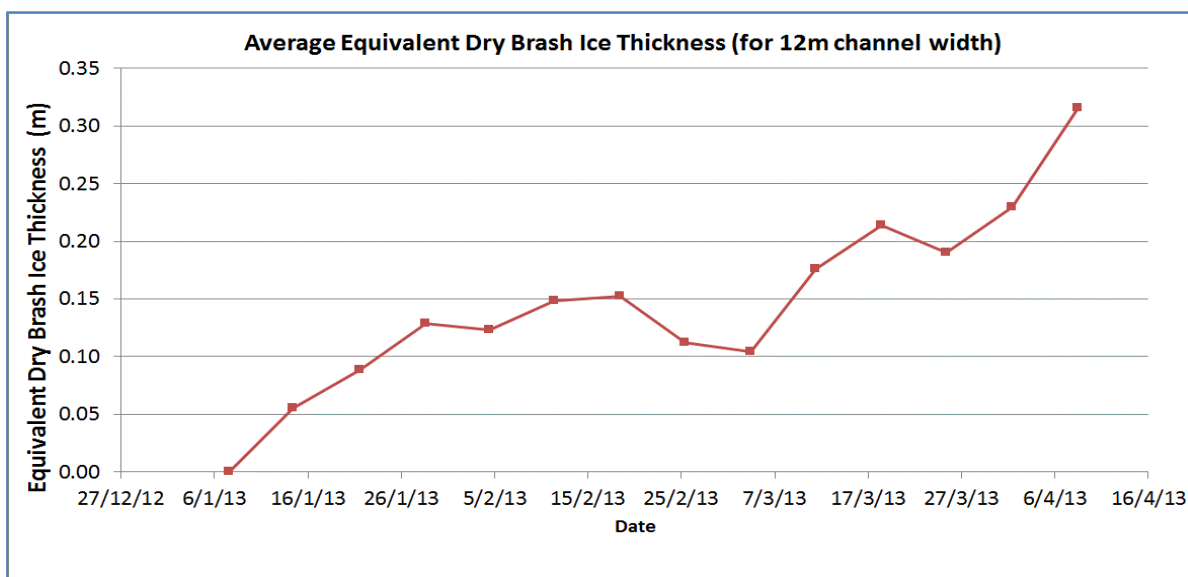


Figure 10-20 Equivalent dry brush ice thickness plot for 12m channel width. DFE was taken as zero.

Table 10-2 Table showing the estimated level ice thickness at each of the measurements

Cross sectional Profiles	Dates	Level Ice thickness in (cm)
1	7/1/13 14:00	36
2	14/1/13 10:00	37.8
3	21/1/13 14:30	48.3
4	28/1/13 14:30	54.5
5	4/2/13 10:00	57
6	11/2/13 10:00	56.5
7	18/2/13 10:00	60.7
8	25/2/13 10:00	60.7
9	4/3/13 10:00	56.7
10	11/3/13 9:00	63
11	18/3/13 9:00	71.5
12	25/3/13 10:00	80.5
13	1/4/13 10:30	70.5
14	8/4/13 10:30	76.8

10.2.4 Estimation of the amount of ice that has moved outside the channel track

According to (Saarinen, Suojanen, & Eranti, 2011), typically half of the brash ice is pushed to the side ridges in the shipping tracks, and in general out of the shipping track. In this study, the proportion of ice that has moved out of the shipping track was estimated for the Lulea brash ice field measurements, using the borehole- profiles from (Westerberg, 2013) and the cross section profiles plotted in this study, shown in section 10.2.1 and in appendix I. The proportion a_{pushed} was calculated for each channel measurement profile, by dividing the area of brash ice outside of the track (outside of the 12m), excluding the level ice, with the total area of brash ice in the channel profile. This was done for three possible different distances of the level ice edge from the edge of the ship track, (0m, 1m, 2m), as it was also done for the creation of the “total ice equivalent” plots. Plots of the a_{pushed} coefficient for the 12m ship track width, using the three possible level ice distances (DFE), are shown in Figure 10-21. Assuming that level ice extends up to the edge of the ship track, as (Ettema & Huang, 1990) and Figure 2-5 suggests, an average a_{pushed} coefficient of 0.36 was estimated, see green line in Figure 10-21.

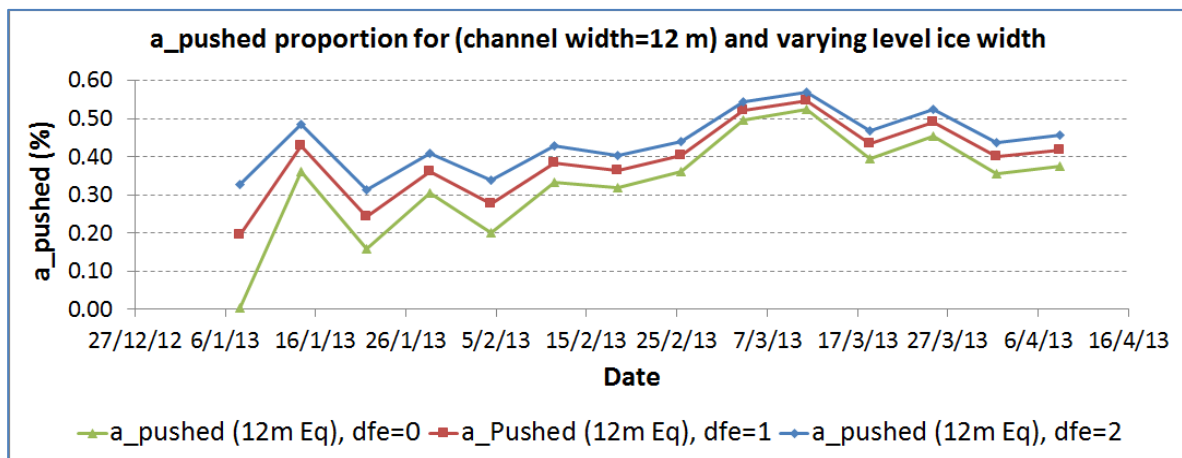


Figure 10-21. Plots of the proportion a_{pushed} , of ice that has moved outside of the shipping track (12m width), in each brash ice field measurement, for different distances (DFE) of the level ice inner edge from the ship track edge.

11. Validation of the developed BIGM models, with Lulea Brash Ice field measurements

11.1 Comparison of the calculated and measured values

In this section, the two solutions of a brash ice growth model, BIGM 1 and BIGM 2, developed and presented in the previous sections of this study, are going to be tested and validated using the brash ice field measurements done in the port of Lulea, discussed in section 10. In order to do that, comparison between the results that the two models give, when they take as input the same environmental conditions at the time the field measurements were performed, and the actual field measurements has to take place. To aid this comparison and make it as pragmatic as possible, the two models/solutions should take as input a number of data, such as:

1. A list of the exact times that the Viscaria tugboat has crossed the tested channel, hence causing a breaking event, see Table 10-1 and Table 11-1.
2. An estimate of the air temperature at the time of the breaking event, see Table 11-1. The air temperature is a basic and essential input/parameter of any ice growth model and hence any Brash Ice Growth model, see sections 3, 4, 5 and 6.
3. An estimate of the wind velocity at the time of the breaking event, see Table 11-1. The wind velocity determines the value of the thermal convective coefficient, see Equations (5-6) and (9-1). Therefore at each breaking instant a different a wind velocity value, would give a different thermal exchange coefficient.
4. An estimate of the porosity of brash ice just after a breaking event, see Table 11-1. Brash ice porosity is an essential input/parameter of any brash ice growth model, see section 7.
5. An estimate of short wave radiation (solar radiation) at the time of a breaking event, see Table 11-1. Short wave radiation is an important component of the flux balance on the top surface of ice (or dry brash ice), see section 5.2. The set of short wave radiation values can only be used by BIGM 2, which can take into account the exact top surface boundary condition, see section 6.
6. An estimate of the relative humidity at the time of a breaking event, see Table 11-1. The relative humidity, determines the latent heat flux exchange at the top surface of ice (or dry brash ice), see Eq. (6-37). Again relative humidity values would only be used by BIGM 2 which takes into account the latent heat flux exchange.
7. An estimate of the long wave radiation at the time of a breaking event, see Table 11-1. Long Wave radiation is usually one of the most important components of the flux balance on the top surface, see section 5.2. As in the case of short wave radiation values, the set of long wave radiation values would only be used by BIGM 2, which takes into account the exact top surface boundary condition.

The list of the exact times that the tested channel was transited, was directly provided from, (Westerberg, 2013). However in order to obtain sets of metocean data at the exact times of breaking events, the raw metocean data in the period between (1st of January-15th of April) from the two

metocean measurements' locations, Lulea Harbour and Lulea Airport, had to be used. From the list of the required input metocean data mentioned above, there were available data for the air temperature, the wind velocity, the short wave radiation and the relative humidity. Time series plots of these raw data are presented in section 10.1.1.

Furthermore the raw data files (1 from the airport and 1 from the harbour), for each of these metocean variables, were used first, to obtain average values of the metocean variables corresponding to each of the 30 instants of breaking events, at each of the measurement locations. The final input set, for each of the metocean variables, was obtained by calculating the mean values, from the average set obtained from the measurements at the airport and the average set obtained from the measurements at the harbour. The final input average sets for the air temperature, the wind speed, the relative humidity and the short wave radiation are presented in Table 11-1.

Regarding the long wave radiation, unfortunately, there was no available field measurements about this metocean component, although, as it is described in (Westerberg, 2013), it was initially planned to collect measurements about long wave radiation as well. In order to include the long wave radiation effect in the simulations (BIGM 2), due its' important impact on solid ice growth, as this was explained in section 5, it was decided to use the monthly average values from (Maykut & Untersteiner, 1971), as it was done in the reference case for Sabetta as well. Therefore an input long wave radiation value was assigned to each breaking instant depending in which month this breaking instant took place. Hence values for long wave radiation for January, February, March and April from the (Maykut & Untersteiner, 1971) set, see Table 8-2, were used to form the 30-values input set, see Table 11-1.

Regarding brash ice porosity, there were 14 estimates of the average brash ice porosity across the whole channel (ship track+ edges), from the 14 brash ice field measurements, see Figure 10-11. Assuming that porosity remained constant between breaking events, these 14 values were used to form the 30 value input set for brash ice porosity, see Table 11-1.

Table 11-1 Data set used for validation. Data for the “Lulea reference simulation case”

Channel Passage	Time of Breaking Event	Temp (Celsius)	Wind Set Summary (m/s)	Short Wave Radiation (W/m^2)	Long Wave Radiation (W/m^2) from MU71	Porosity	Relative Humidity (%)
1	1/4/2013 13:00	-8.15	1.85	2.15	167.88	0.02	0.87
2	1/8/2013 11:00	-10.45	2.22	2.68	167.88	0.03	0.88
3	1/12/2013 23:00	-8.04	2.64	3.62	167.88	0.03	0.89
4	1/15/2013 23:00	-10.34	1.44	4.52	167.88	0.09	0.89
5	1/18/2013 18:45	-16.18	0.78	5.99	167.88	0.09	0.88
6	1/22/2013 20:20	-5.41	3.68	6.75	167.88	0.08	0.79
7	1/25/2013 12:00	-9.77	3.06	9.65	167.88	0.08	0.72
8	1/29/2013 9:00	-9.20	2.53	4.73	167.88	0.15	0.86
9	2/1/2013 21:45	-3.07	4.26	10.97	166.26	0.15	0.95
10	2/5/2013 11:37	-10.30	2.29	12.83	166.26	0.10	0.95
11	2/8/2013 14:30	-13.59	2.50	22.59	166.26	0.10	0.85
12	2/12/2013 22:30	-12.89	2.66	19.95	166.26	0.10	0.85
13	2/15/2013 19:40	-2.84	3.64	12.57	166.26	0.10	0.96
14	2/19/2013 19:20	-5.40	2.29	31.18	166.26	0.13	0.91
15	2/22/2013 10:00	-7.66	2.04	33.23	166.26	0.13	0.87
16	2/27/2013 0:00	-1.68	2.54	48.03	166.26	0.13	0.77
17	3/1/2013 17:45	-2.18	3.13	43.47	166.26	0.13	0.73
18	3/5/2013 11:50	-11.20	2.55	47.52	166.26	0.13	0.73
19	3/9/2013 14:00	-8.09	4.07	73.10	166.26	0.14	0.65
20	3/12/2013 13:30	-9.60	2.19	83.10	166.26	0.14	0.62
21	3/15/2013 16:00	-14.23	1.63	111.68	166.26	0.19	0.53
22	3/19/2013 13:30	-13.42	2.98	93.71	166.26	0.19	0.60
23	3/22/2013 13:15	-6.93	3.52	119.71	166.26	0.21	0.49
24	3/26/2013 11:00	-2.86	2.94	125.98	166.26	0.21	0.55
25	3/29/2013 16:15	-3.89	2.87	167.53	166.26	0.13	0.58
26	4/2/2013 16:40	-3.03	2.78	182.53	187.25	0.18	0.60
27	4/6/2013 22:40	-2.98	3.06	197.53	187.25	0.18	0.58
28	4/9/2013 11:40	-4.61	1.62	212.53	187.25	0.18	0.59
29	4/12/2013 9:00	-2.54	2.50	227.53	187.25	0.18	0.70
30	4/16/2013 11:00	-0.50	3.14	242.53	187.25	0.18	0.78

11.1.1 Results with BIGM 1 (Reference Case: Input temperature, wind, and porosity sets from Table 11-1)

In this section, the basic results for a reference case, with BIGM 1 are going to be presented. The model takes as input the sets of values from Table 11-1, for the temperature, the wind velocity and the porosity. Radiation values and relative humidity values, cannot be included in BIGM 1. Figure 11-1 shows the evolution of the total ice thickness with BIGM 1, for both the cases of having and not having a dry brash ice layer on top of the solid ice layer. In addition it includes two field measurement plots: 1) the total ice average plot within the ship track (12m width) and 2) the equivalent total ice average plot within the ship track, which assumes that all the ice in the cross section of the channel, apart from the level ice, is included in the ship track (12m width), see section 10.2.3. BIGM 1 with bare solid ice gives a total ice thickness, in the end of the cold season, of about 1.67m and BIGM 1 with the inclusion of a dry brash ice (dbi) layer on top, gives a total ice thickness of about 1.4m. Note that both the total ice evolution plots (with dbi and without dbi) are approximately included in the interval between the two total ice field measurement plots [(H_{av}) total] and [Equivalent H_{av} total].

Figure 11-2 shows the variation of the top surface temperature, for the reference case, for both the situations of having and not having a dry brash ice layer. As it can be observed the top surface temperature is very similar in both cases. The slight differences are due to the different thermal conductivity value of the solid ice and the dry brash ice. The top surface temperature in the bare solid ice case, appears to have slightly colder temperatures between January and March, but this reverses in the period between March and end of April.

In general, the observations from the simulations with BIGM 1 using the Lulea field data, are as expected, and they verify the observations, in terms of BIGM 1 characteristics, that were also observed in the Sabetta reference case.

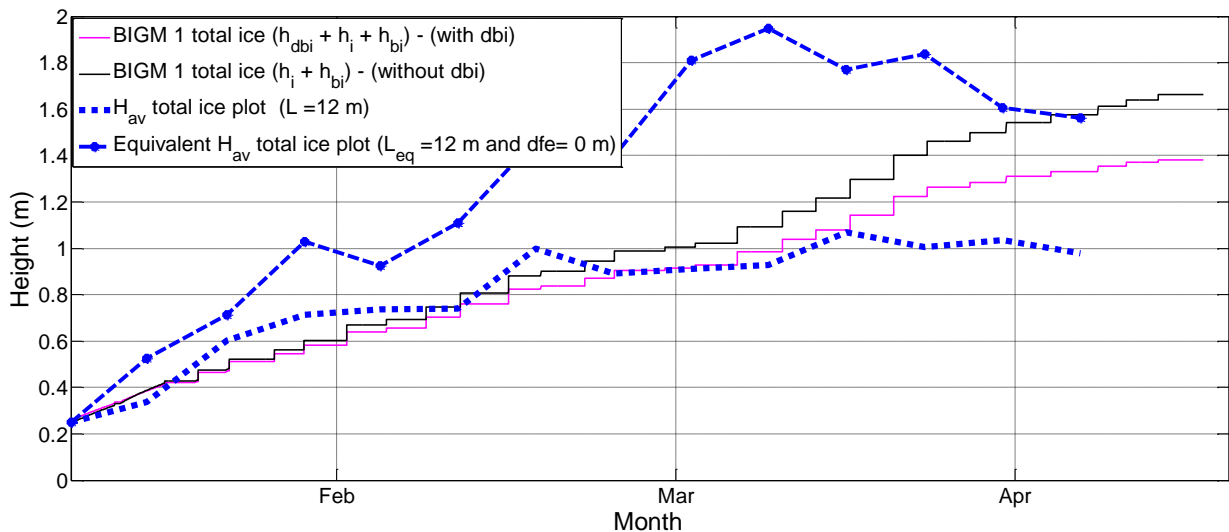


Figure 11-1 Reference case BIGM 1. Cases with and without dry brash ice (dbi) are included. Field measurement plots of the average total ice across the channel and of the equivalent total ice average across the channel are also plotted.

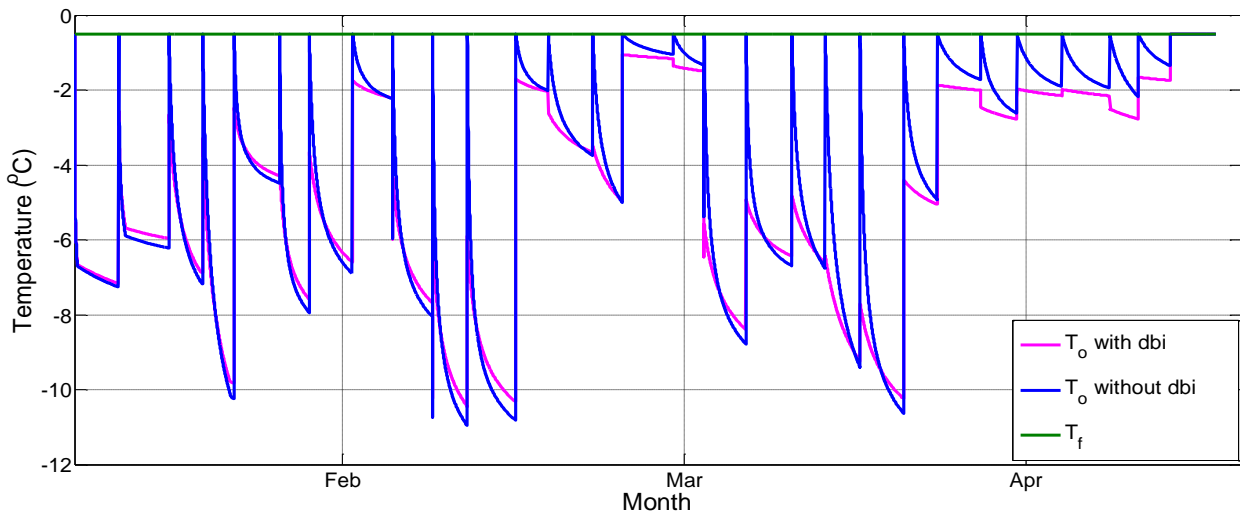


Figure 11-2 Reference case BIGM 1, Plots of the top surface temperature for the cases with and without dry brush ice.

11.1.2 Results with BIGM 2: (Reference Case Input temperature, input wind, input porosity, input radiation sets from Table 11-1). Surface albedo used is 0.64.

This section presents the results for a reference case using BIGM 2. The reference case for BIGM 2 includes the data input used in the reference case for BIGM 1 and additionally data input for the radiation, long wave and short wave, with the use of a surface albedo of 0.64.

Figure 11-3, shows the evolution of the total ice thickness with BIGM 2, for both the cases of having and not having a dry brush ice layer on top of the solid ice layer. Again the two field measurement plots, average and equivalent average total ice plots, are included for comparison. BIGM 2 with bare solid ice gives a total ice thickness, in the end of the cold season, of about of 2.3m and BIGM 2 with the inclusion of the dry brush ice layer on top, gives a total ice thickness of about 1.85m. Figure 11-3, shows that the total ice evolution plots (with dbi and without dbi) with BIGM 2 are better included in the interval between the two total ice field measurement plots, $[(H_{av})_{total}]$ and $[Equivalent H_{av} total]$, than the corresponding ones with BIGM 1.

Figure 11-4, shows the evolution of dry brush ice with BIGM 2 for the reference case, together with the plots of the [average dry brush ice thickness] within the ship track (12m width) and the [average equivalent dry brush ice plot] within the ship track. The model's plot is once more, between the two field measurement plots. At the end of the cold season, a dry brush ice of thickness 16cm is predicted by the model for the reference case, which is much closer to the average dry brush ice plot from the field, than the equivalent dry average one, see Figure 11-4.

Figure 11-5 and Figure 11-6 show the temperature profiles for the cases of "having" and "not having a dry brush ice layer", for the reference case with BIGM 2. Once more, it is observed that the top surface temperatures for these two situations have almost identical values. Moreover, it is observed that the solid ice layers ($T_{i_1} - T_{i_5}$), have a bit higher/hotter temperatures, of the order of $1 - 2^{\circ}C$, in the case of the inclusion of a dry brush ice layer. This, once more indicates the insulating effect of the dry brush ice layer, in the growth of solid ice and in the evolution of brash ice thickness in general. The dry brush ice, keeps the solid ice mass at higher temperatures and this decreases the growth rate of the solid ice thickness.

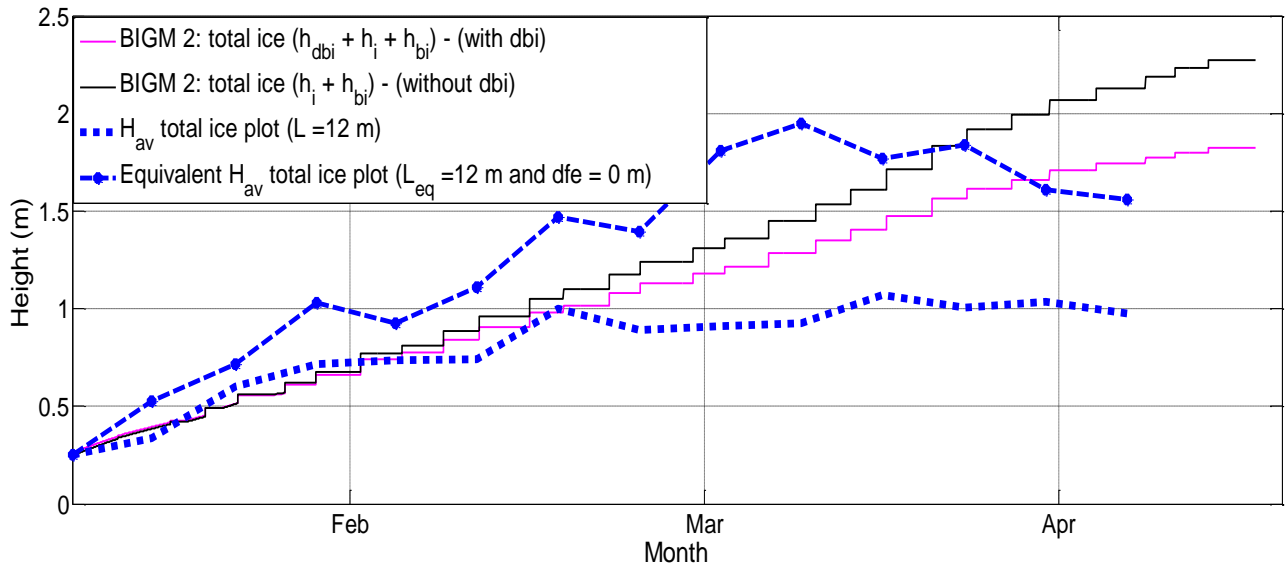


Figure 11-3 Reference Case for BIGM 2 for "with" and "without dry brush ice" cases

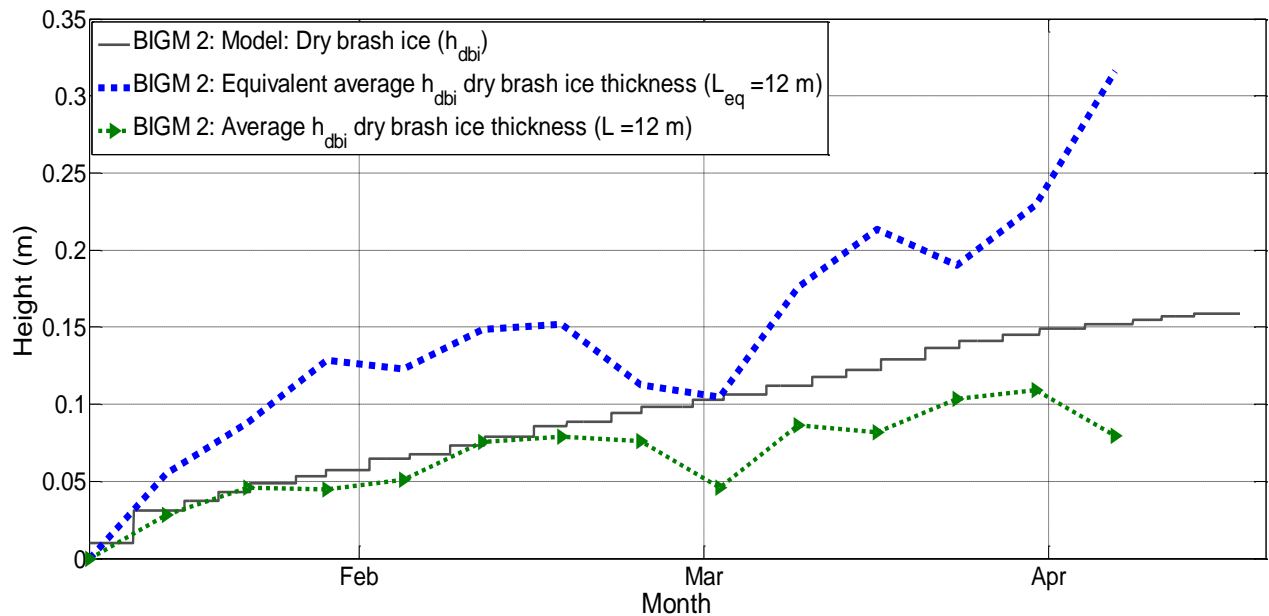


Figure 11-4 Dry brush ice evolution for BIGM 2 (with dry brush ice in the formulation). Also the average dry brush ice plot in the 12m of the ship track from the field measurements, and the average equivalent dry brush ice plot in the 12m of the ship track.

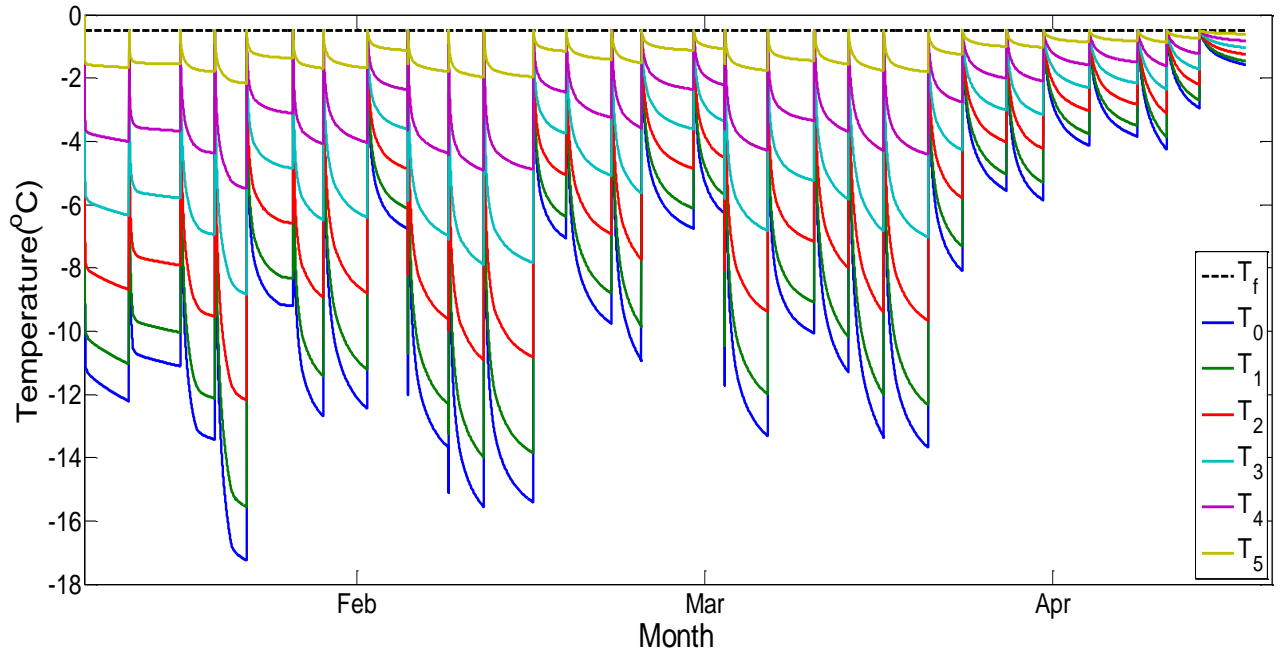


Figure 11-5 Reference Case for BIGM 2. Temperature profile without having dry brash ice

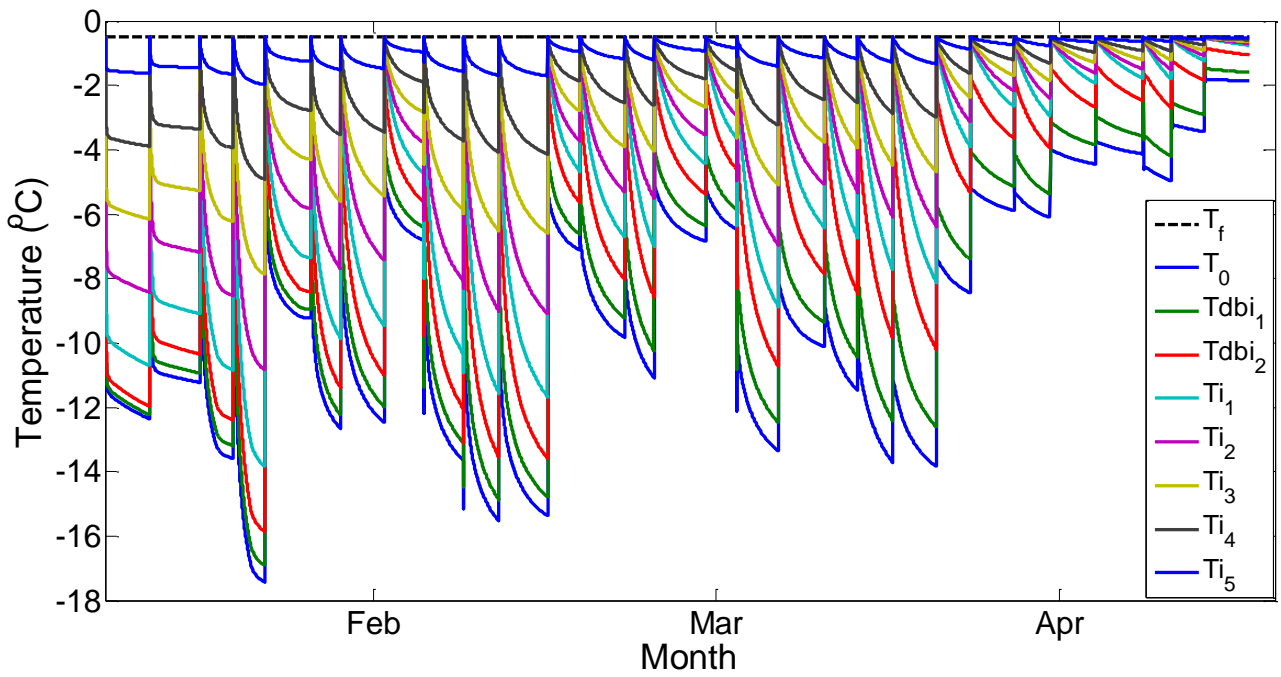


Figure 11-6 Reference Case for BIGM 2. Temperature profile when there is a dry brash ice layer above the solid ice.

11.1.3 Comparison between the Results of BIGM 1 and BIGM 2 for Reference case

In this section, the results of BIGM 1 and BIGM 2, when they take as input data, the reference case for Lulea port, presented in the two previous sections above, are going to be compared.

Figure 11-7, shows the results of the two models for the reference case in the no dry brash ice situation, without applying the radiation input data in BIGM 2. This means that the two models take exactly the same data as input, and as it can be seen from the figure, the evolution of corresponding plots for total ice thickness, wet brash ice thickness, and solid ice thickness exactly coincide. This is another proof of the correct implementation of BIGM 2 (numerical solution), using field data as input this time, since analytical and numerical models, under the same conditions give exactly the same results.

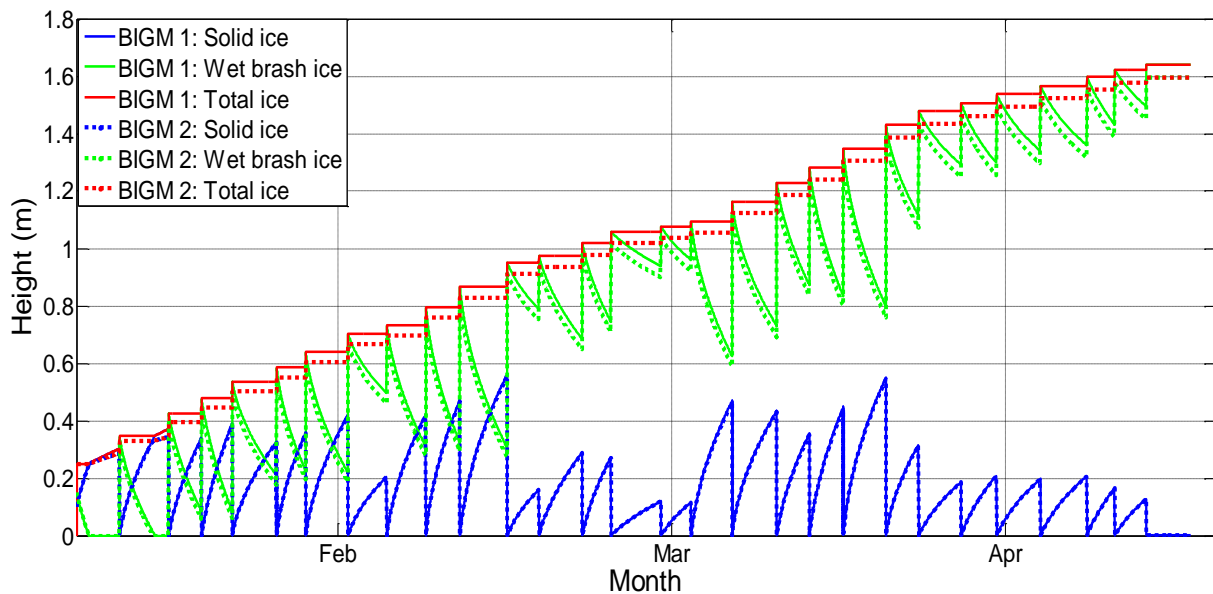


Figure 11-7 Example of the agreement of the two models BIGM 1 and BIGM 2 when the simulations are based on input field data, for the reference case of Lulea. No radiation input data is used in BIGM 2 in this case so that the two models take exactly the same input data. The plots correspond to the “no dry brash ice” situation.

In Figure 11-8, same ice layers thicknesses, as in Figure 11-7, are plotted, with the inclusion of the radiation data input in BIGM 2. As it is observed, the thickness of the total ice for BIGM 2 is increased by about 0.8m, solely due to the radiation effect.

In Figure 11-9, the results of the two models, BIGM 1 and BIGM 2, for the case that a dry brash ice layer is considered on top of the growing solid ice, and radiation input data is included in the formulation of BIGM 2, are presented. Again, the thickness of the total ice for BIGM 2 is increased, approximately by about 0.4m this time.

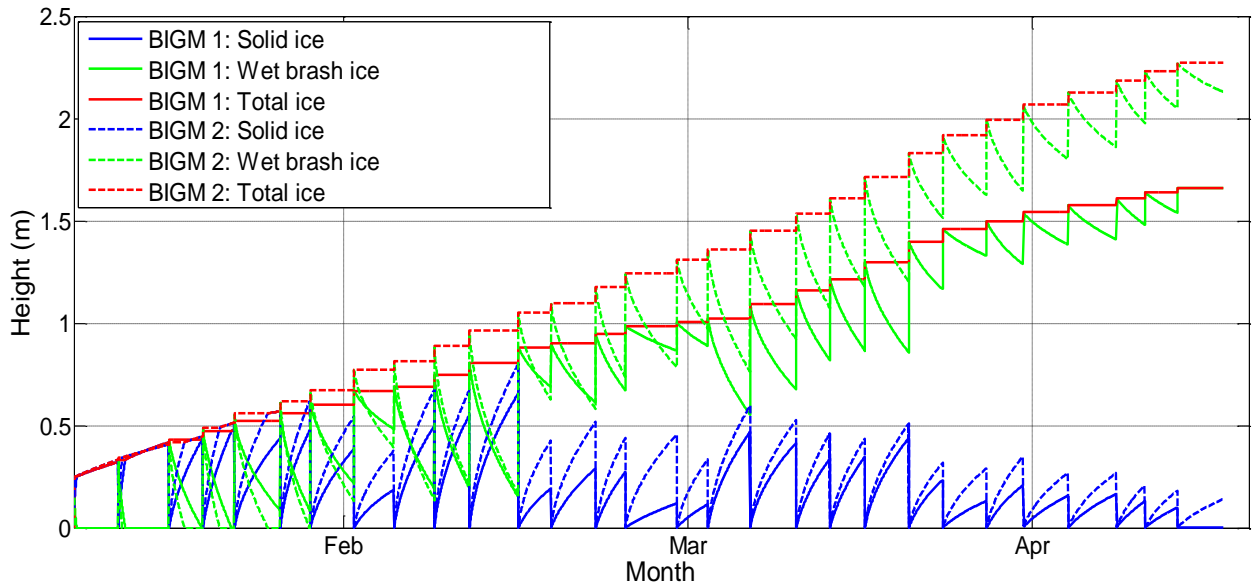


Figure 11-8 BIGM 1 reference case, BIGM 2 reference case with radiation input data also, "no dry brash ice" situation.

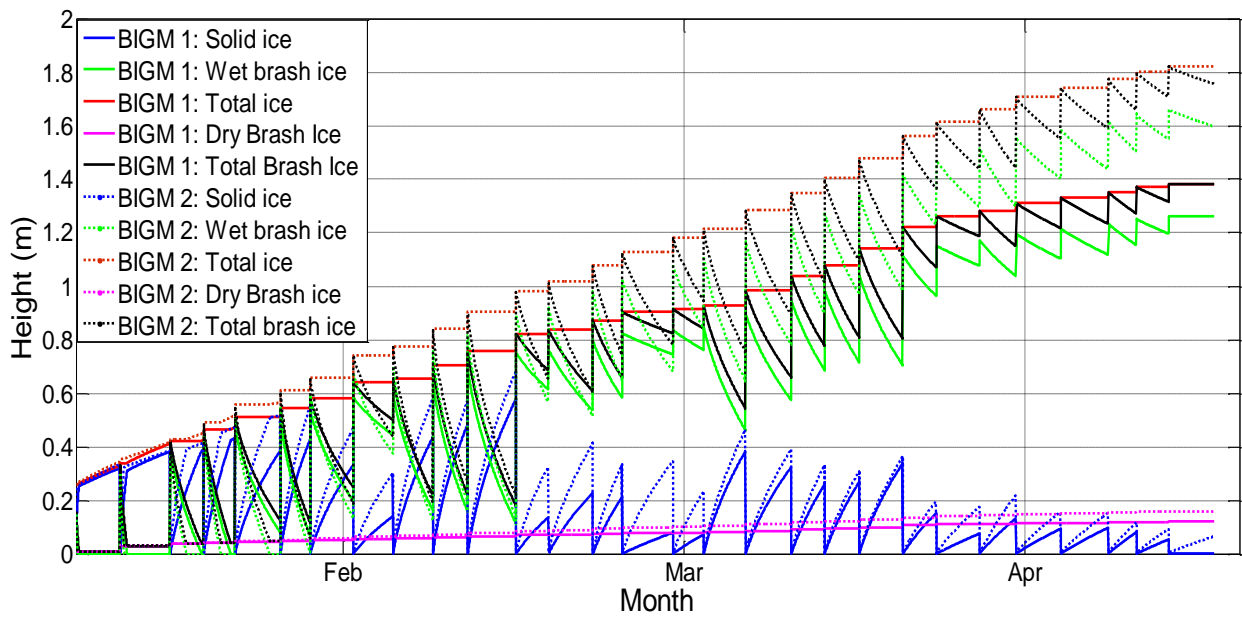


Figure 11-9 BIGM 1 reference case, BIGM 2 reference case with radiation input data also, "with dry brash ice" situation.

11.2 Investigation of how different properties/effects of BIGM 2 affect final total ice thickness results

In this section the effects of different properties/options of BIGM 2 on the evolution of total ice thicknesses are going to be examined, for both the cases of having and not having a dry brash ice layer on top of the solid ice. The properties that are going to be examined are:

1. The variation of thermal conductivity and heat capacity in different thermal layers of the solid ice and dry brash ice mass.
2. The inclusion of the latent heat flux in the top surface flux balance equation, Eq.5-3, using Eq.6-40, and the relative humidity data input from Table 11-1.
3. The inclusion of penetration of a proportion of the non-reflected solar radiation in layers of solid ice and dry brash ice mass.

11.2.1 BIGM 2 Reference Case Including variation of conductivity and specific heat capacity (depending on temperature and salinity)

In all the results presented previously in this study, the thermal properties (the thermal conductivity (λ_i), and heat capacity ($\rho_i c_i$)) were kept constant within the simulations. In this section, the effect of varying the thermal properties in different layers of the solid ice and dry brash ice, using Eq. (6-35) and Eq. (6-36), is going to be examined. The values of the thermal properties in each layer, either solid ice or dry brash ice, is going to be dependent on the temperature and salinity in that layer, at any instant of the simulation. From the work of (AARI, 2005), see section 8.6, it is known that the average seawater salinity near the water surface in Sabetta, is about 3.1 ppt, therefore for simplicity this value is going to be kept constant through the simulation i.e. the seawater salinity is not going to be varied depending on the distance of a solid ice or dry brash ice layer from the water surface. Hence, basically the thermal properties at each layer would be dependent on the temperature of the layer.

Figure 11-10, presents the evolution of the total ice thicknesses with and without dry brash ice, for the reference case using BIGM 2, and applying the variation of the thermal properties.

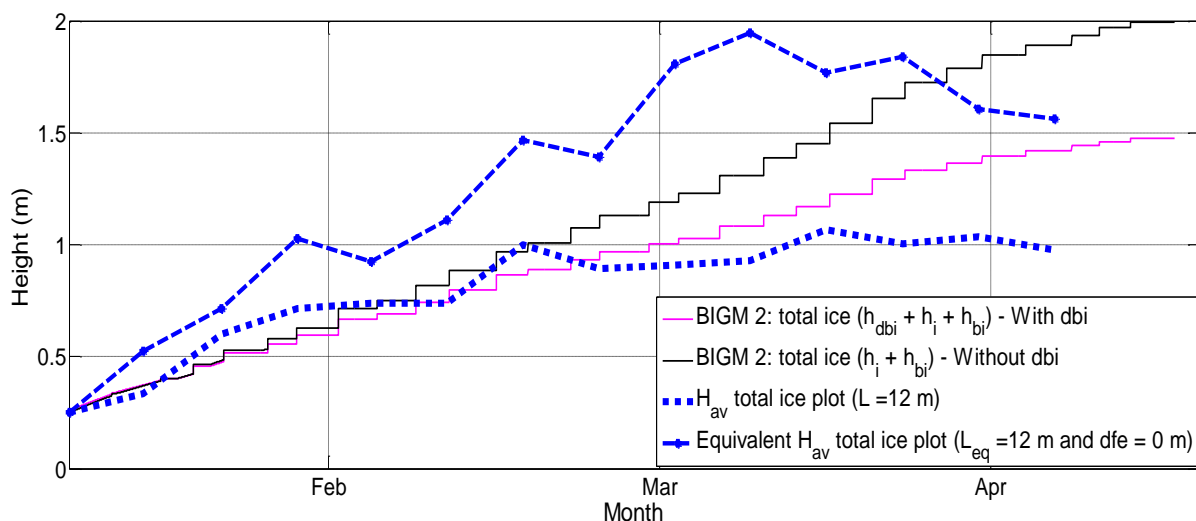


Figure 11-10 BIGM 2 reference case simulation with variation of heat conductivity and heat capacity, in each layer of the solid ice and dry brash ice (for the with dbi plot), depending on temperature and salinity.

Figure 11-10, shows that in both situations, with and without dry brush ice, the variation of the thermal properties with Eq. (6-35) and Eq. (6-36), causes a decrease in the total ice thickness in the end of the cold season. Figure 11-11, illustrates the effect on the total ice thickness in the end of the cold season, in the situation of not having a dry brush ice. The total ice thickness decreases from 2.25m thickness to 2m thickness.

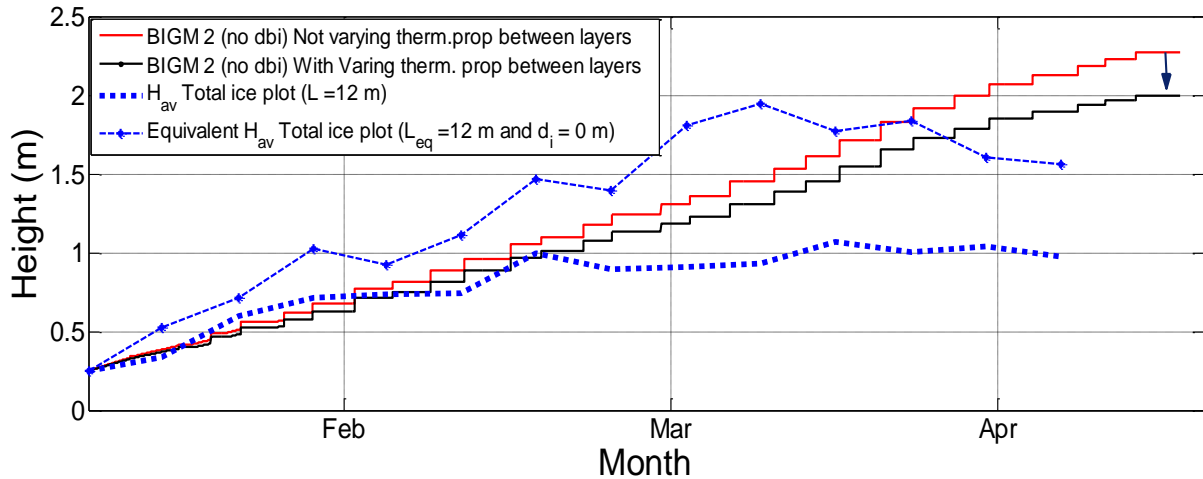


Figure 11-11 Effect on the total ice thickness in the end of the cold season, in the case of not having a dry brush ice layer, in BIGM 2 using the reference case, and having variation of the thermal properties in the ice layers.

Figure 11-12, shows the effect on the total ice thickness in the end of the cold season, in the situation of having a dry brush ice layer on top of the solid ice. The total ice thickness decreases from 1.8m to 1.5m .

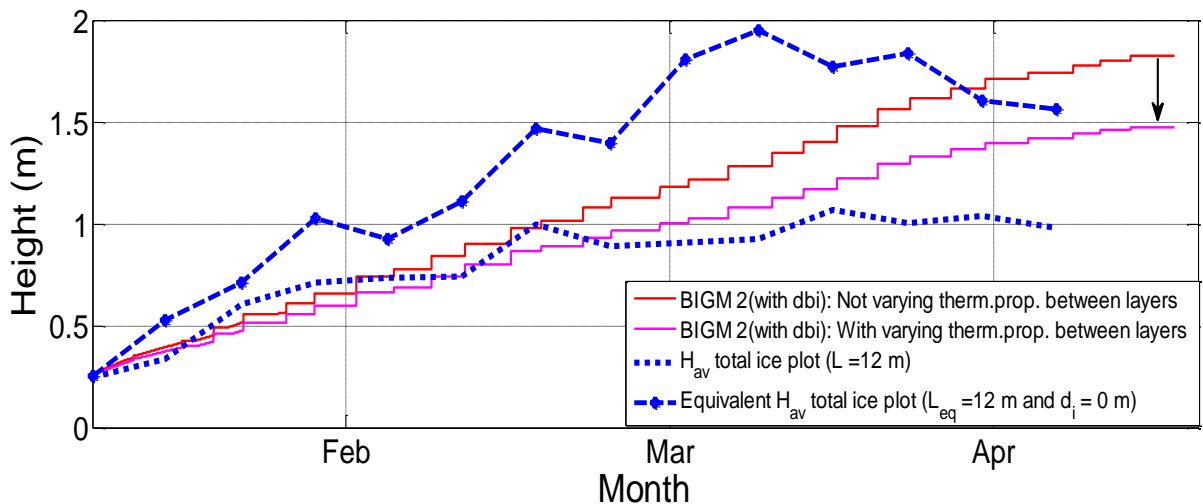


Figure 11-12 Effect on the total ice thickness in the end of the cold season, in the case of having a dry brash ice layer, in BIGM 2 using the reference case.

Figure 11-13 shows the temperature profile in the solid ice mass, when there is variation of the thermal properties, in the case of not having a top dry brash ice layer. Moreover, Figure 11-14 and Figure 11-15, show the corresponding thermal conductivity and heat capacity profiles with time. The value of thermal conductivity in the top solid ice layer in the beginning of the simulation is about $1.95 \text{ Wm}^{-1}\text{K}^{-1}$ and the one in the bottom solid ice layer is about $1.76 \text{ Wm}^{-1}\text{K}^{-1}$. At the end of the simulation the top solid ice layer seems to have a thermal conductivity of $1.7 \text{ Wm}^{-1}\text{K}^{-1}$ and the bottom solid ice layer has a thermal conductivity of $1.4 \text{ Wm}^{-1}\text{K}^{-1}$. These values are within the expected variation range, according to the temperature profile, see Figure 11-13. Also note that the value of the conductivity decreases from top layers to bottom layers of ice as expected. According to Eq. (6-35), the thermal conductivity has a smaller decrease in its value, the colder the temperature of a layer is. The term including the temperature of a layer, see Eq. (6-35), always causes a decrease in the conductivity value. This is the reason why the profile of thermal conductivities is exactly opposite to the profile of temperatures. Between breaking events temperatures are decreasing, whereas thermal conductivity values are increasing, and with time as the simulation approaches the spring months, temperatures are increasing and thermal conductivity values are decreasing, see Figure 11-13 and Figure 11-14.

Regarding the heat capacity, according Eq. (6-36), the lower the temperature of a layer is, the smaller the increment (always +ve) in the heat capacity for that layer, as the temperature is in square brackets in the denominator of the term that changes the value of the heat capacity. The heat capacity profile looks a bit similar to the temperature profile. The lower/colder the temperature of a layer gets, the smaller the amount by which the heat capacity will increase. Between breaking events both the temperature of a layer and the heat capacity of a layer are decreasing, and as the simulation progresses towards the spring months, both the temperature and the heat capacity acquire higher values (i.e. temperature rises). As it is observed from Figure 11-15, the value of the heat capacity increases from top layers towards bottom layers. The value of the heat capacity in the top solid ice layer, in the beginning of the simulation, is about $2.1 \times 10^6 \text{ Jm}^{-3}\text{K}^{-1}$ and the one in the bottom solid ice layer is about $2.5 \times 10^7 \text{ Jm}^{-3}\text{K}^{-1}$. At the end of the simulation, the top solid ice layer seems to have a heat capacity of $4 \times 10^7 \text{ Wm}^{-1}\text{K}^{-1}$ and the bottom solid ice layer has a heat capacity of about $1.6 \times 10^8 \text{ Wm}^{-1}\text{K}^{-1}$. These are within the expected variation range, according to the corresponding temperature profile, see Figure 11-13.

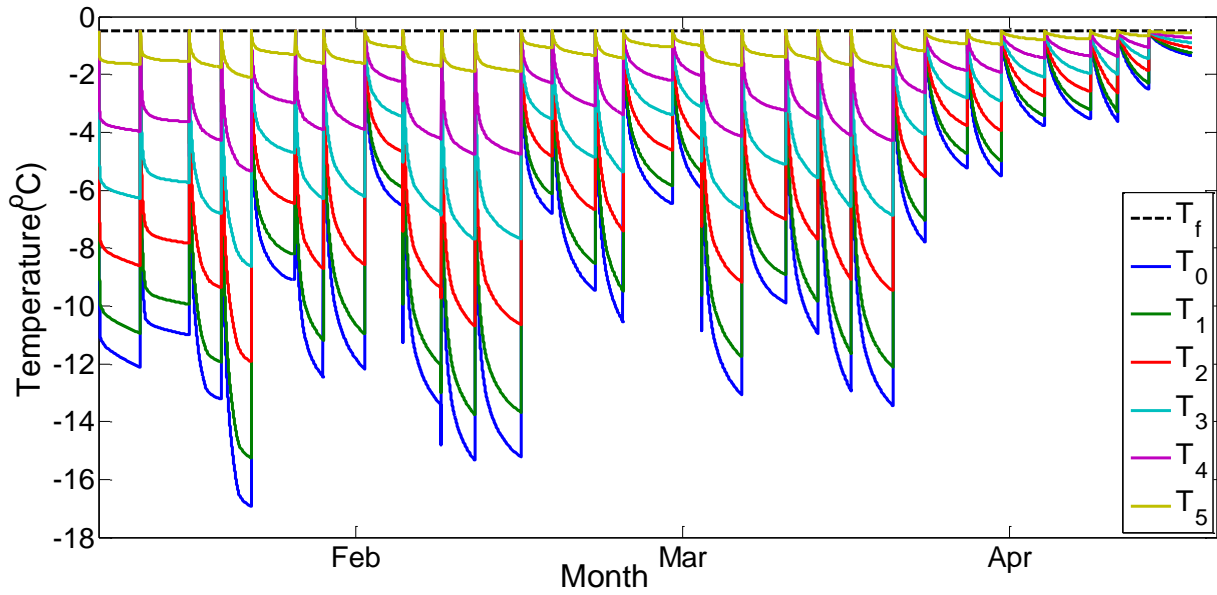


Figure 11-13 Temperature profile in the case of no dry brash ice, and variation of the thermal properties in the solid ice layers. BIGM 2 reference case.

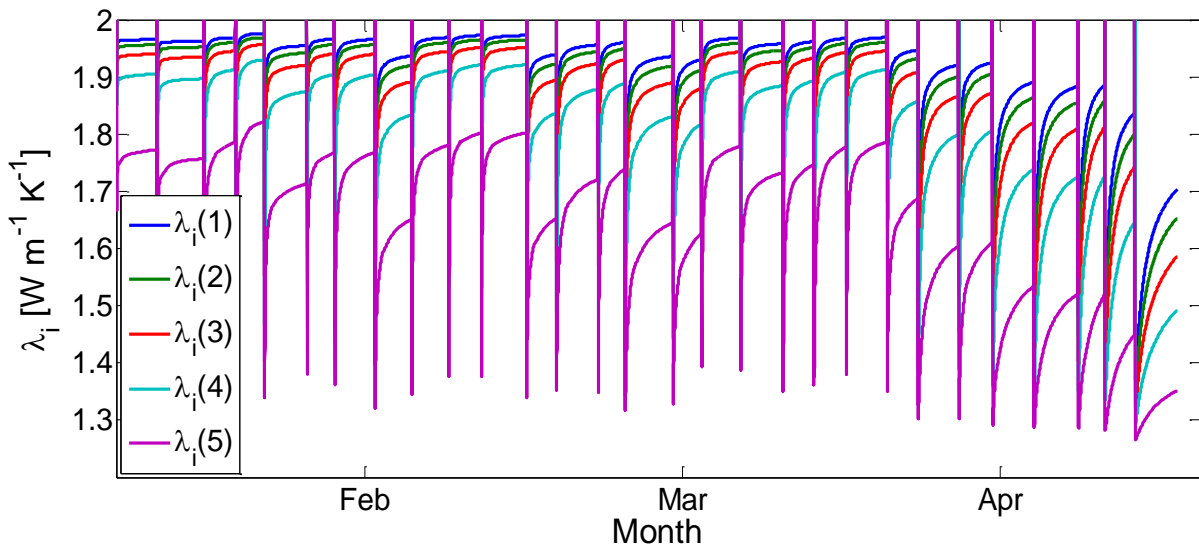


Figure 11-14 Thermal conductivity of ice profile evolution with time, for BIGM 2 reference case, having no dry brash ice.

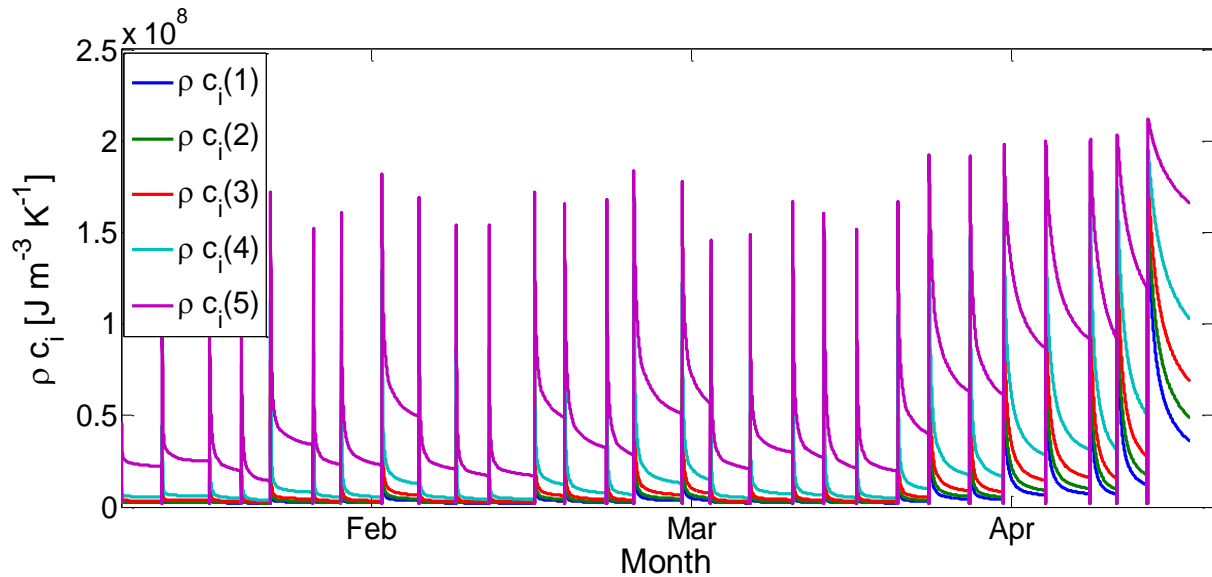


Figure 11-15 Heat Capacity of ice profile evolution with time, for BIGM 2 reference case, having no dry brash ice.

For the situation where there is also a dry brash ice layer, the temperature profile, thermal conductivity profile and heat capacity profile are shown in Figure 11-16, Figure 11-17, and Figure 11-18 respectively.

The value of thermal conductivity in the top dry brash ice layer in the beginning of the simulation is about $1.28 \text{ Wm}^{-1}\text{K}^{-1}$, the one in the top solid ice layer is about $1.96 \text{ Wm}^{-1}\text{K}^{-1}$ and the one in the bottom solid ice layer is about $1.78 \text{ Wm}^{-1}\text{K}^{-1}$. At the end of the simulation the top dry brash ice layer seems to have a thermal conductivity of $1.1 \text{ Wm}^{-1}\text{K}^{-1}$, the top of the solid ice layer has a thermal conductivity of $1.6 \text{ Wm}^{-1}\text{K}^{-1}$ and the bottom solid ice layer has a thermal conductivity of $1.3 \text{ Wm}^{-1}\text{K}^{-1}$. The variation in thermal conductivity in these layers is again in the expected range according to the temperature profile for this case, see Figure 11-16. Note that during the cold period and especially towards the end of the simulation, the solid ice layers have lower conductivity values in the case with dry brash ice on top of solid ice, compared to the case of bare solid ice growth. Again this observation is consistent with the previously mentioned statement that the dry brash ice provides an insulating effect on solid ice growth and generally on solid ice properties. Lower solid ice conductivity values mean lower solid ice growth rate.

The value of the heat capacity in the top dry brash ice layer, at the beginning of the simulation, is about $1.27 \times 10^6 \text{ Jm}^{-3}\text{K}^{-1}$, the one in the top solid ice layer is about $2.1 \times 10^6 \text{ Jm}^{-3}\text{K}^{-1}$ and the one in the bottom solid ice layer is about $2.5 \times 10^7 \text{ Jm}^{-3}\text{K}^{-1}$. At the end of the simulation, the top dry brash ice layer seems to have a heat capacity of $3 \times 10^7 \text{ Jm}^{-3}\text{K}^{-1}$, the top solid ice layer seems to have a heat capacity of $9 \times 10^7 \text{ Jm}^{-3}\text{K}^{-1}$ and the bottom solid ice layer has a heat capacity of about $2 \times 10^8 \text{ Jm}^{-3}\text{K}^{-1}$. Note that in the end of the cold period the solid ice layers have higher heat capacity values, in the case with dry brash ice on top of solid ice, compared to the case of bare solid ice growth. Again this is due to the insulating effect of the dry brash ice mass on top of the solid ice.

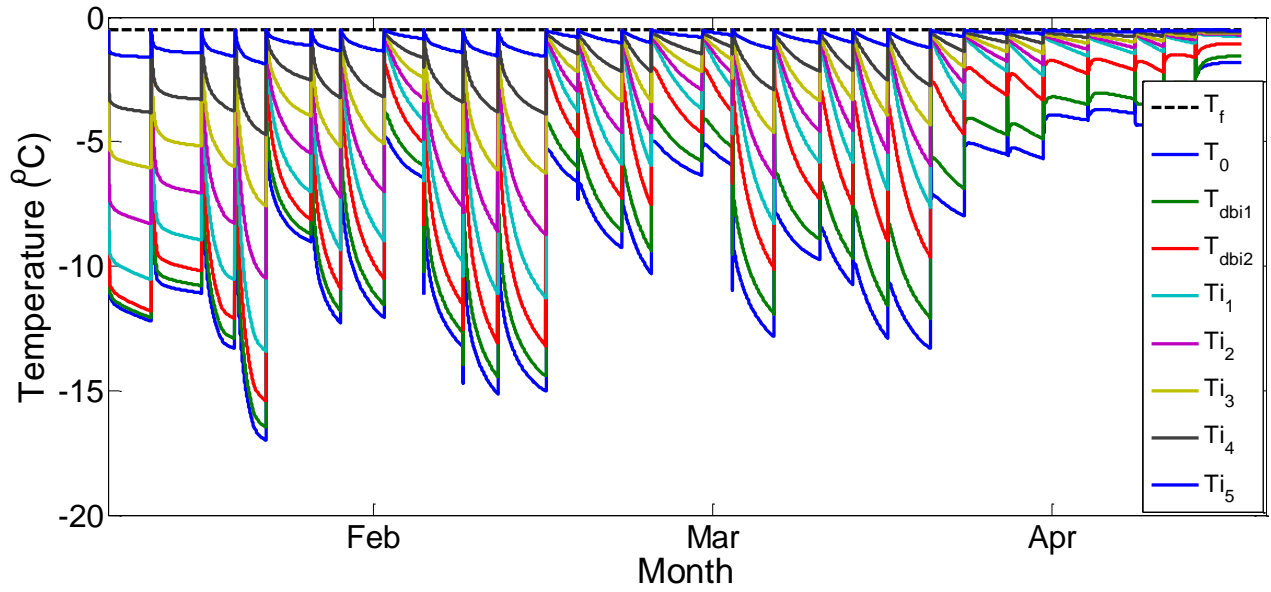


Figure 11-16 Temperature profile in the case of having a dry brash ice on top of the solid ice, and variation of the thermal properties in the dry brash ice and solid ice layers. BIGM 2 reference case.

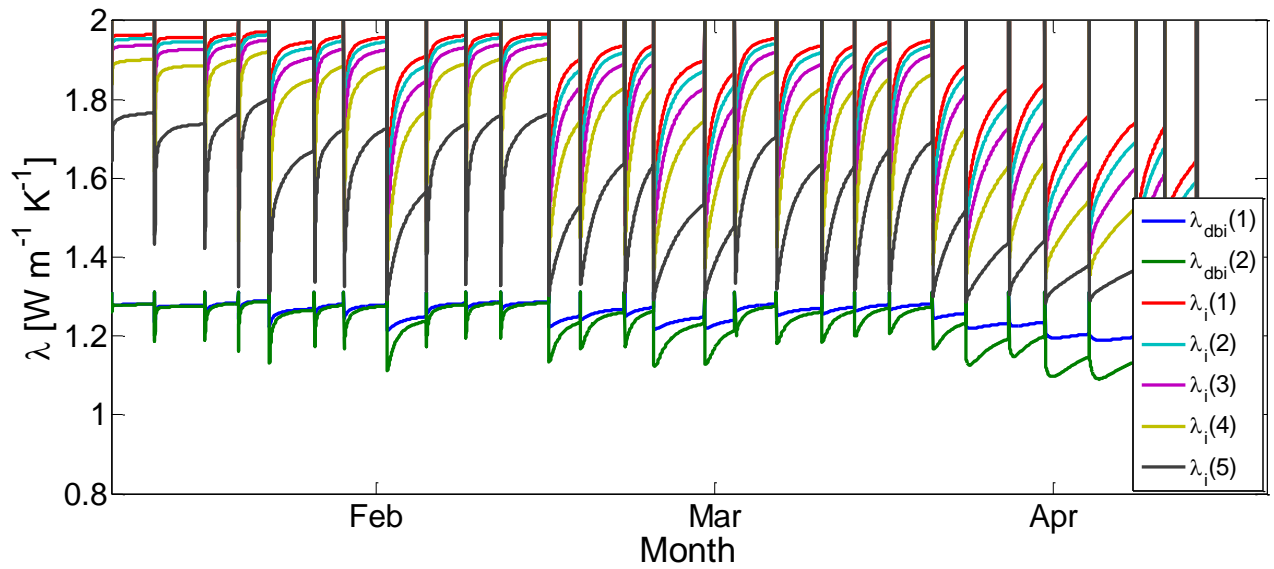


Figure 11-17 Thermal conductivity profile evolution with time for BIGM 2 reference case, having additionally a dry brash ice layer on top of the solid ice.

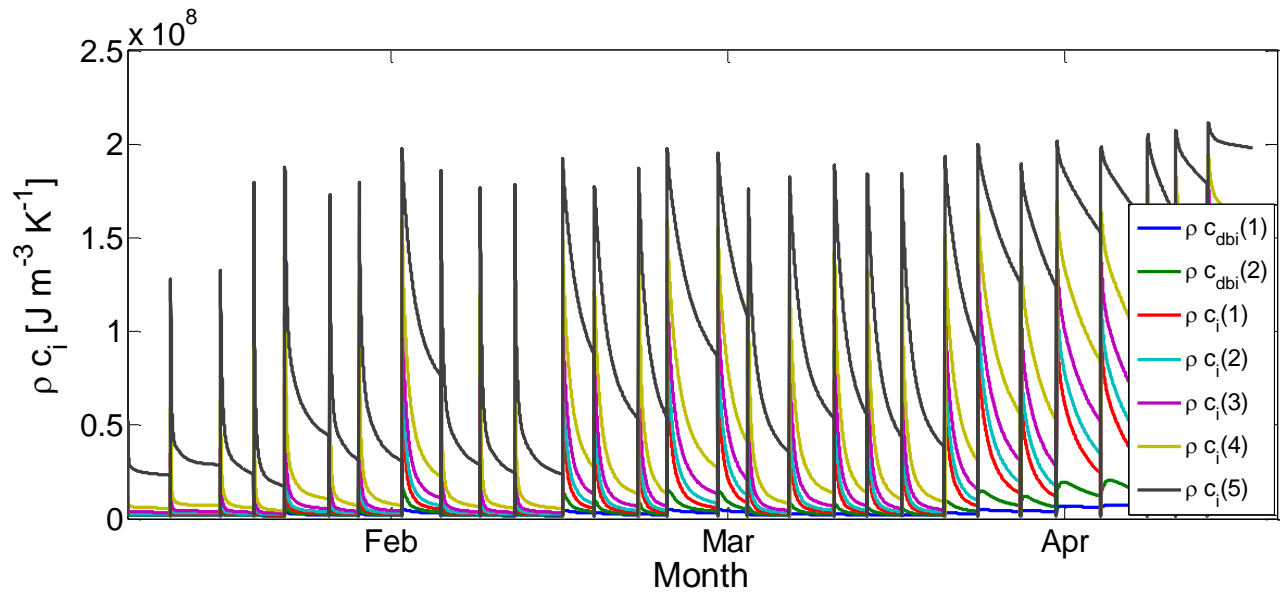


Figure 11-18 Heat capacity profile evolution with time for BIGM 2 reference case, having additionally a dry brash ice layer on top of the solid ice.

11.2.2 BIGM 2 Reference case, including latent heat flux in the top surface flux balance equation

In this section the effect of the latent heat flux in the results of BIGM 2 is going to be discussed. Using the relative humidity set of values from Table 11-1, and Equations (6-39) and (6-40), the latent heat flux is included in the top surface flux balance equation. Eq. (6-40) replaces Eq. (6-7) in the temperature matrix system. According to (Ukita & Martinson, 2001), (Maykut & Untersteiner, 1971) and (Maykut, 1978), the latent heat flux is usually the component with the lowest flux value in the top surface flux balance equation, and hence the lowest impact on solid ice growth. This was verified in this study as well. Figure 11-19, shows the evolution of the total ice thickness, in the reference case of BIGM 2 in the no dry brash ice situation, with and without including the latent heat flux, in the top surface flux balance. As it can be observed the plots are identical with one lying above the other.

Similarly, Figure 11-20 shows the evolution of the total ice thickness in the reference case of BIGM 2, in the situation that a dry brash ice layer is included in the matrix formulation, with and without including the latent heat flux in the top surface flux balance. As it can be observed the plot that includes the latent heat flux effect, is slightly lower than the reference case in the end of the cold season, however the effect is considered is insignificant.

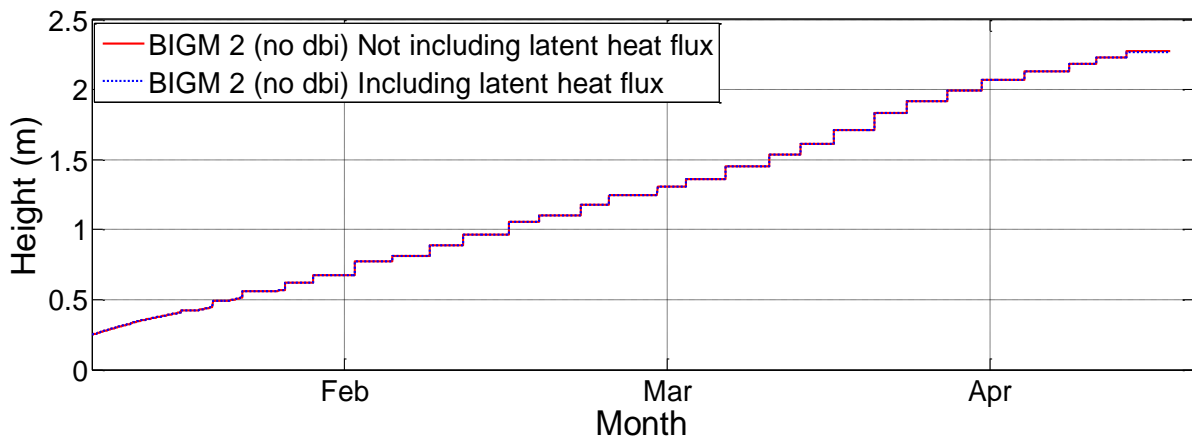


Figure 11-19 Examining the effect of the latent heat flux on solid ice growth, using BIGM 2 reference case with no dry brash ice in the formulation.

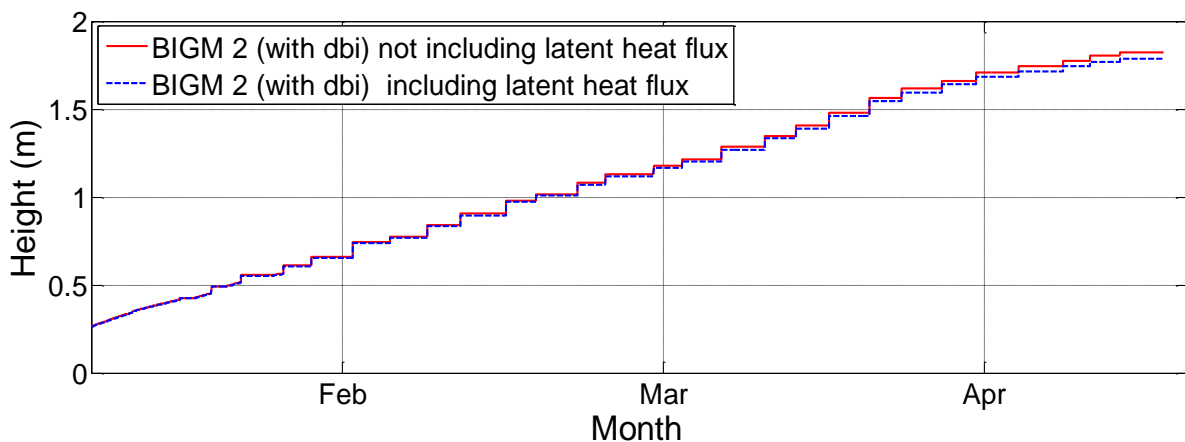


Figure 11-20 Examining the effect of the latent heat flux on solid ice growth, using BIGM 2 reference case with dry brash ice layer, on top of the solid ice, in the formulation.

11.2.3 BIGM 2 reference case, including internal absorption

Internal absorption of solar radiation increases the temperatures within the solid ice and dry brash ice masses and also modifies the temperature balance on the top surface. The way temperatures at different layers of solid ice and dry brash ice increase, has been explained in section 6.1.9. In this section, the effect of internal absorption of an amount of the non-reflected solar radiation is going to be examined, by applying this effect in the reference case of BIGM 2, in both the situations of having and not having a dry brash ice layer above the solid ice.

The proportion of solar radiation absorbed, i_o depends both on the type of the ice and on whether the incident radiation is direct or diffuse. For clear skies (Maykut, 1977), gives an $i_o = 18\%$ for white ice and an $i_o = 43\%$ for blue ice. For the examination of this effect on the reference case of BIGM 2, it was decided to take the average of these two values, hence use a proportion $i_o = 31\%$.

Figure 11-21, presents the evolution of the total ice thicknesses with and without dry brash ice, for the reference case using BIGM 2, with the application of the internal absorption of solar radiation. As it is easily observed, in relation to Figure 11-3, both plots have quite lower total ice thicknesses in the end of the cold season. Moreover the plot corresponding to the case with dry brash ice, shows some melting taking place, due to excessive radiation, in the middle of April and afterwards.

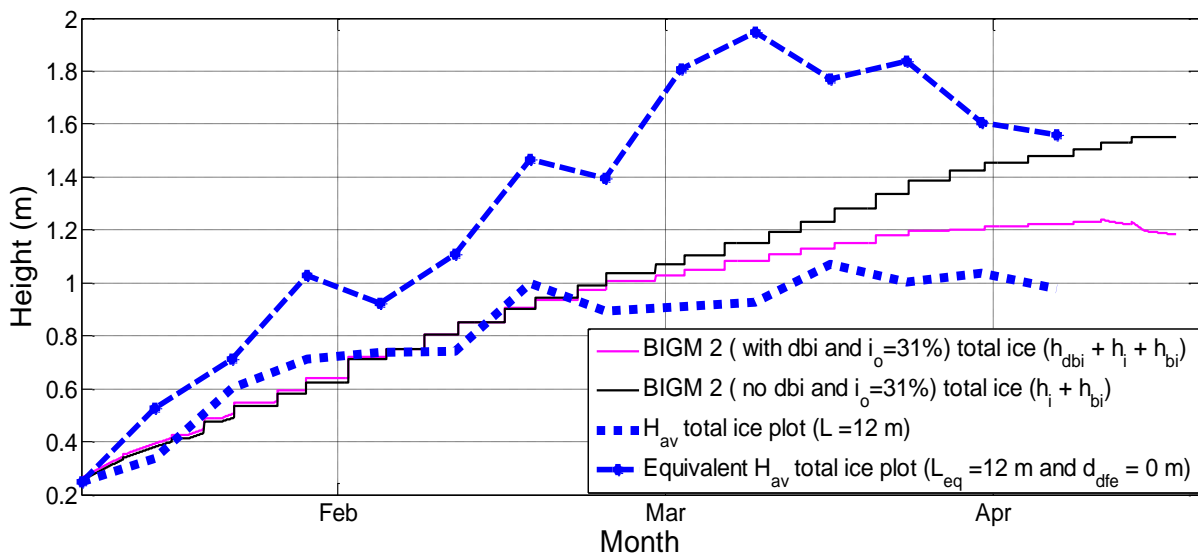


Figure 11-21 . Total Ice layer evolution for the reference case, including internal absorption of 31% of the net non-reflected solar radiation, for BIGM 2 for both the cases with and without dry brash ice.

Figure 11-22 compares the BIGM 2 reference case, and the reference case with the inclusion of internal solar absorption, for the situation where dry brash ice is not included. The two total ice field plots, average and equivalent average for the 12m width ship track, are also included in the figure as a reference. As it can be seen the total ice thickness in the end of the cold season has decreased by about 0.7m due to the internal absorption of 31% of the net solar radiation.

Similarly, Figure 11-23 compares the BIGM 2 reference case, and the reference case with the inclusion of internal solar absorption, for the situation where dry brash ice is included in the formulation. In this case the total ice thickness in the end of the cold season has decreased by about 0.65m due to the internal absorption of 31% of solar radiation.

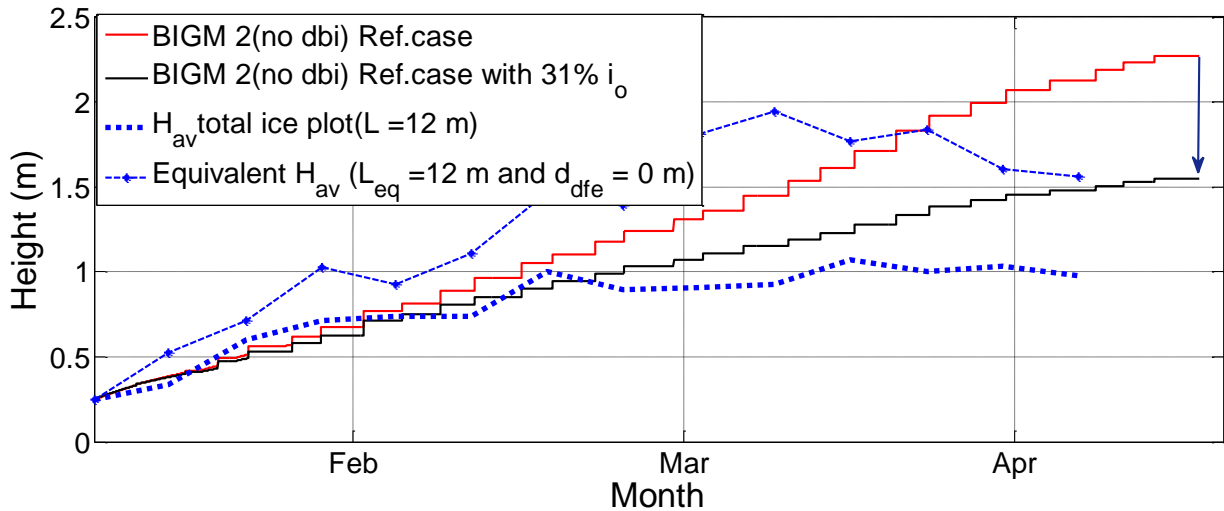


Figure 11-22 Comparison between the reference case of BIGM 2, and the reference case of BIGM 2 with the inclusion of internal solar radiation absorption. No dry brush ice case.

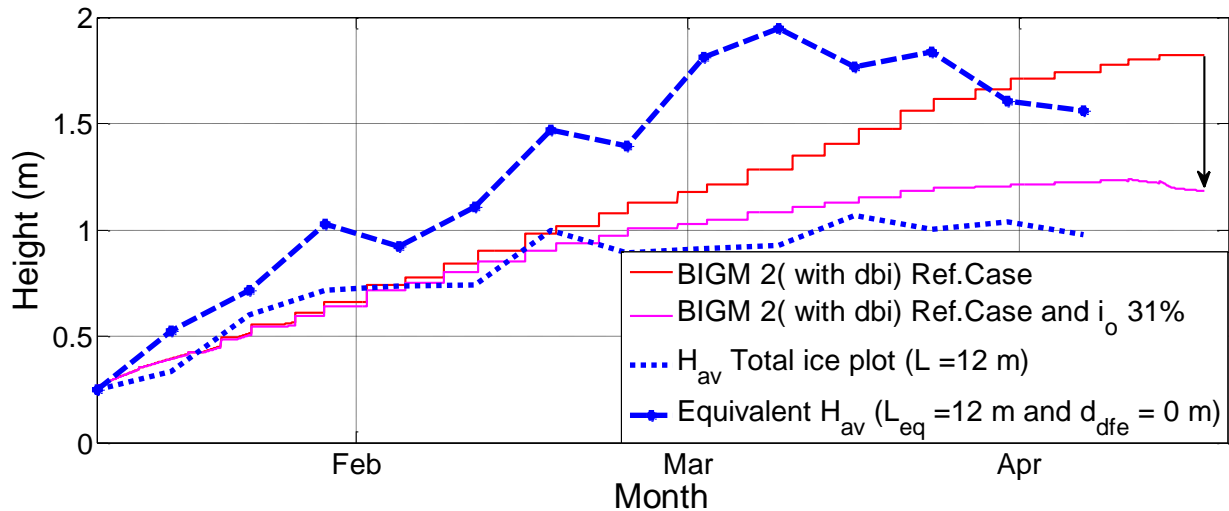


Figure 11-23 Comparison between the reference case of BIGM 2, and the reference case of BIGM 2 with the inclusion of internal solar radiation absorption. Situation with inclusion of dry brush ice in the formulation.

Figure 11-24, shows the evolution of the dry brush ice thickness in the same simulation, together with the average dry brush ice thickness from the field measurements, across the ship track width (12m width). As it can be seen, the two plots show quite good agreement, in terms of dry brush ice thickness evolution. Melting in the dry brush ice plot from BIGM 2, seems to start a few weeks later than the apparent melting shown in the field plot, in April. This can be due to different long wave radiation values in reality from the ones used in the model. It is reminded here that due to lack of field data for long wave radiation, the set of long wave radiation values used in these simulations consists of monthly average values taken from (Maykut & Untersteiner, 1971).

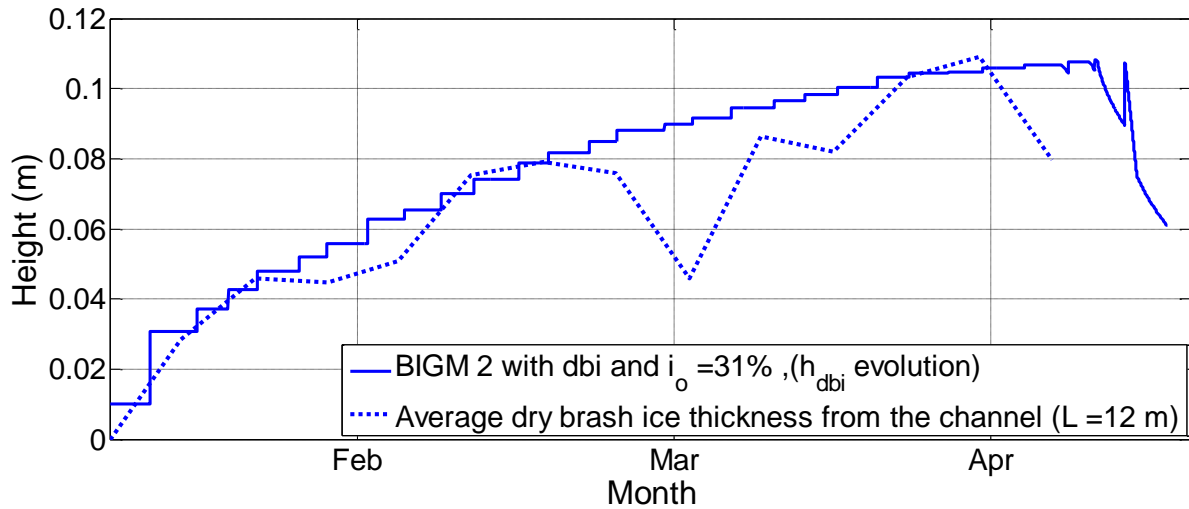


Figure 11-24 Comparison between the reference case of BIGM 2 with the inclusion of internal solar radiation absorption, and the average dry brush ice across the ship track (12 m width).

The temperature profile for the case of not having a dry brush ice layer, is presented in Figure 11-25 and the profile of the corresponding incremental temperatures due to the inner solar absorption, which are calculated as explained in section 6.1.9, is shown in Figure 11-26. Note, that the downward curves in the temperature profile between breaking events that start just after February, which are not presented in previous temperatures profiles shown in this study, is a result of the increasing solar radiation and hence the increasing amount of radiation absorbed by inner solid ice layers, and hence the increasing inner incremental temperatures, see Figure 11-26. The two top solid ice layers, as it is expected, have the greatest incremental temperatures, see Figure 11-26.

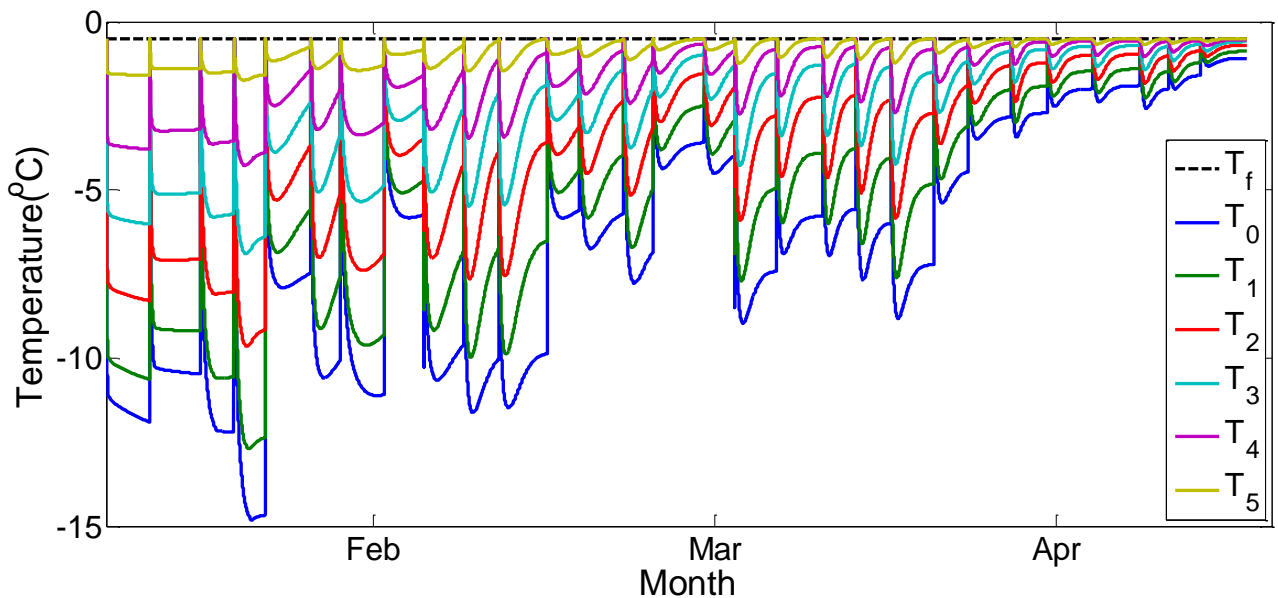


Figure 11-25 Temperature profile in the case of no dry brush ice, for the reference case of BIGM 2 and having 31% internal solar absorption.

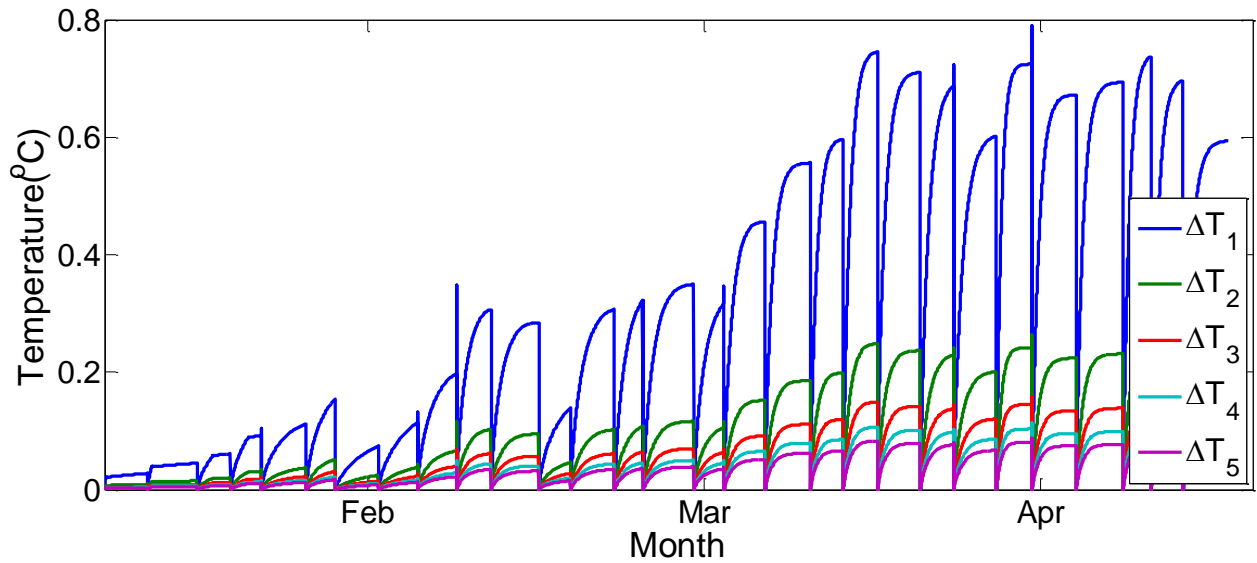


Figure 11-26 Profile of the incremental temperatures in the case of no dry brash ice, for the reference case of BIGM 2 and having 31% internal solar absorption.

The temperature profile for the case of having a dry brash ice layer on top of the solid ice and the related profile of incremental temperatures are shown in Figure 11-27 and Figure 11-28 respectively. In this case, as it is expected the two dry brash ice layers have the greatest incremental temperatures, see Figure 11-28. Note that as the incremental temperatures in the dry brash ice layers are approaching 1°C, melting of dry brash is observed to start taking place, see Figure 11-24.

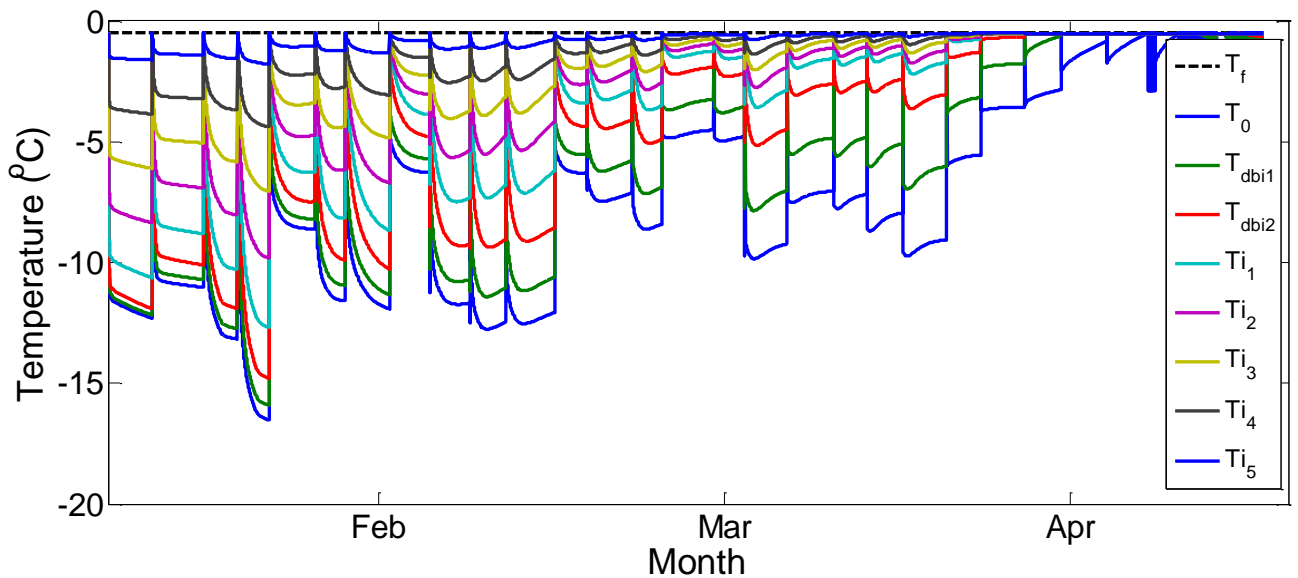


Figure 11-27 Temperature profile in the case of having a dry brash ice layer above the solid ice, for the reference case of BIGM 2 and having 31% internal solar absorption.

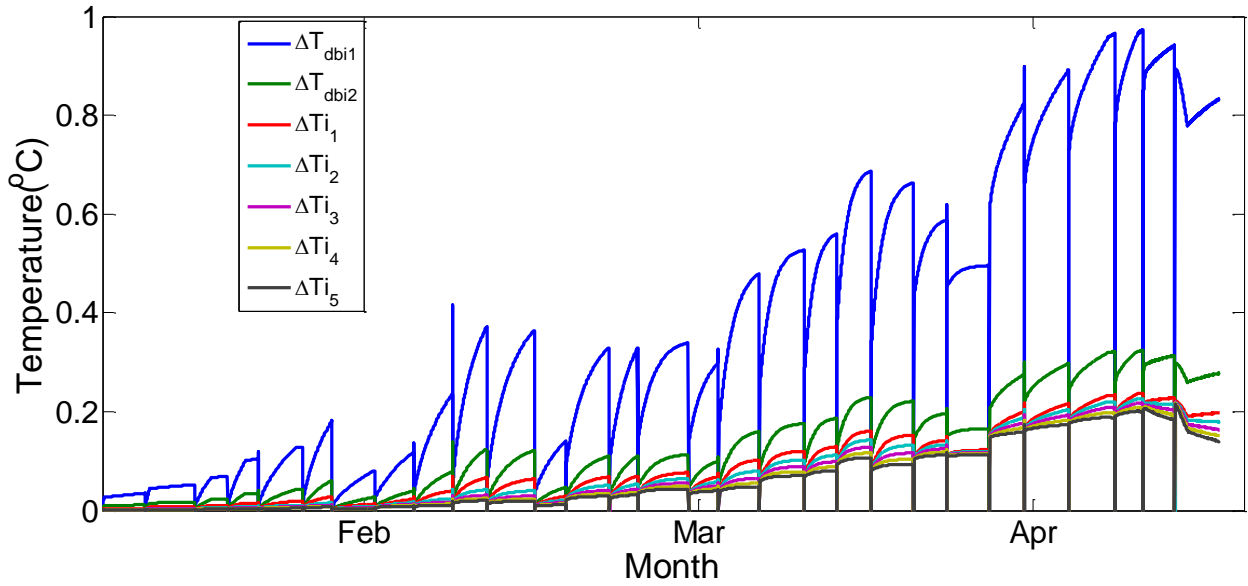


Figure 11-28 Profile of the incremental temperatures in the case of having a dry brash ice layer above the solid ice, for the reference case of BIGM 2 and having 31% internal solar absorption.

Summarizing this section, it was observed that internal absorption causes a decrease in the total ice thickness in the end of the cold season, compared to the reference case which does not include any internal solar radiation absorption. Moreover, this decrease was observed to be slightly smaller in the case of having a dry brash ice layer in the formulation. The dry brash ice thickness evolution from the simulation shows a quite similar pattern to the average dry brash ice plot across the ship track.

11.3 Parametric Study for Lulea reference case

In this section a brief parametric study is going to be performed to test the sensitivity of the results of BIGM 2 with the Lulea reference case input data, see section 11.1.2, to the uncertainty and variability of certain parameters that have been assumed. These parameters are:

1. The surface albedo, a
2. The proportion of solar radiation internal absorption, i_o
3. And the dry brash ice conductivity, λ_{dbi}

Note that BIGM 2 reference case results in section 11.1.2, did not include the effect of internal absorption at all. Therefore the parametric study for i_o only, would have as a reference case the results of section 11.2.3, which is basically the BIGM 2 reference case with the application of an average net internal absorption of solar radiation, of 31%.

The parametric study is performed only for the situation of having a dry brash ice layer above the growing solid ice, as this is most physically correct case.

The set of values that each of the tested parameters is going to have in this parametric study are presented in Table 11-2.

Table 11-2 Summary of the values that each tested parameter takes for this parametric study

Parameter Name	Maximum value	Reference value	Minimum Value
Surface albedo, a	0.83	0.64	0.22
Proportion of solar radiation absorption, i_o	49 %	31 %	18 %
Dry brash ice conductivity, λ_{dbi}	1.706(+30%)	1.312	0.919(-30%)

11.3.1 Surface albedo

Surface albedo in ice, dry brash ice or snow is a coefficient used to determine the amount of solar radiation absorbed by the top surface of the medium, in this case ice, dry brash ice or snow, and the amount of solar radiation reflected by the top surface of the medium. In relation to the ice growth problem and the BIGMs, surface albedo is involved in the top surface flux balance equation, see Eq. (5-3) and Eq. (6-2).

According to (Maykut & Untersteiner, 1971), surface albedo is probably the most important regional factor affecting the heat and mass budgets of the arctic pack ice. During the spring and fall, when surface conditions are more uniform, a is high and relatively constant, however in the summer there are fluctuations in the surface albedo values, hence it can be both low and high, depending on the locations' specific environmental characteristics.

The values that are going to be used for the parametric study for the surface albedo in this study were chosen from (Maykut & Untersteiner, 1971), (Marshunova, 1961) and (Maykut, 1977). The chosen reference case of 0.64 is the yearly average value used by (Marshunova, 1961), and the minimum value from the set of monthly surface albedo values presented in (Maykut & Untersteiner, 1971). The maximum value of 0.83, is the highest surface albedo value between March and May, in the same set of monthly surface albedo values in (Maykut & Untersteiner, 1971). The minimum surface albedo value

of 0.22 was chosen from (Maykut, 1977) as an extreme minimum case, and corresponds to mature melting ice in the summer periods.

Figure 11-29, shows the evolution of the total ice thickness for the 3 surface albedo, a , values. As it is expected, the smaller the surface albedo value the more solar radiation has to be balanced by the top surface flux balance equation, see Eq. (5-3), and hence the less the value of the total ice thickness in the end of the cold season. Note, that in the first months of the simulation, January and February, when the solar radiation is minimal, the plots of the total ice thickness are identical. After March, and even more in April when solar radiation gets more and more intense, the effect of the surface albedo becomes more obvious. The higher the value of the surface albedo, the more solar radiation is reflected and hence the higher the thickness of the total ice. Table 11-3 presents a quantitative analysis of the surface albedo impact on the total ice thickness.

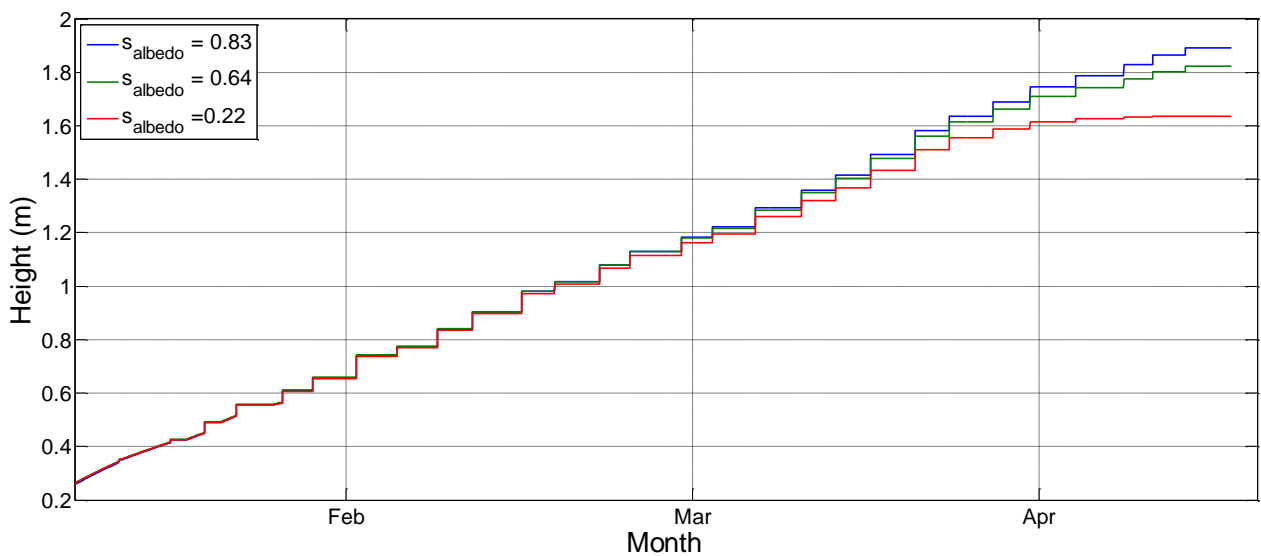


Figure 11-29 Parametric study for surface albedo using the Reference case of Lulea, see section 11.1.2. Total ice evolutions for different values of the surface albedo.

Table 11-3 Variation of the surface albedo on the surface

Surface albedo values	Total Ice thickness at the end of the cold season	
	$h_{tot}(m)$	Impact of surface albedo (%)
$a = 0.83$	1.89	+3.85%
$a = 0.64$	1.82	-
$a = 0.22$	1.63	-10.44%

Figure 11-30, shows the evolution of the solid ice thickness for the 3 surface albedo, a , values. The findings are the same as in the case for the total ice. Until the beginning of March, the surface albedo value does not have any effect on the solid ice thickness, however after March and specifically in April when solar radiation gets quite strong, the surface albedo value has a significant effect on solid ice growth. The lower the surface albedo value is, the higher the solid ice thickness.

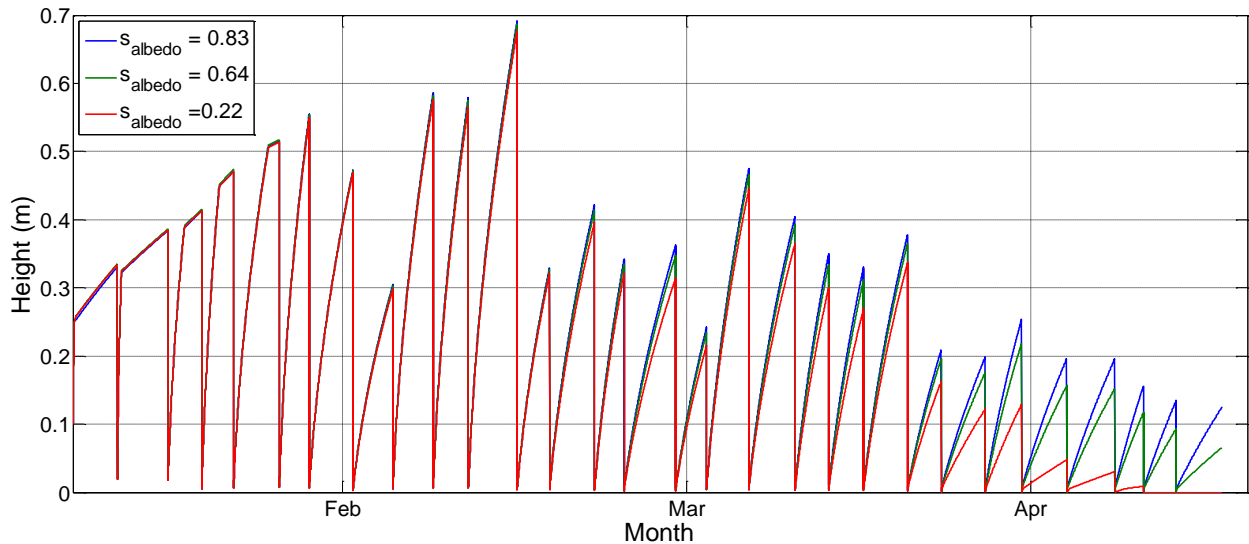


Figure 11-30 Parametric study for surface albedo using the reference case of Lulea. Solid ice evolutions for different values of the surface albedo.

11.3.2 Proportion of solar radiation absorbed i_o

As it was mentioned previously, internal absorption of solar radiation increases the temperatures within the solid ice and dry brash ice masses and also modifies the temperature balance on the top surface. The way temperatures at different layers of solid ice and dry brash ice increase, has been explained in section 6.1.9.

In this section, a parametric study on the proportion of the non-reflected solar radiation, absorbed in the lower layers of solid ice and dry brash ice, is going to be performed. The values that are going to be used for the parametric study, for the proportion of solar radiation absorbed, i_o , in layers of solid ice and dry brash ice, where chosen from (Maykut, 1977). The value of i_o depends both on the type of the ice and on whether the incident radiation is direct or diffuse. As it was also mentioned before, for clear skies (Maykut, 1977), gives an $i_o = 18\%$ for white ice and an $i_o = 43\%$ for blue ice. For the examination of the effect of internal absorption in relation to the reference case, see section 11.1.2, it was decided to take the average of these two values, hence use a proportion $i_o = 31\%$, see section 11.2.3. For cloudy skies, (Maykut, 1977) gives an $i_o = 35\%$ for white ice and an $i_o = 63\%$ for blue ice, and it was decided to take the average of these values as a maximum case in this parametric study, hence, $i_o = 49\%$. As minimum value of i_o , the corresponding value for clear skies and white ice mentioned above was chosen, hence $i_o = 18\%$. Note here, informatively, that the decrease in i_o under clear skies is a result of a greater amount of energy, in the form of solar radiation being in the infrared range, and this range of radiation is mostly absorbed/balanced by the top surface, instead of penetrating the surface and increasing the temperature in the layers of ice mass below.

Figure 11-31, shows the total ice thickness evolution for the 3 different possible values for the proportion of solar radiation absorption. Again, as it is expected, the higher the solar radiation absorption, the smaller the value of the total ice thickness in the end of the cold season. After April all the three plots show some melting taking place due to excessive radiation. Melting in this case where a dry brash ice layer is included above the solid ice, can only be taking place in the dry brash ice layer. In general melting can only take place in the part of the ice above the waterline, the freeboard. Figure 11-32, shows the evolution of dry brash ice for the three possible cases of proportion of solar radiation

absorption, i_o . Melting seems to be taking place, for all three cases in April. Plots of the accumulated melting are shown in Figure 11-33, for all the three possible cases. In the case of $i_o = 49\%$, melting reaches up to 0.11m.

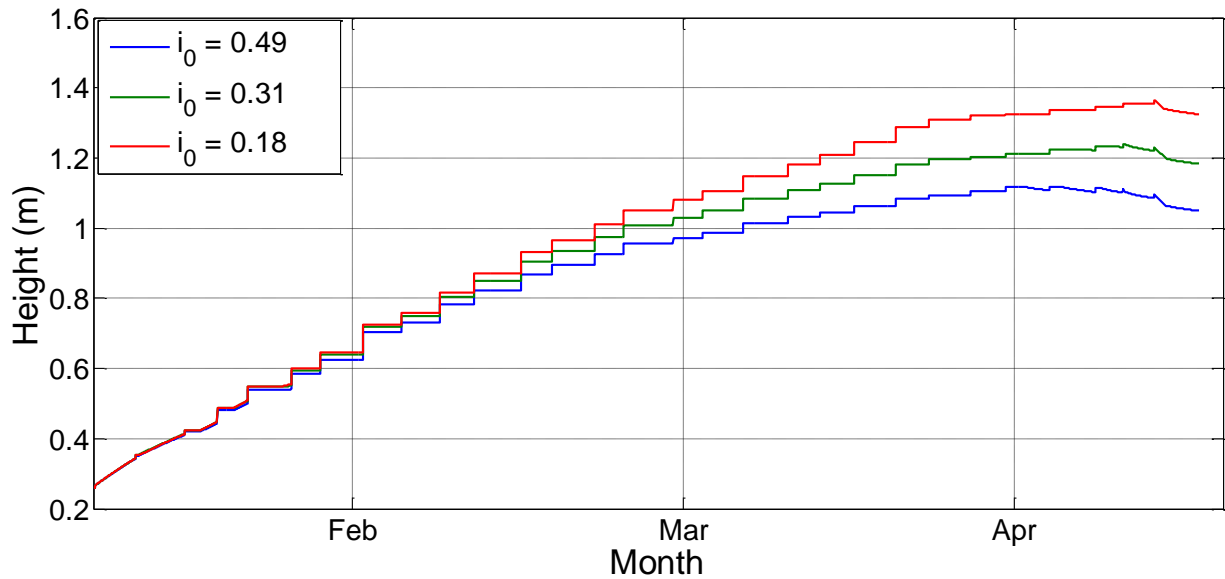


Figure 11-31 BIGM 2 with dry brash ice. Total ice evolutions for the 3 different possible values of solar radiation absorption proportion.

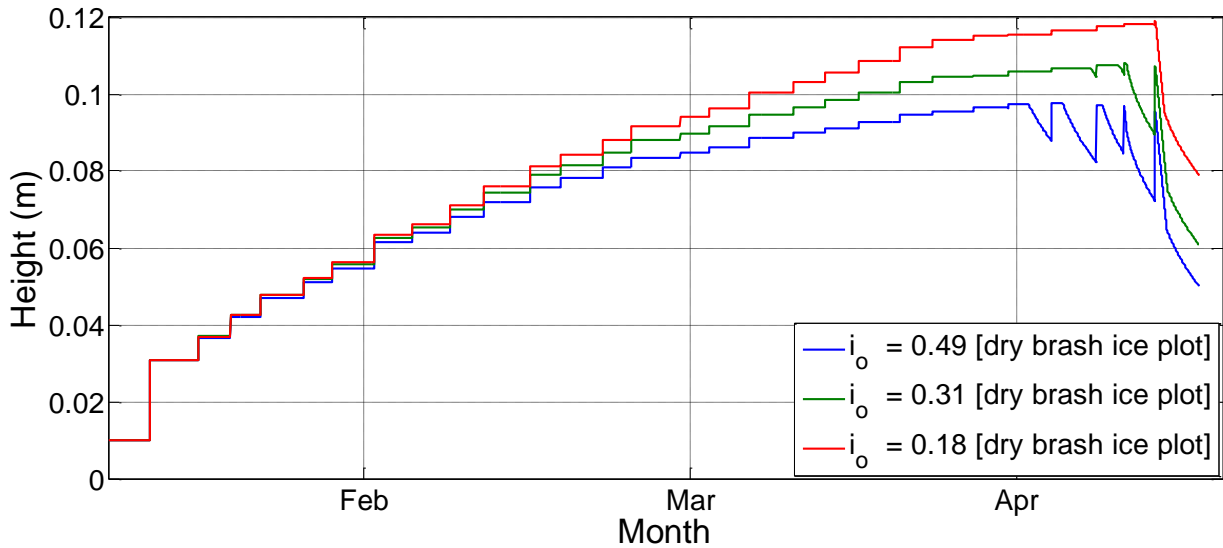


Figure 11-32 Dry brash ice thickness evolutions for the 3 different possible values of solar radiation absorption proportion.

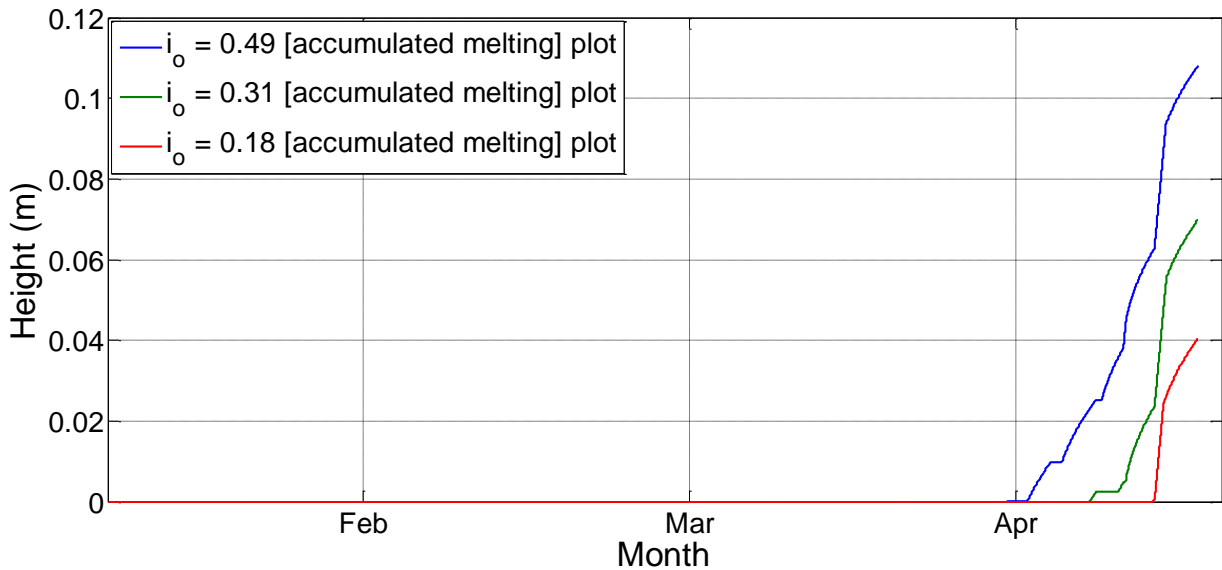


Figure 11-33 Accumulated melting plots, in the 3 possible cases of net solar radiation absorption proportion

Figure 11-34, shows the evolution of the solid ice thickness for the 3 cases of solar radiation absorption. The obvious and expected finding here is that the lower the solar radiation absorption proportion, the higher the thickness of the solid ice. However, what is interesting to notice in this graph is that after the last breaking event of March, solid ice does not regrow for the cases of $i_o = 49\%$ and $i_o = 31\%$. This is because, in these cases and in that stage of the simulation, where temperatures are high, the temperature of the bottom of the solid ice becomes equal to T_f and remains equal to T_f , hence there is no temperature difference to initiate solid ice growth, see Eq. (6-11) and section 6.1.3.

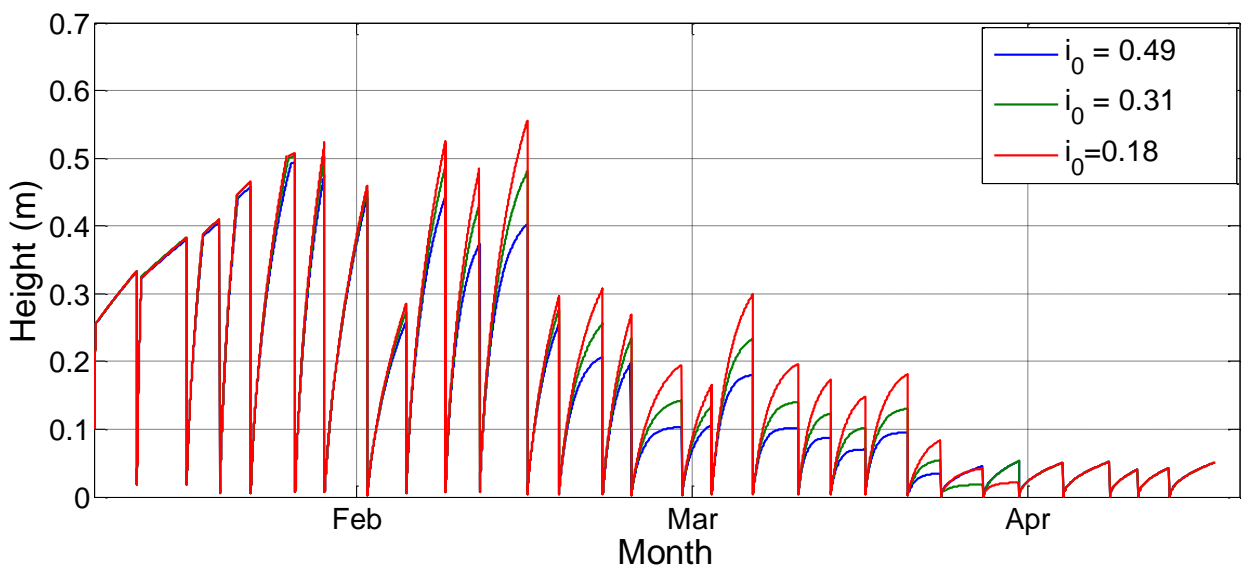


Figure 11-34 Solid ice evolution for the 3 different possible cases of solar radiation absorption proportion.

Table 11-4 and Table 11-5 show quantitative analysis of the impact of solar radiation absorption proportion, on the total ice thickness in the end of the cold season and the maximum value of the solid ice thickness during the cold season, respectively.

Table 11-4 Quantitative analysis of the impact of solar radiation absorption on the total ice thickness in the end of the cold season,

i_o % (solar radiation absorbed below the surface)	Total Ice thickness at the end of the cold season	
	$h_{tot}(m)$	Impact of solar absorption (%)
$i_o = 49\%$	1.05	-0.13/-11%
$i_o = 31\%$	1.18	-
$i_o = 18\%$	1.32	+0.14/+11.9%

Table 11-5 Quantitative analysis of the impact of solar radiation absorption on the maximum solid ice thickness during the cold season.

i_o % (solar radiation absorbed below the surface)	Maximum Solid Ice thickness during the cold season	
	$h_i(m)$	Impact of solar absorption (%)
$i_o = 49\%$	0.49	-0.01/-2%
$i_o = 31\%$	0.50	-
$i_o = 18\%$	0.55	+0.05/10%

11.3.3 Conductivity of dry brash ice

For the conductivity of the dry brash ice, λ_{dbi} , the same values used in the parametric study for the Sabetta reference case are used for the parametric study for the Lulea reference case as well. It is reminded here that the reference value for the conductivity of the dry brash ice was obtained using some assumptions from (Hoobs, 1974). The maximum and minimum values of the parametric study were based on $\pm 30\%$ of this reference value.

Figure 11-35, shows the total ice thickness evolution for the 3 possible values of thermal conductivity of the dry brash ice. Again, as it was observed in the Sabetta reference case as well, the greater the conductivity value of the dry brash ice, the greater the value of the total ice thickness. This also holds for the solid ice thickness as well, see Figure 11-36.

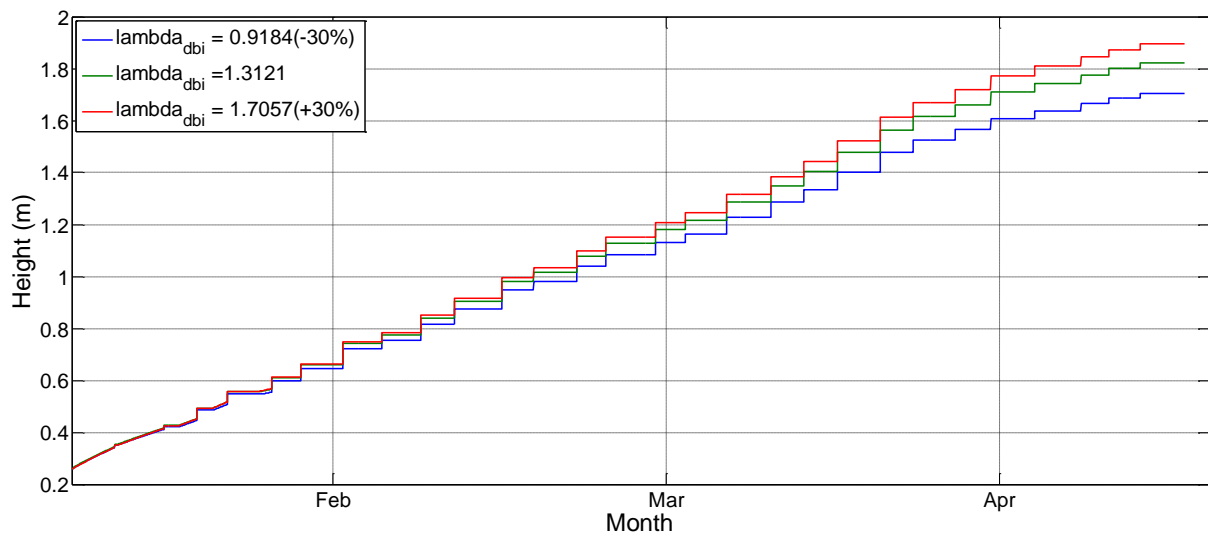


Figure 11-35 Evolution of the total ice thickness, for the 3 possible cases for the thermal conductivity value of the top dry brash ice layer. Reference Lulea case using BIGM 2 with dry brash ice.

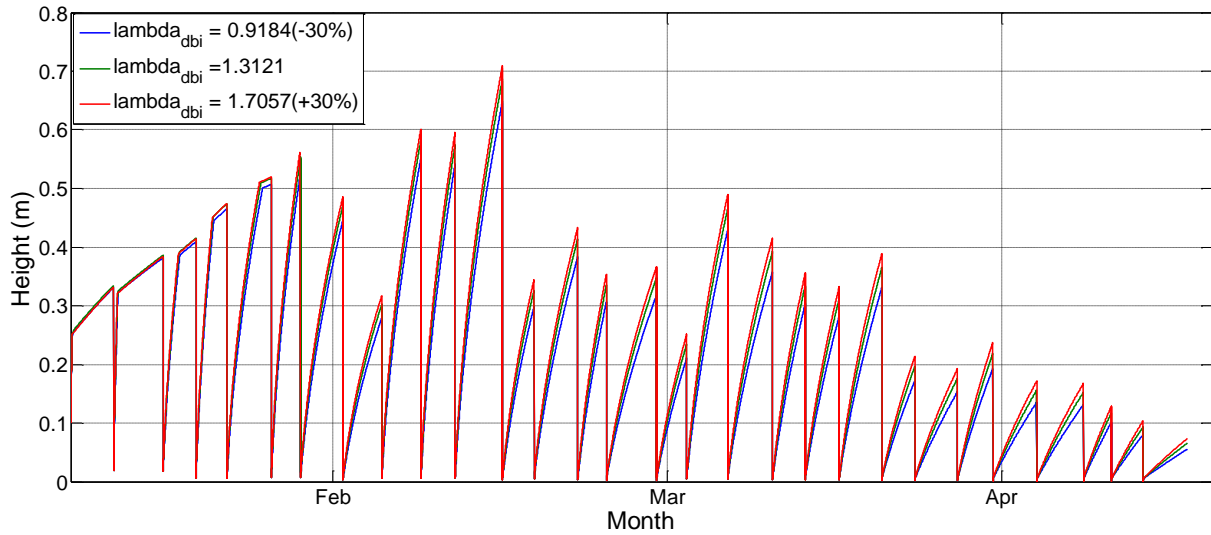


Figure 11-36 Evolution of the solid ice thickness, for the 3 possible cases for the thermal conductivity value of the top dry brush ice layer. Reference Lulea case using BIGM 2 with dry brush ice.

Table 11-6, shows a quantitative analysis of the impact of the thermal conductivity of the dry brush ice layer, on the total ice thickness in the end of the cold season. As it can be seen, as the value of the brush ice conductivity, λ_{dbi} gets higher, the impact of a further increase on the total ice thickness, and also on the solid ice thickness, is decreasing.

Table 11-6 Influence of the dry brush ice conductivity on the total ice thickness in the end of the cold season, BIGM 2 with dry brush ice, reference Lulea Case.

Dry brush Ice conductivity	Total Ice thickness at the end of the cold season	
	$h_{tot}(m)$	Impact of λ_{dbi} (%)
λ_{dbi} (-30%)	1.70	-0.12/-6.59%
λ_{dbi}	1.82	-
λ_{dbi} (+30%)	1.90	+0.08/+4.40%

11.3.4 Synthesis of the parametric study for Lulea Reference case

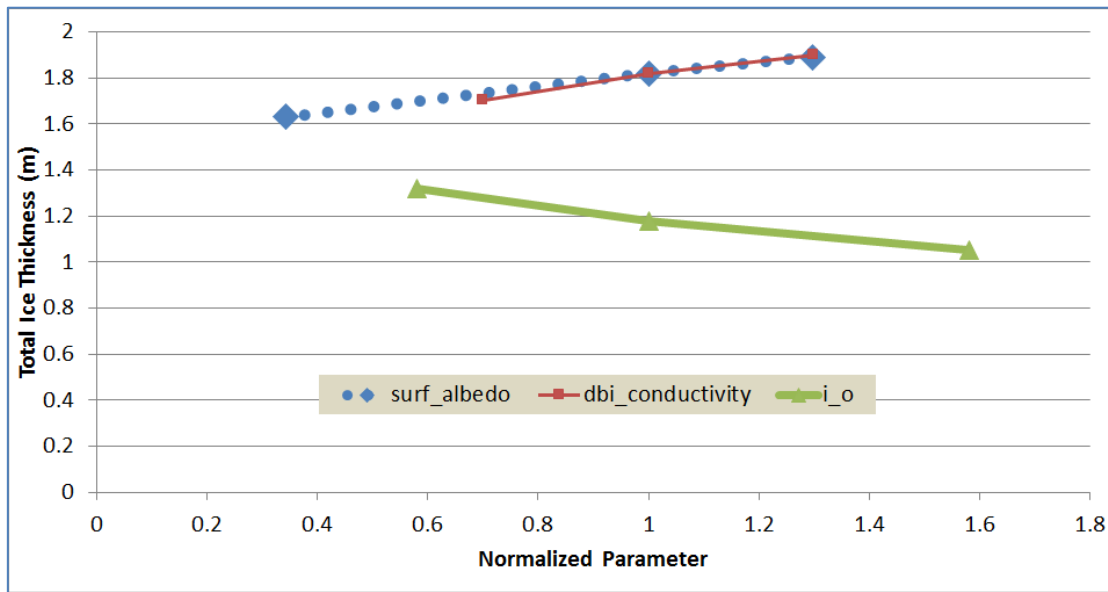


Figure 11-37 Synthesis of the results of the parametric study for Lulea reference case. Sensitivity of the total ice thickness to the three tested input parameters.

In this section, the impact of the variation of each examined parameter on the value of the total ice thickness in the end of the cold season, is going to be compared against the impact of the other examined parameters, as it was exactly done for the Sabetta reference case in section 9.7.7.

In order to be able to include all the input parameters on the abscissa axis, the parameter input values were transformed into a dimensionless form with respect to their reference value. For example the dimensionless value of $i_o = 0.18$, is $i_o = 0.18/0.31$ because its reference values is 0.31, see Table 11-2.

From the graph in Figure 11-37, the input parameter that has the greatest impact, from the examined parameters, on total ice thickness in the end of the cold season, is the proportion of internal solar radiation absorption i_o . The parameter with the second greatest impact is the value of the surface albedo a .

12. Brash Ice Management System in Ports, and estimation of energy needs using BIGM 1 and BIGM 2

12.1 Ice control by melting

Sources of thermal energy close or within the icy water mass, make navigation through brash ice areas easier. These thermal sources, in the form of warm water at a temperature that is at least higher than the freezing (and hence ice melting) temperature, cause some parts of the brash ice to melt. Warm water can easily melt fine particles of ice such as frazil ice, hence reducing the brash ice cohesion within a channel or a port.

However, melting ice with warm water in ports or channels, is most of the times an inefficient procedure as thermal energy easily drifts away, and only a small proportion of it, is actually used to melt ice. (Saarinen, Suojanen, & Eranti, 2011), mentions a number of ports where air bubbler systems or surface current generators have been used to melt ice more efficiently than just using thermal effluents, and to concentrate the melting energy in critical areas such as the berthing areas. The list of ports using these systems includes the ports of Tornio, Kemi Veitsiluoto, Kokkola and Oulu. The air bubbler system used in Oulu is shown in Figure 12-1.

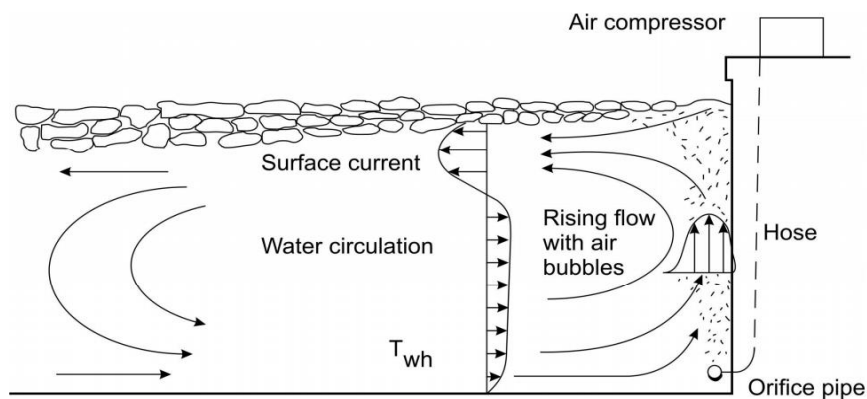


Figure 12-1 Bubbler system used for ice control in Oulu. About 100 MW of thermal effluents are released a few hundred meters upstream from the harbour basin. The bubbler system draws the warm water in and turns it into a surface current that melts brash ice. Extracted from (Saarinen, Suojanen, & Eranti, 2011).

An air bubble system sucks warm water from the bottom, and produces a strong surface current, see Figure 12-1. When this surface current passes under the brash ice layer, it loses energy by melting the brash ice from the bottom. The rougher the underside of the brash ice, the greater the turbulence that would be caused when the surface current passes, and according to (Saarinen, Suojanen, & Eranti, 2011), the more effective the brash ice melting.

Conceptual designs for ice control systems (BIMS) in the Yamal LNG of Sabetta have been made by (Saarinen, Suojanen, & Eranti, 2011). Based on these conceptual designs and other similar designs, Bertin Technologies has performed several CFD analyses to compute the heat and flow transfer induced by possible Brash Ice Management arrangements (BIMS) in the port of Sabetta, see (Bloquin [4], 2013) and (Bloquin, 2014). It is not in the scope of this study to produce a complete design of a possible Brash Ice Management System for the Yamal LNG port. Moreover, it is not in the scope of this study to determine the total amount of energy required to manage ice in the Yamal LNG port, as this requires detailed CFD computations with special softwares. However, using the Brash Ice Growth

models developed in this study, it is possible to give estimates of the energy required to melt ice in Sabetta, if this energy is solely used for melting ice, with an efficiency of 100%.

12.2 Energy estimates for brash ice melting in Sabetta

The way the brash ice management system (BIMS) effect, melting of brash ice, is included into the BIGMs developed in this study, has been explained in section 4.2, and the whole idea is described by Equations (4-24), (4-25) and (4-26). Basically a continuous melting effect is applied during the simulation, due to an external heat flux Q_w , with the amount of brash ice melted, $\Delta h_{bi\text{melted}}$, at every time step, being calculated and subtracted from the remaining brash ice layer, see section 4.2.

Figure 12-2 shows the evolution of total ice thickness, in the situation of having a dry brash ice layer, with BIGM 2 for the Sabetta reference case, with and without applying a BIMS flux $Q_w = 20 \text{ W/m}^2$. Application of conservation of energy, porosity decrease, during breaking events was applied according to section 7. As it is shown, an external heat flux of $Q_w = 20 \text{ W/m}^2$, causes the total ice thickness in the end of the cold season to decrease by 1m, in this case. This decrease of 1m corresponds to the total amount/ thickness of brash ice melted during the cold season.

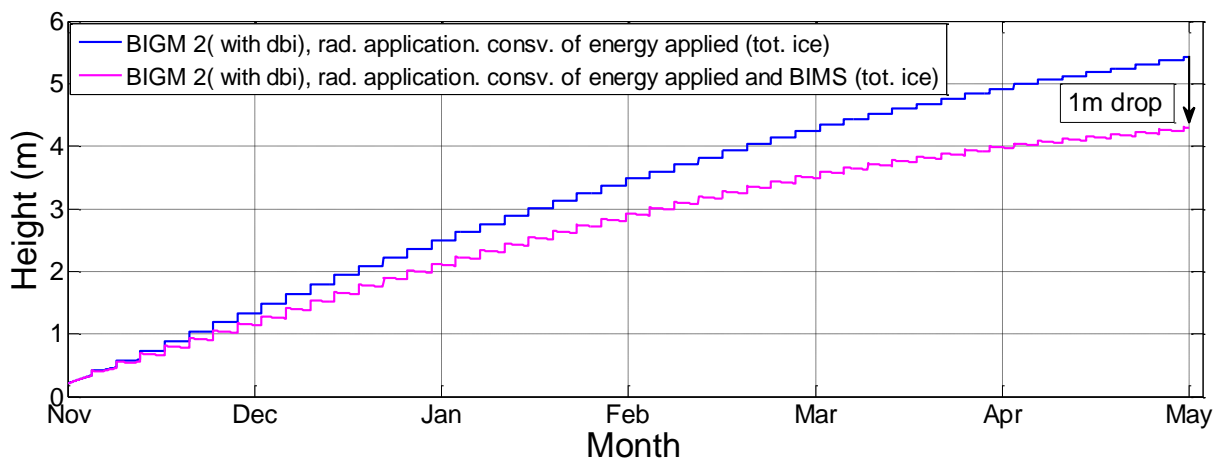


Figure 12-2 BIMS application to decrease total ice thickness by 1m. BIGM 2 with freeboard and application of conservation of energy (porosity decrease after breakings), using Reference Sabetta case as input. A BIMS flux of $Q_w=20 \text{ W/m}^2$ was needed to achieve a 1m decrease in the total ice in the end of the cold season (1m was melted from the brash ice at the bottom).

In Table 12-1, a list of estimated heat flux values to melt 1m of brash ice in the Sabetta area by the end of the cold season, is provided, for situations with and without dry brash ice, and for situations with and without the inclusion of the long wave radiation effect. Moreover an estimate of the power to be provided in the Sabetta port, corresponding to each heat flux value, to achieve the 1m melting, is provided using an approximate Sabetta port area of 0.5 km^2 , see Table 12-1.

Since YAMAL LNG has assumed so far, an acceptable total ice thickness limit for navigation of 4m, the heat flux and the corresponding power needed, to bring the total ice thickness just below the limit of 4m in the Sabetta port, is provided as well, for each of the situations listed in Table 12-1, see Table 12-2.

Figure 12-2 corresponds to the “BIGM 2(with dbi and rad)” case of Table 12-1. Similar plots for the other cases are provided in appendix J.

Table 12-1 Heat flux and power needed to melt 1m of brash ice in the port of Sabetta by the end of the cold season. Estimates of flux and power were done with simulations using both BIGM 1 and BIGM 2(with long wave radiation), applying conservation of energy in all the simulations (porosity decrease after breaking event) and testing both the cases of having and not having a dry brash ice layer on the top of the solid ice.

Flux and Power needed to melt 1m of brash ice in the Sabetta Port	Heat Flux (W/m^2)	Power in MW for 0.5 km² (approx. Sabetta Port Area)
BIGM 1(no dbi)	12	6
BIGM 1(with dbi)	19	9.5
BIGM 2(no dbi and rad)	13	6.5
BIGM 2(with dbi and rad)	20	10

Table 12-2 Heat flux and power needed to bring total ice thickness just below the limit of 4m by the end of the cold season, in the port of Sabetta. Estimates of flux and power were done with simulations using both BIGM 1 and BIGM 2(with long wave radiation), applying conservation of energy in all the simulations (porosity decrease after breaking event) and testing both the cases of having and not having a dry brash ice layer on the top of the solid ice.

Flux and Power needed to bring total ice thickness just below the Yamal LNG limit of 4m	Heat Flux (W/m^2)	Power in MW for 0.5 km² (approx. Sabetta Port Area)
BIGM 1(no dbi)	60	30
BIGM 1(with dbi)	19	9.5
BIGM 2(no dbi and rad)	78	39
BIGM 2(with dbi and rad)	26	13

13. Conclusions and Recommendations

After a detailed review of previous publications and case studies regarding key phenomena, affecting ice growth and brash ice growth, and related analytical and numerical models, this study presents the formulation for two Brash Ice Growth Models, called BIGM 1 and BIGM 2. BIGM 1 is based on the analytical thermodynamic ice growth equations of (Stefan , 1891) and simplified extensions, and BIGM 2 is based on the easily adjustable multiple-layer thermodynamic sea ice model of (Ukita & Martinson, 2001), solved numerically. The two brash ice growth models, use the same ice breaking model to describe breaking events resulting from vessel passages in a channel ship track, and this breaking model has been analytically derived, based on the conservation of mass and energy. In BIGM 1, the solid ice re-growth through the existing brash ice layer is driven solely by the sensible heat flux, as it is the only heat flux that can be included in the analytical thermodynamic equations of the model. On the other hand in BIGM 2, the user has the advantage of including all the heat fluxes involved in the ice growth phenomenon, namely the long wave radiation, short wave radiation, sensible heat flux and latent heat flux, in addition to some physical processes that take place in ice while it is growing, such as the variation of thermal properties in multiple layers in the ice mass, and internal absorption of a proportion of the non-reflected solar radiation, by the multiple layers of the ice mass. Using BIGM 1, is an efficient way to obtain first approximations of the Brash Ice Growth in different situations, however BIGM 2 can provide more pragmatic simulations, due to its' additional features mentioned above, and hence more exact results. It has been proved that under the same conditions and input data, BIGM 1 and BIGM 2 give identical results. The key result that the simulations with the two models give, is the "equivalent" thickness of total ice or total brash ice formation in a ship track, defined as the resulting thickness of brash ice accumulated in a vessel track, of width equal to the vessel beam, if all brash ice is contained in the track.

The feature that changes the results in both brash ice growth models, BIGM 1 and BIGM 2, significantly, is the addition of a dry brash ice layer on top of the growing solid ice. The separation line between the solid ice and the dry brash ice is assumed to be the waterline at all times. The dry brash ice has a lower conductivity than the solid ice and hence it acts as an insulating layer which decreases the rate with which the solid ice grows and hence it decreases the thickness/volume of brash ice in the end of the cold season. This is also proved by the calculation of temperatures in both BIGM 1 and BIGM 2. Observing the temperature profiles in simulations with BIGM 2 shown in this study, in identical situations where in one case the dry brash is layer is included and in the other case the dry brash ice is not included, it is easily seen that corresponding solid ice layer temperatures have higher/hotter temperatures in the situation in which dry brash ice is included. Higher temperatures in the solid ice, result in lower temperature difference between the bottom solid ice sub-layer and the brash ice mass, which is at freezing temperature, and this causes a smaller amount of solid ice growth in each simulation step. The inclusion of this feature is one of the key points of this study, as it is a feature that was not addressed or included in previous brash ice growth models or studies.

In BIGM 2, the application of the effect of the variation of thermal properties, such as the heat capacity and the thermal conductivity, in the sub-layers of solid ice and dry brash ice has shown that it causes a decrease in the total ice thickness in the end of the cold season, and it also causes a decrease in the solid ice thickness during the cold season. This applies to both the situations of having and not having a dry brash ice layer, and it is explained by the decrease in thermal conductivity as the simulation approaches the spring months and at the same time the increase in the heat capacity.

A similar impact in the results of BIGM 2, has the application of the effect of internal absorption of a proportion of the non-reflected solar radiation, by the sub layers of solid ice and dry brash ice. Internal absorption causes a rise in the temperatures inside the whole ice mass, and this rise in temperatures alters the growth rate of solid ice, causing it to decrease, and hence decrease the amount of total ice in the end of the cold season. If a constant absorption proportion is applied during the whole simulation period as it was the case in this study, the amount of solar radiation absorbed is significantly increased towards the spring months where solar radiation acquires high values. If the top surface temperature, in the situation where a dry brash ice layer is included on top of the solid ice in the formulation, acquires values as high as the freezing temperature, melting starts to take place. Note that in a formulation which does not include the dry brash ice layer, melting cannot take place, as the whole ice mass, which consists of solid ice and wet brash ice, is assumed to be below the waterline.

As this study was initiated due to the need of YAMAL LNG to take ice management decisions for their project in the port of Sabetta, the first simulations using the developed models, were aiming to predict the total ice thickness using scenarios formed specifically for the Sabetta approach channel. After an examination of previous reports on the metocean conditions in areas nearby or similar to the Sabetta area, and reviewing previous studies regarding the operation of the YAMAL LNG port and the expected navigation traffic in different operational phases, a reference case was defined to run simulations with BIGM 1 and BIGM 2, and predict the total ice thickness in the approach channel and the port in the end of the cold season. In these simulations the only difference between the input data for BIGM 1 and BIGM 2, was the inclusion in BIGM 2 of sets of monthly average values for the long wave radiation flux. The long wave radiation flux was identified as the most important component, of the available ones, that couldn't be included in BIGM 1 but could be included in BIGM 2. The results of the simulations though, showed that the inclusion of the long wave radiation effect caused only a slight increase in the total ice thickness in the end of the cold season in both the cases, with and without a dry brash ice layer in the formulation. An increase in the ice thickness, due to the inclusion of a long wave radiation effect might seem odd at first sight, but it can be readily explained from the top surface flux balance equation which includes an outgoing long wave radiation term (black-body radiation term) that includes the 4th power of the top surface temperature. Therefore, when the long wave radiation effect is included in the formulation with no other input radiation, for the total ice or solid ice thickness to remain unchanged the input long wave radiation must equal the outgoing long wave radiation at all times. Furthermore, in order to cause a decrease in the total ice thickness in the end of the cold season, the input long wave radiation term must be greater than the output most of the times during the simulation. For the reference case scenario, with the application of the conservation of energy during breaking events, and the long wave radiation effect, the total ice thickness in the end of the cold season was predicted 9.8m for the "no dry brash ice situation" and 5.3m for the "with dry brash ice" situation. As the "with dry brash ice situation" is the most physically correct case, the results from this situation are considered more pragmatic.

As most of the parameters that form the Sabetta reference case, are only approximate average values, a parametric study was performed on a number of identified critical parameters to test the sensitivity of the results, to a change in the value of these parameters. The parametric study was performed using BIGM 2 and including the dry brash ice layer, showing that the results of the simulations in terms of total ice thickness, were most sensitive to changes in the input average brash ice porosity, the input thermal conductivity of the dry brash ice layer, and the input ship track breaking frequency.

The reference case for Sabetta defined in this study is based on the use of multiple tracks in the approach channel to the harbour, five specifically, used alternatively for navigation. Another scenario that has been used by previous studies assumes the use of a single track until it reaches a maximum navigable equivalent brash ice thickness, which is defined by the user. Using this scenario, called “successive tracks” in the report, one can estimate the number of tracks that are going to be required to open during the whole cold season. BIGM 2 with and without the inclusion of the dry brash ice layer was used in a simulation with this scenario to test how a change in the ship track transiting strategy changes the results of the model. Defining a maximum navigable thickness of 6.25m, the simulation estimated that using this ship track transiting strategy, four tracks are going to be needed during the whole cold season, in the case of bare solid ice growth, and only one track in the case of including the dry brash ice layer in the formulation. The latter is a very interesting result as it suggests a decrease in the number of used tracks by a factor of five. However, further tests and simulations using brash ice field data and field metocean measurements, are needed to verify this. In practice, what a different track transiting strategy changes in the model is the track breaking frequency.

After completing simulations using Sabetta port specific scenarios, the two developed models were used to run simulations with input data from the Lulea channel brash ice field measurements and metocean measurements, from the winter 2012-2013. The aim of this task was to show how close the field measurements to the models’ predictions are, when the input data to the models are directly taken from the specific field. Firstly, the field data was analyzed and field average plots of ice thickness across the channel ship track were plotted. Moreover equivalent total ice thickness plots across the channel were produced using certain assumptions, with the basic one being that all the brash ice in each channel measurement, is included within the ship track. It is noted here that from the analysis of the field measurements it was estimated that about 36% of the brash ice moves outside of the ship track. Afterwards, an input set of data for the BIGM models was created including Lulea channel breaking time instants, along with the corresponding metocean and field data for each instant. Simulations using this input data, were run for both BIGM 1 and BIGM 2, with the only difference, in terms of input, for the two simulations being, the inclusion of the radiation values, shortwave and long wave, only in BIGM 2, as it was the case for the Sabetta reference case as well. For the situation with “no dry brash ice” BIGM 2 gave a total ice thickness in the end of the simulation of 2.3m, which was 0.7m greater than what BIGM 1 predicted, and for the situation “with dry brash ice” BIGM 2 gave a thickness of 1.8m which was 0.4m greater than what BIGM 1 predicted. The total ice thickness evolutions with BIGM 2, for both cases “with” and “without dry brash ice”, were better included within the interval between the “average field measurements of total ice thickness plot” and the “equivalent average field measurements of total ice thickness plot”. The two field plots can be seen as a minimum and a maximum limit respectively, of the prediction of the total ice thickness.

Applying different effects in simulations with the Lulea reference case using BIGM 2, such as the variation of thermal properties in ice and dry brash ice layers and the application of internal solar radiation absorption, caused the total ice thickness plots in the end of the simulation to decrease, bringing the plots closer to the “average field measurements of total ice thickness plot”. Looking specifically the plot of BIGM 2, which includes dry brash ice in the formulation, in which an internal solar radiation absorption of 31% was applied, it is seen that is extremely close to the plot of “average field measurements of total ice thickness plot”. Moreover the dry brash ice plot from the model seems to match the “average field measurements plot for the dry brash ice thickness”, even showing melting taking place in mid-April, just as it seems to be happening in the field.

The availability of field input data for various metocean components affecting the ice growth and hence the brash ice growth problem, in the Lulea simulation case, allowed us to perform a parametric analysis for more “insight” ice growth problem parameters, such as the surface albedo and the proportion of net solar radiation internal absorption. From the parametric study synthesis, comparing the impact due to a change in the value of the surface albedo, the net solar radiation absorption proportion and the dry brash ice conductivity, for the Lulea simulation case, it was concluded that the variation in the value of the proportion of the net solar radiation absorption, has the greatest impact in the total ice thickness value in the end of the cold season. The impact of a change in the surface albedo was also important and it was found to be greater than the impact due to a change in the value of the dry brash ice conductivity. However it has to be noted that these results are relevant and are based on the chosen sets of values used in the parametric study for each varying parameter, and also on the field specific metocean data. For example in a location where solar radiation is very low during the whole simulation period, the thermal conductivity of the dry brash ice could be the parameter with the greater impact on the results, if it is varied.

In both of the BIGM models developed in this study, a Brash Ice Management system (BIMS) effect was introduced from the basic principles of growth and melting of ice. Basically the BIMS effect, is identically applied in the models as a continuous melting effect during the simulations, due to an external heat flux applied in the bottom of brash ice, causing a brash ice strip to melt in every simulation time step. Using the reference case of Sabetta, the study provides estimates for the values of this external heat flux required to melt 1m of brash ice and to bring the total ice thickness below 4m in the end of the simulation period. These estimates are done for different situations using simulations from both BIGM 1 and BIGM 2. For the situation which is the most physically correct case, BIGM 2 with dry brash ice and application of long wave radiation, it was estimated that a constant heat flux value of $Q_w = 20 \text{ W/m}^2$, is required to melt 1m of brash ice, by the end of the cold season, and a heat flux value of $Q_w = 26 \text{ W/m}^2$ is required to bring the total ice thickness just below 4m by the end of the cold season. It has to be reminded here that the calculations done in this study, assume that this energy is going to be used solely for melting of the brash ice with 100% efficiency, something that is definitely not true in reality. In reality thermal energy would drift away in the port or approach channel and dissipate. Our estimates for melting of ice can be used by Yamal LNG, for narrow and closed locations where thermal energy cannot easily drift away, such as the berthing areas inside the port.

The models developed in this study and especially BIGM 2, showed very good predictions of the total ice thickness evolution in the Lulea reference case, where exact field brash ice porosity and field metocean data were used. Although the scenarios used in this study for the Sabetta reference case, may give good approximations and estimations of the brash ice growth problem in the area of Sabetta, in order to have more accurate and valid results, field input data, such as the ones from Lulea, are necessary. If this data is available, the models of this study can be used to give very good estimates of the total ice or brash ice thickness in Sabetta at certain periods of the year, and these estimates and predictions can be given to Yamal LNG with confidence.

Finally, the models developed in this study, can be used in the future by TOTAL for different projects and in different situations. They can be used again to estimate brash ice growth in similar, to the Yamal LNG projects, in the Arctic area, but they can also be used as metocean-climatological models that would predict ice growth under different environmental conditions, in different locations, since they have the ability to take as input sets of multiple field data.

Appendix

A. Derivation of Porosity decrease (no dry brush ice, BIGM 1 and 2)

$$H_{tot} = \sum_{k=1}^{Ni} h_{i,k} (H_i(T_f) + Cp_i(T_{i,k} - T_f)) + H_i(T_f) \cdot h_{bi}(1 - p_{bi}) + H_w(T_f) \cdot p \cdot h_{binew} \quad (1)$$

where $H_i(T_f)$ and $H_w(T_f)$ are the enthalpies of ice and water respectively at the freezing temperature T_f , h_i is the thickness of the solid ice and T_{av} is the average temperature of the brush ice mixture just after breaking. Also here it is reminded that the latent heat of fusion at T_f , L_i , is equal to $H_w(T_f) - H_i(T_f)$.

The enthalpy of brush ice layer after return to thermal equilibrium is given by:

$$H_{tot} = H_i(T_f) \cdot (1 - p_{binew}) \cdot h_{binew} + H_w(T_f) \cdot p_{binew} \cdot h_{binew} \quad (2)$$

But (1) = (2) and re-arranging:

$$\begin{aligned} \sum_{k=1}^{Ni} h_{i,k} (H_i(T_f) + Cp_i(T_{i,k} - T_f)) &= -H_i(T_f) \cdot h_{bi}(1 - p_{bi}) - H_w(T_f) \cdot p \cdot h_{binew} + \\ &H_i(T_f) \cdot (1 - p_{binew}) \cdot h_{binew} + H_w(T_f) \cdot p_{binew} \cdot h_{binew} \\ \sum_{k=1}^{Ni} h_{i,k} (H_i(T_f) + Cp_i(T_{i,k} - T_f)) &= h_{binew} [H_i(T_f) - H_w(T_f)p + p_{binew} [H_w(T_f) - H_i(T_f)]] - H_i(T_f) \cdot h_{bi}(1 - p_{bi}) \\ \sum_{k=1}^{Ni} h_{i,k} (H_i(T_f) + Cp_i(T_{i,k} - T_f)) &= h_{binew} [H_i(T_f) - H_w(T_f)p] + h_{binew} p_{binew} Li - H_i(T_f) \cdot h_{bi}(1 - p_{bi}) \\ \sum_{k=1}^{Ni} h_{i,k} (H_i(T_f) + Cp_i(T_{i,k} - T_f)) - h_{binew} [H_i(T_f) - H_w(T_f)p] &+ H_i(T_f) \cdot h_{bi}(1 - p_{bi}) = h_{binew} p_{binew} Li \\ p_{binew} &= \frac{\sum_{k=1}^{Ni} h_{i,k} Cp_i(T_{i,k} - T_f)}{h_{binew} Li} + \frac{-h_{binew} [H_i(T_f) - H_w(T_f)p] + H_i(T_f) h_{bi}(1 - p_{bi}) + h_i H_i(T_f)}{h_{binew} Li} \\ p_{binew} &= \frac{\sum_{k=1}^{Ni} h_{i,k} Cp_i(T_{i,k} - T_f)}{h_{binew} Li} + \frac{H_i(T_f) [h_i - h_{binew} + h_{bi}(1 - p_{bi})] + H_w(T_f) [p h_{binew}]}{h_{binew} Li} \quad (4) \end{aligned}$$

$$\text{But, } h_{binew}(1 - p) = h_i + h_{bi}(1 - p_{bi}) \quad (5)$$

But substituting (5) into (4), and simplifying, the second term of Eq.4 simplifies to p . Hence:

$$p_{binew} = \frac{\sum_{k=1}^{Ni} h_{i,k} Cp_i(T_{i,k} - T_f)}{h_{binew} Li} + p \quad (6)$$

For BIGM 1, using exactly the same method and idea, this changes simply to:

$$p_{binew} = p + \frac{h_i C p_i (T_{av} - T_f)}{L_i h_{binew}} \leq p$$

Derivation Completed

B. Derivation of Eq. (4-15) Ice Growth Equation in the case of having dry brash ice (freeboard), Thermodynamics BIGM 1

Deriving:
$$\rho_i p L_i (dh_i / dt)_{hi} = \frac{h_c (T_f - T_a)}{1 + h_c h_i / \lambda_i + h_c h_{dbi} / \lambda_{dbi}}$$

$$1. \quad h_c (T_o - T_a) = \frac{1}{\left(\frac{h_i}{\lambda_i} + \frac{h_{dbi}}{\lambda_{dbi}}\right)} (T_f - T_o) \quad (1)$$

$$2. \quad h_c (T_o - T_f + T_f - T_a) = \frac{1}{\left(\frac{h_i}{\lambda_i} + \frac{h_{dbi}}{\lambda_{dbi}}\right)} (T_f - T_o) \quad (2)$$

$$3. \quad h_c (T_o - T_f) + h_c (T_f - T_a) = \frac{1}{\left(\frac{h_i}{\lambda_i} + \frac{h_{dbi}}{\lambda_{dbi}}\right)} (T_f - T_o) \quad (3)$$

$$4. \quad -\frac{h_c (T_o - T_f)}{\left(\frac{h_i}{\lambda_i} + \frac{h_{dbi}}{\lambda_{dbi}}\right)} + \frac{h_c (T_f - T_a)}{\left(\frac{h_i}{\lambda_i} + \frac{h_{dbi}}{\lambda_{dbi}}\right)} = 1 \quad (4)$$

$$5. \quad \frac{h_c (T_f - T_a)}{\left(\frac{h_i}{\lambda_i} + \frac{h_{dbi}}{\lambda_{dbi}}\right)} = 1 + h_c \left(\frac{h_i}{\lambda_i} + \frac{h_{dbi}}{\lambda_{dbi}}\right) \quad (5)$$

$$6. \quad \frac{h_c (T_f - T_a)}{1 + h_c h_i / \lambda_i + h_c h_{dbi} / \lambda_{dbi}} = \frac{1}{\left(\frac{h_i}{\lambda_i} + \frac{h_{dbi}}{\lambda_{dbi}}\right)} (T_f - T_o) \quad (6)$$

$$7. \quad \rho_i p L_i (dh_i / dt)_{hi} = \frac{h_c (T_f - T_a)}{1 + h_c h_i / \lambda_i + h_c h_{dbi} / \lambda_{dbi}} \text{ Derivation completed} \quad (7)$$

C. Relation between wet brash ice and dry brash ice just after breaking

Archimedes principle states: A body totally or partially immersed in a fluid is subject to an upward force equal in magnitude to the weight of fluid it displaces.

Assuming the total ice column (wet brash ice +dry brash ice), after a breaking event, as one body and also that the wet brash ice has the same porosity as the dry brash ice, and also excluding the water from the brash ice mass for the application of the Archimedes principle, we have:

$$(h_{tot})\rho_i(1-p) = (h_{bi})(\rho_w)(1-p) \quad (1)$$

$$(h_{dbi} + h_{bi})\rho_i(1-p) = (h_{bi})(\rho_w)(1-p) \quad (2)$$

$$(-h_{bi})\rho_i + (h_{bi})\rho_w = (h_{dbi})(\rho_i) \quad (3)$$

$$h_{dbi} = \frac{(h_{bi})\rho_w}{\rho_i} - h_{bi} = h_{bi} \left(\frac{\rho_w - \rho_i}{\rho_i} \right) \quad (4)$$

D. Inclusion of the latent heat flux equation to the top surface flux equilibrium equation

From (Maykut, 1978) the latent heat flux is given by:

$$F_L = 0.622 \rho_i L_v C_e u \frac{(f e_{sa} - e_{so})}{p_o} \quad (1)$$

Where ,

C_e is the evaporation coefficient(see Deardorff 1968 for the value)

e_{so} saturation vapour pressure at the ice surface

e_{sa} saturation vapour pressure in the air (at a reference height)

f relative humidity (%)

p_o is the surface pressure

L_v latent heat of vapourization

ρ_i is the density of the air

u is the wind speed

The saturation vapour pressure for either ice or air, can be expressed as:

$$e_s = aT^4 + bT^3 + cT^2 + dT + e' \quad (2)$$

where a, b, c, d and e are constants and T is the temperature of the surface of the ice or air respectively, depending on which saturation vapor pressure is calculated.

The constants shown in Eq. (2) have the following values:

$$a = 2.7798202 \times 10^{-6}$$

$$b = -2.6913393 \times 10^{-3}$$

$$c = 0.97920849$$

$$e' = 9653.1925$$

Moreover $C_e = 1.75 \times 10^{-3}$ and $L_v = 2.49 \times 10^6 \text{ J / kg}^{-1}$

The top surface flux equilibrium equation, when latent heat flux is included, is modified as follows:

$$Q_{RAD} - \varepsilon_{LW} \sigma T_o^4 + h_c (T_a - T_o) + 0.622 \rho_i L C_e u \frac{(f e_{sa} - e_{so})}{p_o} + \lambda_i \left(\frac{\partial T_i}{\partial z} \right)_{z=0} = 0 \quad (3)$$

And in more detail:

$$Q_{RAD} - \varepsilon_{RAD} \sigma T_o^4 + h_c (T_a - T_o) + 0.622 \rho_i L C_e u \frac{(f [a T_{air}^4 + b T_{air}^3 + c T_{air}^2 + d T_{air} + e'] - [a T_o^4 + b T_o^3 + c T_o^2 + d T_o + e'])}{p_o} + \lambda_i \left(\frac{\partial T_i}{\partial z} \right)_{z=0} = 0$$

In order for the modified surface equation to be included into the matrix system a re-arrangement of the equation is necessary. Firstly the terms containing the top surface temperature, where the top surface temperature term is of higher order than the second order, need to be linearized. Hence from

the linearization of $T_{o_{m+1}}^4$, $T_{o_{m+1}}^3$, $T_{o_{m+1}}^2$:

$$T_{o_{m+1}}^4 = T_o^4 + 4T_o^3 (T_{o_{m+1}} - T_o) = T_o^4 + 4T_o^3 T_{o_{m+1}} - 4T_o^4 = -3T_o^4 + 4T_o^3 T_{o_{m+1}}$$

$$T_{o_{m+1}}^3 = T_o^3 + 3T_o^2 (T_{o_{m+1}} - T_o) = T_o^3 + 3T_o^2 T_{o_{m+1}} - 3T_o^3 = -2T_o^3 + 3T_o^2 T_{o_{m+1}}$$

$$T_{o_{m+1}}^2 = T_o^2 + 2T_o (T_{o_{m+1}} - T_o) = T_o^2 + 2T_o T_{o_{m+1}} - 2T_o^2 = -T_o^2 + 2T_o T_{o_{m+1}}$$

Substituting back the linearized terms into the top surface equation we have:

$$Q_{RAD} - \varepsilon_{RAD} \sigma (-3T_o^4 + 4T_o^3 T_{o_{m+1}}) + h_c (T_a - T_o) + \frac{h_L}{p_o} \left[f [a T_{air}^4 + b T_{air}^3 + c T_{air}^2 + d T_{air} + e'] - [a (-3T_o^4 + 4T_o^3 T_{o_{m+1}}) + b (-2T_o^3 + 3T_o^2 T_{o_{m+1}}) + c (-T_o^2 + 2T_o T_{o_{m+1}}) + d T_o + e'] \right] + \frac{2\lambda_i}{\Delta h_i} (T_1 - T_{o_{m+1}}) = 0$$

$$Q_{RAD} + 3\varepsilon_{RAD} \sigma T_o^4 - 4\varepsilon_{RAD} \sigma T_o^3 T_{o_{m+1}} + h_c T_a - h_c T_{o_{m+1}} + h_L f [a T_{air}^4 + b T_{air}^3 + c T_{air}^2 + d T_{air} + e'] + 3h_L a T_o^4 - 4h_L a T_o^3 T_{o_{m+1}} + 2h_L b T_o^3 - 3h_L b T_o^2 T_{o_{m+1}} + h_L c T_o^2 - 2h_L c T_o T_{o_{m+1}} - h_L d T_{o_{m+1}} - h_L e' + \frac{2\lambda_i}{\Delta h_i} (T_1) - \frac{2\lambda_i}{\Delta h_i} (T_{o_{m+1}}) = 0 \quad (4)$$

Re-arranging into the appropriate form for inclusion into the matrix system:

$$Q_{RAD} + 3\varepsilon_{RAD}\sigma T_o^4 + h_c T_a + h_L f \left[aT_{air}^4 + bT_{air}^3 + cT_{air}^2 + dT_{air} + e \right] + 3h_L aT_o^4 + 2h_L bT_o^3 + h_L cT_o^2 - h_L e' =$$

$$T_{o_{m+1}} \left[4\varepsilon_{RAD}\sigma T_o^3 + h_c + 4h_L aT_o^3 + 3h_L bT_o^2 + 2h_L cT_o + h_L d + \frac{2\lambda_i}{\Delta h_i} \right] - \frac{2\lambda_i}{\Delta h_i} (T_1) = 0$$

(5)

E. Calculation sequence in ice growth cycle, BIGM 2 (no dbi)

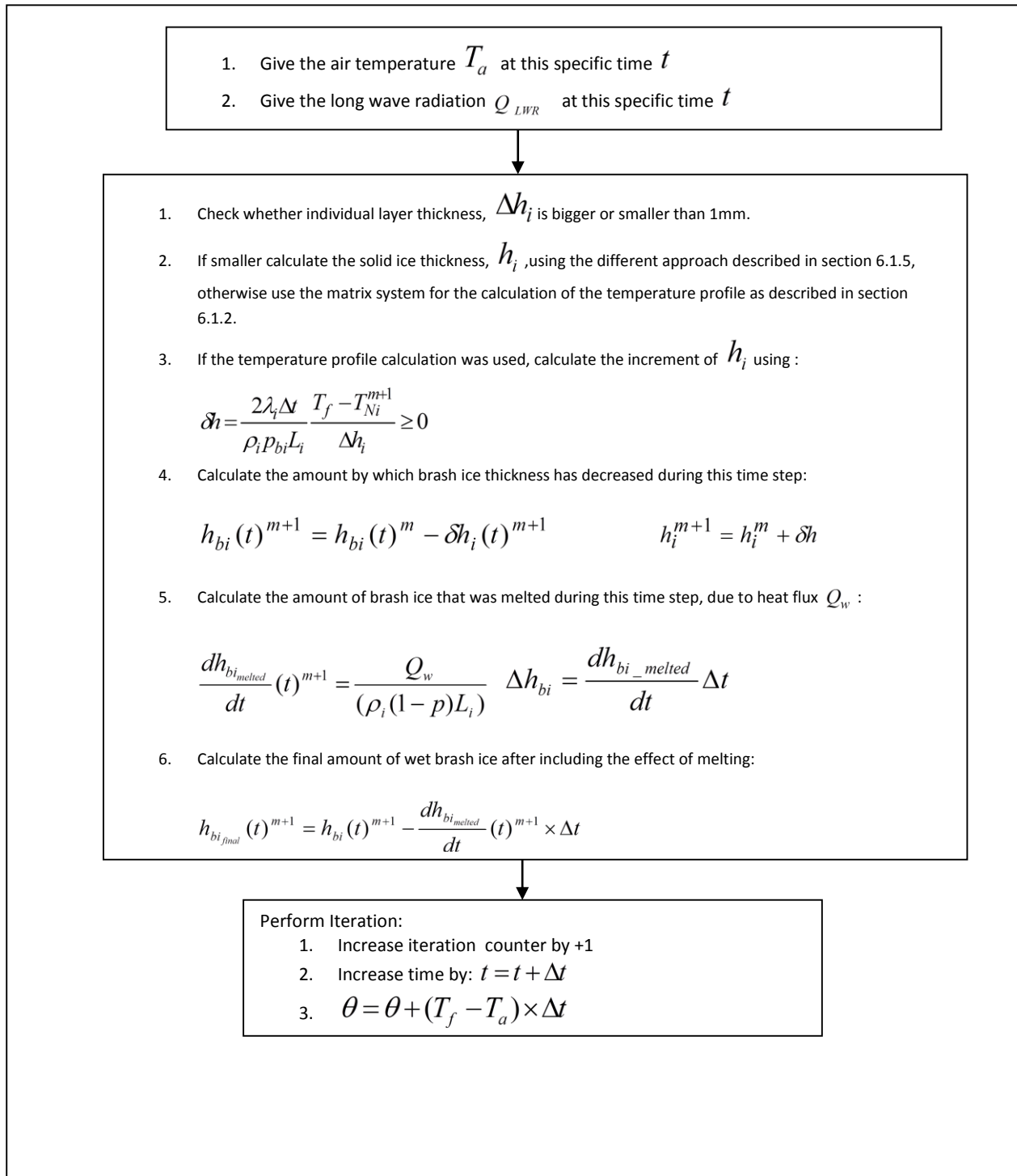


Figure E- 1 Calculation Sequence in the ice growth cycle for BIGM 2 with no dry brash ice. For BIGM 2 with dry brash ice the only thing that changes in the sequence above is the use of the matrix system with the inclusion of the dry brash ice layer.

F. Viscaria tugboat specifications

1. Built: In 2000
2. Call Sign: SMVK
3. Port of registration: Luleå
4. Class: LR+100 A1-1A SUPER
5. Length over all: 35,8 m
6. Width: 12,0 m
7. Depth Unloaded: 6,70 m
8. Tonnage: 603 BRT
9. Main Engine(s): 1xWärtsilä 12V32D 4500kw
10. Auxilary engine(s): 2xScania DS 9 95M
11. Speed: 14 knots
12. Accommodation: 7

Information extracted from, (MOENMARIN, 2015).

G. Metocean Data of Lulea Port Measurements

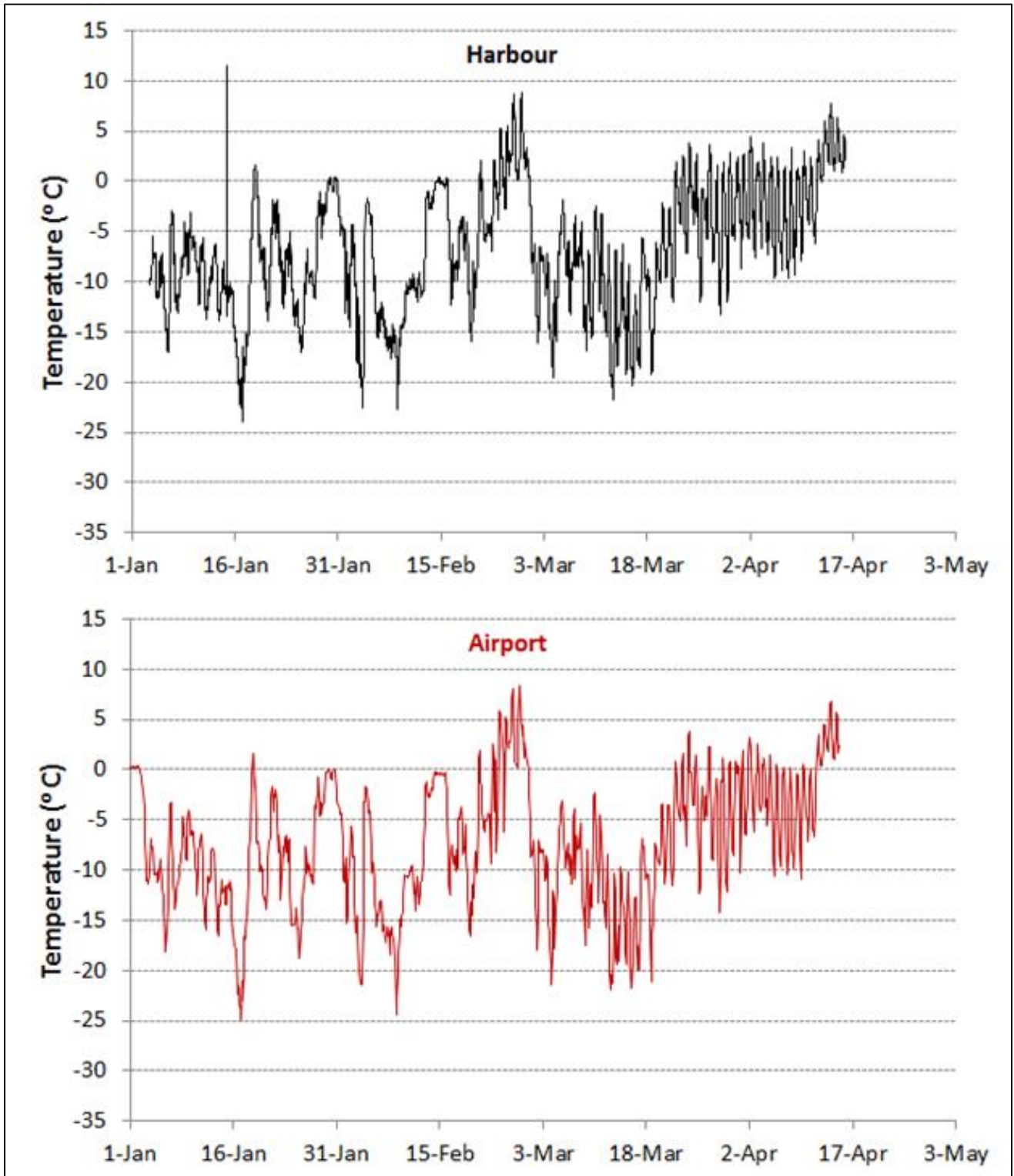


Figure G-1 Air temperature plots from data from Harbour and Airport weather stations of Lulea

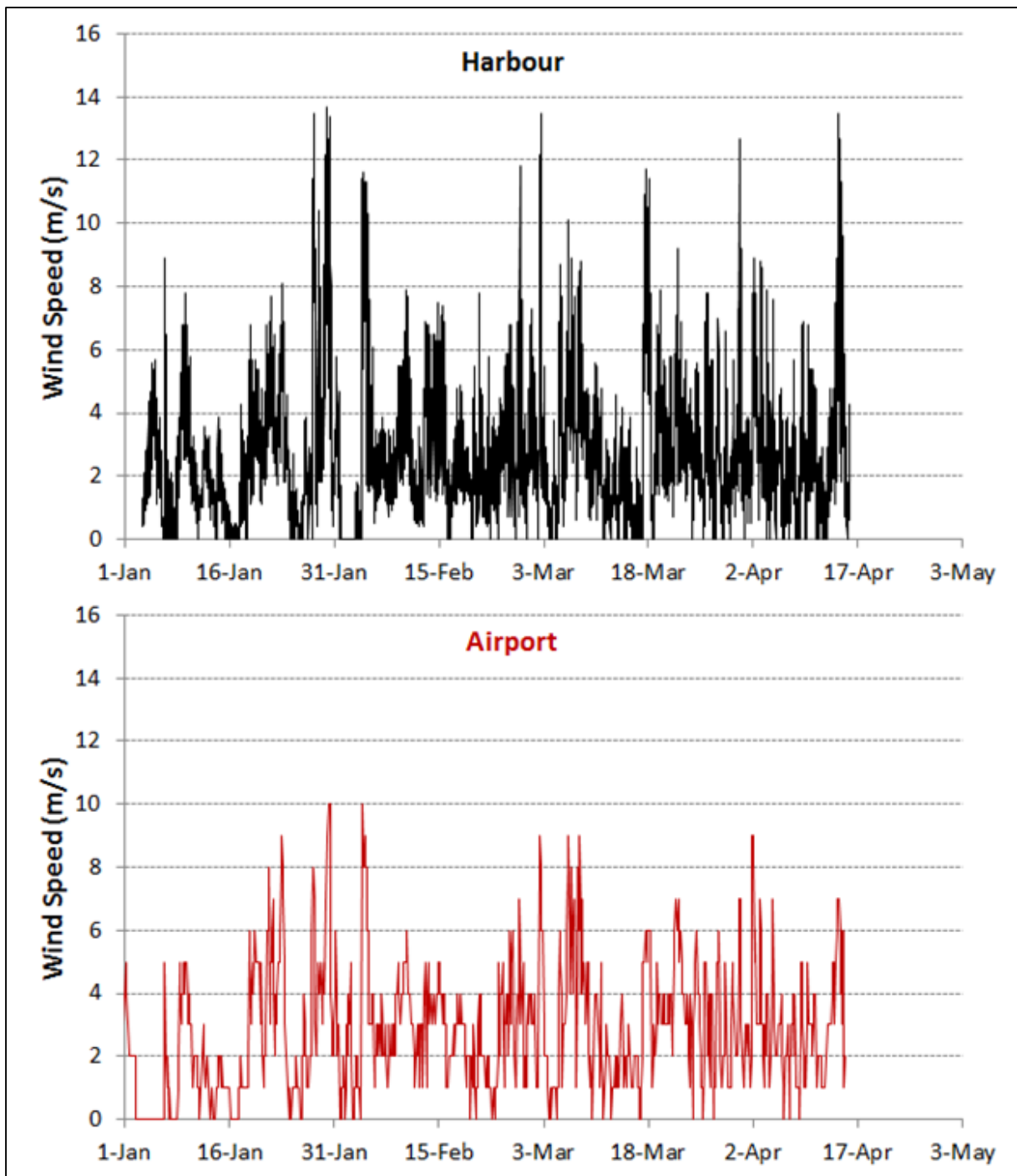


Figure G-2 Wind speed plots from data from Harbour and Airport weather stations of Lulea

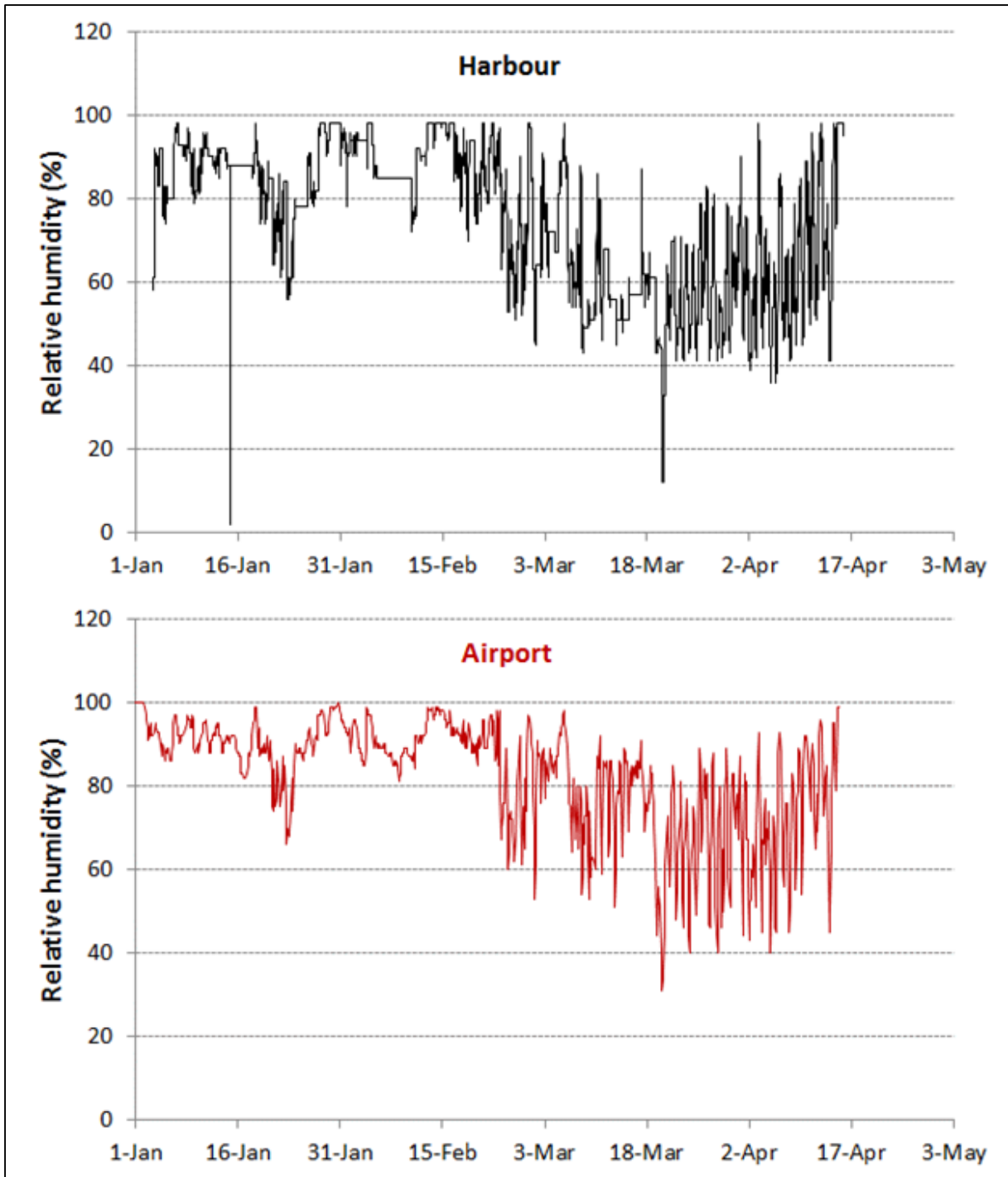


Figure G-3 Relative Humidity plots from data from Harbour and Airport weather stations of Lulea

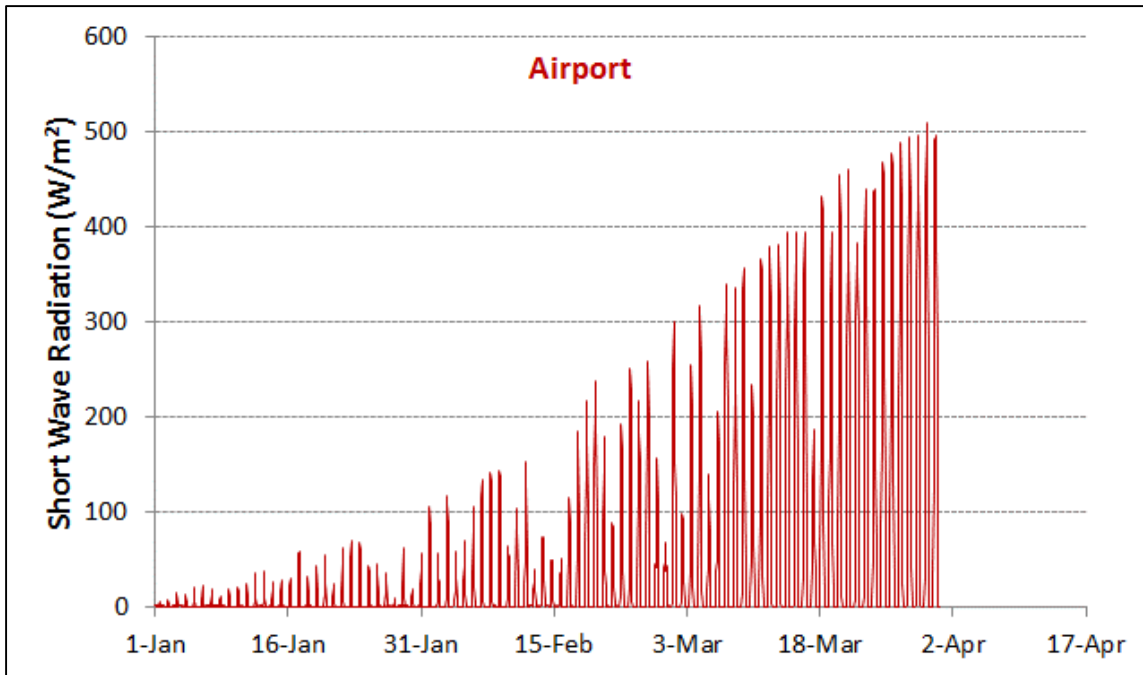


Figure G-4 Short wave radiation plot from data from airport weather station of Lulea

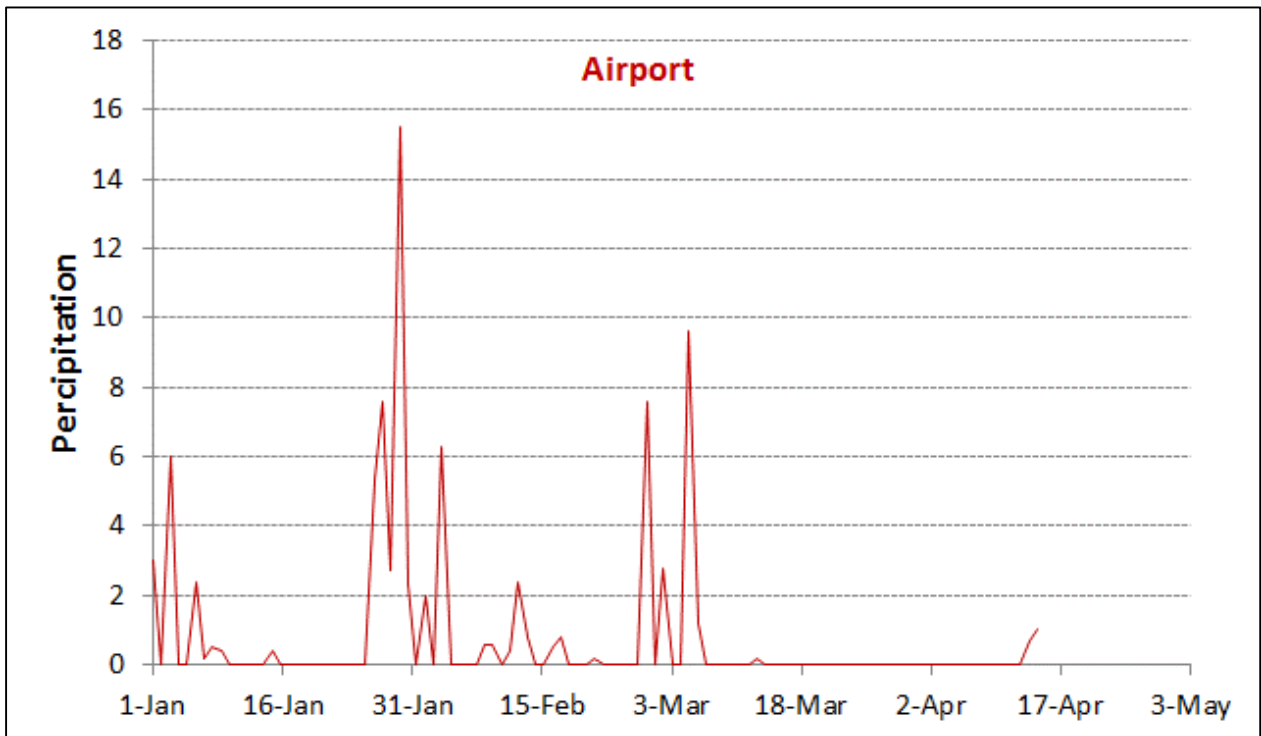


Figure G-5 Precipitation plot from data from airport weather station of Lulea. Precipitation is measured in (mm).

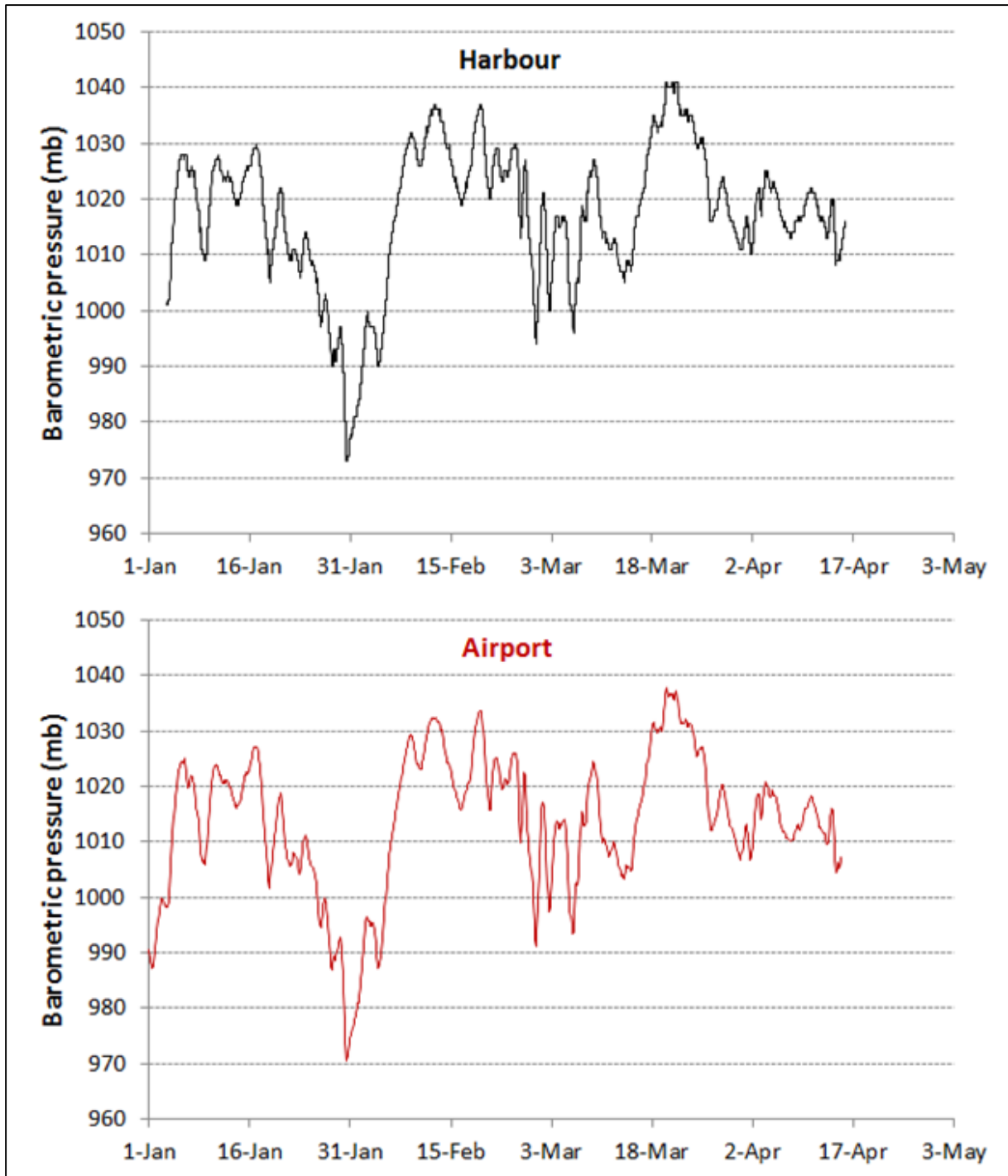


Figure G-6 Barometric pressure plots from data from the harbour and airport weather stations of Lulea

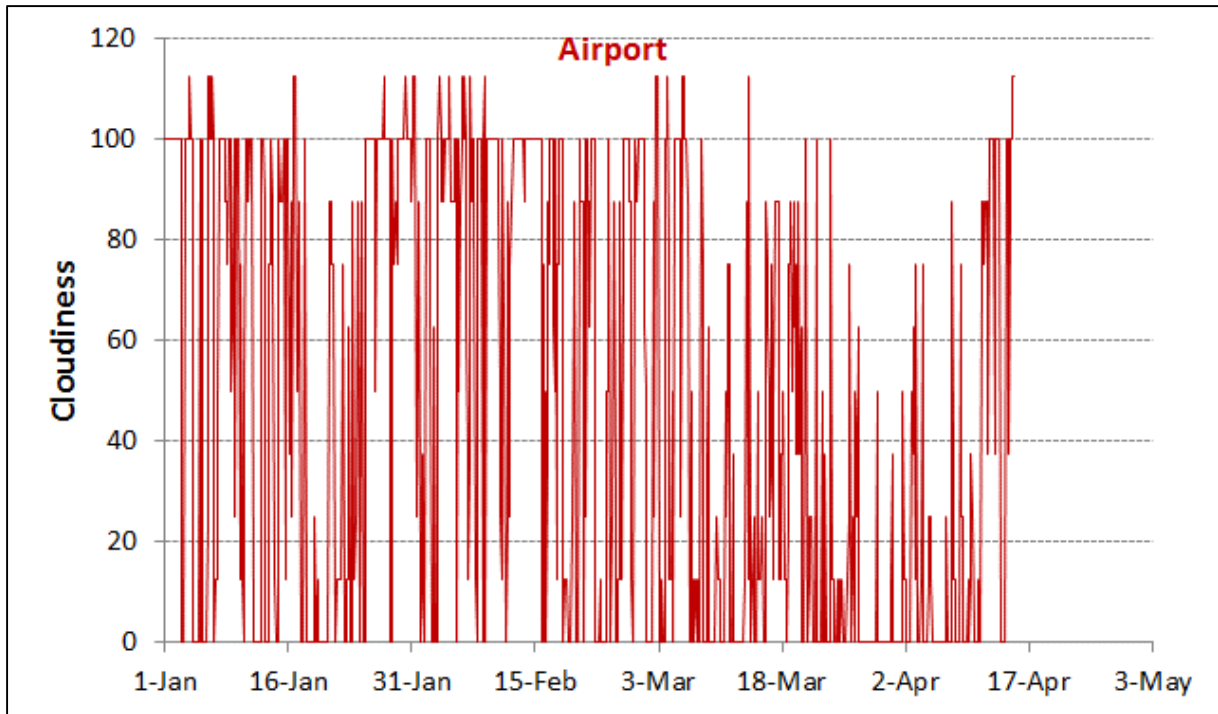


Figure G-7 Cloudiness plot from data from airport weather station of Lulea. Cloudiness is measured in (%) with (0%) meaning "clear sky" and (100%) meaning "completely overcast".

H. Ice thickness plots from Lulea field Measurements

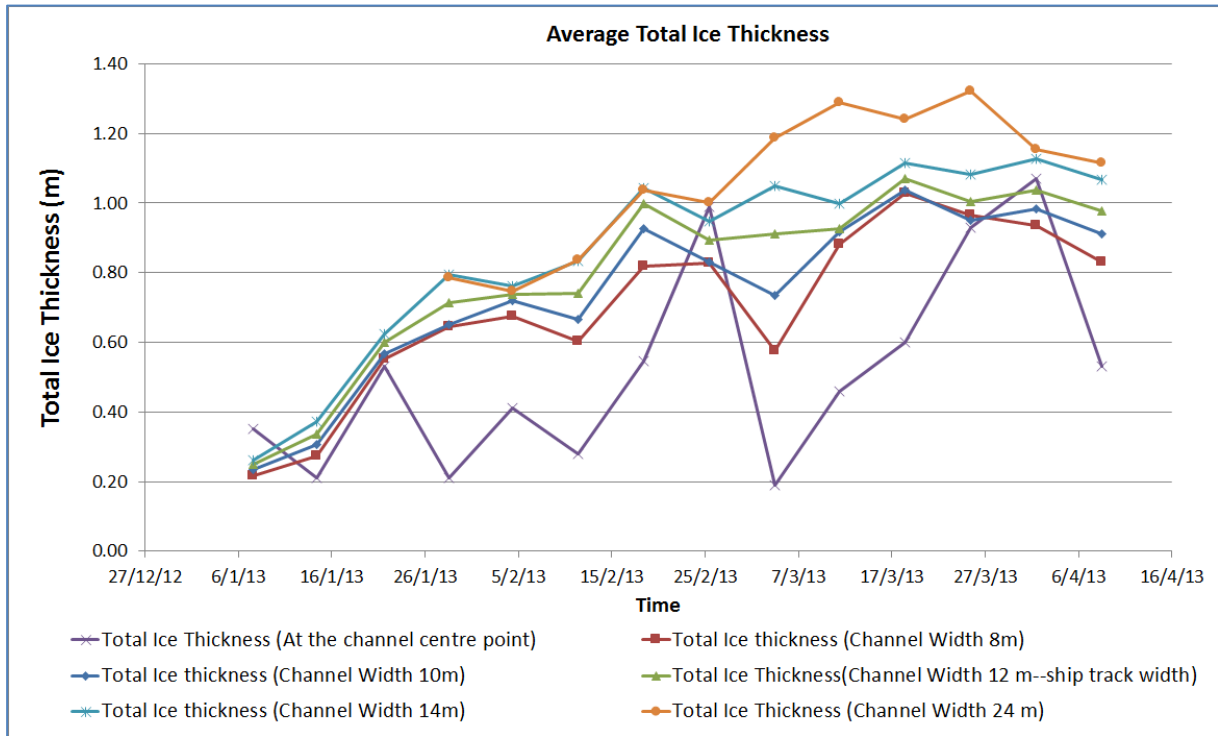


Figure H- 1 Average total ice thickness plots across different widths in the channel

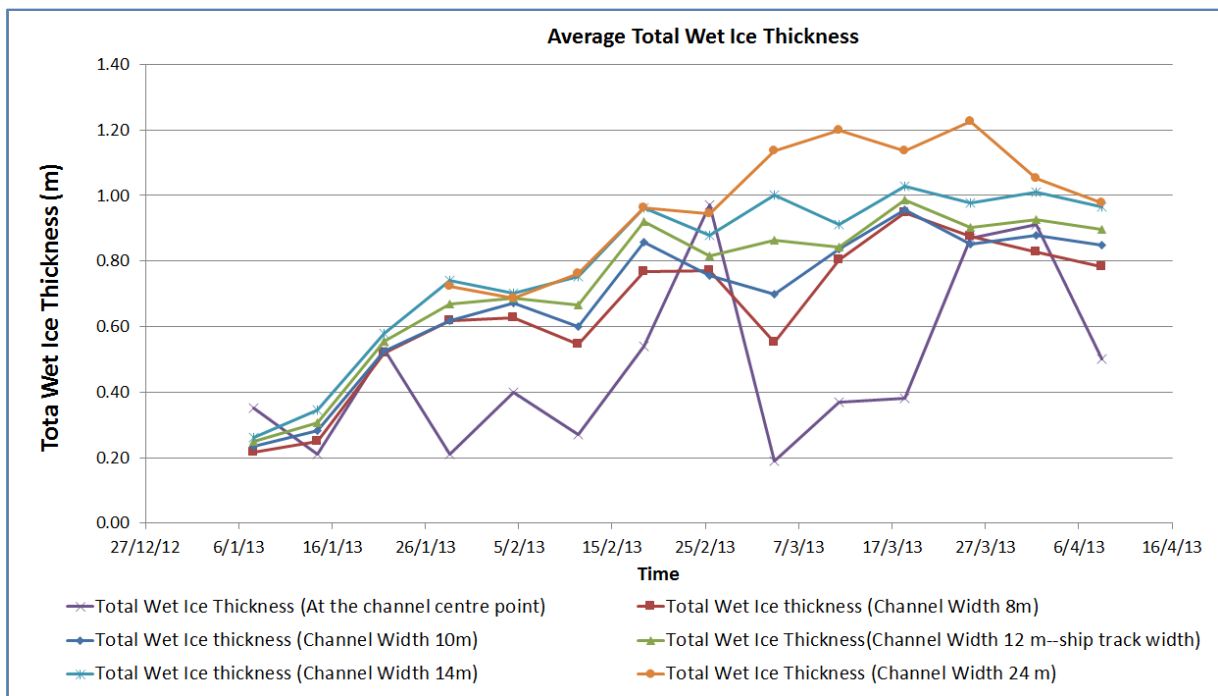


Figure H- 2 Average total wet ice thickness plots across different widths in the channel

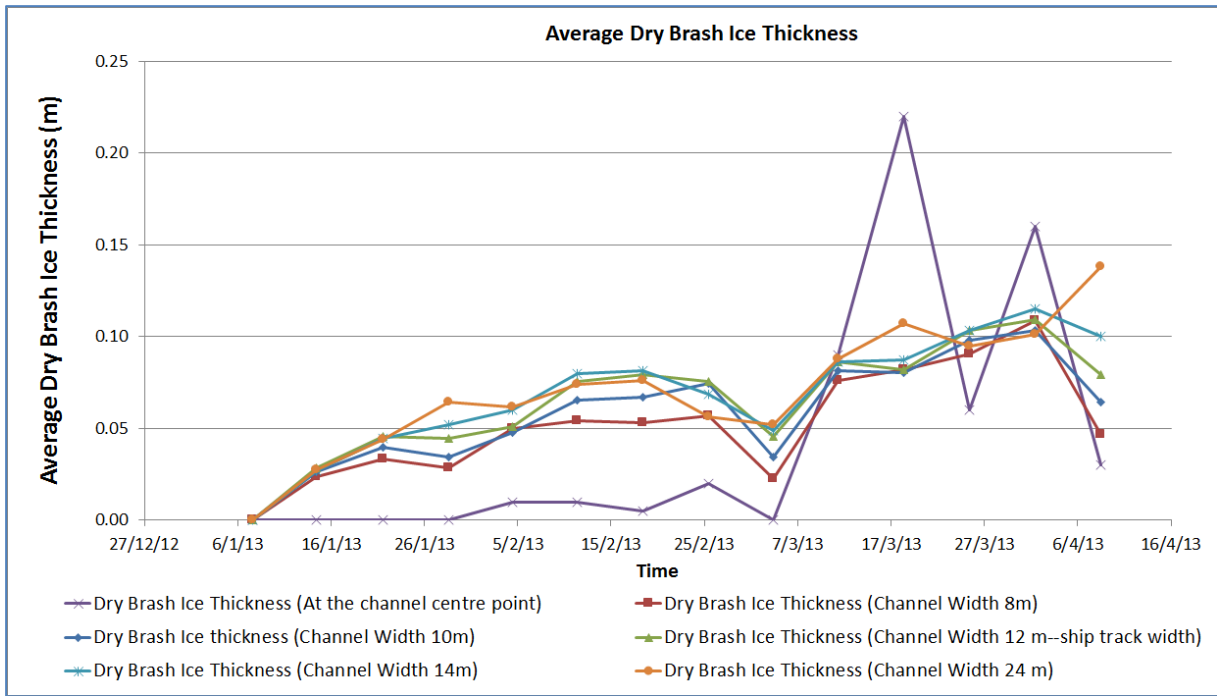


Figure H- 3 Average wet ice thickness plots across different widths in the channel

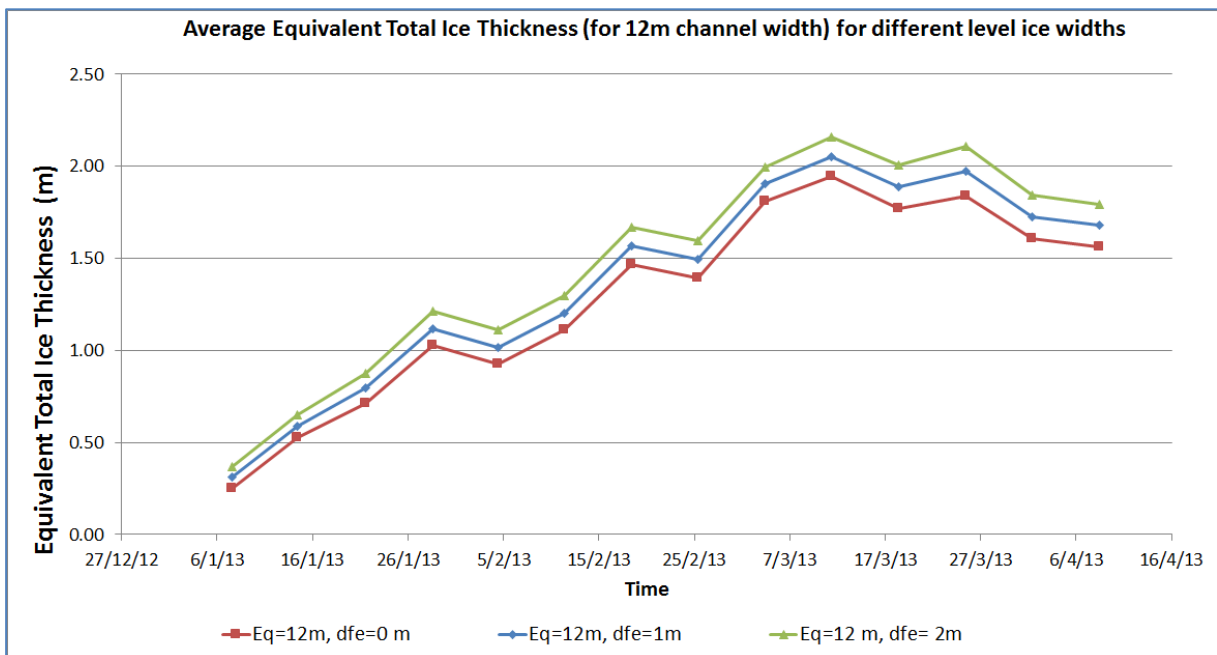


Figure H- 4 Total ice thickness equivalent plots for the 12 m ship track, for different distances of the level ice inner edge from the edge of the ship track. (dfe =0,1,2)

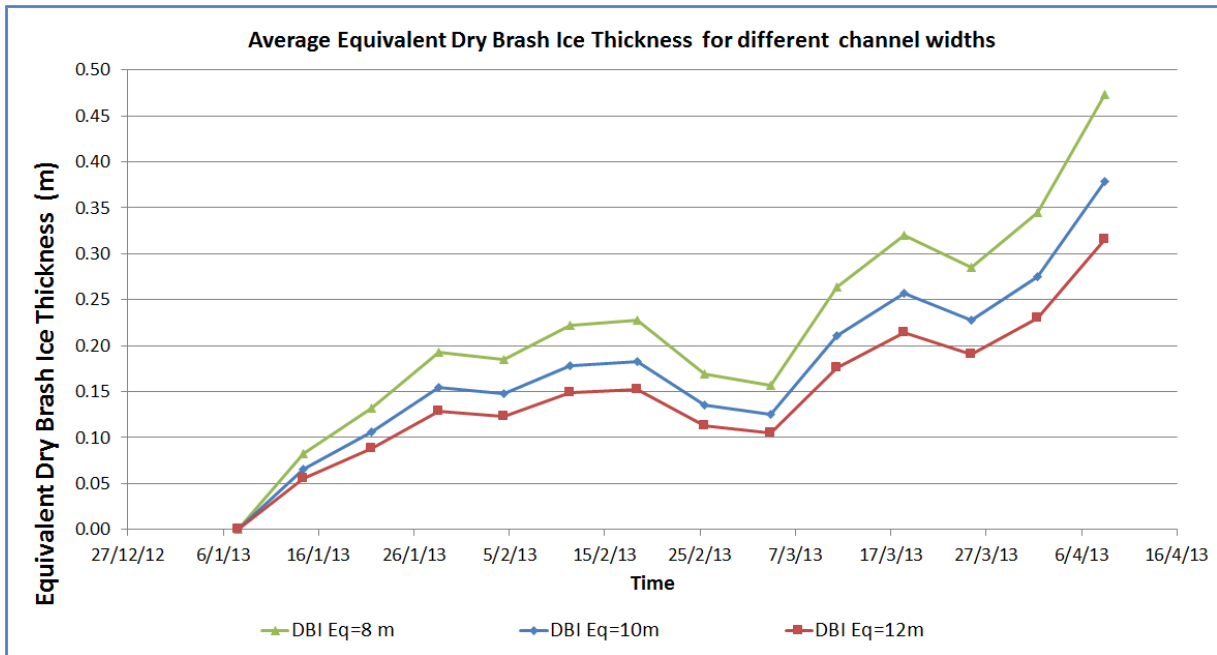


Figure H- 5 Average equivalent dry brush ice thickness plots for different channel widths

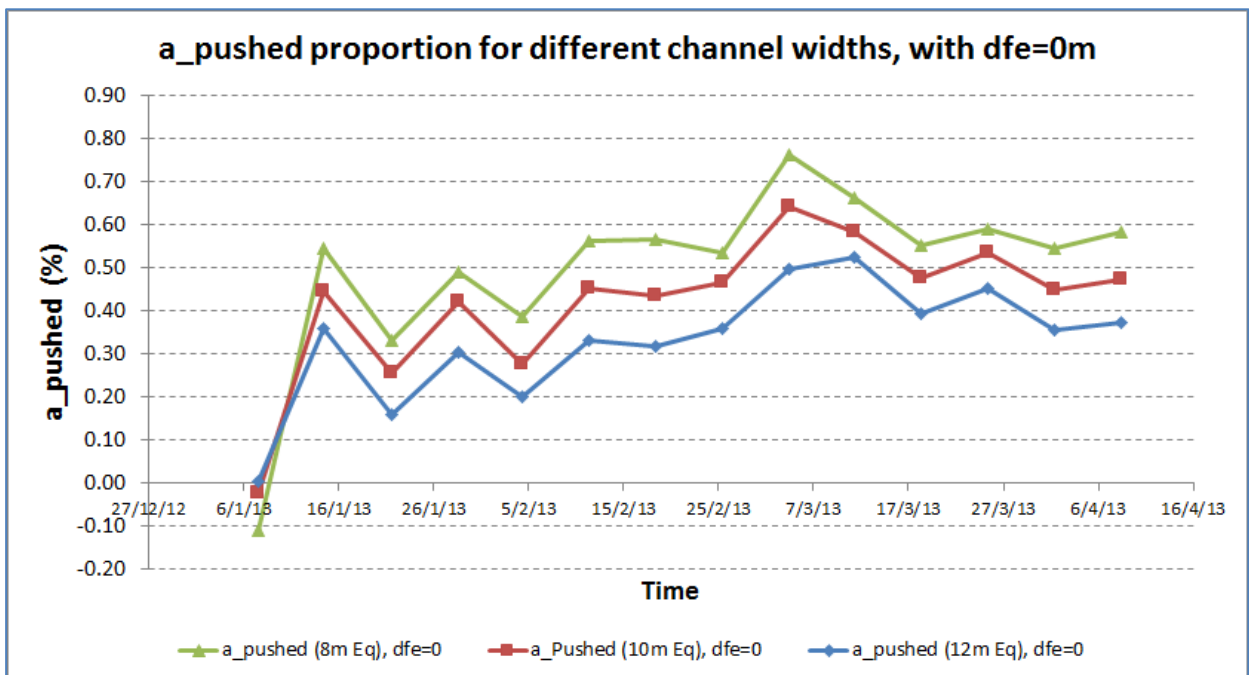


Figure H- 6 Calculation of the proportion of brush ice, a_{pushed} moved outside the shipping track, for different channel widths.

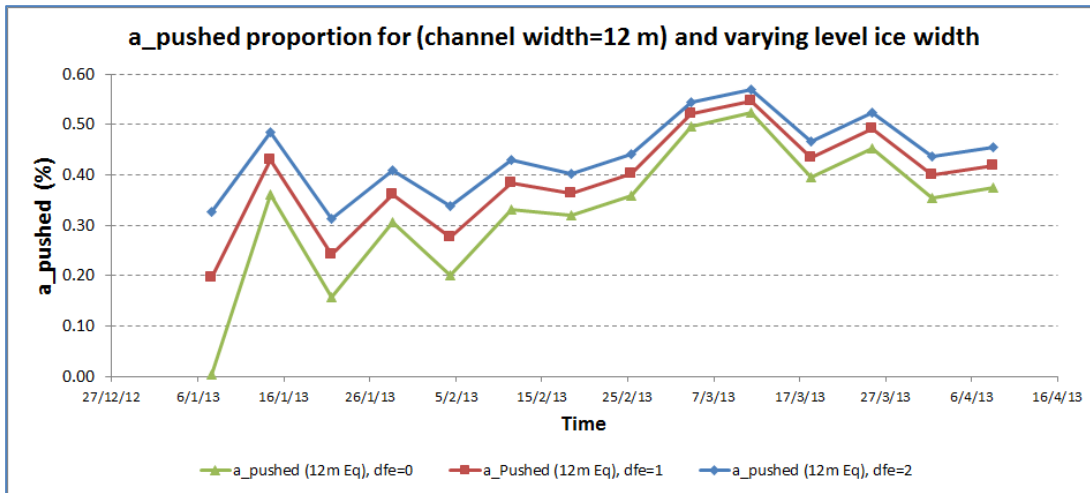


Figure H- 7 Calculation of the proportion of brash ice, a_{pushed} moved outside the shipping track, for ship track width (12m) using different possible distances (dfe) of the inner edge of the level ice from the edge of the ship track.

I. Brash Ice Profiles along the tested channel in Lulea

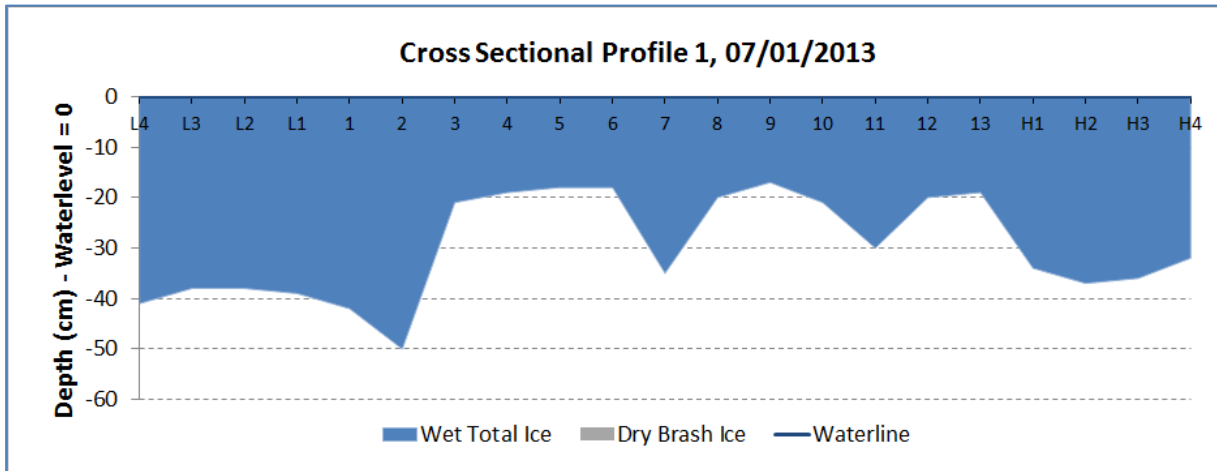


Figure I- 1 Cross sectional profile 1

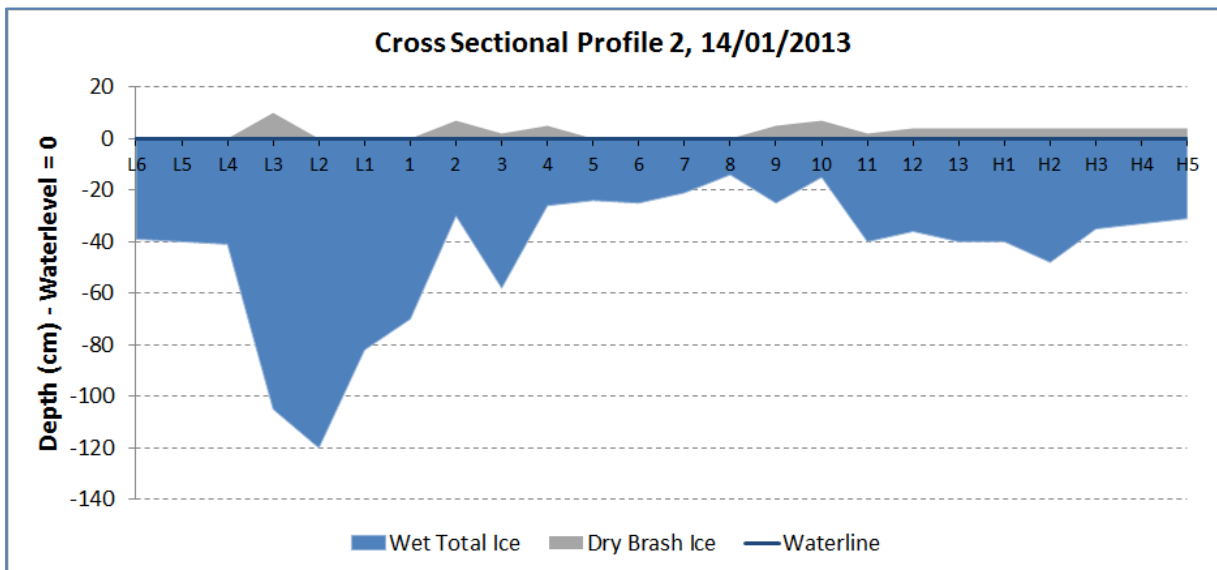


Figure I- 2 Cross sectional profile 2

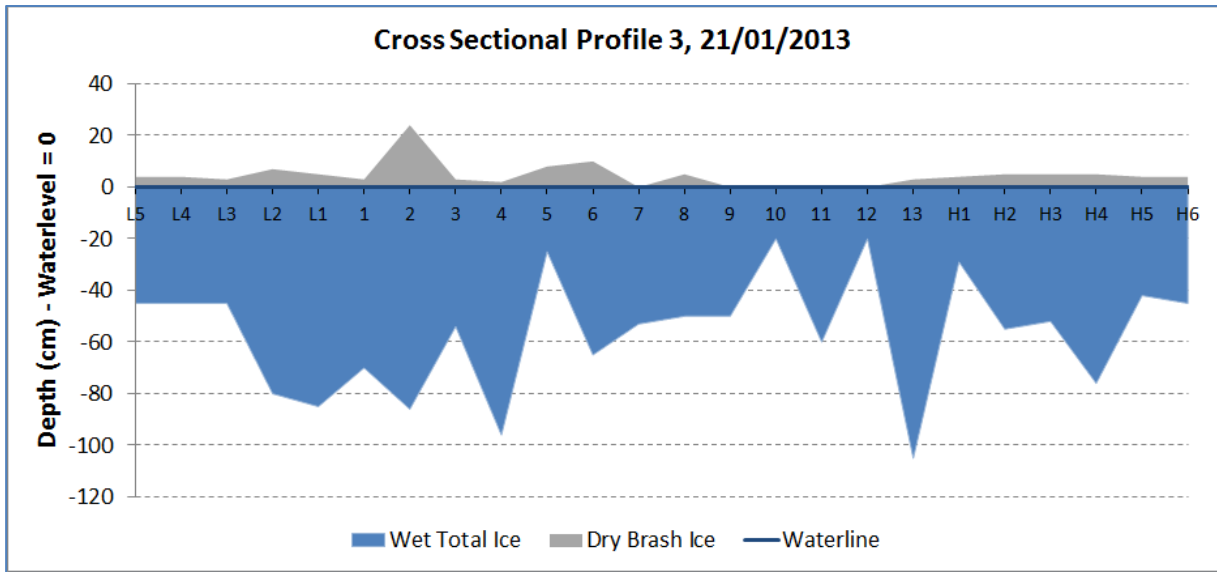


Figure I- 3 Cross sectional profile 3

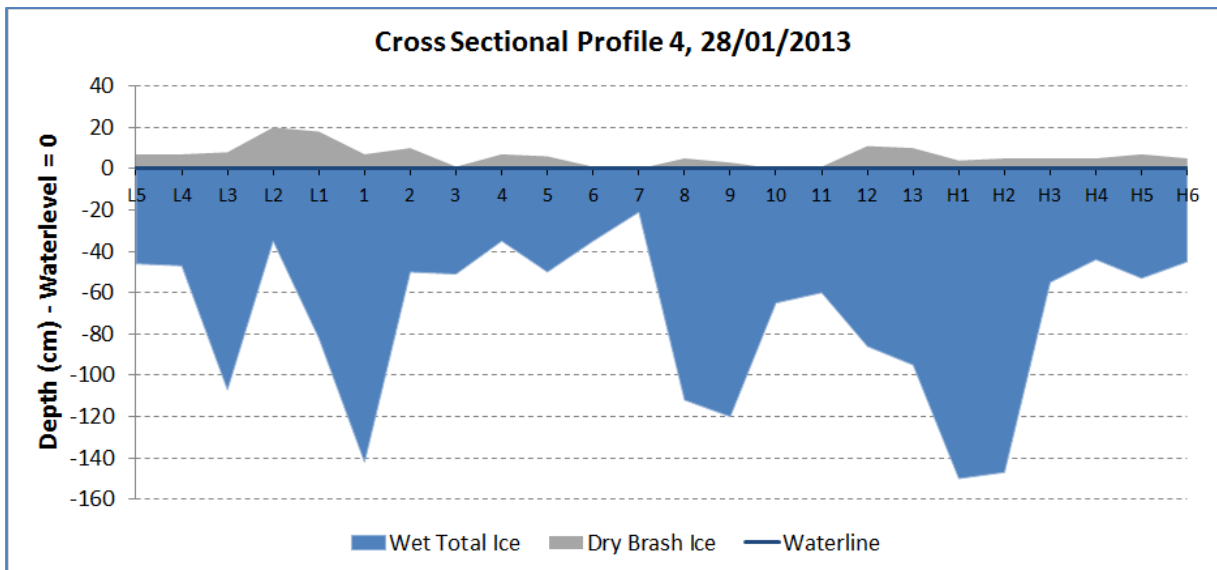


Figure I- 4 Cross sectional profile 4

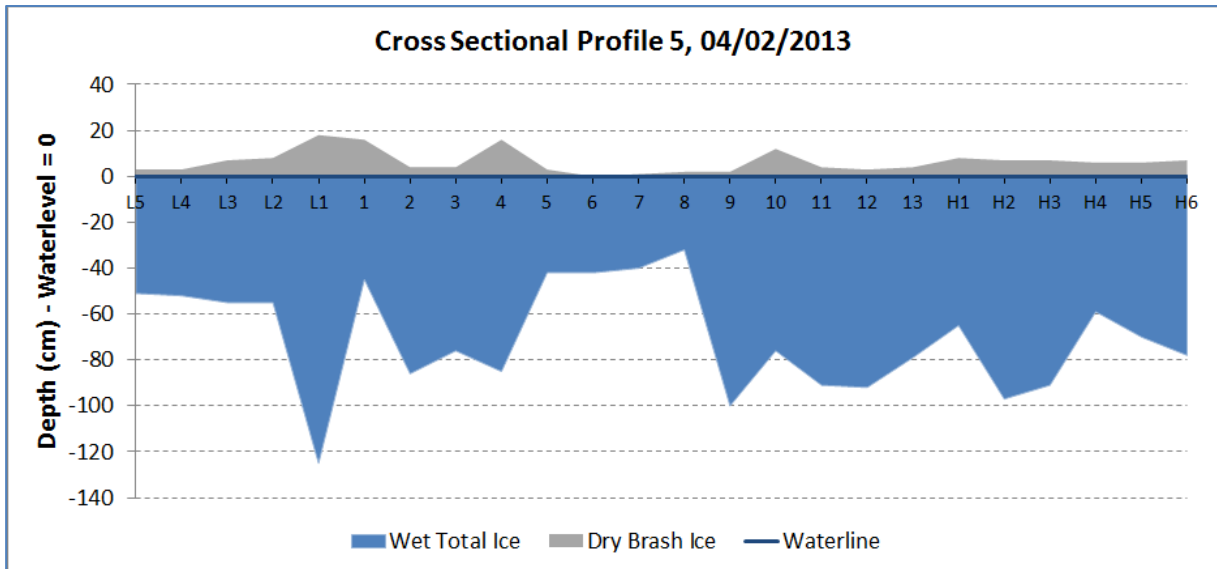


Figure I- 5 Cross sectional profile 5

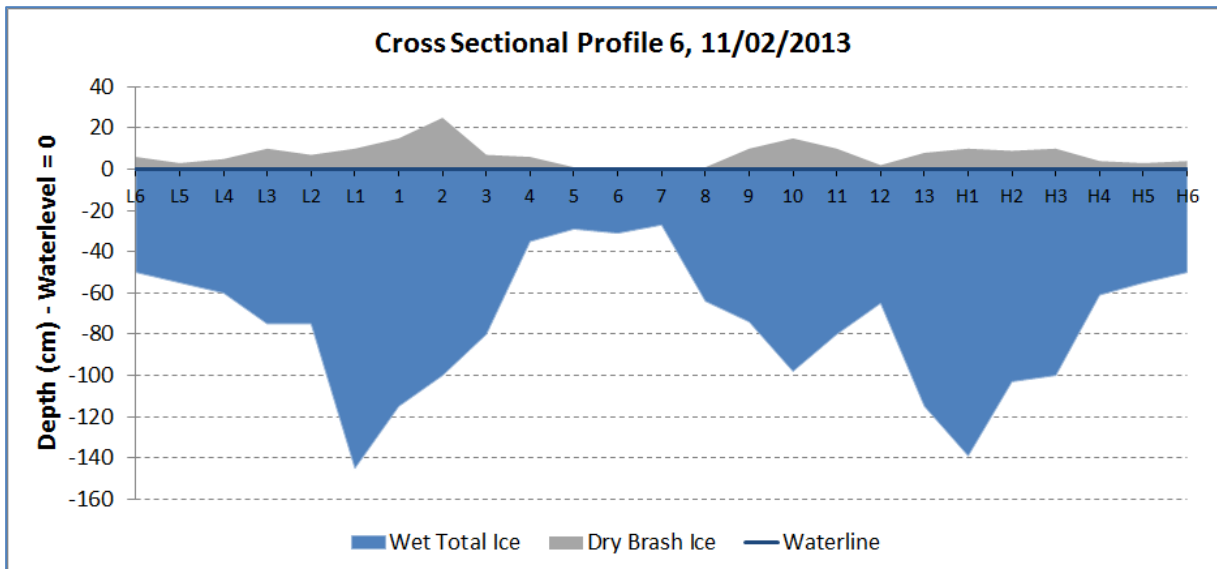


Figure I- 6 Cross sectional profile 6

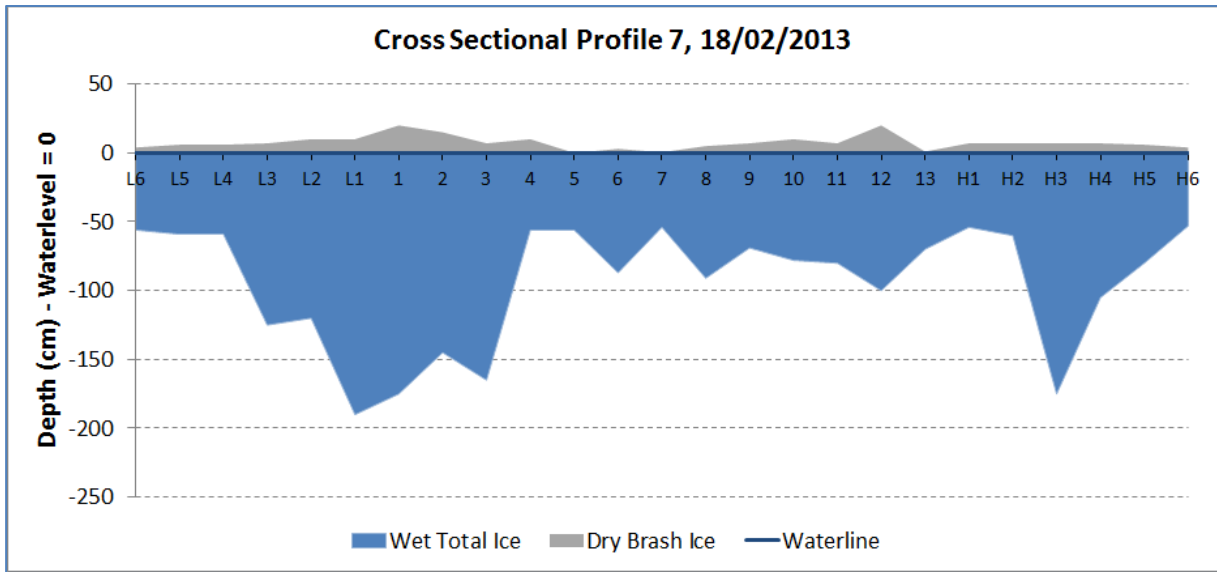


Figure I- 7 Cross sectional profile 7

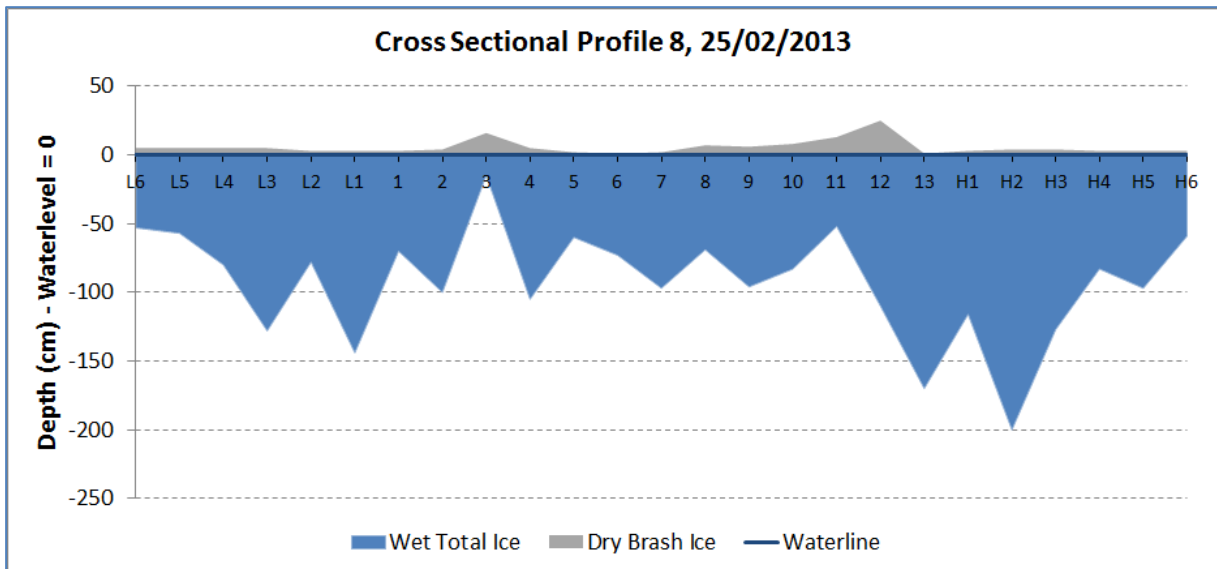


Figure I- 8 Cross sectional profile 8

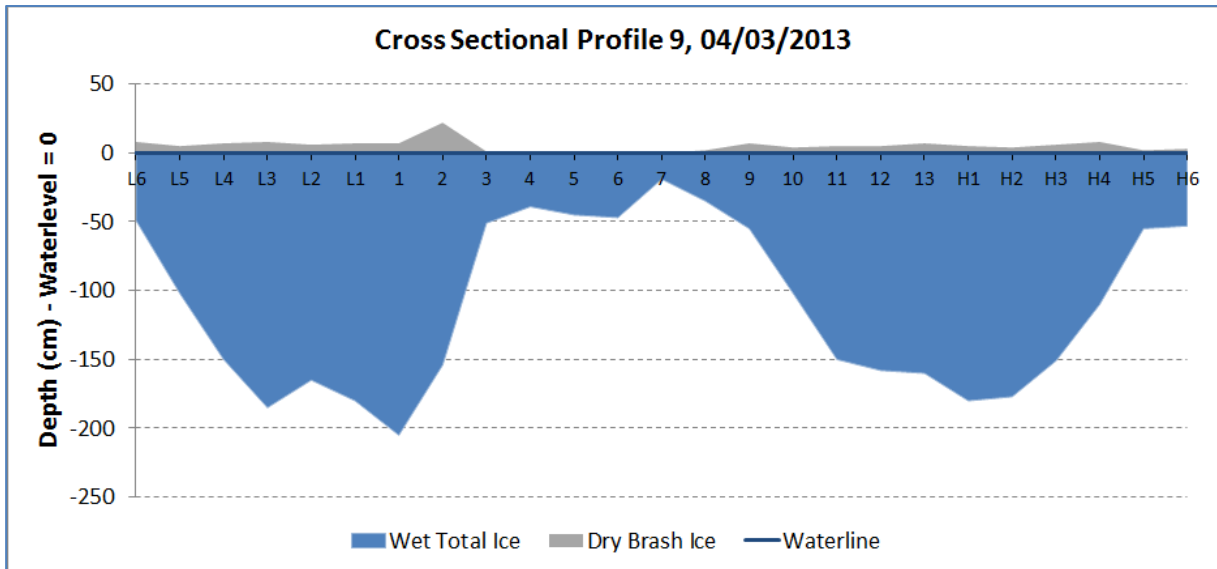


Figure I- 9 Cross sectional profile 9

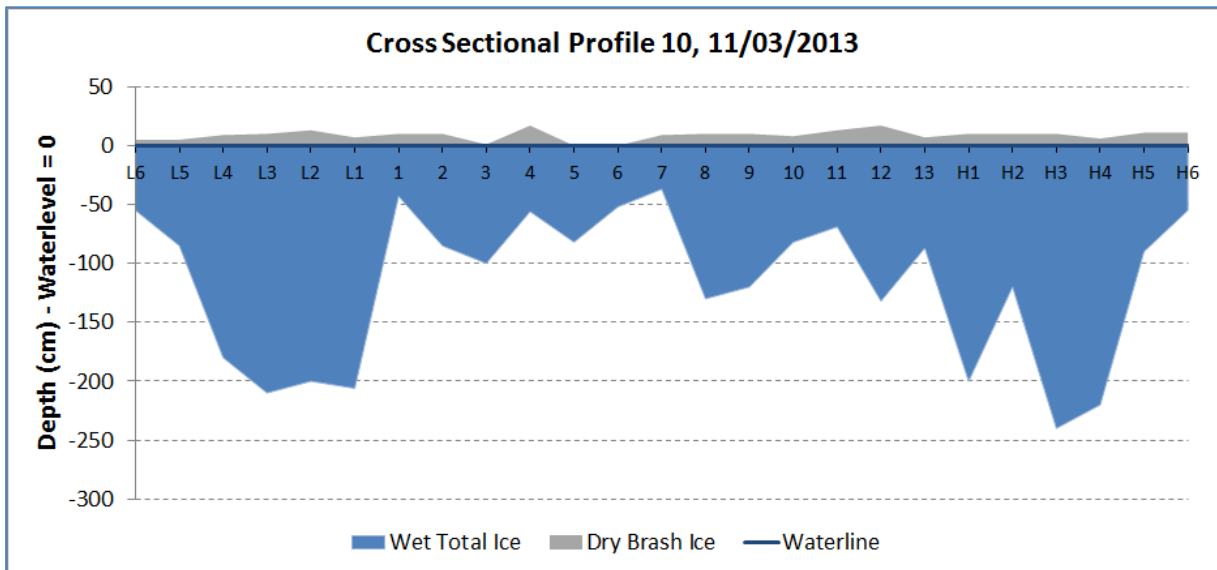


Figure I- 10 Cross sectional profile 10

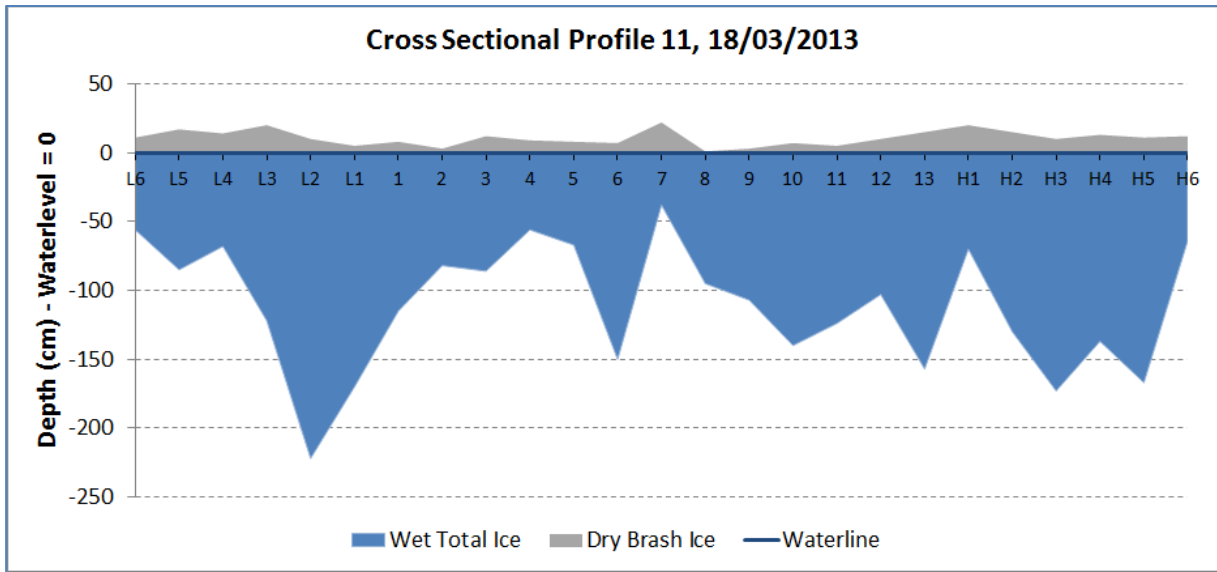


Figure I- 11 Cross sectional profile 11

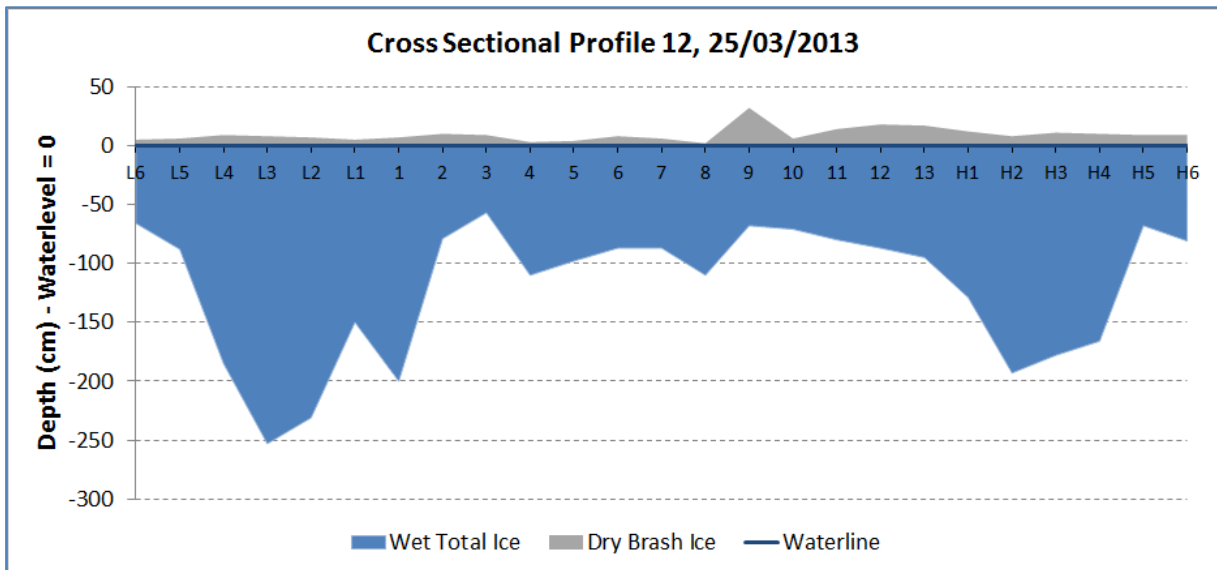


Figure I- 12 Cross sectional profile 12

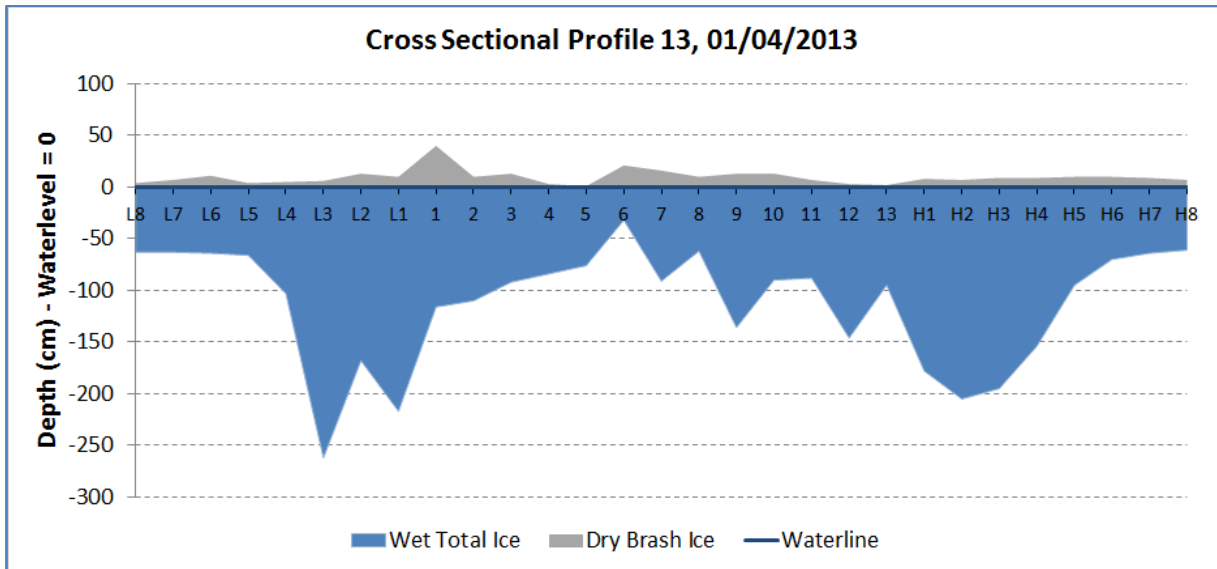


Figure I- 13 Cross sectional profile 13

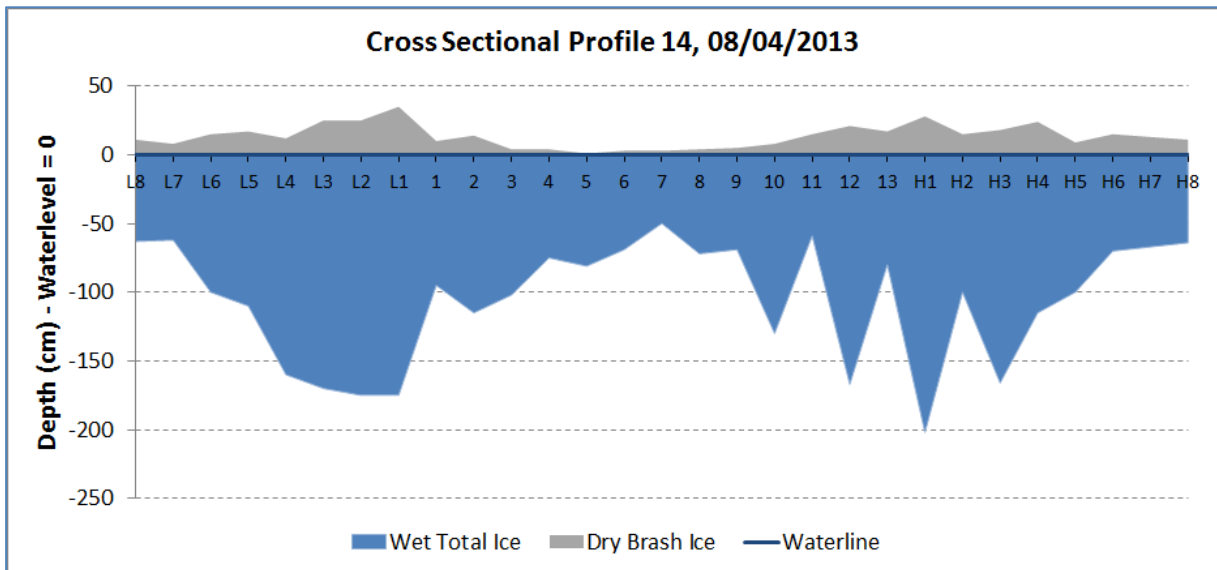


Figure I- 14 Cross sectional profile 14

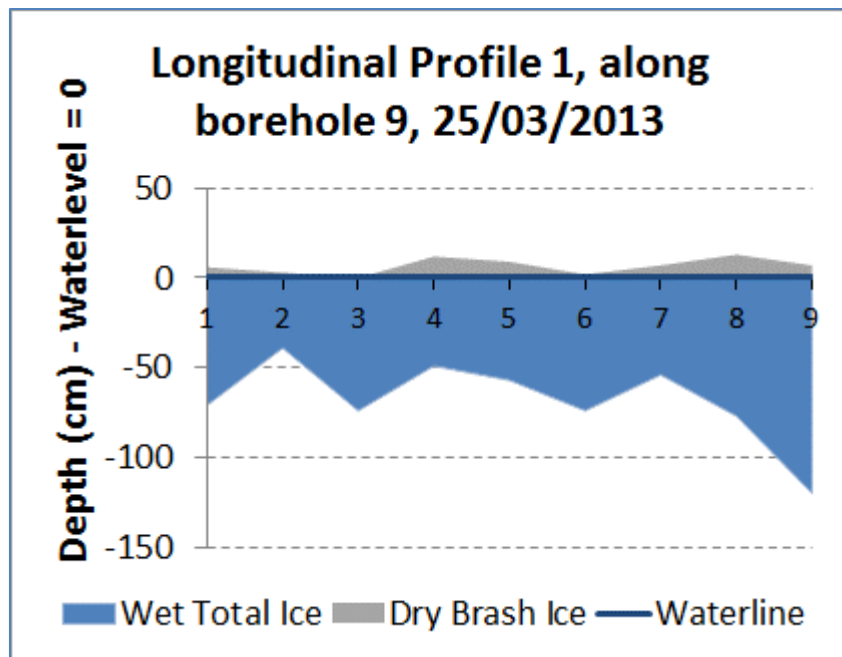


Figure I- 15 Longitudinal profile 1

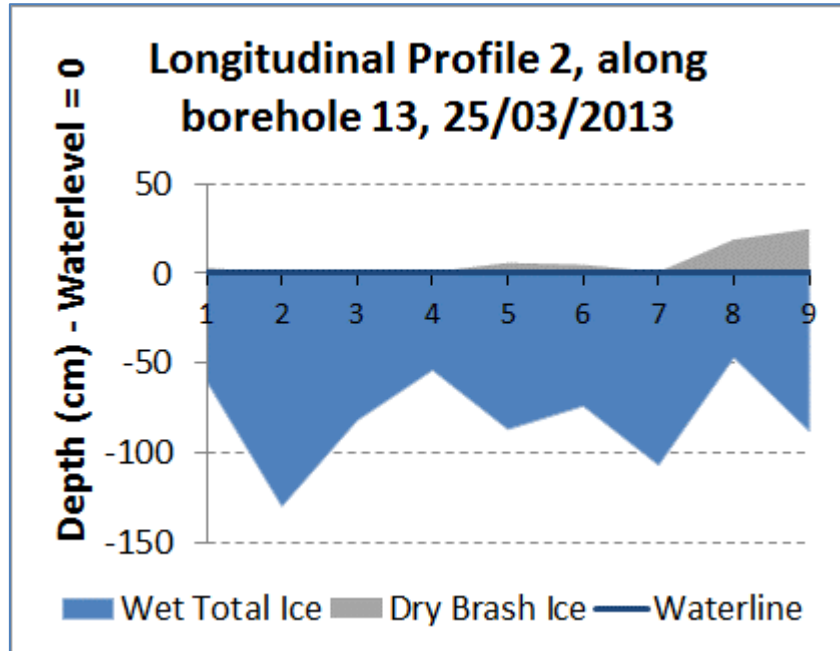


Figure I- 16 Longitudinal profile 2

J. BIMS application in different situations

1. BIGM 2 with dbi and no radiation application

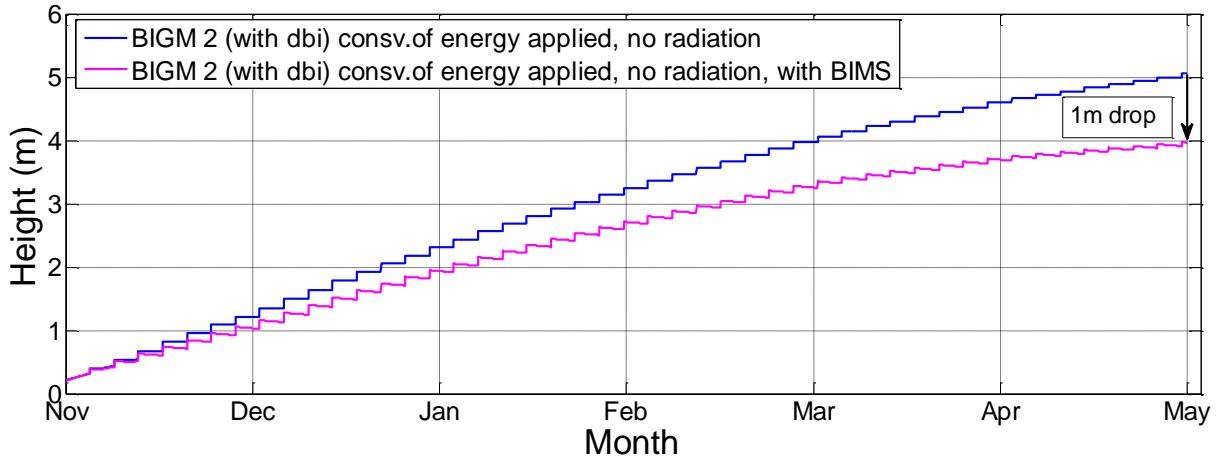


Figure J-1 BIMS application to decrease total ice thickness by 1m. BIGM 2 with freeboard and application of conservation of energy (porosity decrease after breakings), using Reference Sabetta case as input. No application of radiation. A BIMS flux of $Q_w=19 \text{ W/m}^2$ was needed to achieve a 1m decrease in the total ice (1m was melted from the brash ice at the bottom).

2. BIGM 2 no dbi and radiation application

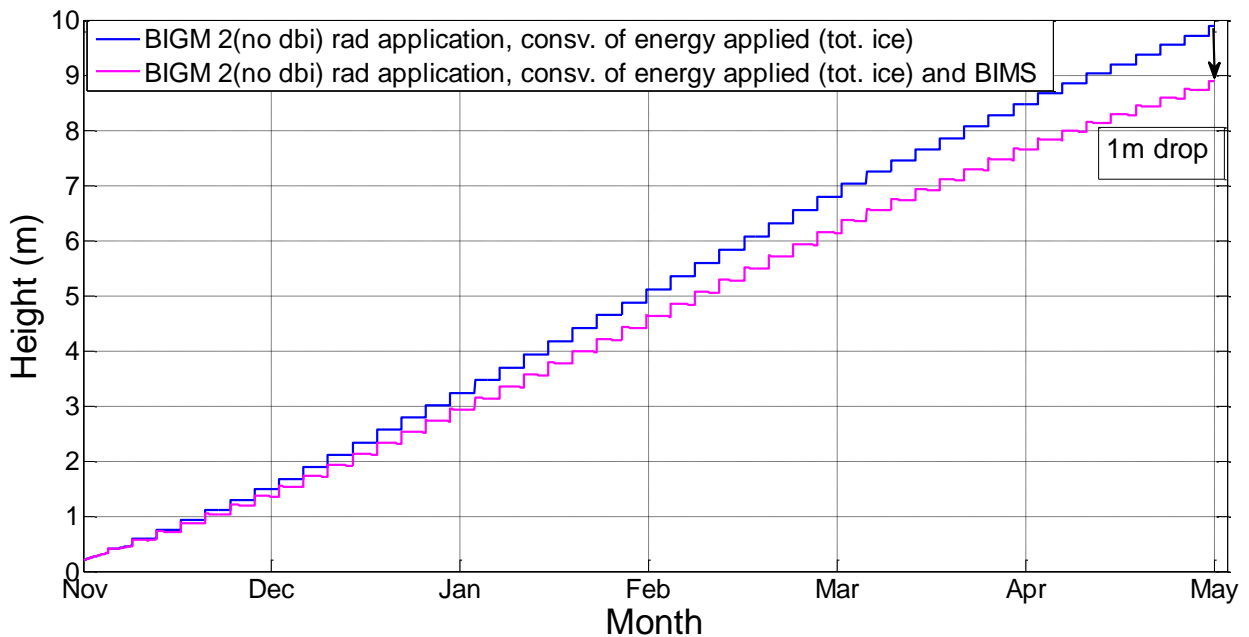


Figure J-2 BIMS application to decrease total ice thickness by 1m. BIGM 2 with no freeboard and application of conservation of energy (porosity decrease after breakings), using Reference Sabetta case as input with radiation. A BIMS flux of $Q_w=13 \text{ W/m}^2$ was needed to achieve a 1m decrease in the total ice (1m was melted from the brash ice at the bottom).

3. BIGM 2 no dbi and no radiation application

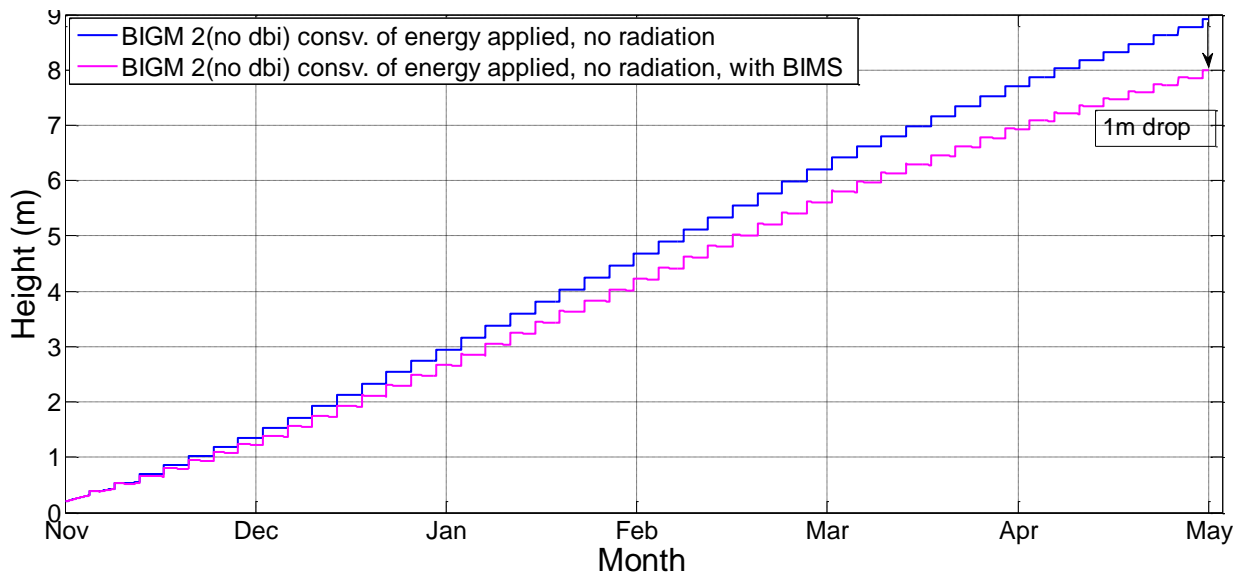


Figure J-3 BIMS application to decrease total ice thickness by 1m. BIGM 2 with no dry brash ice and application of conservation of energy (porosity decrease after breakings), using Reference Sabetta case as input. No application of radiation. A BIMS flux of $Q_w=12 \text{ W/m}^2$ was needed to achieve a 1m decrease in the total ice (1m was melted from the brash ice at the bottom).

References

- AARI. (2005). *General characteristics of hydrometeorological and ice conditions of the southwestern Kara Sea including the Ob'-Taz area*. Arctic and Antarctic Research Institute (AARI).
- Anderson, J. (1961). Growth Rate of Sea Ice. *Journal of Glaciology*, 3, 1170-1172.
- Ashton, G. (1973). Ice breaking by tow on the Mississippi River. *USA Cold Regions and Research and Engineering Laboratory*.
- Assur, A. (1958). Composition of sea ice and its tensile strength, in the Arctic Sea. *Publication by the National Academy of Sciences, USA*, 598, 106-138.
- Bitz, C., & Lipscomb, W. (1999). An energy conserving thermodynamic model of sea ice. *Journal of Geophysical Research*, 104, (C7), 15,699-15,677.
- Bloquin [1], R. (2013). *Brash Ice growth modelling: Specification file*. Bertin Technologies.
- Bloquin [2], R. (2013). *Brash Ice Growth Modelling: Definition File*. Bertin Technologies.
- Bloquin [3], R. (2013). *Brash Ice Growth modelling: Parametric study-synthesis and analysis of first results*. Bertin Technologies.
- Bloquin [4], R. (2013). *Brash Ice Management in Sabetta Harbour : Results and Synthesis*. Bertin Technologies.
- Bloquin, R. (2014). *BIMS pre-feed study for Sabetta port MOF*. Bertin Technologies.
- Cheng, B. (2002). *On the modelling of sea ice thermodynamics and air-icecoupling in the Bohai sea and the Baltic Sea*. University of Helsinki, May 2002.
- Deardorff, J. (1968). Dependence of air-sea transfer coefficients on bulk stability. *Journal of Geophysical Research*, 73(8), 2549–2557.
- Ebert, E., & Curry, J. (1993). An intermediate one-dimensional thermodynamic sea ice model for investigating ice-atmosphere interactions. *Journal of Geophysical Research*, 98(C6), 10,085-10,109.
- Ettema, R., & Huang, H.-P. (1990). *Ice Formation in Frequently Transited Navigation Channels*. USA cold regions Research and Engineering Laboratory. Retrieved December 1990
- Flato, G., & Brown, R. (1996). Variability and Climate sensitivity of landfast Arctic sea ice. *Journal of Geophysical Research*, 98(C6), 10,085-10,109.
- Fletcher, J. (1965). *The Heat Budget of the Arctic Basin and its relation to climate*. Santa Monica, California: The Rand Corporation.
- Hoobs, P. (1974). *Ice Physics*. Oxford, Oxford, England: Clarendon Press.
- Huwald, H. (2005). A multilayer sigma-coordinate thermodynamic sea ice model: Validation against Surface Heat Budget of the Arctic Ocean (SHEBA)/Sea Ice Model Intercomparison Project Part 2 (SIMIP2) data. *Journal of Geophysical Research, Volume 110, Issue C5*.

- Jobson, H. (1973). The dissipation of excess heat from power systems. *American Society of Civil Engineers Journal, Div 99*, 89-103.
- Kannari, P. (1983). Measurements of Characteristics and propulsion performance of a ship in ice-clogged channels. *Proceedings, 7th International conference on Port and Ice Engineering under Arctic Conditions. 2*, pp. 600-609. Helsinki, Finland: Espo Finland: Valtion teknillinen tutkimuskeskus.
- Leparanta, M. (1992). A review of Analytical models of sea ice growth. *Atmosphere-Ocean*, 123-138.
- Marshunova, M. (1961). Principal characteristics of the radiation balance of the underlying surface and of the atmosphere in the Arctic. *Proceedings of the Arctic Antarctic Research Institute*, 229. Translated by the Rand Corporation.
- Maykut, G. (1977). The optical properties of ice and snow in the arctic basin. *Journal of Glaciology*, 18(80), 445-463.
- Maykut, G. (1978). Energy exchange over young sea ice in the central Arctic. *Journal of Geophysical Research*, 83(67), 3646-3658.
- Maykut, G. (1982, September 20). Large scale heat exchange and ice production in the central Arctic. *JOURNAL OF GEOPHYSICAL RESEARCH*, 87(NO,C10), 7971-7984.
- Maykut, G., & Untersteiner, N. (1971). Some results from a time dependent, thermodynamic model of sea ice. *Journal of Geophysical Research*, 76, 1550-1575.
- Meurant, O. (2012). *Port Operation Simulations ARENA Model- Functional Specification*. Arelia.
- MOENMARIN. (2015). *Viscaria Tugboat Specifications*. Retrieved from MOENMARIN: <http://www.moenmarin.no/index.php/slepebater-tugs/119-viscaria>
- Saarinen, S., Suojanen, R.-A., & Eranti, E. (2011). *Concept of port ice control system and terminal fleet for the Sabetta LNG terminal*. Helsinki: Aker Arctic Technology Inc.
- Sandkvist, J. (1980). Observed Growth of Brash Ice in ship's tracks. *Research report series, No 42*. Lulea, Sweden: Water Resources Engineering, University of Lulea.
- Sandkvist, J. (1978). Problems in keeping year-round navigation in the Lulea Harbour. *Proceedings, IAHR Symposium on ice problems*. Lulea: Water Resources Engineering, University of Lulea Sweden.
- Sandkvist, J. (1978). Problems in keeping year-round navigation in the Lulea Harbour. *Proceedings, IAHR Symposium on Ice problems. 42*. Lulea, Sweden: Water Resources Engineering, University of Lulea.
- Sandkvist, J. (1981). Conditions in brash ice covered channels with repeated passages. *Proceedings, 6th international Conference on Port and Ocean Engineering under Arctic Conditions (POAC81)* (pp. 244-252). Quebec, Canada: Universite Laval.

- Sandkvist, J. (1982). Vertical block sizes in brash ice covered channels. *Water Resources Engineering, University of Lulea, Research Report Series, A, No.101*. Lulea, Sweden.
- Sandkvist, J. (1986). Brash Ice behaviour in frequented ship channels. *Water Resources Engineering, University of Lulea, Research Report Series A, No.139*. Lulea, Sweden.
- Schwarzacher, W. (1959). Pack-ice studies in the Arctic Ocean. *Journal of Geophysical Research, Volume 64(12)*, 2357-2367.
- Semtner, A. (1976). A model for the thermodynamic growth of sea ice in numerical investigations of climate. *Journal of Physical Oceanography*, 379-389.
- Stefan, J. (1891). Über die Theorie der Eisbildung, insbesondere über Eisbildung im Polarmeere. *Ann. Phys proceedings*, (pp. 269-286).
- Tuovinen, P. (1978). The size distribution of ice blocks in a broken channel. *Helsinki University of Technology, Ship Hydrodynamics Laboratory, Memorandum M-78*. Otaniemi, Finland.
- Ukita, J., & Martinson, D. (2001). An efficient adjustable-layering thermodynamic sea-ice model formulation for high-frequency forcing. *Annals of glaciology*, 33, 253-260.
- Untersteiner, N. (1961). On the mass and heat budget of Arctic Sea Ice. *Arch. Meteorol. Geophys. Bioklimatol., Ser. A*, 151-182.
- Westerberg, V. (2013). *Brash Ice Field Trials in Port of Lulea 2012/ 2013*. Goteborg: SSPA.
- Williams, M., & Lattes, P. (2012). *Metocean conditions at Ob' Bay*. DEV/TEC/GEO-ECO11-082. Retrieved November 2012